Chiroptical properties of helical-shaped π-conjugated systems based on five- and six-membered rings

A thesis submitted by

Bishwanath Mahato

to

Indian Institute of Technology Guwahati

in fulfillment of the requirements for the degree of

Doctor of Philosophy

Department of Chemistry

Indian Institute of Technology Guwahati

Guwahati 781039

INDIA

June 2023

Chiroptical properties of helical-shaped π-conjugated systems based on five- and six-membered rings

Doctoral Thesis

Author:

Bishwanath Mahato

Roll No. 176122020

Supervisor:

Dr. Aditya N. Panda

Department of Chemistry

Indian Institute of Technology Guwahati

Guwahati 781039

INDIA

June 2023

Declaration

I, Bishwanath Mahato, declare that this thesis titled, 'Chiroptical properties of helical-shaped π-conjugated systems based on five- and six-membered rings' and the work presented in it are my own. I confirm that this work was done by me during the period from July 2017 to February 2023 in candidature for the degree of Doctor of Philosophy at Indian Institute of Technology Guwahati under the guidance and supervision of Dr. Aditya N. Panda, professor, Department of Chemistry. Any part of this thesis has not previously been submitted for a degree or any other qualification at this Institution or any other university/institution. Where I have consulted the published work of others, this is always clearly attributed. I have acknowledged all main sources of help.

Signed: Bishwanath Mahato

Bishwanath Mahato

Date: 20/06/2023

Certificate

This is to certify that the thesis titled " *Chiroptical properties of helical-shaped π-conjugated systems based on five- and six-membered rings* " submitted for the award of degree of Doctor of Philosophy by **Bishwanath Mahato** is the record of research work carried out by him during the period July 2017 to February 2023 under my guidance and supervision. This work has not formed the basis for the award of any degree, diploma, associateship, fellowship or other titles in this Institution or in any other university/institution.

Signed:

Dr. Aditya N. Panda
Professor

Date: 20/6/23

Acknowledgements

First and foremost, I would like to express my sincere gratitude to my thesis advisor Dr. Aditya Narayan Panda for giving me the opportunity to work with him. I warmly appreciate his guidance, ideas, patience and contribution of time to my research work. I am thankful to him for his continuous support, motivation and encouragements throughout my PhD career. The lessons that I have learned in the last five years through his valuable advices will help me immensely in my future academic and personal life. I express my heartiest gratitude with profound respect to him for the excellent example he has shown as a good teacher and friendly supervisor.

I would like to thank my doctoral committee members, **Prof. Ashish Kumar Gupta**, **Dr. Manabendra Sarma** and **Prof. Parameswar K. Iyer** for their insightful comments, valuable suggestions and encouragements.

I would like to acknowledge the financial support from Indian Institute of Technology, Guwahati. I am very thankful to the Department of Chemistry for giving me the opportunity to work as a research scholar in this department. I acknowledge the computational facility from Param-Ishan, IIT Guwahati.

I gratefully recall the knowledge that I have gained from my university and school teachers. I am indebted to all of them.

I thank my labmates Mohd. Shavez, Iban, and Palak for their company and cooperation in lab.

I thank Bitan, Araghni, Bapan, Munendra, Laxmi raman, Sagir, Haobam Kisan Singh, Nasima, Tipu, Abu, Rupa, Ching Thain Moi, Sourav, Manoj, Kisan, Mukesh, Vivek, Mittunjay, Shantiram da, Sumit da, Sudip, Arindom, Buddhadev, Vinod, Debojit, Khadimul, and Retwik for motivating and encouraging me in my PhD days.

I am thankful to all of my school, university and IIT friends.

I wish to convey my heartiest thank to all my villagers who love me so much whenever I am in my village.

Finally and most importantly, I thank all the members of my big family, especially my parents, sister and grandmother for their unconditional support and encouragement.

I dedicate this thesis to respected teacher Dr. Aditya N. Panda and my parents.

Synopsis

Polycyclic aromatic hydrocarbons (PAH) show interesting optical, electronic and photophysical properties. Among these, the non-planar PAHs with twisted π-systems have been in increasing demand due to their potential in different fields of material science. Helical shaped molecules are inherently chiral, and therefore, in recent times, a large number of helical shaped systems have been developed. Widely used pristine helicenes possess lower values of fluorescence quantum yields (Φ_{FL}) and dissymmetry factor for emission (g_{CPL}). Literature shows that designing of light-emitting molecules with higher values of Φ_{FL} and g_{CPL} is not an easy task. In recent times, various types of modified helical structures including multiple helicenes are reported. In case of single-helicenes, typical modifications are based on either increasing the number of π-conjugated rings (i.e., either helical length or lateral extension) or substitution of hydrogen atoms by other functionals groups. At this juncture, computational studies are very useful for studying and designing molecules with improved chiroptical properties. In this thesis, excited-states properties of screw-shaped pyridine-thiophene oligomers and various helicenes are reported. Effects of helical/lateral length extension and fluorine substitution on the ground and excited state properties are reported. Methods such as Density Functional Theory (DFT), time-dependent DFT (TD-DFT) and wavefunction based algebraic diagrammatic construction scheme of second order (ADC(2)) are used in these studies. Below we provide a chapter-wise overview of the thesis.

Chapter 1: Introduction

Chapter 1 provides an overview of chirality in helical systems, types of helical systems and their various applications. Towards the end of the chapter, I discuss the motivation behind the present work and provide an outline of the thesis.

Chapter 2: Methodology

This chapter presents the theoretical and computational methods used in the thesis. Basics of the Hartree-Fock theory, DFT and TD-DFT are briefly mentioned. Few commonly used DFT functionals for studying ground and excited state properties are also mentioned. In addition, an introduction to the algebraic diagrammatic construction (ADC) scheme for the polarization propagator is also provided. Thereafter one electron transition density matrix (1-TDM) is introduced, and various descriptors used in the thesis to analyze excited state properties are described.

Chapter 3: Excited-state properties of pyridine-thiophene oligomers: DFT vs RI-ADC(2)

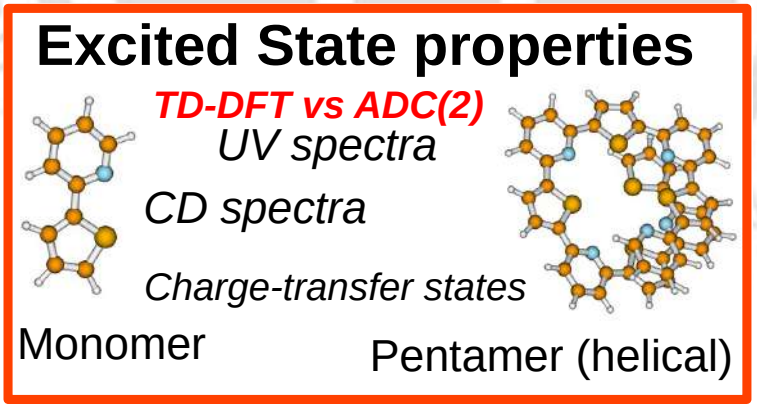

In this chapter, structural and chiroptical properties of pyridine-thiophene (PT) oligomers (n=1-5) are studied. For each oligomer, analysis of excited state properties were performed using fifteen DFT functionals and the results are compared against the RI-ADC(2) results. Three sets of functionals, generalized gradient approximation (GGA) based functionals, long-range corrected versions of those GGA functionals, and a few hybrid functionals. Analysis was performed by comparing the excited state energies

and values of some excited-state descriptors such as d_{exc}, PR_{NTO} and ω_{CT} obtained. CAM-B3LYP, M06-2X, and ωB97XD among the hybrid functionals show comparable results to that of the RI-ADC(2). For these three functionals, the absorption peaks are slightly red-shifted compared to ADC(2), however in the cases of B3LYP and PBE0, peaks are more shifted. Unlike the above hybrid functionals, the long-range (*lc*) corrected versions of GGA functionals (such as *lc*-blyp, *lc*-pbe, *lc*-SVWN, *lc*-TPSS and *lc*-OLYP) show blue-shift in energy in comparison to that of RI-ADC(2) for all the oligomers. Among the five oligomers, **(PT)**$_3$-**(PT)**$_5$ are optically active. **(PT)**$_4$ and **(PT)**$_5$ show more intense CD peaks compared to **(PT)**$_3$. At CAM-B3LYP/def2-TZVP level, **(PT)**$_4$ appears as the most efficient circularly polarized light (CPL) emitter with g_{CPL}= -0.006 and fluorescence rate constant (K_f) value of 0.193 ns^{-1}.

Chapter 4: Chiroptical properties of polyaza[9]helicene and its derivatives

In this chapter, effect of derivatization on structural and chiroptical properties of polyaza[9]helicene (**9Ha**) are reported. First two derivatives are obtained by laterally extending **9Ha** with fusion of pyrazine and quinoxaline units, denoted as **9HaP** and **9HaQ**, respectively. The third one is a helically extended version of **9Ha**, denoted as **11Ha**. Absorption, CD and CPL properties of all four systems are studied using the PBE0 functional. It is observed that the absorption bands are red-shifted from **9Ha** to **11Ha**, due to extension of π-conjugation. Although both **9HaQ** and **11Ha** contain the same number of rings, **11Ha** shows very small intensity peaks. The parent **9Ha**

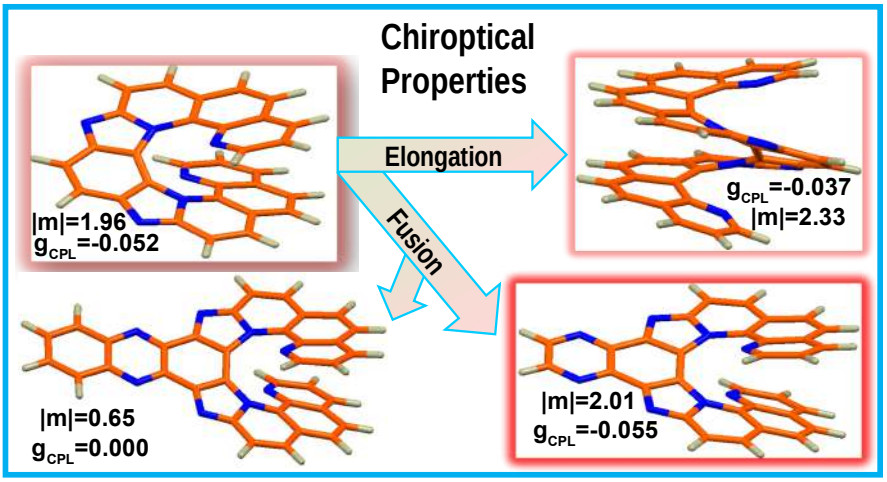

and the three derivatives are fully helical and optically active. **9Ha** shows strongest CD bands among all. In **9Ha**, the lowest energy negative CD band corresponds to the $S_0 \rightarrow S_1$

transition with the g_{CD} value of -0.066. In the other three cases, g_{CD} values for this transition are smaller than in **9Ha** and it follows the order : **9Ha>9HaP>11Ha>9HaQ**. Quinoxaline-ring fusion and helical extension in **9Ha** show improved K_f values which is due to significant increase in the electric dipole transition moments for the $S_1 \rightarrow S_0$ transitions. Considering the $S_1 \rightarrow S_0$ transition, while **9HaP** shows the largest g_{CPL} value, **9HaQ** shows the smallest.

Chapter 5: Effect of fluorination on chiroptical properties of carbo[5-8]helicenes

In this chapter, the excited states properties of di-, tetra- and octafluorinated carbo[5-8]helicenes are reported. In difluorination, one ortho hydrogen at each terminal is substituted by a fluorine atom. Similarly, two and four hydrogen atoms at each terminal are substituted by fluorine atoms for tetra- and octafluorination, respectively. Excited states properties such as UV-vis and CD spectra of all the fluorinated carbohelicenes are computed at the ADC(2)/def2-TZVP level, and the results are compared against the results for their respective parent carbohelicene. In pristine helicenes and their fluorinated derivatives, two dominant absorption bands are observed. However, intensity of the lower energy bands in cases of carbo[7-8] helicenes and derivatives are significantly smaller than the intensities in carbo[5-6]helicenes. In carbo[5-6]helicenes, g_{CPL} decreases with an increase in the degree of fluorination, except in tetrafluorinated carbo[6]helicene. Di- and tetrafluorination in carbo[7]helicene, and all three types of fluorination in carbo[8]helicene produce improved g_{CPL} results. Results are analyzed in terms of dipole transition moment vectors and the angle between the two vectors.

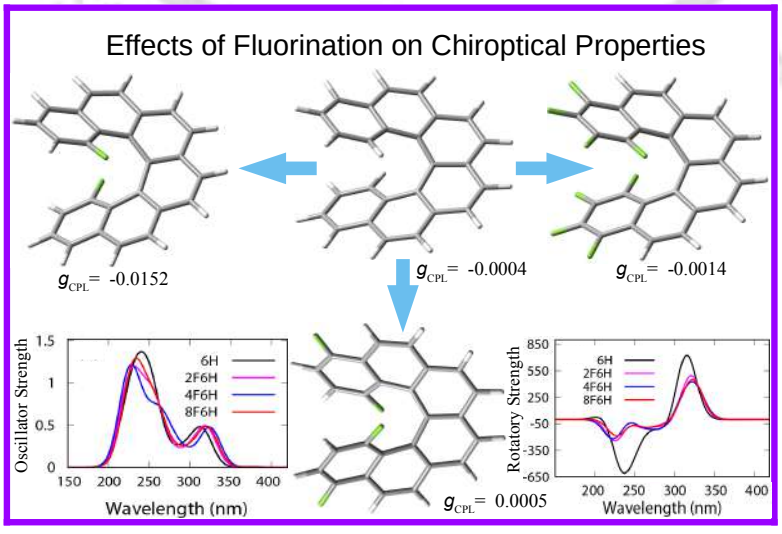

Chapter 6: Summary and conclusions

A brief summary of the thesis and concluding remarks are presented in this chapter. In this thesis, chiroptical properties of pyridine-thiophene oligomers ($(\mathbf{PT})_1$-$(\mathbf{PT})_5$), polyazahelicenes, and carbo[5-8]helicenes along with their fluorinated derivatives are shown. In Chapter 3, chiroptical properties of $(\mathbf{PT})_1$-$(\mathbf{PT})_5$ are shown at DFT and RI-ADC(2) levels. In addition, characterization of excited-states were performed using some descriptors such as d_{exc}, ω_{CT}, and PR_{NTO}. In the next chapter, chiroptical properties of **9Ha** and its three derivatives are reported. This chapter mainly shows the change in the chiroptical properties over ring-fusions and chain elongation in **9Ha**. In Chapter 5, chiroptical properties of carbo[5-8]helicenes and their fluorinated derivatives are discussed.

Published/submitted articles:

1. Bishwanath Mahato, Aditya N. Panda. Assessing the Performance of DFT Functionals for Excited-State Properties of Pyridine-Thiophene Oligomers. *J. Phys. Chem. A* **2021**, 125, 115-125.

2. Bishwanath Mahato, Aditya N. Panda. Effects of Heterocyclic Ring Fusion and Chain Elongation on Chiroptical Properties of Polyaza[9]helicene: A Computational Study. *J. Phys. Chem. A* **2022**, 126, 8, 1412-1421.

3. Bishwanath Mahato, Aditya N. Panda. Effect of Terminal Fluorination on Chiroptical Properties of Carbo[5-8]helicenes: A Systematic Computational Study at RI-ADC(2) level. Accepted for publication in *J. Phys. Chem. A* **2023** .

4. Abhishek Saharia, Bishwanath Mahato, Brijesh Kumar Mishra, Aditya N.Panda. Effect of Fluorine Substitution on Absorption and Emission Properties of Figure-eight-shaped [5]Helicene Dimer : A Computational Study at RI-MP2/RI-ADC(2) Level. *ChemPhysChem*, **2023**, e202300006.

Attended Conferences:

1. Poster presentation in Theoretical Chemistry Symposium 2021, IISER Kolkata

2. Poster presentation in Chemical Research Society of India 28^{th} National Symposium in Chemistry 2022, IIT Guwahati

3. Poster presentation in North-East Research Conclave 2022, IIT Guwahati

4. Poster presentation in Research and Industrial Conclave 2022, IIT Guwahati

5. Poster presentation in Frontiers in Chemical Sciences 2022, IIT Guwahati

Contents

List of Figures xvii

List of Tables xxiii

Abbreviations xxix

1 Introduction 1
- 1.1 Types of helical-shaped systems . . . 2
  - 1.1.1 Single-stranded helical systems . . . 2
    - 1.1.1.1 Ortho-substituted ring systems . . . 3
    - 1.1.1.2 Fused-ring systems . . . 3
  - 1.1.2 Multi-stranded helical systems . . . 3
    - 1.1.2.1 Double helicenes . . . 3
    - 1.1.2.2 Triple helicenes . . . 4
    - 1.1.2.3 Quadruple and larger helicenes . . . 5
- 1.2 Motivation . . . 5
- 1.3 Thesis outline . . . 7

2 Theoretical and computational methodologies 9
- 2.1 Time-independent Schrödinger equation . . . 9
- 2.2 Born-Oppenheimer approximation . . . 10
- 2.3 The One-Electron wavefunction and Hartree-Fock method . . . 11
- 2.4 Post-Hartree-Fock methods . . . 12
  - 2.4.1 Møller-Plesset perturbation theory . . . 12
- 2.5 Density functional theory . . . 14
  - 2.5.1 Exchange-correlation functionals . . . 15
- 2.6 Dispersion-corrected DFT . . . 17
- 2.7 Time-dependent density functional theory (TD-DFT) . . . 19
- 2.8 Algebraic diagrammatic construction scheme for the polarization propagator 21
- 2.9 Rotatory strength and dissymmetry factor . . . 22
- 2.10 One-electron transition density matrix . . . 23
  - 2.10.1 Charge transfer number (Ω_{AB}) . . . 23
  - 2.10.2 Total charge transfer (ω_{CT}) . . . 24
  - 2.10.3 Exciton size (d_{exc}) . . . 24
  - 2.10.4 Participation ratio of NTOs (PR_{NTO}) . . . 25

3 Excited-state properties of pyridine-thiophene oligomers: DFT vs RI-ADC(2) 27
- 3.1 Introduction . . . 28
- 3.2 Computational details . . . 30
- 3.3 Results and discussion . . . 31
  - 3.3.1 Structures of oligomers and first vertical excitation energies . . . 31
  - 3.3.2 Absorption spectra . . . 32
  - 3.3.3 CD spectra . . . 36

3.3.4 Analysis of excited states . . . 39
3.4 Emission properties . . . 46
3.5 Conclusions . . . 46

4 Chiroptical properties of polyaza[9]helicene and its derivatives 49
4.1 Introduction . . . 50
4.2 Computational methodology . . . 51
4.3 Results and discussion . . . 52
4.3.1 Ground state structures . . . 52
4.3.1.1 UV spectra . . . 56
4.3.1.2 CD spectra . . . 59
4.3.2 Excited-state structures and chiroptical properties . . . 60
4.4 Conclusions . . . 64

5 Effect of fluorination on chiroptical properties of carbo[5-8]helicenes 65
5.1 Introduction . . . 66
5.2 Computational methodology . . . 67
5.3 Results and discussion . . . 69
5.3.1 Ground-state structures, absorption and CD spectra . . . 69
5.3.2 UV spectra . . . 71
5.3.3 CD spectra . . . 76
5.3.4 Structures in the S_1 states and emission properties . . . 80
5.4 Conclusions . . . 86

6 Summary and conclusions 89

Appendix A 113

Appendix B 135

Appendix C 145

List of Figures

3.1 Optimized structures of **(PT)** oligomers: (a)-(e) show monomer to pentamer structures. These structures are obtained at RI-MP2/def2-SVP level. The gray, white, yellow and blue colours indicate C, H, S and N atoms, respectively. 30

3.2 First excitation energy (λ^1_{abs}) values and oscillator strengths (f_{osc}) for $\mathbf{(PT)}_1$ to $\mathbf{(PT)}_5$ plotted against $1/n$. The results are obtained at RI-ADC(2)/avdz-vdz level. 32

3.3 Absorption spectra of $\mathbf{(PT)}_1$ and $\mathbf{(PT)}_2$. Results obtained using CAM-B3LYP, M06-2X, ωB97XD, B3LYP and PBE0 functionals are plotted and compared against the ADC(2) results. 33

3.4 Absorption spectra of $\mathbf{(PT)}_3$, $\mathbf{(PT)}_4$ and $\mathbf{(PT)}_5$. Results obtained using CAM-B3LYP, M06-2X, ωB97XD, B3LYP and PBE0 functionals are plotted and compared against the ADC(2) results. 35

3.5 CD spectra of **(PT)** helical oligomers, n=3 (a) , 4 (b) and 5 (c). 37

3.6 Angles between electric and magnetic transition dipole moments for ADC(2) and three DFT functionals. Results for first five excited states for $\mathbf{(PT)}_3$(a), $\mathbf{(PT)}_4$(b) and $\mathbf{(PT)}_5$(c) are shown. 38

3.7 Natural transition orbitals for the S_1-S_5 states of $\mathbf{(PT)}_1$. The results are obtained at RI-ADC(2)/avdz-vdz level of theory. 41

3.8 Natural transition orbitals for the S_1 and S_5 states of $\mathbf{(PT)}_5$. S_1 and S_5 are described by two and three sets of NTOs, respectively. The results are obtained at RI-ADC(2)/avdz-vdz level of theory. 42

3.9 Electron hole correlation plots of $\mathbf{(PT)}_1$ (top two rows) and $\mathbf{(PT)}_5$ (bottom two rows) at ADC(2) and CAM-B3LYP levels. Results for first five excited states are shown. The main diagonal going from lower left to upper right indicates local excitations and the off-diagonal elements indicate excitations between different sites. 43

3.10 Exciton size (d_{exc}), charge transfer (ω_{CT}), and participation ratio of NTOs (PR_{NTO}) of lowest five excited states of plotted against oligomer chain length. Results obtained at CAM-B3LYP, BLYP, and *lc*-BLYP functionals are compared against the ADC(2) results. 45

4.1 Optimized geometries of **9Ha**(i), **9HaP**(ii), **9HaQ**(iii), and **11Ha**(iv). Optimizations were carried out at PBE0-D3/def2-SVP level. Torsional angles ϕ_1 and ϕ_2 are marked. In addition, the torsional angles $\angle$abcd, $\angle$abcd$'$, and $\angle$dbcd$'$ denoted as ϕ_3, ϕ_4, and ϕ_5, respectively, are also shown for **9Ha**. The same set of angles is also used in cases of **9HaP**, **9HaQ**, and **11Ha**. In this figure, carbon, hydrogen and nitrogen atoms are shown in grey, white and blue colors, respectively. 53

4.2 Absorption spectra of **9Ha**. Results obtained using PBE0, B3LYP, M06-2X CAM-B3LYP and ωB97XD functionals are plotted and compared against the ADC(2) results. 54

4.3 Absorption spectra of **9Ha**, **9HaP**, **9HaQ**, and **11Ha**. The results are obtained at PBE0-D3/def2-TZVP level. A half-width at half-maximum of 0.25 eV is used. 57

4.4 Natural transition orbitals for some selected excited state transitions of **9HaP**. Results are obtained at TD-PBE0/def2-TZVP level. An isovalue of 0.03 a.u. is used in each case. Charge-transfer and locally excited transitions are denoted as CT and LE, respectively. 58
4.5 CD spectra of **9Ha**, **9HaP**, **9HaQ**, and **11Ha**. Results are obtained at TD-PBE0/def2-TZVP level of theory. 59
4.6 EDTM (first row) and MDTM (second row) densities of **9Ha** (a), **9HaP** (b), **9HaQ** (c), and **11Ha** (d) for the $S_1 \rightarrow S_0$ transitions. The four columns in each section correspond to total and three components, respectively. Magnitudes of these vectors are in CGS units. The magnitudes in CGS units are obtained from the values in atomic units (a.u.) as follows: $|\boldsymbol{\mu}|$/esu·cm=(254.1746 $\times$ 10^{-20} esu·cm) $\times$ $|\boldsymbol{\mu}|$/a.u. and $|\boldsymbol{m}|$/erg·G^{-1} =(-1) $\times$ (0.927401 $\times$ 10^{-20}/erg·G^{-1}) $\times$ $|\boldsymbol{m}|$/a.u.. Results are obtained using the Multiwfn3.8 software.[263] Isovalue = 0.002 a.u. is used. 61
4.7 Directions of EDTM and MDTM vectors of **9Ha**, **9HaP**, **9HaQ**, and **11Ha** for the transitions $S_1 \rightarrow S_0$. While the vectors in **9Ha**, **9HaP**, and **9HaQ** lie in the YZ plane, these are in the XZ plane for **11Ha**. 62

5.1 Structure of **6H**. The hydrogens at the terminal rings are replaced by fluorine atoms to produce di- (substituting the hydrogens by fluorine atoms at 1 and 1′ positions) tetra- (substituting the hydrogens by fluorine atoms at 1, 1′, 4 and 4′ positions) and octafluoro-**6H** (substituting all the four hydrogens by fluorine atoms at each terminal unit). Similar substitutions are carried out for **5H**, **7H** and **8H**. 67
5.2 Ground state optimized geometries of **2F5H**(i), **4F5H**(ii), **8F5H**(iii), **2F6H**(iv), **4F6H**(v), **8F6H**(vi), **2F7H**(vii), **4F7H**(viii), **8F7H**(ix), **2F8H**(x), **4F8H**(xi) and **8F8H**(xii). Optimizations were carried out at RI-SCS-MP2/def2-TZVP level. In the case of **4F6H**, five carbon atoms are marked as a, b, c, d and e, and two torsional angles, ∠a-b-c-d (denoted as ϕ_1) and ∠b-c-d-e, (denoted as ϕ_2) are defined. The same set of angles is used in other cases as well. In **4F7H**, two carbon-carbon bond distances are marked as r_1 and r_2. R_{pitch} is calculated as $(r_1+r_2)/2$. Carbon, hydrogen and fluorine atoms are shown as grey, white, and green colors, respectively. 69
5.3 Dihedral angles ϕ_1 and ϕ_2 plotted for pristine helicenes and their fluorinated derivatives. 69
5.4 Absorption spectra of **5H** (a), **6H** (b), **7H**(c) and **8H** (d) along with their respective derivatives. The results are obtained at RI-ADC(2)/def2-TZVP level. A half-width at half-maximum value of 15 nm is used for each curve. 72
5.5 Natural transition orbitals for some selected excited states of **8F8H**. Results are obtained at RI-ADC(2)/def2-TZVP level. 76
5.6 CD spectra of **5H** (a), **6H** (b), **7H** (c) and **8H** (d) along with their fluorinated derivatives. Results are obtained at RI-ADC(2)/def2-TZVP level of theory. A half-width at half-maximum value of 15 nm is used for each curve. 77
5.7 Variations in magnitudes of electric dipole transition ($|\boldsymbol{\mu}|$) and magnetic dipole transition moments ($|\boldsymbol{m}|$) for carbo[5-8]helicenes and their fluorinated derivatives for $S_1 \rightarrow S_0$ transitions 83

5.8 Directions of EDTM (red) and MDTM (black) vectors of **6H**, **2F6H**, **4F6H**, and **8F6H** for the $S_1 \rightarrow S_0$ transitions. Results are obtained at RI-ADC(2)/def2-TZVP level of theory. 84
5.9 Dissymmetry factors for emission (g_{CPL} in top panel) and fluorescence rate constants (K_{f} in ns^{-1} in the bottom panel) for carbo[5-8]helicenes and their fluorinated derivatives 86

A1 Absorption spectra of $\mathbf{(PT)}_1$(a) and $\mathbf{(PT)}_2$(b). Results obtained using RI-ADC(2) and various pure functionals are shown. 113
A2 Absorption spectra of $\mathbf{(PT)}_1$(a) and $\mathbf{(PT)}_2$(b). Results obtained using RI-ADC(2) and various long-range corrected pure functionals are shown. . 114
A3 Absorption spectra of PT oligomers, n=3 (a), 4 (b) and 5 (c). Results obtained using RI-ADC(2) and various pure functionals are shown. 115
A4 Absorption spectra of PT oligomers, n=3 (a), 4 (b) and 5 (c). Results obtained using RI-ADC(2) and various long-range corrected pure functionals are shown. 116
A5 CD spectra of PT oligomers, n=3 (a), 4 (b) and 5 (c). Results obtained using RI-ADC(2) and various pure functionals are shown. 117
A6 CD spectra of PT oligomers, n=3 (a), 4 (b) and 5 (c). Results obtained using RI-ADC(2) and various long-range corrected pure functionals are shown. 118
A7 Electron hole correlation plots of $\mathbf{(PT)}_1$ at ADC(2), CAM-B3LYP, *lc*-PBE, and PBE levels. Results for first five excited states are shown. The main diagonal going from lower left to upper right indicates local excitations and the off-diagonal elements indicate excitations between different sites. 134
A8 Electron hole correlation plots of $\mathbf{(PT)}_5$ at ADC(2), CAM-B3LYP, *lc*-PBE, and PBE levels. Results for first five excited states are shown. The main diagonal going from lower left to upper right indicates local excitations and the off-diagonal elements indicate excitations between different sites. 134
B1 Fragmentation scheme of **9Ha**, **9HaP**, **9HaQ**, and **11Ha** for CT analysis. 135
B2 Electron-hole correlation plots of S_1, S_2, and S_6 states of **9Ha** at ADC(2), PBE0, B3LYP, M06-2X, CAM-B3LYP and ωB97XD levels. **9Ha** is divided into three fragments, hence each plot shows a 3 × 3 Ω matrix. Diagonal field going from lower left to upper right indicates local excitations and the off-diagonal elements show charge-transfer excitations. The squares in the middle and terminals of the plot represent the *5-6-5* and terminals units, respectively, as shown in the Figure B1. The vertical axis shows the location of an electron, while the horizontal axis indicates the location of a hole. 137
B3 Natural transition orbitals for some selected excited states of **9Ha**. Results are obtained at TD-PBE0/def2-TZVP level. Isovalue = 0.03 a.u. is used. Charge transfer and locally excited transitions are written as CT and LE, respectively. 139
B4 Natural transition orbitals for some selected excited states of **9HaQ**. Results are obtained at TD-PBE0/def2-TZVP level. Isovalue = 0.03 a.u. is used. Charge transfer and locally excited transitions are written as CT and LE, respectively. 140

B5 Natural transition orbitals for some selected excited states of **11Ha**. Results are obtained at TD-PBE0/def2-TZVP level. Isovalue = 0.03 a.u. is used. Charge transfer and locally excited transitions are written as CT and LE, respectively. 141
B6 Lowest excited state optimized geometries of **9Ha**(i), **9HaP**(ii), **9HaQ**(iii), and **11Ha**(iv). Optimizations were carried out at PBE0-D3/def2-SVP level. Torsional angles ϕ_1 and ϕ_2 are shown. In addition, the torsional angles ∠abcd and ∠abcd′ are also shown, these two are denoted as ϕ_2 and ϕ_4, respectively, for **9Ha**. Same pattern is followed for **9HaP**, **9HaQ**, and **11Ha** to show the torsional angles. In this figure, carbon, hydrogen and nitrogen atoms are shown as grey, white, and blue colors, respectively. 142
B7 Natural transition orbitals for $S_1 \rightarrow S_0$ transitions of **9Ha**, **9HaP**, **9HaQ**, and **11Ha**. Calculated from S_1 optimized geometry at PBE0-D3/def2-SVP level. Isovalue= 0.03 a.u. is used. 143
C1 Fragmentation Scheme Used for Excited State Analysis using TheoDORE in cases of octafluorinated **5H**(a), **6H** (b), **7H** (c), and **8H** (d). Similar fragment definitions are used for other cases. 146
C2 Natural transition orbitals for some selected excited states of **2F5H**. Results are obtained from vertical excitation calculation at RI-ADC(2)/def2-TZVP level. 158
C3 Natural transition orbitals for some selected excited states of **4F5H**. Results are obtained from vertical excitation calculation at RI-ADC(2)/def2-TZVP level. 159
C4 Natural transition orbitals for some selected excited states of **8F5H**. Results are obtained from vertical excitation calculation at RI-ADC(2)/def2-TZVP level. 160
C5 Natural transition orbitals for some selected excited states of **2F6H**. Results are obtained from vertical excitation calculation at RI-ADC(2)/def2-TZVP. 161
C6 Natural transition orbitals for some selected excited states of **4F6H**. Results are obtained from vertical excitation calculation at RI-ADC(2)/def2-TZVP. 162
C7 Natural transition orbitals for some selected excited states of **8F6H**. Results are obtained from vertical excitation calculation at RI-ADC(2)/def2-TZVP. 163
C8 Natural transition orbitals for some selected excited states of **2F7H**. Results are obtained from vertical excitation calculation at RI-ADC(2)/def2-TZVP. 164
C9 Natural transition orbitals for some selected excited states of **4F7H**. Results are obtained from vertical excitation calculation at RI-ADC(2)/def2-TZVP. 165
C10 Natural transition orbitals for some selected excited states of **8F7H**. Results are obtained from vertical excitation calculation at RI-ADC(2)/def2-TZVP. 166
C11 Natural transition orbitals for some selected excited states of **2F8H**. Results are obtained from vertical excitation calculation at RI-ADC(2)/def2-TZVP. 167

C12 Natural transition orbitals for some selected excited states of **4F8H**. Results are obtained from vertical excitation calculation at RI-ADC(2)/def2-TZVP. 168
C13 Natural transition orbitals corresponding to $S_1 \rightarrow S_0$ transitions in **5H** and its fluorinated derivatives. Results are obtained at RI-ADC(2)/def2-TZVP level. 170
C14 Frontier molecular orbitals (HOMO-1 (H-1), HOMO (H), LUMO (L) and LUMO+1 (L+1)) for **5H**, **2F5H**, **4F5H** and **8F6H**. 170
C15 Natural transition orbitals corresponding to $S_1 \rightarrow S_0$ transitions in **6H** and its fluorinated derivatives. Results are obtained at RI-ADC(2)/def2-TZVP level. 171
C16 Frontier molecular orbitals (HOMO-1 (H-1), HOMO (H), LUMO (L) and LUMO+1 (L+1)) for **6H**, **2F6H**, **4F6H** and **8F6H**. 171
C17 Natural transition orbitals corresponding to $S_1 \rightarrow S_0$ transitions in **7H** and fluorinated derivatives. Results are obtained at RI-ADC(2)/def2-TZVP level. 172
C18 Frontier molecular orbitals (HOMO-1 (H-1), HOMO (H), LUMO (L) and LUMO+1 (L+1)) for **7H**, **2F7H**, **4F7H** and **8F7H**. 172
C19 Natural transition orbitals corresponding to $S_1 \rightarrow S_0$ transitions in **8H** and fluorinated derivatives. Results are obtained at RI-ADC(2)/def2-TZVP level. 173
C20 Frontier molecular orbitals (HOMO-1 (H-1), HOMO (H), LUMO (L) and LUMO+1 (L+1)) for **8H**, **2F8H**, **4F8H** and **8F8H**. 173
C21 Directions of EDTM (in red) and MDTM (in blue) vectors of **5H** along with its three fluorinated derivatives for the $S_1 \rightarrow S_0$ transitions. Results are obtained at RI-ADC(2)/def2-TZVP level of theory. 174
C22 Directions of EDTM (in red) and MDTM (in blue) vectors of **7H** along with its three fluorinated derivatives for the $S_1 \rightarrow S_0$ transitions. Results are obtained at RI-ADC(2)/def2-TZVP level of theory. 174
C23 Directions of EDTM (in red) and MDTM (in blue) vectors of **8H** along with its three fluorinated derivatives for the $S_1 \rightarrow S_0$ transitions. Results are obtained at RI-ADC(2)/def2-TZVP level of theory. 174

List of Tables

3.1 First excitation energies (λ^1_{abs}) and oscillator strengths (f_{osc}) of $\mathbf{(PT)}_{n=1,5}$. Results obtained using RI-ADC(2) method and various hybrid functionals are shown. All energies are in nanometer (nm) and are obtained using a combination of aug-cc-pVDZ and cc-pVDZ basis sets. 33

3.2 Vertical excitation energies (λ_{abs} in nm), corresponding oscillator strengths (f_{osc}), rotational strengths (R in 10^{-40} erg-esu-cm/Gauss) and dissymmetry factors (g_{CD}) for $\mathbf{(PT)}_5$. In addition, contributions of most important transitions are shown too. Results obtained using the ADC(2) method and CAM-B3LYP, PBE and *lc*-PBE functionals are shown. All results are obtained using a combination of aug-cc-pVDZ and cc-pVDZ basis sets. 36

3.3 Participation ratio of natural transition orbitals (PR_{NTO}), charge transfer (ω_{CT}), and exciton size (d_{exc} in Å) of first five excited states of $\mathbf{(PT)}_1$(top) and $\mathbf{(PT)}_5$(bottom) at RI-ADC(2) and CAM-B3LYP levels of theory. . . 40

3.4 Emission energies (λ_{em} in nm), Corresponding Oscillator Strength(f_{osc}), $|\boldsymbol{\mu}|$, $|\boldsymbol{m}|$, cos θ, R, g_{CPL}, K_{f}, and $|\boldsymbol{\mu}|/|\boldsymbol{m}|$ of $\mathbf{(PT)}_3$,$\mathbf{(PT)}_4$, and $\mathbf{(PT)}_5$. $|\boldsymbol{\mu}|$, $|\boldsymbol{m}|$ and R are in esu·cm, erg·G^{-1} and esu·cm·erg·G^{-1} units, respectively. K_{f} is in ns^{-1}. All the considered transitions are $S_1 \rightarrow S_0$. 46

4.1 Values of Selected Torsional Angles (ϕ in degrees) and R_{pitch} (in Å) of the Ground State (S_0) and the Lowest Singlet Excited State (S_1) Optimized Geometries of **9Ha**, **9HaP**, **9HaQ**, and **11Ha**. 54

4.2 Excitation Energy (λ_{abs} in nm), Corresponding Oscillator Strength(f_{osc}), Orbitals Involved in the Transitions, $|\boldsymbol{\mu}|$, $|\boldsymbol{m}|$, cos θ, R, g_{CD} and $|\boldsymbol{m}|/|\boldsymbol{\mu}|$of **9Ha**, **9HaP**, **9HaQ**, **11Ha**. $|\boldsymbol{\mu}|$, $|\boldsymbol{m}|$, and R are in esu·cm, erg·G^{-1} and esu·cm·erg·G^{-1} units, respectively. 56

4.3 Emission Energy (λ_{em} in nm), Corresponding Oscillator Strength(f_{osc}), $|\boldsymbol{\mu}|$, $|\boldsymbol{m}|$, cos θ, R, g_{CPL}, K_{f}, and $|\boldsymbol{m}|/|\boldsymbol{\mu}|$ of **9Ha**,**9HaP**, **9HaQ**, and **11Ha**. $|\boldsymbol{\mu}|$, $|\boldsymbol{m}|$ and R are in esu·cm, erg·G^{-1} and esu·cm·erg·G^{-1} units, respectively. K_{f} is in ns^{-1}. Reported g_{CPL} of **9Ha** is 0.027 at 546 nm. All the Considered Transitions are $S_1 \rightarrow S_0$. 60

5.1 Values of selected torsional angles (ϕ, degrees) and R_{pitch} (Å) of ground state (S_0) and lowest singlet excited state (S_1) optimized geometries of **5H-8H**, and their di-, tetra- and octafluorinated derivatives 70

5.2 Excitation Energy (λ_{abs} in nm), Corresponding Oscillator Strength (f_{osc}), $|\boldsymbol{\mu}|$, $|\boldsymbol{m}|$, cos θ, R, g_{CD}, $|\boldsymbol{m}|/|\boldsymbol{\mu}|$ and Orbitals Involved in the Transitions for **2F5H**, **8F5H**, **2F6H**, **8F6H**, **2F7H**, **8F7H**, **2F8H** and **8F8H** . . . 74

5.3 Emission energies (λ_{em}, nm), Corresponding Oscillator Strength(f_{osc}), $|\boldsymbol{\mu}|$, $|\boldsymbol{m}|$, cos θ, R, g_{CPL}, $|\boldsymbol{m}|/|\boldsymbol{\mu}|$, and K_{f} of **5H**, **6H**, **7H** and **8H**, and their fluorinated derivatives. 81

A1 Excitation energies (λ_{abs}s), oscillator strengths (f_{osc}s), major configurations involved in the transitions, rotatory strengths (R), PR_{NTO}s, ω_{CT}s, and d_{exc}s of first five excited states of $\mathbf{(PT)}_1$ at ADC(2) and TD-DFT levels using hybrid fuctionals. 119

A2 Excitation energies (λ_{abs}s), oscillator strengths (f_{osc}s), major configurations involved in the transitions, rotatory strengths (R), PR_{NTO}s, ω_{CT}s, and d_{exc}s of first five excited states of $\mathbf{(PT)}_1$ at TD-DFT level using pure fuctionals. . . . 120
A3 Excitation energies (λ_{abs}s), oscillator strengths (f_{osc}s), major configurations involved in the transitions, rotatory strengths (R), PR_{NTO}s, ω_{CT}s, and d_{exc}s of first five excited states of $\mathbf{(PT)}_1$ at TD-DFT level using long-range corrected versions of pure fuctionals. . . . 121
A4 Excitation energies (λ_{abs}s), oscillator strengths (f_{osc}s), major configurations involved in the transitions, rotatory strengths (R), PR_{NTO}s, ω_{CT}s, and d_{exc}s of first five excited states of $\mathbf{(PT)}_2$ at ADC(2) and TD-DFT levels using hybrid fuctionals. . . . 122
A5 Excitation energies (λ_{abs}s), oscillator strengths (f_{osc}s), major configurations involved in the transitions, rotatory strengths (R), PR_{NTO}s, ω_{CT}s, and d_{exc}s of first five excited states of $\mathbf{(PT)}_2$ at TD-DFT level using pure fuctionals. . . . 123
A6 Excitation energies (λ_{abs}s), oscillator strengths (f_{osc}s), major configurations involved in the transitions, rotatory strengths (R), PR_{NTO}s, ω_{CT}s, and d_{exc}s of first five excited states of $\mathbf{(PT)}_2$ at TD-DFT level using long-range corrected versions of pure fuctionals. . . . 124
A7 Excitation energies (λ_{abs}s), oscillator strengths (f_{osc}s), major configurations involved in the transitions, rotatory strengths (R), PR_{NTO}s, ω_{CT}, and d_{exc}s of first five excited states of $\mathbf{(PT)}_3$ at ADC(2) and TD-DFT levels using hybrid fuctionals. . . . 125
A8 Excitation energies (λ_{abs}s), oscillator strengths (f_{osc}s), major configurations involved in the transitions, rotatory strengths (R), PR_{NTO}s, ω_{CT}s, and d_{exc}s of first five excited states of $\mathbf{(PT)}_3$ at TD-DFT level using pure fuctionals. . . . 126
A9 Excitation energies (λ_{abs}s), oscillator strengths (f_{osc}s), major configurations involved in the transitions, rotatory strengths (R), PR_{NTO}s, ω_{CT}s, and d_{exc}s of first five excited states of $\mathbf{(PT)}_3$ at TD-DFT level using long-range corrected versions of pure fuctionals. . . . 127
A10 Excitation energies (λ_{abs}s), oscillator strengths (f_{osc}s), major configurations involved in the transitions, rotatory strengths (R), PR_{NTO}s, ω_{CT}s, and d_{exc}s of first five excited states of $\mathbf{(PT)}_4$ at ADC(2) and TD-DFT levels using hybrid fuctionals. . . . 128
A11 Excitation energies (λ_{abs}s), oscillator strengths (f_{osc}s), major configurations involved in the transitions, rotatory strengths (R), PR_{NTO}s, ω_{CT}s, and d_{exc}s of first five excited states of $\mathbf{(PT)}_4$ at TD-DFT level using pure fuctionals. . . . 129
A12 Excitation energies (λ_{abs}s), oscillator strengths (f_{osc}s), major configurations involved in the transitions, rotatory strengths (R), PR_{NTO}s, ω_{CT}s, and d_{exc}s of first five excited states of $\mathbf{(PT)}_4$ at TD-DFT level using long-range corrected versions of pure fuctionals. . . . 130
A13 Excitation energies (λ_{abs}s), oscillator strengths (f_{osc}s), major configurations involved in the transitions, rotatory strengths (R), PR_{NTO}s, ω_{CT}s, and d_{exc}s of first five excited states of $\mathbf{(PT)}_5$ at ADC(2) and TD-DFT levels using hybrid fuctionals. . . . 131

A14 Excitation energies (λ_{abs}s), oscillator strengths (f_{osc}s), major configurations involved in the transitions, rotatory strengths (R), PR_{NTO}s, ω_{CT}s, and d_{exc}s of first five excited states of $\mathbf{(PT)}_5$ at TD-DFT level using pure fuctionals. . . . 132
A15 Excitation energies (λ_{abs}s), oscillator strengths (f_{osc}s), major configurations involved in the transitions, rotatory strengths (R), PR_{NTO}s, ω_{CT}s, and d_{exc}s of first five excited states of $\mathbf{(PT)}_5$ at TD-DFT level using long-range corrected versions of pure fuctionals. . . . 133
B1 Excitation energies (λ_{abs} in nm), corresponding Oscillator Strength (f_{osc}), R, ω_{CT}, PR_{NTO}, and d_{exc} of **9Ha**. Results obtained at different TD-DFT and RI-ADC(2) levels. . . . 136
B2 Excitation energies(λ_{abs} in nm), corresponding Oscillator Strength (f_{osc}), R, ω_{CT}, PR_{NTO}, and d_{exc} of **9HaP**, **9HaQ**, and **11Ha**. Results obtained at TD-PBE0/def2-TZVP/DCM level. . . . 138
B3 Charge-transfer (ω_{CT}) and $|\boldsymbol{\mu}|$ of **9Ha**,**9HaP**, **9HaQ**, and **11Ha** for $S_1 \rightarrow S_0$ transitions. . . . 144
C1 Values of Selected Torsional Angles (ϕ, degrees) and R_{pitch} (Å) of Crystal Structures of **6H**, **4F6H**, **8F6H**, **7H**, **1F7H**, **2F′7H**, **4F7H**, **8H**, and **1F8H**. [a]See Ref[275]. [b]See Ref[55]. [c]See Ref[282]. [j]See Ref[283]. [d]See Ref[284]. [e]See Ref[285]. [f]See Ref[56]. [g]See Ref[286]. . . . 147
C2 Excitation energies (λ_{abs}, nm), Corresponding Oscillator Strength(f_{osc}), Orbitals involved in the transitions, $|\boldsymbol{\mu}|$, $|\boldsymbol{m}|$, cos θ, R, g_{CD} and $|\boldsymbol{m}|/|\boldsymbol{\mu}|$ of **5H**. $|\boldsymbol{\mu}|$, $|\boldsymbol{m}|$, and R are in esu·cm, erg·G^{-1} and esu·cm·erg·G^{-1} units, respectively. . . . 148
C3 Excitation energies (λ_{abs}, nm), Corresponding Oscillator Strength(f_{osc}), Orbitals involved in the transitions, $|\boldsymbol{\mu}|$, $|\boldsymbol{m}|$, cos θ, R, g_{CD} and $|\boldsymbol{m}|/|\boldsymbol{\mu}|$ of **2F5H**. $|\boldsymbol{\mu}|$, $|\boldsymbol{m}|$, and R are in esu·cm, erg·G^{-1} and esu·cm·erg·G^{-1} units, respectively. . . . 148
C4 Excitation energies (λ_{abs}, nm), Corresponding Oscillator Strength(f_{osc}), Orbitals involved in the transitions, $|\boldsymbol{\mu}|$, $|\boldsymbol{m}|$, cos θ, R, g_{CD} and $|\boldsymbol{m}|/|\boldsymbol{\mu}|$ of **4F5H**. $|\boldsymbol{\mu}|$, $|\boldsymbol{m}|$, and R are in esu·cm, erg·G^{-1} and esu·cm·erg·G^{-1} units, respectively. . . . 149
C5 Excitation energies (λ_{abs}, nm), Corresponding Oscillator Strength(f_{osc}), Orbitals involved in the transitions, $|\boldsymbol{\mu}|$, $|\boldsymbol{m}|$, cos θ, R, g_{CD} and $|\boldsymbol{m}|/|\boldsymbol{\mu}|$ of **8F5H**. $|\boldsymbol{\mu}|$, $|\boldsymbol{m}|$, and R are in esu·cm, erg·G^{-1} and esu·cm·erg·G^{-1} units, respectively. . . . 149
C6 Excitation energies (λ_{abs}, nm), Corresponding Oscillator Strength(f_{osc}), Orbitals involved in the transitions, $|\boldsymbol{\mu}|$, $|\boldsymbol{m}|$, cos θ, R, g_{CD} and $|\boldsymbol{m}|/|\boldsymbol{\mu}|$ of **6H**. $|\boldsymbol{\mu}|$, $|\boldsymbol{m}|$, and R are in esu·cm, erg·G^{-1} and esu·cm·erg·G^{-1} units, respectively. . . . 150
C7 Excitation energies (λ_{abs}, nm), Corresponding Oscillator Strength(f_{osc}), Orbitals involved in the transitions, $|\boldsymbol{\mu}|$, $|\boldsymbol{m}|$, cos θ, R, g_{CD} and $|\boldsymbol{m}|/|\boldsymbol{\mu}|$ of **2F6H**. $|\boldsymbol{\mu}|$, $|\boldsymbol{m}|$, and R are in esu·cm, erg·G^{-1} and esu·cm·erg·G^{-1} units, respectively. . . . 150
C8 Excitation energies (λ_{abs}, nm), Corresponding Oscillator Strength(f_{osc}), Orbitals involved in the transitions, $|\boldsymbol{\mu}|$, $|\boldsymbol{m}|$, cos θ, R, g_{CD} and $|\boldsymbol{m}|/|\boldsymbol{\mu}|$ of **4F6H**. $|\boldsymbol{\mu}|$, $|\boldsymbol{m}|$, and R are in esu·cm, erg·G^{-1} and esu·cm·erg·G^{-1} units, respectively. . . . 151

C9 Excitation energies (λ_{abs}, nm), Corresponding Oscillator Strength(f_{osc}), Orbitals involved in the transitions, $|\boldsymbol{\mu}|$, $|\boldsymbol{m}|$, cos θ, R, g_{CD} and $|\boldsymbol{m}|/|\boldsymbol{\mu}|$ of **8F6H**. $|\boldsymbol{\mu}|$, $|\boldsymbol{m}|$, and R are in esu·cm, erg·G^{-1} and esu·cm·erg·G^{-1} units, respectively. 151

C10 Excitation energies (λ_{abs}, nm), Corresponding Oscillator Strength(f_{osc}), Orbitals involved in the transitions, $|\boldsymbol{\mu}|$, $|\boldsymbol{m}|$, cos θ, R, g_{CD} and $|\boldsymbol{m}|/|\boldsymbol{\mu}|$ of **7H**. $|\boldsymbol{\mu}|$, $|\boldsymbol{m}|$, and R are in esu·cm, erg·G^{-1} and esu·cm·erg·G^{-1} units, respectively. 152

C11 Excitation energies (λ_{abs}, nm), Corresponding Oscillator Strength(f_{osc}), Orbitals involved in the transitions, $|\boldsymbol{\mu}|$, $|\boldsymbol{m}|$, cos θ, R, g_{CD} and $|\boldsymbol{m}|/|\boldsymbol{\mu}|$ of **2F7H**. $|\boldsymbol{\mu}|$, $|\boldsymbol{m}|$, and R are in esu·cm, erg·G^{-1} and esu·cm·erg·G^{-1} units, respectively. 152

C12 Excitation energies (λ_{abs}, nm), Corresponding Oscillator Strength(f_{osc}), Orbitals involved in the transitions, $|\boldsymbol{\mu}|$, $|\boldsymbol{m}|$, cos θ, R, g_{CD} and $|\boldsymbol{m}|/|\boldsymbol{\mu}|$ of **4F7H**. $|\boldsymbol{\mu}|$, $|\boldsymbol{m}|$, and R are in esu·cm, erg·G^{-1} and esu·cm·erg·G^{-1} units, respectively. 153

C13 Excitation energies (λ_{abs}, nm), Corresponding Oscillator Strength(f_{osc}), Orbitals involved in the transitions, $|\boldsymbol{\mu}|$, $|\boldsymbol{m}|$, cos θ, R, g_{CD} and $|\boldsymbol{m}|/|\boldsymbol{\mu}|$ of **8F7H**. $|\boldsymbol{\mu}|$, $|\boldsymbol{m}|$, and R are in esu·cm, erg·G^{-1} and esu·cm·erg·G^{-1} units, respectively. 153

C14 Excitation energies (λ_{abs}, nm), Corresponding Oscillator Strength(f_{osc}), Orbitals involved in the transitions, $|\boldsymbol{\mu}|$, $|\boldsymbol{m}|$, cos θ, R, g_{CD} and $|\boldsymbol{m}|/|\boldsymbol{\mu}|$ of **8H**. $|\boldsymbol{\mu}|$, $|\boldsymbol{m}|$, and R are in esu·cm, erg·G^{-1} and esu·cm·erg·G^{-1} units, respectively. 154

C15 Excitation energies (λ_{abs}, nm), Corresponding Oscillator Strength(f_{osc}), Orbitals involved in the transitions, $|\boldsymbol{\mu}|$, $|\boldsymbol{m}|$, cos θ, R, g_{CD} and $|\boldsymbol{m}|/|\boldsymbol{\mu}|$ of **2F8H**. $|\boldsymbol{\mu}|$, $|\boldsymbol{m}|$, and R are in esu·cm, erg·G^{-1} and esu·cm·erg·G^{-1} units, respectively. 154

C16 Excitation energies (λ_{abs}, nm), Corresponding Oscillator Strength(f_{osc}), Orbitals involved in the transitions, $|\boldsymbol{\mu}|$, $|\boldsymbol{m}|$, cos θ, R, g_{CD} and $|\boldsymbol{m}|/|\boldsymbol{\mu}|$ of **4F8H**. $|\boldsymbol{\mu}|$, $|\boldsymbol{m}|$, and R are in esu·cm, erg·G^{-1} and esu·cm·erg·G^{-1} units, respectively. 155

C17 Excitation energies (λ_{abs}, nm), Corresponding Oscillator Strength(f_{osc}), Orbitals involved in the transitions, $|\boldsymbol{\mu}|$, $|\boldsymbol{m}|$, cos θ, R, g_{CD} and $|\boldsymbol{m}|/|\boldsymbol{\mu}|$ of **8F8H**. $|\boldsymbol{\mu}|$, $|\boldsymbol{m}|$, and R are in esu·cm, erg·G^{-1} and esu·cm·erg·G^{-1} units, respectively. 155

C18 Charge Transfer (ω_{CT}), Participation Ratio of Natural Transition Orbitals (PR_{NTO}) and Exciton Size (d_{exc} in Å) for **5H** and its three fluorinated derivatives. Results are obtained at RI-ADC(2)/def2-TZVP level. 156

C19 Charge Transfer (ω_{CT}), Participation Ratio of Natural Transition Orbitals (PR_{NTO}) and Exciton Size (d_{exc} in Å) for **6H** and its three fluorinated derivatives. Results are obtained at RI-ADC(2)/def2-TZVP level. 156

C20 Charge Transfer (ω_{CT}), Participation Ratio of Natural Transition Orbitals (PR_{NTO}) and Exciton Size (d_{exc} in Å) for **7H** and its three fluorinated derivatives. Results are obtained at RI-ADC(2)/def2-TZVP level. 157

C21 Charge Transfer (ω_{CT}), Participation Ratio of Natural Transition Orbitals (PR_{NTO}) and Exciton Size (d_{exc} in Å) for **8H** and its three fluorinated derivatives. Results are obtained at RI-ADC(2)/def2-TZVP level. 157

C22 Emission Energies(λ_{em}, nm), Contributions from Various Transitions, Participation Ratio of Natural Transition Orbitals (PR_{NTO}), Exciton Size (d_{exc}, Å), and Charge Transfer (ω_{CT}) of **5H**, **2F5H**, **4F5H**, **8F5H**, **6H**, **2F6H**, **4F6H**, **8F6H**, **7H**, **2F7H**, **4F5H**, **8F7H**, **8H**, **2F8H**, **4F8H**, and **8F8H** for the $S_1 \rightarrow S_0$ transitions. Results are obtained at RI-ADC(2)/def2-TZVP level. 169

Abbreviations

ϵ	epsilon
θ	theta
ω	omega
Ω	Omega
π	pi
Ψ	Psi
ψ	psi
μ	mu
λ	lambda
ϕ	Uppercase phi
φ	Lowercase phi
ν	nu
χ	chi
∇	operator
Å	Angstrom
%	Percentage
λ_{abs}	Excitation energy
λ^{1}_{abs}	First excitation energy
λ_{em}	Emission energy
HF	Hartree-Fock
MP	Møller-Plesset
MO	Molecular orbital
BO	Born-Oppenheimer
TD	Time dependent
DFT	Density functional theory
DFT-D3	Density functional theory including Grimme's D3 version
CAM	Coulomb-attenuating method
GGA	Generalized gradient approximation

HOMO	Highest occupied molecular orbital
LUMO	Lowest unoccupied molecular orbital
PT	Pyridine-thiophene
f_{osc}	Oscillator strength
R	Rotatory strength
g_{CD}	Dissymmetry factor for absorption
g_{CPL}	Dissymmetry factor for emission
lc	long-range corrected
UV	Ultraviolet
CT	Charge transfer
LE	Locally excited
CD	Circular dicroism
NTO	Natural transition orbital
Qx	Quinoxaline
Φ_{FL}	Fluorescence quantum yield
K_{f}	Fluorescence rate constant
DTM	Dipole transition moment
EDTM	Electric dipole transition moment
MDTM	Magnetic dipole transition moment
1-TDM	One-electron transition density matrix
ADC(2)	Second order algebraic diagrammatic construction
CC2	Second order coupled-cluster
d_{exc}	Exciton size
PR_{NTO}	Participation ratio of NTOs
ω_{CT}	Charge transfer
R_{pitch}	Helical pitch

Chapter 1

Introduction

Chirality refers to non-superimposability of mirror images of a molecule. It is ubiquitous in nature, e.g., in α-helix proteins and helical DNAs. The two stereoisomers are called enantiomers differentiated by either "right-handedness" or "left-handedness". Chirality can appear in optically active molecules or in polyaromatics with helical scaffolds. Helicenes, screw-shaped polycyclic aromatic compounds consisting of *ortho*-fused aromatic rings, are common examples of helical scaffolds.[1–4] While helicenes consisting of solely fused benzene rings are known as carbohelicenes, others containing one or more hetero atoms along the chain are known as heterohelicenes. Due to their inherent chirality, they exhibit intrinsic chiroptical properties.[1,5,6] Their stable helical structures make these strongly luminescent, circular dichroism (CD) and circularly polarized luminescence (CPL) active. Helical structures, in particular helicenes, are of fundamental importance in various research fields of material science such as in emissive layers of organic light emitting diodes (OLEDs),[7–11] in hole-transport layers of pervoskite solar cells,[12–20] in the asymmetric catalysis,[21–23] in enantioselective fluorescent sensors,[24] bioimaging,[25] and displays[26] etc. Due to the above reasons, there has been surge in studies of helical structures in recent times to design compounds with better chiral properties. Chirality in the ground state is usually investigated using the CD spectroscopy. Here, the differential absorption of left- and right-polarized lights is measured. Similar to the ground state chirality, differential emission of left- and right-handed circularly polarized light is measured using CPL technique. This corresponds to the excited state chirality. Efficiencies of CD and CPL active systems are evaluated in terms of dissymmetry factors, g_{CD} and g_{CPL}, corresponding to CD and CPL, respectively.[27] These two parameters are defined as

$$g_{\mathrm{CD}}(\lambda) = 2\Delta\epsilon(\lambda)/\epsilon(\lambda) \tag{1.1}$$

and

$$g_{\mathrm{CPL}}(\lambda) = 2\Delta I(\lambda)/I(\lambda), \tag{1.2}$$

respectively. Here, ϵ/I and $\Delta\epsilon/\Delta I$ are the sum and difference in intensities of left and right polarized lights, respectively, for absorption/emission. The maximum value of either g_{CD} or g_{CPL} is ± 2, denoting completely left- or right-polarized absorption or emission.

Typically, helical organic organic molecules show small chirality. In the recent past, many chiral molecules with good absorption, and in particular, luminescence properties have been designed. Small changes in the structures of the helical systems, making ring substitutions, and making double/triple helicenes have been taken up in recent times to achieve large g_{CPL} values. Below we provide a quick overview of different types of helical-shaped systems, and their applications in various devices. This is followed by an outline of the thesis work.

1.1 Types of helical-shaped systems

There are various types of helical-shaped molecules reported in the literature, starting from the single-stranded to multi-stranded helical systems.[3,28,29] Below we discuss typical helical systems reported in the literature.

1.1.1 Single-stranded helical systems

The single-stranded helical systems consist of single helicenic units of either P (right-handed) or M (left-handed) configurations. Pristine carbo[n]helicenes and their derivatives are the most common example of this class of helical systems.

1.1.1.1 Ortho-substituted ring systems

Small-sized oligomers of ortho-substituted heterocyclic rings are linear in structure and achiral in nature. However, chain elongation of such oligomers results in non-planar structures and induces chiral properties in the systems. In this regard, many five-membered ring-based conducting polymers such as polythiophene[30–33] and polypyrrole,[31,34–38] have been studied. In recent times, helical polyfurans have also been synthesized.[39–42] Among the polymers of phenylene, *ortho*-phenylenes have been shown to form helices.[43–46]

1.1.1.2 Fused-ring systems

In 1956, Newman and Lednicer first synthesized the fully helical carbo[6]helicene.[47] Thereafter, many medium to large-sized multi-layered carbohelicenes up to carbo[16]helicene[48] have been synthesized till date.[3,29] In addition, several modified carbohelicenes based on either substitution[49–57] or lateral ring-fusion[7,58–63] have also been synthesized.[3,29] For example, perylene diimide[60] and hexabenzocoronene[62] have been commonly used skeletons for lateral π extension. In addition, fluorene-[64] and azaine-fused[65] are also in use. In addition, many heterohelicenes based on oxygen[66,67], nitrogen[68], sulphur[68,69] and others are also reported.[29]

1.1.2 Multi-stranded helical systems

In addition to conventional single-stranded helicenes, double and multiple helicenes, entailing more than one helicene subunit in one molecule, have emerged as a new class of chiral polycyclic aromatic hydrocarbons (PAHs).

1.1.2.1 Double helicenes

Among the various multiple helicenes, double helicenes are the simplest and most studied family of helicenes. These include double carbo[5-8]helicenes. In 1959, Clar and co-workers very first reported the [X]-shaped double [5]helicene or Hexabenzoperylene.[70]

Further, Miao et al. synthesized its alkoxy derivatives in 2012.[71] In these [X]-shaped helicenes, each component shares the same benzene ring in the middle[70,71] or the C-C bond of that ring.[72] In addition to these [X]-type double carbo[5]helicenes, [S]-type double carbo[5]helicene[73] sharing one terminal ring of each unit was also reported. Further, in some cases, the terminals of two moieties are connected via one or two C-C bonds[74,75] producing either [S]-type or figure-eight shaped molecules, respectively. Similar to double carbo[5]helicenes, fusion of two pristine carbo[6]helicenes produced double carbo[6]helicenes of various shapes.[28] For example, two fused carbo[6]helicene units produce [S]- and [M]-shaped double carbo[6]helicenes, sharing the central[76,77] and terminal[78] naphthalene rings, respectively. In the former case, the two terminals are anti to each other, while those are cis in the latter case. Further, there are some double carbo[6]helicenes, sharing either one ring[78,79] or a bond.[80] Recently, Mori et al.[81] reported an isometric [X]-type double carbo[6]helicene, sharing the naphthalene unit in the middle. In addition, [S]-shaped double aza[6]helicene has also been reported by Tanaka et al.[82] Unlike the carbo[5,6]helicenes, no [S]-type double carbo[7]helicene in the anti-form has been reported to date. However, a classic example of M-shaped double carbo[7]helicene that shares a terminal naphthalene unit was reported as early as 1974 by Martin et al..[78] In 2003, Cobas et al. reported an asymmetric double helicene made up of lateral fusion of carbo[7]helicene and carbo[5]helicene.[83] In recent times, there has been an increase in studies of π-extended multiple helicenes.[28,60,84–88] These are based on some common π-conjugated units such as hexabenzo-fused double carbo[6]helicene[85], pyrene-fused [X]-shaped double carbo[7]helicene[88], hexapole carbo[7]helicene fused with hexa-peri-hexabenzocoronene core[86], perylene diimide-embedded double carbo[8]helicenes[60] etc.. Further, in addition to benzo-annulated double carbohelicenes, multiple helicenes containing one or more hetero atoms in the core have also been explored extensively.[28,89]

1.1.2.2 Triple helicenes

A few multihelicenes, triple helicene, quadruple helicene, and quintuple helicene, have been reported. The first triple helicene was prepared by the pyrolysis of cyclobuta[l]phenanthrene-1,2-dione in 1982 is hexabenzotriphenylene.[90] Further studies were carried out by various

groups.[91–93] In 1999, Barnett et al. reported two stereoisomers of hexabenzotriphenylene of D_3 and C_2 symmetries, sharing triphenylene unit in the core.[91] Further, Watanabe et al.[94] synthesized the very first more twisted and three-bladed propeller-shaped triple carbo[5]helicenes of C_3 symmetry in 2017. A trimer of bowl-shaped corannulene, a π-extended version of triple [5]helicene, i.e., hexabenzotriphenylene, was also prepared.[84] Further triperylene hexaimides based triple carbo[5]helicenes along with its nitrogen doped and selenium derivatives are also reported.[95,96]

1.1.2.3 Quadruple and larger helicenes

Unlike double and triple helicenes, quadruple helicenes are limited. In 2013, Dichtel et al.[97] synthesized extended and partially fused quadruple carbo[5]helicene as a π-elongated derivative of double [5]helicene[70] (i.e., hexabenzoperylene). It contains four carbo[5]helicene units and none of these four units share any ring among themselves. Further, quadruple hetero[5]helicene was synthesized by Itami and co-workers from dithia[6] and carbo[5] helicenes.[98] Recently, Xiao et al. reported quadruple carbo[5]helicene, composed of four indene units, in which no fully shared benzene ring is present.[99]

Fewer numbers of quintuple helicenes are reported in literature. Those quintuple helicenes are based on corannulene units. For example, Itami and co-workers[100,101], synthesized propeller-shaped quintuple carbo[6]helicene and quintuple decathia[6]helicene. Both of these are composed of a corannulene unit and six helicenic moieties. In 2022, Tanaka et. al reported azahelicene-fused corannulenes.[102] In 2017, the groups of Kamikawa[103] and Gingras[104] synthesized chiral propeller-shaped D_3 symmetric sextuple helicene. It consisted of three external and three internal carbo[5]helicene units. In addition, carbo[5]helicene-based unique circular and cage shaped molecules are also reported, where two helicene units get connected via several linkers, instead of ring fusion.[105–107]

1.2 Motivation

Helicenes have been an important area of research for their applications in the field of material science. However, performance of pristine helicenes are less compared to

metal-based helical systems and multihelicenes in terms of fluorescence quantum yield (Φ_{FL}) and g_{CPL}. For pristine carbo[n>4]helicenes, Φ_{FL} values remain below 0.05 and it decreases with increase in helical length[108,109], while g_{CPL} values are reported to be less than 0.01[57,81,110] for the carbo[5-7]helicenes. Therefore, this has been an active area of research to explore effects of various molecular modifications to improve both Φ_{FL} and g_{CPL} values. Modifications such as lateral ring extensions, insertion of electron-donating and -withdrawing groups in to the core, and doping by heteroatoms onto the helix have been carried out and this has been shown to produce improved chiroptical properties.[28,29,66–69,111] In 1996, Hasobe and co-workers[69] reported tetrathia[9]helicene and its quinoxaline (*Qx*)-fused derivatives showing up to ≈ 28-fold increase in the Φ_{FL}values compared to that of carbo[9]helicene. Later in 2014, they also reported *Qx*-fused carbo[7]helicene[58] with improved results. Recently, Otani et al.[11] reported polyaza[5-9]helicenes with improved Φ_{FL} and g_{CPL} values compared to those of traditional carbohelicenes.[57,81,108–110] In this case, polyaza[9]helicene (**9Ha**) was found to be the one with the highest value of g_{CPL} (i.e., 0.027) among the single-stranded [9]helicenes. Further, the same group reported Qx-fused polyaza[5,7]helicenes[112] with larger Φ_{FL} values compared to their respective carbohelicenes. In addition to *Qx* unit, there are helicenes fused with large π-conjugated units, such as perylene diimide[60] and pyrene[61] etc.

Similar to laterally extended helicenes, substituted-helicenes[3,29,57] also act as better light emitters compared their respective pristine carbohelicenes. For example, in 2017 Kubo et al.[54] reported dimethoxy and dicyano substituted carbo[5]helicenes with Φ_{FL}=0.10-0.23, which is 2.5-5.75 fold increment compared to its parent system. Similarly, dimethoxy and dicyano substituted carbo[7]helicenes[57] also show improved luminescence properties. Halogenation of carbohelicenes rings is another strategy to tune the chiroptical properties.[51,55] In 2019, Církva et al.[55] reported the synthesis of tetrafluoro- and octafluoro-carbo[6]helicenes and observed systematic increase in Φ_{FL} with increase in the number of fluorine atoms. Looking at the literature reports, it is clear that a lot more understanding is required to fully grasp the effects of substitution and ring-fusion on the optoelectronic properties. Computational studies at this juncture are of great help to design the systems, and study their chiroptical properties. In this thesis, our

aim is to contribute towards understanding of the effects of substitution and ring-fusion on the chiroptical properties.

1.3 Thesis outline

In this thesis, we present the results of computational studies of ortho-substituted pyridine-thiophene oligomers and ortho-fused helicenes. Computational studies are carried out at DFT/TD-DFT and ADC(2) levels of theory. In Chapter 2, theoretical and computational methods are briefly discussed. In Chapter 3, a comparative study of excited-state properties of pyridine-thiophene **(PT)** oligomers (n=1-5) at different levels is presented. Results of fifteen DFT functionals are compared against the RI-ADC(2) results for each oligomer. $\mathbf{(PT)}_4$ appears as the strongest CPL active system, with g_{CPL}=-0.0059 at λ_{em}=389 nm, obtained at CAM-B3LYP level. In Chapter 4, the effects of lateral ring-fusion and chain elongation on the chiroptical properties of polyazahelicenes are presented. Among the three derivatives of polyaza[9]helicene (**9Ha**), pyrazine-fused **9Ha** (i.e., **9HaP**) shows the best results with the largest values of g_{CPL} of -0.055. In the fifth Chapter, we show the effects of fluorination on the chiroptical properties of carbohelicenes. A systematic study was carried out by substituting hydrogen atoms by fluorine atoms to different degrees. The last chapter presents the overall conclusions of the thesis work.

Chapter 2

Theoretical and computational methodologies

2.1 Time-independent Schrödinger equation

The Schrödinger equation for a system of n electrons and N nuclei is written as

$$\hat{H}\ \Psi_i(r_1, r_2\ ...r_n, R_1, R_2\ ...R_N) = E_i\ \Psi_i(r_1, r_2\ ...r_n, R_1, R_2\ ...R_N), \tag{2.1}$$

where $\hat{H}$ is the Hamiltonian operator consisting of all the operators corresponding to the kinetic and potential energies. $\Psi_i(r_1, r_2\ ...r_n, R_1, R_2\ ...R_N)$ is the i^{th}-state wavefunction, and is a function of positions of the electrons ($\mathbf{r}$) and nuclei ($\mathbf{R}$). In Eq. 2.1, E_i is the total energy of the system in the i^{th}-state. In atomic units, the Hamiltonian operator in the Eq. 2.1 is expressed as,[113]

$$H = -\frac{1}{2}\sum_{i=1}^{n}\nabla_{\text{i}}^2 - \sum_{I=1}^{N}\frac{1}{2M_I}\nabla_I^2 - \sum_{i=1}^{n}\sum_{I=1}^{N}\frac{Z_I}{r_{iI}} + \sum_{I=1}^{N}\sum_{J>I}^{N}\frac{Z_I Z_J}{R_{IJ}} + \sum_{i=1}^{n}\sum_{j>i}^{n}\frac{1}{r_{ij}}. \tag{2.2}$$

Here, the lowercase letters (i, j) and uppercase letters (I, J) denote the electrons and the nuclei, respectively. M_I is the mass of the nucleus, and Z_I and Z_J are the atomic numbers of the nuclei I and J, respectively. The distances between two electrons (i, j) and two nuclei (I, J) are denoted as r_{ij} and R_{IJ}, respectively. On the other hand, r_{iI} denotes the distance between an electron, i and a nucleus, I. The above Eq. 2.2 can be written more compactly as

$$\hat{H} = \hat{T}_{\text{e}}(\mathbf{r}) + \hat{T}_{\text{N}}(\mathbf{R}) + \hat{V}_{\text{eN}}(\mathbf{r},\mathbf{R}) + \hat{V}_{\text{NN}}(\mathbf{R}) + \hat{V}_{\text{ee}}(\mathbf{r}). \tag{2.3}$$

Here, the first and second terms correspond to the kinetic energies of electrons and nuclei, respectively. The last three terms correspond to the three potential energy operators.

2.2 Born-Oppenheimer approximation

The Born-Oppenheimer (BO) approximation is the basis of quantum mechanical calculations of atomic and molecular systems. It relies upon the fact that electrons are much lighter than nuclei, and move much faster compared to nuclei. In this scenario, electronic and nuclear parts of a molecular wave function can be separated, and the total wave function can be written as the product of two wavefunctions, one dependent on the electronic coordinates, and the other on the nuclear coordinates,

$$\Psi(r_1, r_2 \ldots r_n, R_1, R_2 \ldots R_N) = \psi(r_1, r_2 \ldots r_n)\varphi(R_1, R_2 \ldots R_N). \tag{2.4}$$

Here, $\psi(\mathbf{r})$ and $\varphi(\mathbf{R})$ represent the electronic and nuclear wavefunctions, respectively. Within the BO approximation, nuclei are treated as nearly fixed with respect to electron motion. This results in the so-called electronic Hamiltonian (by neglecting the kinetic energy operator for the nuclei and considering the nucleus-nucleus repulsion term ($\hat{V}_{\mathrm{NN}}(\mathbf{R})$) as a constant). The electronic Hamiltonian is written as

$$\hat{H}_{\mathrm{el}} = \hat{T}_{\mathrm{e}}(\mathbf{r}) + +\hat{V}_{\mathrm{eN}}(\mathbf{r,R}) + \hat{V}_{\mathrm{ee}}(\mathbf{r}) \tag{2.5}$$

and the electronic wavefunction as,

$$\psi_{\mathrm{el}} = \psi_{\mathrm{el}}(\mathbf{r;R}). \tag{2.6}$$

Here, ψ_{el} depends on the electronic coordinates and parametrically on the nuclear coordinates. The corresponding electronic Schrödinger equation is

$$\hat{H}_{\mathrm{el}}\psi_{\mathrm{el}} = E_{\mathrm{el}}\psi_{\mathrm{el}}, \tag{2.7}$$

where, $E_{\rm el}$ is the corresponding energy. The total energy of a system is

$$E = E_{\rm el} + \hat{V}_{\rm NN}(\mathbf{R}). \tag{2.8}$$

2.3 The One-Electron wavefunction and Hartree-Fock method

In the Eq. 2.6, $\psi_{\rm el}$ is a function of coordinates of all the electrons in the system. A convenient way proposed by Hartree[114] is to rewrite $\psi_{\rm el}$ as a product of one-electron functions corresponding to each electron as

$$\psi(r_1, r_2 \ ...r_n) = \phi_1(r_1)\phi_2(r_2)...\phi_{\rm n}(r_n). \tag{2.9}$$

Such a format for wavefunction can solve the Schrödinger equation exactly if the $\hat{V}_{\rm ee}(\mathbf{r})$ in the Hamiltonian operator in Eq. 2.5 is replaced with an effective field, $\hat{V}_i^{\rm eff}$. $\hat{V}_i^{\rm eff}$ is the potential exerted on an electron from average position of other electrons. This leads to the following equation for each ϕ_i, known

$$\left(-\frac{1}{2}\nabla_i^2 - \sum_{I=1}^{N} \frac{Z_I}{r_{iI}} + \hat{V}_i^{\rm eff} \right)\phi_i \ = \epsilon_i \phi_i. \tag{2.10}$$

Solution to this equation for a set of functions ϕ_i is non-trivial as the term $\hat{V}_i^{\rm eff}$ itself depends on all the functions ϕ_i. A self-consistent field procedure is used to solve the above equations. The above format of the wave function shown in Eq. 2.5 does not satisfy the Pauli exclusion principle.[115] To overcome this, Fock[116] suggested to use the Slater determinant

$$\psi(r_1, r_2 \ ...r_n) \ = \ \frac{1}{\sqrt{n!}} \begin{vmatrix} \phi_1(e_1) & \phi_2(e_1) & \dots & \phi_{\rm n}(e_1) \\ \phi_1(e_2) & \phi_2(e_2) & \dots & \phi_{\rm n}(e_2) \\ \vdots & \vdots & & \vdots \\ \phi_1(e_n) & \phi_2(e_n) & \dots & \phi_{\rm n}(e_n) \end{vmatrix} = \left| \phi_1 \phi_2 \dots \ \phi_{\rm n} \right| \tag{2.11}$$

which is antisymmetric and follows the Pauli exclusion principle. The factor $\frac{1}{\sqrt{n!}}$ is the normalized factor. This determinant has n electrons occupying n spin orbitals. Rows

are labeled by electrons, first row is for electron-one (e_1), second row is for electron-two (e_2) and so on. Columns are labeled by spin orbitals ϕ_1, ϕ_2, ..., ϕ_n. In the HF theory, a single Slater determinant is used as an approximation to the electronic wave function.

2.4 Post-Hartree-Fock methods

The HF method does not consider electron correlation effects. The electron-correlation effects can be introduced by various post-HF methods such as Møller-Plesset perturbation theory [117], coupled-cluster based methods [118,119], and multi-configurational methods such as the complete active space self-consistent field (CASSCF) [120–122] methods. Below, I provide an overview of the MP methods which is used in the thesis work.

2.4.1 Møller-Plesset perturbation theory

In 1934, Møller and Plesset [117] developed the methods for applying perturbation theory to molecular systems. In Møller-Plesset (MP) perturbation theory, the full Hamiltonian (excluding the kinetic energy term for nuclei, $\hat{T}_N(\mathbf{R})$) in Eq. 2.3 is divided into the HF part and a perturbation component which contains the electron-correlation part. Essentially, the HF calculation is taken as the starting point of the perturbation expansion, and the zeroth-order problem can be written as

$$\hat{H}^{(0)}\psi_0^{(0)} = E_0^{(0)}\psi_0^{(0)}, \tag{2.12}$$

where the subscripts of E and ϕ refer to the ground state. In the MP perturbation, the perturbation component can be expressed as

$$\hat{V} = \hat{H} - \hat{H}^{(0)} = \sum_{p \geq q} \frac{1}{r_{pq}} - \sum_{p,i} [\hat{J}_i(p) - \hat{K}_i(p)]. \tag{2.13}$$

In the above equation, $\hat{J}_i$ and $\hat{K}_i$ are the Coulomb and exchange operators that form the HF potential. These two are written as

$$\hat{J}_i(1)\phi_j(1) = \left[\int dr_2 \phi_i^*(2) \frac{1}{r_{12}} \phi_i(2)\right] \phi_j(1) \tag{2.14}$$

and

$$\hat{K}_i(1)\phi_j(1) = \left[\int dr_2 \phi_i^*(2)\frac{1}{r_{12}}\phi_j(2)\right]\phi_i(1), \tag{2.15}$$

where ϕs are the spin orbitals. The first-order correction to the energy obtained after operating the perturbation operator is given as

$$E_{\mathrm{MP}}^{(1)} = \langle\phi^{(0)}|\,\hat{V}\,|\phi^{(0)}\rangle = V_{00} = -\frac{1}{2}\sum_{ij}\langle ij|\,|ij\rangle\,, \tag{2.16}$$

where $\langle ij|\,|ij\rangle$ is an antisymmetrized two-electron integral over the occupied spin orbitals ϕs and defined as[113]

$$\langle ij|\,|kl\rangle = \langle ij|kl\rangle - \langle ij|lk\rangle = \int dr_1\ dr_2\ \phi_i^*(r_1)\phi_j^*(r_2)r_{12}^{-1}(1-\hat{P}_{12})\phi_k(r_1)\phi_l(r_2). \tag{2.17}$$

Here P_{12} is an operator which interchanges the coordinates of two electrons. The total MP1 energy is

$$E(\mathrm{MP1}) = \sum_{\mathrm{i=1}}^{\mathrm{N}}\epsilon_{\mathrm{i}} - \frac{1}{2}\sum_{ij}\langle ij|\,|ij\rangle\,. \tag{2.18}$$

Eq. 2.18 shows that the MP1 energy is the same as the HF energy. The second-order correction to energy ($E_{\mathrm{MP}}^{(2)}$) which leads to MP2 is given by

$$E_{\mathrm{MP}}^{(2)} = \frac{1}{4}\sum_{ij}^{occ}\sum_{ab}^{vir}\langle ij|\,|ab\rangle\,a_{ij}^{ab} \tag{2.19}$$

with

$$a_{ij}^{ab} = (\epsilon_i + \epsilon_j - \epsilon_a - \epsilon_b)^{-1}\,\langle ab|\,|ij\rangle\,. \tag{2.20}$$

As a consequence of the Brillouin theorem[123], the single excitations do not contribute. In addition, triple- and other higher-order excitations are excluded because of the Slater-Condon rules[124]. Therefore, finite matrix elements in the case of second-order correction are obtained only for the double excitations as shown in Eq. 2.19.

Grimme[125–127] proposed a variant of MP2, known as the spin-component-scaled

MP2 (SCS-MP2), for improving the ground state energies. It scales the terms involving electron pairs with same spin (SS) and opposite spin (OS) separately, The SCS-MP2 correlation correction is given as

$$E_{\mathrm{C}}(\mathrm{SCS-MP2}) = p_{\mathrm{OS}} E_{\mathrm{c}}^{\mathrm{OS}}(\mathrm{MP2}) + p_{\mathrm{SS}} E_{\mathrm{c}}^{\mathrm{SS}}(\mathrm{MP2}) \tag{2.21}$$

where p_{OS} and p_{SS} are empirically fit terms, with best values of 6/5 and 1/13, respectively.

2.5 Density functional theory

Electron density, denoted as $\rho(\mathbf{r})$, is extracted from the electronic wave function. In contrast to the wave function which is dependent on 4n variables, i.e., on three spatial and one spin coordinate for each electron, $\rho(\mathbf{r})$ is a function of three variables only, i.e., of x, y, and z coordinates. As proposed by Kohn and Sham (KS),[128] the energy functional is given as

$$E[\rho(\mathbf{r})] = T[\rho(\mathbf{r})] + V_{\mathrm{ne}}[\rho(\mathbf{r})] + V_{\mathrm{ee}}[\rho(\mathbf{r})] + E_{\mathrm{xc}}[\rho(\mathbf{r})], \tag{2.22}$$

where the first term is the kinetic energy of a system of non-interacting electrons with density same as the density of the real system. The second term is the nuclear-electron attraction energy expressed as

$$V_{\mathrm{ne}}[\rho(\mathbf{r})] = \sum_{I}^{N} \int \frac{Z_I}{|\mathbf{r} - \mathbf{r}_I|} \rho(\mathbf{r}) \mathrm{d}\mathbf{r}, \tag{2.23}$$

and the third term corresponds to the electron-electron repulsion energy,

$$V_{\mathrm{ee}}[\rho(\mathbf{r})] = \frac{1}{2} \int \int \frac{\rho(\mathbf{r}_1)\rho(\mathbf{r}_2)}{\mathbf{r}_1 - \mathbf{r}_2} \mathrm{d}\mathbf{r}_1 \mathrm{d}\mathbf{r}_2. \tag{2.24}$$

The last term, $E_{\mathrm{xc}}[\rho(\mathbf{r})]$, is the the exchange-correlation functional. Energy minimization is carried out by solving an eigenvalue equation analogous to the Hartree equations

as

$$\hat{h}_{\mathrm{i}}^{\mathrm{KS}}\chi_{\mathrm{i}} = E_{\mathrm{i}}\chi_{\mathrm{i}}. \tag{2.25}$$

The KS orbitals are also separable (similar to HF MOs). As a result, it is possible to solve the Eq.2.25 using similar set of steps as in the Hartree-Fock-Roothaan method. DFT has distinct advantages over the wave function based methods in that it produces the electron correlation energy at a similar computational cost to that of the HF method. However, the real problem in DFT is about the exchange-correlation term. To overcome this, various functionals have been proposed in the literature. However, in DFT, it is not possible to correct the performance of a particular functional systematically, unlike in the case of configuration interaction, where the performance can be improved by increasing the number and type of wavefunctions employed in the wavefunction expansion.

2.5.1 Exchange-correlation functionals

The exchange-correlation functional is written as a sum of an exchange part and a correlation part. These two terms are expressed in terms of energy density ϵ, which is dependent on the $\rho(\mathbf{r})$ as

$$E_{\mathrm{XC}}[\rho(\mathbf{r})] = E_{\mathrm{X}}[\rho(\mathbf{r})] + E_{\mathrm{C}}[\rho(\mathbf{r})] = \int \rho(\mathbf{r})\epsilon_{\mathrm{X}}[\rho(\mathbf{r})]\mathbf{dr} + \int \rho(\mathbf{r})\epsilon_{\mathrm{C}}[\rho(\mathbf{r})]\mathbf{dr}. \tag{2.26}$$

A series of approximate treatments have been applied to the exchange-correlation term leading to the non-empirical Jacob's ladder scheme.[129–131] Each rung in the Jacob's ladder defines a set of assumptions used in creating an exchange-correlation expression. The first rung in the ladder is the local density approximation (LDA), which assumes that ϵ_{X} can be calculated from just the density. A simple example of LDA is Dirac's treatment of a uniform gas, where the exchange energy density is treated as

$$\epsilon_{\mathrm{X}}^{\mathrm{LDA}} = -C_{\mathrm{X}}\rho^{1/3}. \tag{2.27}$$

However, in cases where the α and β spin densities are not equal, it is extended to the local spin density approximation (LSDA). The second rung of the ladder is the generalized gradient approximation (GGA). The third rung, meta-GGA functional, includes a dependence on the Laplacian of the density ($\nabla^2\rho$) or on the orbital kinetic energy density (τ). The fourth rung, the hybrid functionals, includes a dependence on exact HF exchange. The fifth one includes the unoccupied KS orbitals.

In DFT method, the most widely used exchange component is one proposed by Becke[132], which included a correction term involving derivative of density. The most widely used correlation functionals are proposed by Lee, Yang, and Parr[133] (referred to as *LYP*) and by Perdew and Wang[134](referred to as *PW91*). The hybrid functionals contain exchange-correlation functionals with some amount of the HF exchange. One of the most widely used hybrid functional is B3LYP consisting of Becke's exchange functional along with the LYP correlation functional:

$$E_{\mathrm{XC}}^{\mathrm{B3LYP}} = (1-a)E_{\mathrm{X}}^{\mathrm{LSDA}} + aE_{\mathrm{X}}^{\mathrm{HF}} + bE_{\mathrm{X}}^{\mathrm{B}} + (1-c)E_{\mathrm{C}}^{\mathrm{LSDA}} + cE_{\mathrm{C}}^{\mathrm{LYP}}, \tag{2.28}$$

where $E_{\mathrm{X}}^{\mathrm{B}}$ is the gradient corrected exchange energy obtained from the Becke functional[132], and $E_{\mathrm{C}}^{\mathrm{LYP}}$ is the correlation energy corresponding to the LYP correlation functional[133]. The three parameters a, b, and c are optimized to 0.20, 0.72 and 0.81, respectively. There are many other hybrid functionals reported in literature, such as PBE0 (second-rung functional)[135,136], HSE[137], O3LYP[138], hybrid meta functionals of M06 family and others.

Range-separated hybrid functionals produce more accurate excited states properties compared to the most commonly used standard functionals, especially when charge transfer excitations are involved. In the range-separation scheme of exchange-correlation functional, the electron–electron interaction operator $\frac{1}{r_{12}}$ is split into short-range and long-range components using standard error function as[139,140]

$$\frac{1}{r_{12}} = \frac{1-\mathrm{erf}(\mu r_{12})}{r_{12}} + \frac{\mathrm{erf}(\mu r_{12})}{r_{12}}, \tag{2.29}$$

where $r_{12} = |\mathbf{r}_1 - \mathbf{r}_2|$ is the distance between the electrons 1 and 2, erf(X) is the error

function, and μ is the range separation parameter. The first and second term account for the short-range and long-range interactions, respectively. One of the range-separated functionals is CAM-B3LYP. Applying the Coulomb-attenuating method to the B3LYP functional, Yanai et al.[141] introduced the CAM-B3LYP functional. Here, the form of Eq. 2.29 was generalized using two extra parameters α and β as,

$$\frac{1}{r_{12}} = \frac{1-[\alpha+\beta\cdot\mathrm{erf}(\mu r_{12})]}{r_{12}} + \frac{\alpha+\beta\cdot\mathrm{erf}(\mu r_{12})}{r_{12}}, \tag{2.30}$$

where $0\leq \alpha+\beta \leq 1$, $0\leq \alpha \leq 1$, and $0\leq \beta \leq 1$. The parameter α corresponds to the HF exchange contribution over the whole range by a factor of α, and β corresponds to DFT counterpart over the whole range by a factor of 1-(α+β). The extra flexibility arising from these two parameters allows to verify importance of the HF exchange contribution for the short-range region and the DFT counterpart for the long-range region. In CAM-B3LYP, HF exchange contributions at short- and long-ranges are 0.19 and 0.65, respectively.

2.6 Dispersion-corrected DFT

DFT has been an widely used method for electronic structures calculation and a series of DFT functionals have been proposed for different purposes. However, traditional DFT functionals does not taken care of the weak-interactions, such as hydrogen-bonding and van der Waals interactions. These interactions are indispensable in chemistry, biochemistry and materials science. The most widely used method to incorporate dispersion interaction is the Grimme's DFT-D[142] method. In this approach, a dispersion term, E_{disp} is added to the KS-DFT energy shown in Eq. 2.22, and the total dispersion corrected energy ($E_{\mathrm{DFT-D}}$) is expressed as[143]

$$E_{\mathrm{disp}} = -\frac{1}{2}\sum_{A\neq B}\sum_{n=6,8,10....} s_n \frac{C_{\mathrm{n}}^{\mathrm{AB}}}{R_{\mathrm{AB}}^{\mathrm{n}}} f_{\mathrm{damp}}(R_{\mathrm{AB}}), \tag{2.31}$$

where the sum is over the all the atom pairs. $C_{\mathrm{n}}^{\mathrm{AB}}$ is the dispersion coefficient of nth-order, dependent on particular atom pair AB. R_{AB} is the internuclear distance, s_{n} is a

scaling factor and f_{damp} is a damping function. The most common expressions for the damping functions are,[144]

$$f_{\text{damp}}(R_{\text{AB}}) = \frac{1}{1 + 6(R_{\text{AB}}/(s_{r,n}R_0^{\text{AB}}))^{-\gamma}} \tag{2.32}$$

or[143,145]

$$f_{\text{damp}}(R_{\text{AB}}) = \frac{1}{1 + e^{-\gamma(R_{\text{AB}}/s_{r,n}R_0^{\text{AB}}-1)}}, \tag{2.33}$$

where R_0^{AB} defines the cut-off radius for the atom pair AB, $s_{\text{r,n}}$ is the functional dependent radii scaling factor, and γ determines the steepness of the function for small R_{AB}.

The first two versions of DFT-D methods, i.e., DFT-D1[142] and DFT-D2[143] versions include only the n=6 term. However, in DFT-D3,[146] terms for n=6,8 are included. The original DFT-D3 method employs the damping function proposed by Chai and Head-Gordon[144] shown in Eq. 2.32. The second version, denoted as DFT-D3BJ, uses the damping form shown by Becke and Johnson. The form of f_{damp} by Becke and Johnson is

$$f_{\text{damp,BJ}}(R_{\text{AB}}^0) = a_1\sqrt{\frac{C_8^{\text{AB}}}{C_6^{\text{AB}}}}R_{\text{AB}}^0 + a_2 \tag{2.34}$$

and the dispersion energy employing $f_{\text{damp,BJ}}(R_{\text{AB}}^0)$ is

$$E_{\text{disp}}^{\text{D3(BJ)}} = -\frac{1}{2}\sum_{A,B} s_6\frac{C_6^{AB}}{R_6^{AB} + [f_{\text{damp,BJ}}(R_{\text{AB}}^0)]^6} + s_8\frac{C_8^{AB}}{R_8^{AB} + [f_{\text{damp,BJ}}(R_{\text{AB}}^0)]^8}. \tag{2.35}$$

Here, a_1 and a_2 are the free fit parameters. It has been observed that mean deviations for a benchmark data set that involve weak interactions, chemical reactions, and conformations are reduced by at least 1 kcal/mol with the inclusion of the D3 corrections for a range of functionals.[147,148]

2.7 Time-dependent density functional theory (TD-DFT)

Ground state DFT deals with systems subjected to static external potentials. However, to study systems under influence of external electromagnetic fields, the time-dependent version of the DFT is used. TD-DFT is a formally exact approach, and is the go-to method today to compute excited states and optical properties of large systems. The Runge-Gross theorem[149] is the basis for TD-DFT, like it was the Hohenberg-Kohn theorem for DFT. It states that there is a one-to-one mapping between the time-dependent external potential $v(r,t)$ and the time-dependent density of the system. In cases where external potential is small, perturbation theory can be used. Below we briefly show the linear response approach as derived by Marques and Gross.[150] If the ground-state density is $\rho^{(0)}$ and $v^{(1)}$ is the first order perturbed potential turned on at t_0, the density then can be expressed in a perturbative series as follows[151]

$$\rho(\boldsymbol{r},t) = \rho^{(0)}(\boldsymbol{r}) + \rho^{(1)}(\boldsymbol{r},t) + \rho^{(2)}(\boldsymbol{r},t) + \cdots, \tag{2.36}$$

where $\rho^{(1)}(\boldsymbol{r},t)$ is the component depending linearly on the $v^{(1)}$ and is expressed as

$$\rho^{(1)}(\boldsymbol{r},\omega) = \int d^3\boldsymbol{r}'\chi(\boldsymbol{r},\boldsymbol{r}',\omega)v^{(1)}(\boldsymbol{r}',\omega). \tag{2.37}$$

χ is the linear density-density response function. The $\rho^{(1)}$ can be calculated using the KS system as

$$\rho^{(1)}(\boldsymbol{r},\omega) = \int d^3\boldsymbol{r}'\chi_{\mathrm{KS}}(\boldsymbol{r},\boldsymbol{r}',\omega)v^{(1)}_{\mathrm{KS}}(\boldsymbol{r}',\omega), \tag{2.38}$$

where χ_{KS} $(\boldsymbol{r},\boldsymbol{r}',\omega)$ is density response function for the non-interacting electrons. χ_{KS}, in terms of unperturbed stationary KS orbitals, is written as

$$\chi_{\mathrm{KS}}(\boldsymbol{r},\boldsymbol{r}',\omega) = \lim_{\eta\to 0^+}\sum_{jk}^{\infty}(f_k - f_j)\frac{\phi_j(\boldsymbol{r})\phi_j^*(\boldsymbol{r}')\phi_k(\boldsymbol{r}')\phi_k^*(\boldsymbol{r})}{\omega - (\epsilon_j - \epsilon_k) + i\eta}, \tag{2.39}$$

where $\phi_{\mathrm{j}}(\boldsymbol{r})$ and ϵ_{j} are the KS eigenfunctions and eigenvalues, respectively. f_j shows the occupation number of the j-th orbital in the KS ground state. The term $v^{(1)}_{\mathrm{KS}}$ in the Eq.

2.38 can be calculated as

$$v_{\mathrm{KS}}^{(1)}(\boldsymbol{r},t) = v^{(1)}(\boldsymbol{r},t) + v_{\mathrm{Hartree}}^{(1)}(\boldsymbol{r},t) + v_{\mathrm{XC}}^{(1)}(\boldsymbol{r},t), \tag{2.40}$$

where the second term accounts for the classical electrostatic interaction between the electrons

$$v_{\mathrm{Hartree}}^{(1)}(\boldsymbol{r},t) = \int d^3r' \frac{\rho^{(1)}(\boldsymbol{r'},\boldsymbol{t})}{|\boldsymbol{r}-\boldsymbol{r'}|}. \tag{2.41}$$

The last term is the XC part in $\rho^{(1)}$ of the functional $v_{\mathrm{XC}}[\rho]$,

$$v_{\mathrm{XC}}^{(1)}(\boldsymbol{r},t) = \int dt' \int d^3r' \frac{\delta v_{\mathrm{XC}}(\boldsymbol{r},t)}{\delta\rho(\boldsymbol{r'},t')}\rho^{(1)}(\boldsymbol{r'},t') = \int dt' \int d^3r' f_{\mathrm{XC}}(\boldsymbol{r}t,\boldsymbol{r'}t')\rho^{(1)}(r',t') \tag{2.42}$$

where $f_{\mathrm{XC}}(\boldsymbol{r}t,\boldsymbol{r'}t')$ is the XC kernel.

Using the above results and transforming to frequency, Eq. 2.37 can be rewritten as

$$\begin{aligned}\rho^{(1)}(\boldsymbol{r},\omega) = &\int d^3r' \chi_{\mathrm{KS}}(\boldsymbol{r},\boldsymbol{r'},\omega)v^{(1)}(\boldsymbol{r'},\omega) + \\ &\int d^3x \int d^3r' \chi_{\mathrm{KS}}(\boldsymbol{r},\boldsymbol{x},\omega)\left[\frac{1}{|\boldsymbol{x}-\boldsymbol{r'}|} + f_{\mathrm{XC}}(\boldsymbol{x},\boldsymbol{r'},\omega)\right]\rho^{(1)}(\boldsymbol{r'},\omega).\end{aligned} \tag{2.43}$$

From Eqs 2.37 and 2.43, we have

$$\begin{aligned}\chi(\boldsymbol{r},\boldsymbol{r'},\omega) = &\int d^3x \int d^3x^3 \chi(\boldsymbol{r},\boldsymbol{x},\omega)\left[\frac{1}{|\boldsymbol{x}-\boldsymbol{x'}|} + f_{\mathrm{XC}}(\boldsymbol{x},\boldsymbol{x'},\omega)\right]\chi_{\mathrm{KS}}(\boldsymbol{x'},\boldsymbol{r'},\omega) + \\ &\chi_{\mathrm{KS}}(\boldsymbol{r},\boldsymbol{r'},\omega).\end{aligned} \tag{2.44}$$

This equation shows the exact representation of the linear response theory, and self-consistent solution of this equation can produce the response function, χ, of an interacting system. This will lead to a pseudo-eigenvalue equation which yields excitation energies.

2.8 Algebraic diagrammatic construction scheme for the polarization propagator

The algebraic diagrammatic construction (ADC) [152–157] scheme for the polarization propagator is a single-reference wave function based method to study the excited states and properties. The method is analogous to the MPn method for the ground states, and hence, is a perturbative method which can be systematically improved. Below we show a quick and short review of the methodology based on the intermediate-state formalism.

Denoting the ground state wavefunction as $|\Psi_0\rangle$, excited state wavefunctions, $|\Psi_J\rangle$ can be constructed by applying an excitation operator, $\hat{C}_J$ as

$$|\Psi_J\rangle = \hat{C}_J \ |\Psi_0\rangle \, .$$

The excitation operator, $\hat{C}_J$, can be written in terms of annihilation and creation operators as follows:

$$\hat{C}_J = \hat{a}_a^\dagger \ \hat{a}_i; \hat{a}_a^\dagger \hat{a}_b^\dagger \hat{a}_i \hat{a}_j; i < j, a < b.$$

While $\hat{a}_a^\dagger \ \hat{a}_i$ denotes the formation of singly-excited states, $\hat{a}_a^\dagger \hat{a}_b^\dagger \hat{a}_i \hat{a}_j$ denotes the formation of doubly-excited states. In the above equation, the subscripts $a, b, ...$ and $i, j, ...$ refer to virtual and occupied orbitals, respectively. The intermediate states (IS) are orthogonalized using the Gram-Schmidt procedure. The matrix elements of the ADC matrix are obtained by expressing the shifted Hamiltonian in the IS basis as

$$M_{ij} = \langle \Psi_I | \hat{H} - E_0 | \Psi_J \rangle \, ,$$

where E_0 denotes the exact ground state energy. The hermitian eigenvalue problem is solved by diagonalizing the matrix M. A compact form of the above is

$$MX = X\Omega,$$

where Ω and X denote the diagonal eigenvalues and eigenvectors, respectively.

The Rayleigh-Schrödinger perturbation theory can be used at this point to write the matrix M as

$$M = M^{(0)} + M^{(1)} + M^{(2)} + M^{(3)} + ... + M^{(i)}.$$

This expansion shows that elements can be considered up to a certain order of expansion which makes it easier to treat the correlation. Accordingly, while ADC(1) denotes the first order in perturbation equivalent to CIS, ADC(2) denotes the second order.

2.9 Rotatory strength and dissymmetry factor

Rotatory strength (R) is the imaginary part of the result of scalar product between electric dipole transition moment (EDTM) and magnetic dipole transition moment (MDTM) between the ground state and excited states. It is expressed as[158–160]

$$R = Im[\langle\Psi_0|\hat{\mu}|\Psi_n\rangle\langle|\Psi_n|\hat{m}|\Psi_0\rangle], \tag{2.45}$$

where Ψ_0 and Ψ_n are the ground and excited states, respectively. $\hat{\mu}$ and $\hat{m}$ are the electric and magnetic transition dipole moment operators, respectively. For an electronic transition, dissymmetry factors, g_{CD} and g_{CPL}, as mentioned in Eq. 1.1-1.2 can be calculated as[28,161]

$$g_{\mathrm{CD}}(g_{\mathrm{CPL}}) = 4 \times \frac{R}{D+G} = \frac{4|\boldsymbol{\mu}||\boldsymbol{m}|\cos\theta}{|\boldsymbol{\mu}|^2 + |\boldsymbol{m}|^2}, \tag{2.46}$$

where D and G are EDTM and MDTM strengths, respectively, corresponding to absorption (emission). $|\boldsymbol{\mu}|$ and $|\boldsymbol{m}|$ are the magnitudes of the EDTM and MDTM, respectively. θ in Eq. 2.46 denotes the angle between the two vectors, and therefore, it determines the magnitude of R.

2.10 One-electron transition density matrix

Fragment-based excited state analysis is based on the concept of correlated hole-electron pair.[162,163] For this an effective hole-electron wavefunction is required. This wave function can be written as an integral of the one-electron transition density matrix (1-TDM) between the ground and excited states,

$$\gamma^{0I}(r_h, r_e) = n \int \cdots \int \phi^0(r_h, r_2, \ldots, r_n)\, \phi^I(r_e, r_2, \ldots, r_n)\, dr_2 \ldots dr_n. \tag{2.47}$$

Here γ^{0I} is 1-TDM between ground (0) and excited (I) states, ϕ^0 and ϕ^I refer to the ground and excited-state wavefunctions, respectively. r_h and r_e represent the coordinates of hole and electron, respectively. The matrix representation of 1-TDM is given as

$$\gamma^{0I}(r_h, r_e) = \sum_{\mu v} D^{0I}_{\mu v} \chi_\mu(r_h) \chi_v(r_e) \tag{2.48}$$

where χ_μ and χ_v are the atomic orbital of the basis $\{\chi_\eta\}$ and the 1-TDM element $D^{0I}_{\mu v}$ is expressed as

$$D^{0I}_{\mu v} = \langle \phi^0 | \hat{a}^\dagger_\mu \hat{a}_v | \phi^I \rangle \tag{2.49}$$

where $\hat{a}^\dagger$ and $\hat{a}$ are the one-particle creation and annihilation operators, respectively. μ and v are the orbital indices. The exciton wavefunction obtained using this construction is very useful to analyze a variety of excited-state descriptors[162,164,165], such as charge transfer number, total charge-transfer, partition ratio of natural transition orbitals, exciton size etc..

2.10.1 Charge transfer number (Ω_{AB})

Charge transfer number (Ω_{AB}) is expressed as

$$\Omega_{AB} = \int_A \int_B \gamma^{0I}(r_h, r_e)^2\, dr_e\, dr_h, \tag{2.50}$$

considering that hole is present at the fragment A and electron at the fragment B. After collecting all the Ω value contributions from all the fragments A, B and so on, it is possible to visualize it in a pseudo-color matrix plot. This plot is known as Ω-plot or electron-hole correlation plot.[165] In the case of two fragments, it is simply a 2 × 2 plot (as shown in the Figure 3.9 in the chapter 3). In the plot, the local excitation contributions, originating from the same fragments ($\Omega_{\mathrm{A=B}}$), are shown in the main diagonal from lower left to upper right. The charge-transfer contributions ($\Omega_{\mathrm{A\neq B}}$), on the other hand, appear off-diagonally.

2.10.2 Total charge transfer (ω_{CT})

ω_{CT} shows the amount of charge-transfer during a particular transition. It depends on the fragmentation scheme employed for the charge-transfer analysis. It is defined by summing over the off-diagonal element of Ω_{AB} yielding

$$\omega_{CT} = \frac{1}{\Omega} \sum_{A,B\neq A} \Omega_{AB}. \tag{2.51}$$

The value of ω_{CT} range from 0 to 1, where value close to 0 indicates locally excited state or Frenkel excitonic state and 1 for fully charge transfer state.

2.10.3 Exciton size (d_{exc})

Exciton size is defined as the averaged electron-hole separation, and expressed as,[165]

$$\begin{aligned} d^2_{exc} = \left\langle (r_h - r_e)^2 \right\rangle_{exc} &= \frac{\langle \chi_{exc} | (r_h - r_e)^2 | \chi_{exc} \rangle}{\langle \chi_{exc} | \chi_{exc} \rangle} \\ &= \frac{1}{\Omega} \iint \gamma^{0I}(r_h, r_e)(r_h - r_e)^2 \gamma^{0I}(r_h, r_e)\, dr_h\, dr_e. \end{aligned} \tag{2.52}$$

The above equation can be rewritten by dividing the double integral into two separate regions of the atoms M and N,

$$d^2_{exc} = \frac{1}{\Omega} \sum_{M,N} \int_M \int_N \gamma^{0I}(r_h, r_e)(r_h - r_e)^2 \gamma^{0I}(r_h, r_e)\, dr_h\, dr_e. \tag{2.53}$$

Further, by approximating the term ((r_{h} -r_{e})^2) as the squared distance (d_{MN}) between the two nuclei of the atoms M and N, it can be expressed as

$$d_{exc}^2 \approx \frac{1}{\Omega} \sum_{M,N} d_{MN}^2 \int_M \int_N \gamma^{0I}(r_h, r_e)\gamma^{0I}(r_h, r_e)\, dr_h\, dr_e. \tag{2.54}$$

From Eq. 2.50, the approximate exciton size can be rewritten in a more compact form as

$$\tilde{d}_{exc} = \sqrt{\frac{1}{\Omega} \sum_{M,N} \Omega_{MN} d_{MN}^2}. \tag{2.55}$$

2.10.4 Participation ratio of NTOs (PR_{NTO})

PR_{NTO} is defined as PR_{NTO}=$(\sum_i \lambda_i)^2 / \sum_i \lambda_i^2$,[162,166] where λ_i is the weight of the transition between two states. PR_{NTO} provides the number of natural transition orbitals (NTO) participating to produce an excited state. NTO itself is obtained by a singular value decomposition of the 1-TDM.

Chapter 3

Excited-state properties of pyridine-thiophene oligomers: DFT vs RI-ADC(2)

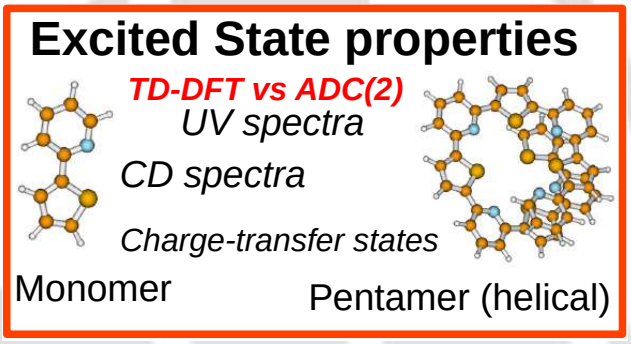

Figure: DFT vs ADC(2) for oligomers of pyridine-thiophene.

In this chapter, performances of various DFT functionals to reproduce the absorption and CD spectra of pyridine-thiophene oligomers are examined. Starting from a linear system like monomer, calculations are carried out at ADC(2) and DFT levels till a helical system like pentamer is formed. Analysis of excited-state properties shows that the state ordering patterns or results regarding natural transition orbitals from these DFT functionals sometimes differ from the ADC(2) results. A part of the content of this chapter is published in *J. Phys. Chem. A*, **2021**, 125, 1, 115-125.

3.1 Introduction

Over the last few decades, DFT based methods have been widely used in chemistry, biology and materials science. In contrast to the electron-correlated wave function based methods, DFT methods are able to handle large-sized systems due to their low computational cost. The method has been very successful while predicting ground state structures and properties. In materials science, modeling of organic layers in OLEDs, organic photovoltaics (OPVs) and organic field-effect transistors (OFETs), DFT has been the preferred method producing qualitatively correct ground state results. However, DFT has its limitations because of the use of approximate exchange-correlation functionals, although the theory itself is exact. In addition to DFT, linear-response TD-DFT [149,167] is the most widely used single-reference method till date for studying excited states. But computations for the properties of excited states using standard TD-DFT has not been as successful as DFT. Description of closely-lying excited states [168,169] or excited states arising out of multiple excitations [169–173] are problems for TD-DFT as it relies on single-determinant expression of ground state wave function. In addition, charge-transfer excited states are also not properly described using TD-DFT methods. [174–180] Further, failure of standard DFT functionals to describe excited states of extended π-conjugated systems has also been highlighted. [181–188] To address these issues, a large number of functionals, including so-called range-separated functionals have been developed in recent times and the usual strategy has been to benchmark the TD-DFT results against either experimental results or results from wave function based methods such as the second-order coupled-cluster (CC2), [189] the second/third order algebraic diagrammatic construction (ADC(2)/ADC(3)), [152–154,190] symmetry-adapted-cluster configuration interaction (SAC-CI) [191–193] or if possible, from multi-configurational methods such as complete active space self-consistent field (CASSCF) [120,121] methods.

Our group has been interested in studying co-oligomers based on six- membered rings like phenyl, pyridine and five-membered rings like furan, pyrrole and thiophene. [194,195] Oligomers based on these rings tend to form helical structures as the chain length increases. [194,195] A helix is inherently chiral and hence, molecules become optically active

only being helical without having any asymmetric carbons. Helical polymers are important because of potential applications in materials used for chiral recognition, liquid crystals and optical materials.[196–199] Noncovalent interactions such as π-π and hydrogen bonding interactions help in stabilizing these type of systems. In recent times, synthetic helical polymers based on furan, thiophene etc. have garnered a lot of attention.[39,200,201] In earlier studies,[194,195] our group reported interaction energies, absorption spectra, and CD spectra of oligomers based on furan, thiophene, pyrrole, phenyl and pyridine. All those studies were carried out at DFT (and TD-DFT) level of theory. It was observed that stability increases with increase in the size of helix. In addition, it was also found that for major electronic transitions, molecular orbitals (MO) other than the frontier orbitals contribute significantly. To take the studies further, in the present article, we aim to assess the accuracy of TD-DFT results taking into account various functionals against the ADC(2) results. For the purpose, we have taken into account the pyridine-thiophene **(PT)** oligomers. We have considered oligomers up to pentamers only. It is notable that monomer and polymers of **(PT)** have already been synthesized and spectroscopically characterized.[202–207,207–210] In particular, π-donating and π-accepting capabilities of five-membered and six-membered rings, respectively, in these type of systems have been of much interest and a lot of work has been carried out. ADC(2) calculations for oligomers larger than pentamers (containing ten rings in our case) are time-consuming and since a pentamer is already in a helix conformation, we start from linear structures and proceed till a helix is formed. In Sec. 3.2, computational details are described. This is followed by results and discussion section in which we present a comparison of the absorption and CD spectra results obtained using various DFT functionals with the ADC(2) results. Later in the section, we provide a quantitative comparison of the excited state properties by computing few excited state descriptors. Next, we have carried out a brief discussion over emission properties of $\mathbf{(PT)}_3$-$\mathbf{(PT)}_5$. In the last section, we provide a summary and conclude.

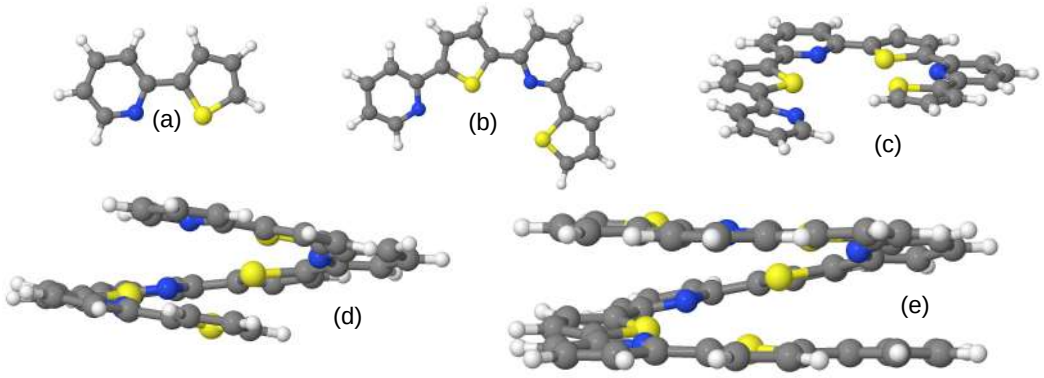

FIGURE 3.1: Optimized structures of **(PT)** oligomers: (a)-(e) show monomer to pentamer structures. These structures are obtained at RI-MP2/def2-SVP level. The gray, white, yellow and blue colours indicate C, H, S and N atoms, respectively.

3.2 Computational details

As mentioned already, oligomers up to pentamers are considered. In these oligomers, ortho- position of pyridine ring is connected to the ortho- position of the five-membered heterocyclic ring in a syn- fashion, i.e. the hetero atoms on the six- and five- membered rings are on the same side. This results in **B**-type structures of Ref.[194]. Ground state optimizations for all the oligomers are carried out at MP2 level of theory and using the def2-SVP[211] basis set. Using the ground state optimized geometries, excited state calculations are carried out at ADC(2) level[152,153] using avdz-vdz basis set. Here avdz-vdz refers to two different basis sets used for different atoms: aug-cc-pVDZ[212] (denoted as avdz) was used for N- and S- atoms while cc-pVDZ[213] (denoted as vdz) is used for all the other atoms. The above mentioned ground and excited state ab initio studies at ADC(2) level are carried out using the TURBOMOLE V7.1[214] software. Resolution-of-identity (RI) approximation[215–217] is used in all the calculations.

Time-dependent DFT calculations are performed using the Gaussian 09[218] program and the avdz-vdz basis sets. For these TD-DFT studies, we have considered only some of the popular functionals. In particular, fifteen different functionals are chosen: Five pure functionals such as BLYP[219–221], SVWN[222,223], PBE[224,225], OLYP[220,226], TPSS[227], and their long-range(lc) corrected versions lc-blyp, lc-pbe, lc-SVWN, lc-TPSS and lc-OLYP[228] are chosen. For hybrid functionals, two global hybrids B3LYP[229], PBE0[230], and long-range corrected hybrid CAM-B3LYP[141] and the dispersion-encompassing ωB97XD[144,231]

are used. In addition, the hybrid meta GGA functional M06-2X[232] is also used. All these TD-DFT calculations used the optimized geometries obtained at RI-MP2/def2-SVP level. UV and CD spectra are generated using the Gabedit software.[233] Gaussians with a half width at half-maximum 0.15 eV are used for the purpose. For the characterization of the excited states at both RI-ADC(2) and DFT levels, TheoDORE 1.7.2[234] is used. All the above calculations are carried out in the gas phase. Optimizations of optically active **(PT)**$_3$-**(PT)**$_5$ in their S_1 states were carried out at TD-CAM-B3LYP method using the same set of basis sets for investigating luminescence properties.

3.3 Results and discussion

3.3.1 Structures of oligomers and first vertical excitation energies

Ground state structures of the **(PT)** oligomers (n=1-5) are shown in Fig. 3.1. Optimized structures are similar to those shown in Ref.[194] which were obtained at B3LYP/6-31G(d,p) level. As the figure shows, **(PT)**$_{n=1,2}$ are planar. As the terminals come closer, **(PT)**$_{n=3}$ start becoming helical, and **(PT)**$_{n=4,5}$ are fully helical systems.

The first excitation energies (λ^1_{abs}s) and oscillator strengths (f_{osc}s) obtained using ADC(2) and hybrid functionals are plotted in Fig. 3.2 as a function of inverse oligomer length ($1/n$). The results are also tabulated in Table 3.1. As the figure and table show, λ_{abs} values (in nm) increases as the chain length increases. But, as observed in Ref.[194], it is difficult to extrapolate these energies to infinite chain length. f_{osc} values, on the other hand, show that until the molecule is not helical (i.e. till n=2), the regular increase pattern in f_{osc} happens. But as soon as helix formation starts, the value starts decreasing and for pure helical systems like **(PT)**$_4$ and **(PT)**$_5$, the f_{osc} values are very small. It is to be noted here that f_{osc} value for **(PT)**$_5$ is slightly larger than that for **(PT)**$_4$. But the values for $S_0 \rightarrow S_1$ transitions are very small once the helix is formed and as shown in Ref.[194], higher energy transitions carry larger f_{osc} values. Similar results are obtained in our case too as shown in Table 3.2. As the results show, λ_{abs} and f_{osc} values by CAM-B3LYP, ωB97XD and M06-2X functionals are very close to each other. In addition, ADC(2) values are pretty well reproduced by these three functionals. In

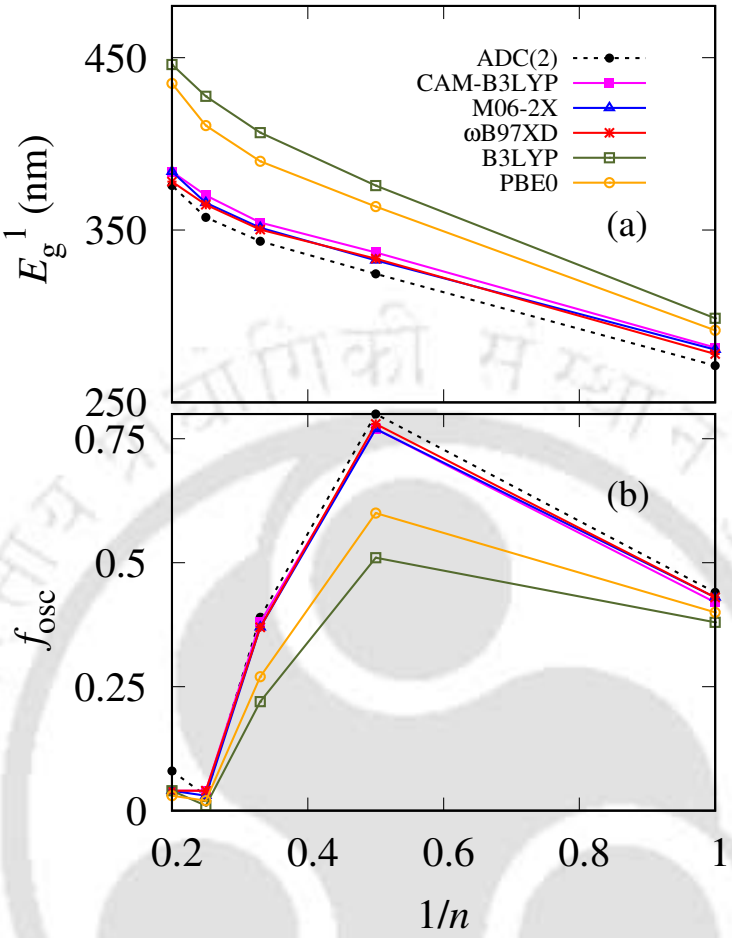

FIGURE 3.2: First excitation energy (λ^1_{abs}) values and oscillator strengths (f_{osc}) for $\mathbf{(PT)}_1$ to $\mathbf{(PT)}_5$ plotted against $1/n$. The results are obtained at RI-ADC(2)/avdz-vdz level.

contrast, λ^1_{abs} values obtained using B3LYP and PBE0 hybrid functionals differ by more than 15 nm from the ADC(2) values, for all the oligomers.

3.3.2 Absorption spectra

For comparison of the absorption spectra, oligomers are divided into two groups; in the first, monomer and dimer are together and in the second, other three are grouped together. Computed absorption spectra of monomer and dimer are shown in Fig. 3.3. For the other three, results are shown in Fig. 3.4. For $\mathbf{(PT)}_1$, ADC(2) results show three prominent transitions between 171 to 271 nm. The first transition at 271 nm arises from

TABLE 3.1: First excitation energies (λ^1_{abs}) and oscillator strengths (f_{osc}) of $\mathbf{(PT)}_{n=1,5}$. Results obtained using RI-ADC(2) method and various hybrid functionals are shown. All energies are in nanometer (nm) and are obtained using a combination of aug-cc-pVDZ and cc-pVDZ basis sets.

	λ^1_{abs}(nm)/f_{osc}					
	ADC(2)	CAM-B3LYP	ωB97XD	M06-2X	B3LYP	PBE0
$\mathbf{(PT)}_1$	271/0.44	282/0.42	280/0.43	278/0.43	299/0.38	292/0.40
$\mathbf{(PT)}_2$	324/0.80	337/0.77	333/0.78	333/0.77	376/0.51	363/0.60
$\mathbf{(PT)}_3$	343/0.39	354/0.38	350/0.37	351/0.37	407/0.22	390/0.27
$\mathbf{(PT)}_4$	357/0.03	369/0.04	364/0.04	366/0.03	428/0.01	410/0.02
$\mathbf{(PT)}_5$	376/0.08	381/0.04	375/0.04	379/0.04	451/0.04	433/0.04

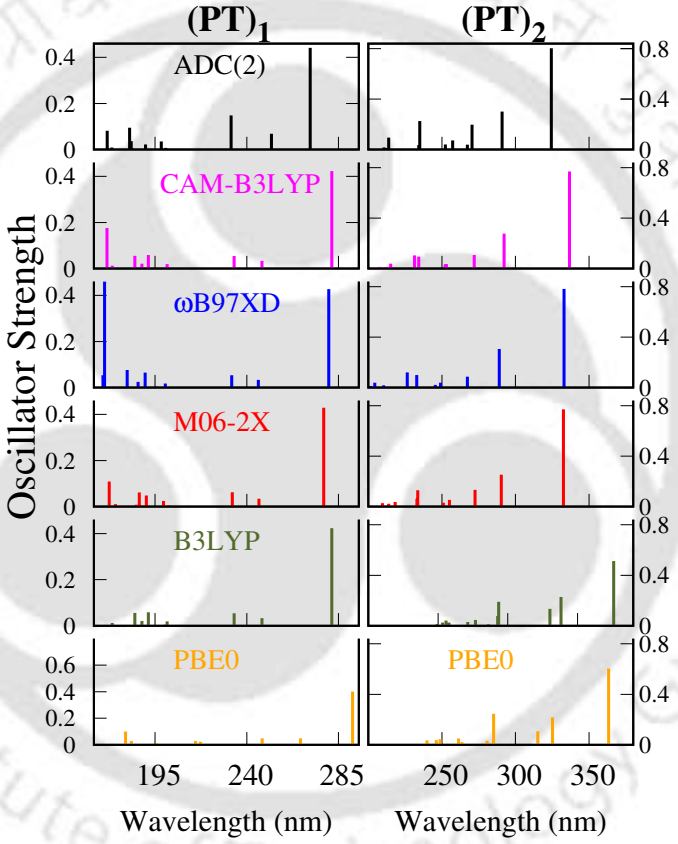

FIGURE 3.3: Absorption spectra of $\mathbf{(PT)}_1$ and $\mathbf{(PT)}_2$. Results obtained using CAM-B3LYP, M06-2X, ωB97XD, B3LYP and PBE0 functionals are plotted and compared against the ADC(2) results.

a pure highest occupied molecular orbital (H) to lowest unoccupied molecular orbital (L) transition. The second peak at 232 nm arises from a combination of transitions from H-1 and H to L. The third peak appears at 183 nm. DFT results from hybrid functionals CAM-B3LYP, M06-2X and ωB97XD match well among each other and with the ADC(2) results. But the results obtained using other two hybrid functionals shown

in Fig. 3.3 differ from the ADC(2) results. Both PBE0 and B3LYP excitation energies are red-shifted with respect to ADC(2). It is to be noted that peaks of CAM-B3LYP, M06-2X and ωB97XD functionals are also red-shifted with respect to ADC(2), but the shifts are larger in cases of B3LYP and PBE0. The results for pure functionals and long-range corrected versions of these pure functionals are shown in Figs A1-A2. As seen, various pure functionals produce the same absorption spectra. Similarly, the long-range corrected pure functionals also produce the same spectra. But, while spectra obtained using the pure functionals are red-shifted, spectra obtained using *lc-* functionals are blue-shifted in comparison with the benchmark ADC(2) data. For $\mathbf{(PT)}_2$, there are four major peaks appearing at 324 nm, 291 nm, 270 nm and 235 nm in ADC(2) results. The first peak at 324 nm corresponds to a purely H→L transition. The one at 291 nm arises due to H→L+1 and H-1→L transitions. As was the case with $\mathbf{(PT)}_1$, results of CAM-B3LYP, M06-2X and ωB97XD functionals mostly match with the ADC(2) results. But the peaks obtained using B3LYP and PBE0 are red-shifted by ∼ 50 nm. Results for pure and long-range corrected functionals are shown in Figs. A1-A2 and these results are again either red- or blue-shifted from the ADC(2) results.

In $\mathbf{(PT)}_3$, four peaks with larger intensities appear at 343 nm, 314 nm, 300 nm and 271 nm. These three peaks are due to transitions to ^{1}A, ^{2}A, ^{3}A and ^{9}A excited states, respectively. The first peak arises because of H → L excitation. The second one is due to a combination of excitations, from H → L+1 and H-1 → L. In $\mathbf{(PT)}_3$ case too, B3LYP and PBE0 results do not match with ADC(2) results. Their results are red-shifted and the transitions are with much smaller f_{osc} values. But CAM-B3LYP, ωB97XD and M06-2X are much closer to the ADC(2) results and are able to reproduce the absorption spectra. For example, the first transition in CAM-B3LYP differs only by 11 nm from ADC(2). Even the MOs involved in these transitions and their contributions (refer Table. A7) are similar to the ADC(2) results.

ADC(2) results for $\mathbf{(PT)}_4$ shows two major peaks appearing at 329 nm (f_{osc}=0.87) and 323 nm (f_{osc}=0.60), respectively. The peak at 329 nm corresponds to three sets of transitions H-1→L, H→L+2, and H→L+1. On the other hand, the second one arises due to H→L and H-1→L+1. CAM-B3LYP shows a slightly red-shifted two peaks again

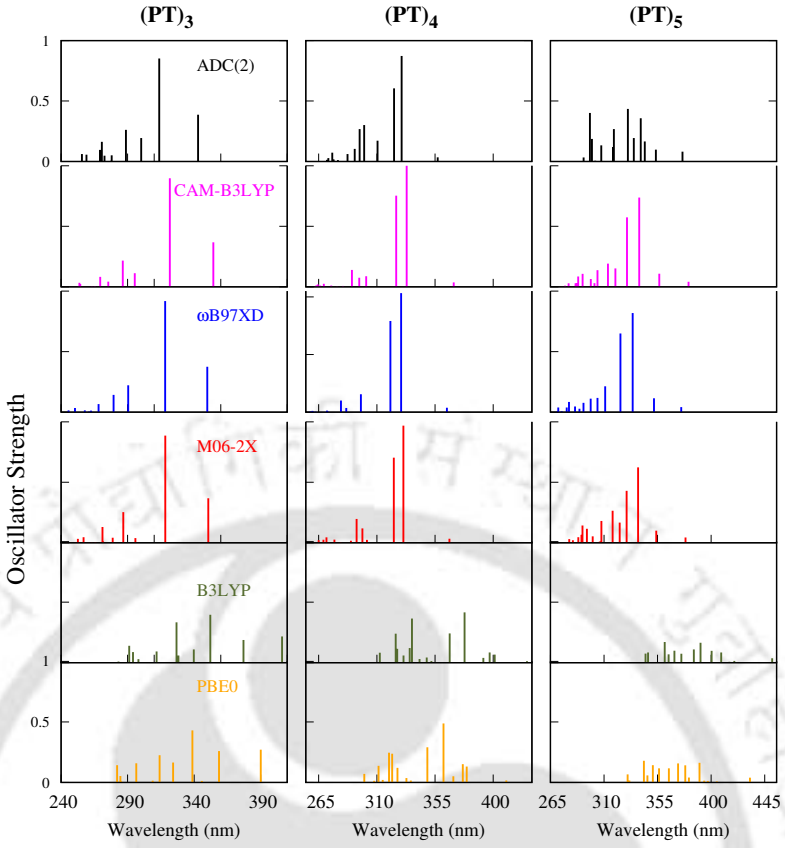

FIGURE 3.4: Absorption spectra of $\mathbf{(PT)}_3$, $\mathbf{(PT)}_4$ and $\mathbf{(PT)}_5$. Results obtained using CAM-B3LYP, M06-2X, ωB97XD, B3LYP and PBE0 functionals are plotted and compared against the ADC(2) results.

and the f_{osc} values are slightly larger in both the cases. Results of M06-2X and ωB97XD are similar to CAM-B3LYP.

As seen in Fig. 3.4, $\mathbf{(PT)}_5$, the largest unit considered in our study, has many peaks with large f_{osc} values between 293 nm and 379 nm. CAM-B3LYP, ωB97XD, and M06-2X functionals produce, again, similar absorption spectra. λ_{abs}, f_{osc} and major transitions involved in transitions for the first ten excited states of $\mathbf{(PT)}_5$ are tabulated in Table 3.2. As observed, λ_{abs} values obtained by ADC(2) and CAM-B3LYP the first three states are very close to each other. Similar results are obtained with M06-2X and ωB97XD functionals. From S_4 onward, differences between the energies are larger than 6 nm. f_{osc} values of CAM-B3LYP are comparatively larger from the ADC(2) peaks for many states. In addition, important configurations involved in the transitions are also different, except for two states out of ten. It is worth mentioning here that in a helical system such as $\mathbf{(PT)}_5$, many configurations participate in electronic excitations and this

TABLE 3.2: Vertical excitation energies (λ_{abs} in nm), corresponding oscillator strengths (f_{osc}), rotational strengths (R in 10^{-40} erg-esu-cm/Gauss) and dissymmetry factors (g_{CD}) for **(PT)**$_5$. In addition, contributions of most important transitions are shown too. Results obtained using the ADC(2) method and CAM-B3LYP, PBE and *lc*-PBE functionals are shown. All results are obtained using a combination of aug-cc-pVDZ and cc-pVDZ basis sets.

States	ADC(2)			CAM-B3LYP			PBE			*lc*-PBE		
	λ_{abs}	f_{osc}	R	λ_{abs}	f_{osc}	R	λ_{abs}	f_{osc}	R	λ_{abs}	f_{osc}	R
1	376	0.08	-684.71	381	0.04	-820.47	552	0.01	-10.93	341	0.05	-1038.48
	H→L (63.9%)			H→L (49.7%)			H→L (76 %)			H→L (36.1%)		
2	354	0.10	478.56	356	0.11	562.56	545	0.01	-15.91	324	0.13	625.35
	H-2→L (51.0%)			H-2→L (37.8%)			H→L+1 (87 %)			H→L+3 (35.4%)		
3	344	0.17	-101.95	340	0.74	-65.57	536	0.00	-11.96	308	1.09	43.18
	H→L+1 (32.0%)			H-1→L+1 (30%)			H-1→L (85 %)			H→L+2 (20.5%)		
4	341	0.36	-66.95	329	0.57	-265.05	523	0.00	-3.18	302	0.74	-208.46
	H-1→L+1 (43.3%)			H→L+1 (28.8%)			H-1→L+1 (77.5 %)			H-1→L+2 (18.1%)		
5	335	0.19	40.79	320	0.15	140.23	521	0.01	-14.82	282	0.34	380.11
	H→L+3 (26.3%)			H→L+3 (34.5%)			H→L+2 (50.5 %)			H-2→L+4 (37.0%)		
6	330	0.43	-6.69	313	0.19	186.96	516	0.00	6.90	266	0.01	27.58
	H→L+2 (38.8%)			H-1→L+3 (21.6%)			H-2→L (60.1 %)			H-1→L+2 (12.8 %)		
7	318	0.27	-43.27	305	0.14	-64.29	504	0.01	-39.14	264	0.02	-53.24
	H-1→L+2 (24.8%)			H-2→L+3 (32.4%)			H-1→L+2 (32.8 %)			H-2→L+3 (8.5 %)		
8	318	0.12	-2.30	302	0.03	3.56	478	0.06	-144.54	264	0.02	70.44
	H-1→L (26.9%)			H→L+1 (16.6%)			H-2→L+2 (38.8 %)			H-6→L (18.0 %)		
9	308	0.13	-48.72	299	0.07	83.56	473	0.03	-43.24	260	0.00	-3.51
	H-1→L+2 (23.3%)			H→L+2 (19.7%)			H-1→L+3 (44.3 %)			H→L+1 (15.7 %)		
10	306	0.00	21.01	292	0.11	74.68	467	0.088	253.83	254	0.02	23.28
	H-2→L+4 (19.3%)			H-1→L (15.7%)			H→L+3 (48.7 %)			H-2→L+2 (8.5%)		

is particularly important for higher excited states. PBE functional, as the table shows, produces λ_{abs}s and f_{osc}s which are very different than the ADC(2). In contrast, the excitation energies by a long-range corrected functional like *lc*-PBE are blue-shifted by more than 27 nm. More discussion regarding the excited state properties is given in a later section when analysis of the excited states is carried out.

3.3.3 CD spectra

Theoretical calculation of CD spectra is very sensitive to the level of method used. In this section, we have compared the CD spectra calculated using various DFT functionals against the ADC(2) results. The velocity gauge form is used throughout. Monomer and dimer of **(PT)** are planar, and hence, these two are optically inactive. In these two cases, EDTM and MDTM are orthogonal to each other producing zero rotatory strength. Starting from the trimer, helix formation starts and systems become optically active

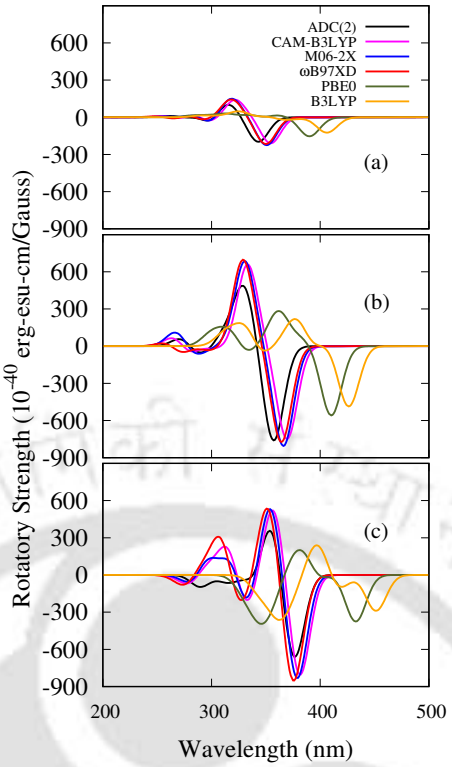

FIGURE 3.5: CD spectra of **(PT)** helical oligomers, n=3 (a) , 4 (b) and 5 (c).

producing non-zero R values. As $\mathbf{(PT)}_3$ is not complete helical, it shows comparatively weaker intensities in its CD spectra shown in the Fig. 3.5a. In this case, ADC(2) shows three major peaks, in addition to showing two smaller peaks in the high energy region. The third peak at 289 nm is very weak in comparison to the first and second. Functionals like CAM-B3LYP, M06-2X and ωB97XD are able to reproduce the ADC(2) peaks, but the peaks are red-shifted by few nanometers. B3LYP and PBE0, as in the UV case, produce very different results. Both $\mathbf{(PT)}_4$ and $\mathbf{(PT)}_5$, being fully helices, produce much larger intensity peaks. As observed in the case of CD for $\mathbf{(PT)}_3$, results of CAM-B3LYP, M06-2X and ωB97XD mostly match with the two major peaks of ADC(2) very well. But in the high-energy region around 288 nm, these DFT functionals show peaks with much higher intensities compared to the results of ADC(2), particularly in the case of $\mathbf{(PT)}_5$. Rotatory strengths of $\mathbf{(PT)}_5$ obtained with ADC(2), and CAM-B3LYP, PBE, and *lc*-PBE functionals for the first ten states are shown in Table 3.2. Results of other functionals for the first five states are shown in the Tables A1-A15. As shown in Table 3.2, the absolute values of R produced by CAM-B3LYP and *lc*-PBE functionals are larger than the ADC(2) results for all the states except S_3 in CAM-B3LYP, and

S_3 and S_9 in *lc*-BLYP. Results of pure and long-range corrected pure functionals are

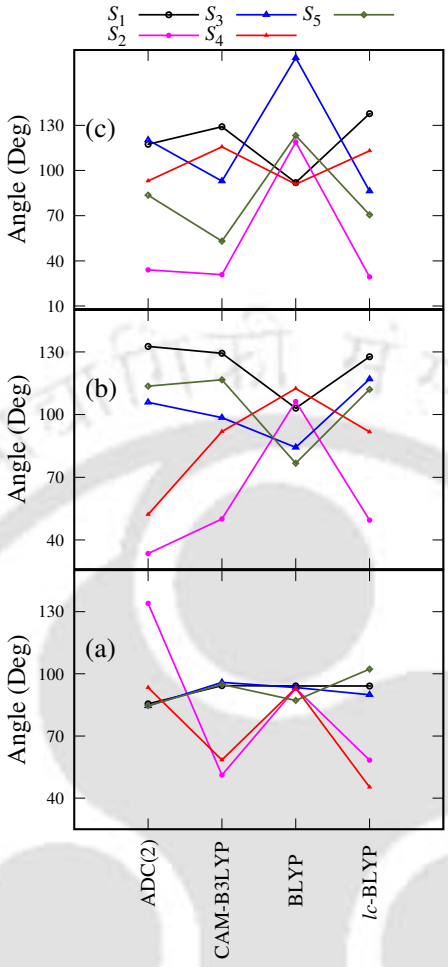

FIGURE 3.6: Angles between electric and magnetic transition dipole moments for ADC(2) and three DFT functionals. Results for first five excited states for $\mathbf{(PT)}_3$(a), $\mathbf{(PT)}_4$(b) and $\mathbf{(PT)}_5$(c) are shown.

shown in Figs. A5 and A6, respectively. As observed in the cases of UV spectra, five pure functionals' band regions are much beyond the ADC(2) results and produce red-shifted CD peaks with much lower intensities compared to ADC(2). *lc*-corrected pure functionals improve the results over the pure functionals, but the peaks are blue-shifted compared to the ADC(2) results. In this case, peaks of five functionals overlap each other.

Fig. 3.6 shows the variations in θ as a function of ADC(2) and three different hybrid functionals for first five excited states of $\mathbf{(PT)}_3$, $\mathbf{(PT)}_4$, and $\mathbf{(PT)}_5$. For $\mathbf{(PT)}_3$,

similar θs are obtained using all the methods for S_1, S_3, and S_5 states. But variations are observed in cases of S_2 and S_4. In these two cases, BLYP angles are larger than those with CAM-B3LYP and *lc*-BLYP, and closer to ADC(2) angles. In contrast, in cases of $\mathbf{(PT)}_4$ and $\mathbf{(PT)}_5$, CAM-B3LYP and *lc*-BLYP results are mostly closer to the angles obtained with ADC(2) and BLYP angles are either much smaller or larger than the other two DFT results.

3.3.4 Analysis of excited states

As observed in the above two sections, there are variations among the excited state results obtained using pure and hybrid functionals as well as between the functionals and ADC(2). To gain an understanding of the underlying differences among the methods, a comprehensive exciton-based analysis is adapted to study the excited state characteristics. In extended π-conjugated systems, descriptions based on molecular orbitals do not usually provide a complete picture.[188,235] Rather, a coupled electron-hole pair based picture is more appropriate providing a quantitative measure of excitonic effects. The excitonic analysis based on 1-TDM was carried out using the TheoDORE package.[234] The idea is to partition the 1-TDM into contributions from various fragments and then, compute the values of various descriptors to analyze the excited states. For details of the descriptors and their derivations, see Refs.[162,163,165,236–239]. In our case, each ring in the oligomer is considered as one fragment. Hence, in $\mathbf{(PT)}_1$, there are two fragments. Similarly, in dimer, trimer, tetramer and pentamer, there are four, six, eight and ten fragments, respectively. We have considered descriptors such as total charge-transfer (ω_{CT}), exciton size (d_{exc}) and participation ratio of natural transition orbitals (PR_{NTO}) for the analysis.[162,163,165,236–239] Below we discuss the results for $\mathbf{(PT)}_1$ and $\mathbf{(PT)}_5$ only, $\mathbf{(PT)}_1$ representing a linear/planar system and $\mathbf{(PT)}_5$ a helix.

Table 3.3 shows a comparison of the values of above descriptors obtained using CAM-B3LYP functional against the ADC(2) results for $\mathbf{(PT)}_1$ and $\mathbf{(PT)}_5$. Values of ω_{CT} indicates the type of excited state. While ω_{CT} is one for a completely charge-separated state, it is zero for a local/Frenkel excited state. For $\mathbf{(PT)}_1$, ω_{CT} values vary between 0.05 for the S_4 to 0.46 for S_1. ADC(2) results are reproduced by CAM-B3LYP

TABLE 3.3: Participation ratio of natural transition orbitals (PR_{NTO}), charge transfer (ω_{CT}), and exciton size (d_{exc} in Å) of first five excited states of $\mathbf{(PT)}_1$(top) and $\mathbf{(PT)}_5$(bottom) at RI-ADC(2) and CAM-B3LYP levels of theory.

	ADC(2)			CAM-B3LYP		
State	PR_{NTO}	ω_{CT}	d_{exc}	PR_{NTO}	ω_{CT}	d_{exc}
	$\mathbf{(PT)}_1$					
S_1	1.09	0.46	3.33	1.00	0.51	3.45
S_2	1.00	0.35	2.88	1.00	0.30	2.79
S_3	1.76	0.43	3.28	1.44	0.51	3.51
S_4	1.00	0.05	2.24	1.17	0.42	3.19
S_5	1.29	0.41	3.12	1.00	0.14	2.47
	$\mathbf{(PT)}_5$					
S_1	1.74	0.75	5.22	2.33	0.75	5.28
S_2	1.86	0.73	5.10	2.00	0.77	5.66
S_3	1.84	0.86	6.18	2.03	0.80	5.40
S_4	1.96	0.83	5.50	1.75	0.75	5.58
S_5	2.11	0.90	6.04	2.08	0.95	6.15

except that the order of S_4 and S_5 seems interchanged with respect to ω_{CT}. Since most of the ω_{CT} values in this case lie around 0.4-0.5, it is difficult to assign those as local or charge-transfer states by looking at only ω_{CT}. A conclusion regarding this will be derived while discussing electron-hole correlation plots and natural transition orbitals later in the section. But S_4 in ADC(2) (or S_5 in CAM-B3LYP) is identified as a local excited state because of its very small ω_{CT}. For $\mathbf{(PT)}_5$, all the excited states shown in the table are either partially or complete charge-transfer states (ω_{CT} values are between 0.72 and 0.95). In this case too, the hybrid functional is able to reproduce the ADC(2) results. d_{exc} denotes the average electron-hole distance and is a critical measure of the local or charge-transfer state. The inference given by ω_{CT} values is reproduced by the d_{exc} values. Comparatively small ($\leq$ 3.33 Å) and large values ($\geq$ 5.1 Å) hint at the local and charge-transfer nature of the excited states for $\mathbf{(PT)}_1$ and $\mathbf{(PT)}_5$, respectively. PR_{NTO} provides the number of natural transition orbitals (NTOs) participating to describe an excited state. PR_{NTO} values clearly show that while S_1, S_2 and S_4 are described by single set of NTOs, S_3 and S_5 require two sets of NTOs. For $\mathbf{(PT)}_1$, the NTOs involved in the transitions are shown in Fig. 3.7. From the figure, it is clear that S_1, S_2, S_3 and S_4 are local excited states. The S_5 state having ω_{CT} value of 0.41 is identified as a charge-transfer state from the NTOs. While S_2 and S_4 are identified as n-π^* states,

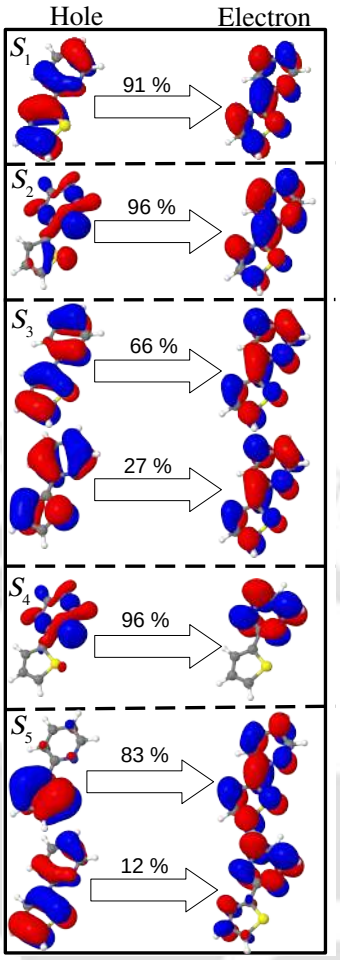

FIGURE 3.7: Natural transition orbitals for the S_1-S_5 states of $\mathbf{(PT)}_1$. The results are obtained at RI-ADC(2)/avdz-vdz level of theory.

the other three are π-π^* states. From PR_{NTO} values for $\mathbf{(PT)}_1$, it is observed that CAM-B3LYP results are in accordance with the ADC(2) results except that the order for S_4 and S_5 states is interchanged, in accordance with the ω_{CT} results. In the case of ADC(2) results for $\mathbf{(PT)}_5$, two and three NTOs participate for the S_1 and S_5 states, respectively. CAM-B3LYP results shown in the Table 3.3 for $\mathbf{(PT)}_5$ differ from the ADC(2) results in the case of PR_{NTO}. For example, the S_1 state in CAM-B3LYP shows the involvement of three NTOs although the contribution of the third NTO is very small. Fig. 3.8 shows the NTOs for the S_1 and S_5 states. In case of S_1, the initial and final orbitals are towards the overlapping regions of the oligomer for the first transition and the opposite is observed for the second transition in case of S_1 state. In contrast for the S_5 state, initial and final orbitals for the first two transitions are located towards the terminals of the rings with smaller contributions from the other regions. It is also to

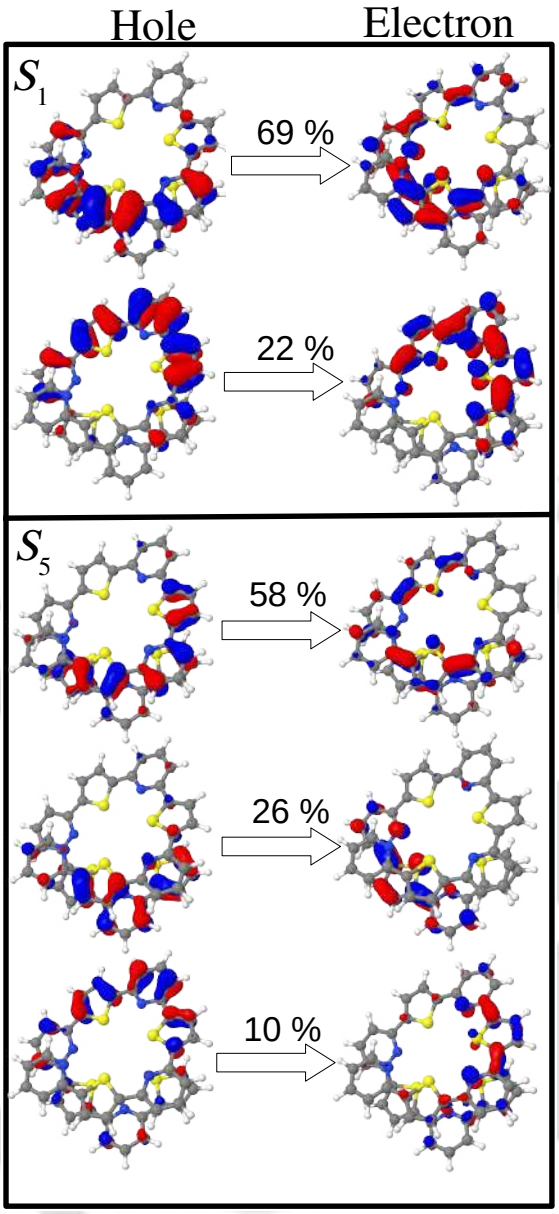

FIGURE 3.8: Natural transition orbitals for the S_1 and S_5 states of $\mathbf{(PT)}_5$. S_1 and S_5 are described by two and three sets of NTOs, respectively. The results are obtained at RI-ADC(2)/avdz-vdz level of theory.

be noted here that holes and electrons are localized at slightly different positions giving rise to a small charge-transfer character to S_1. In case of S_5, on the other hand, a clear separation of holes and electrons is observed making this a charge-transfer state.

In addition to the above descriptors, characters of the excited states are also investigated by using electron-hole correlation plots of the Ω matrices. The results for $\mathbf{(PT)}_1$ and $\mathbf{(PT)}_5$ are plotted in Fig. 3.9 for ADC(2) and CAM-B3LYP functionals. Each square in the plot indicates a fragment; for $\mathbf{(PT)}_1$, there are two fragments, hence

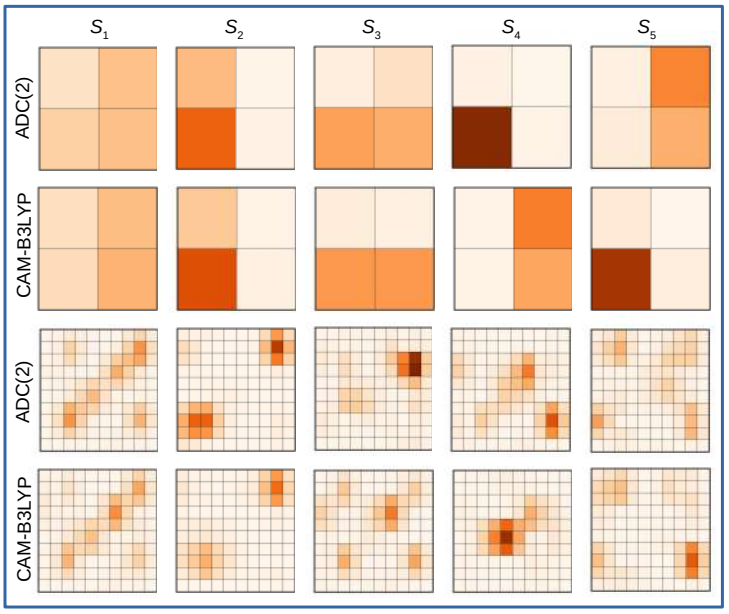

FIGURE 3.9: Electron hole correlation plots of $\mathbf{(PT)}_1$ (top two rows) and $\mathbf{(PT)}_5$ (bottom two rows) at ADC(2) and CAM-B3LYP levels. Results for first five excited states are shown. The main diagonal going from lower left to upper right indicates local excitations and the off-diagonal elements indicate excitations between different sites.

the plot shows a 2×2 matrix and for $\mathbf{(PT)}_5$, there are ten fragments, hence the plot shows a 10×10 matrix. While the diagonal field indicates the extension of exciton, i.e. the probability of local excitations at different rings, the off-diagonal field indicates the extent of charge-transfer between the rings. For $\mathbf{(PT)}_1$, the plots show that ADC(2) and CAM-B3LYP results are in sync with each other for S_1, S_2 and S_3 states. In addition, the state ordering is changed for S_4 and S_5 states while going from ADC(2) to CAM-B3LYP. The S_1 state is delocalized over the whole system for $\mathbf{(PT)}_1$ with little charge-transfer characteristics. Similarly, both S_2 and S_3 are predominantly local excited states. The S_4 state (in ADC(2)) for $\mathbf{(PT)}_1$ is a pure local excited state. For $\mathbf{(PT)}_5$, S_1 shows a large diagonal length, i.e. the state is delocalized almost over the whole system. In addition, appearance of off-diagonal elements implies some amount of charge transfer, as predicted by the ω_{CT} values in the Table 3.3. On the other hand, S_2 shows a low density region spanning over four rings and charge transfer is concentrated mostly around the terminal rings. For S_3, S_4 and S_5 states, there are significant amounts of charge transfers as shown and this is in accordance with the ω_{CT} values discussed in

the previous paragraph. CAM-B3LYP results mostly resemble the ADC(2) results except for the S_4 state. S_4 in case of CAM-B3LYP shows the exciton localization around the central rings with smaller amount of charge-transfer between neighboring units. In addition, it is observed that the S_4 state obtained using ADC(2) and S_3 state obtained using CAM-B3LYP resemble each other very closely. Results of a pure functional, PBE, and a long-range corrected pure functional, *lc*-PBE, are shown in Figs. A7-A8. For both $\mathbf{(PT)}_1$ and $\mathbf{(PT)}_5$, results of PBE functional differ considerably from the ADC(2) results. *lc*-PBE, a representative of the long-range corrected pure functionals, mostly reproduces the results of CAM-B3LYP for all the states, although the local excitations are little bit more localized for few states. For $\mathbf{(PT)}_5$, *lc*-PBE reproduces the CAM-B3LYP results for the first four states, but significant differences are observed for the S_5.

Results for all the oligomers and all the DFT functionals are tabulated in Tables A1-A15. Results of M06-2X and ωB97XD functionals are very close to CAM-B3LYP results for all the oligomers, as observed in UV and CD spectra. Results of B3LYP and PBE0 are similar to each other. For $\mathbf{(PT)}_1$, differences in the values of the descriptors between these two and a functional like CAM-B3LYP are small. But for $\mathbf{(PT)}_5$, large differences are observed in the values of PR_{NTO} and d_{exc}. While PR_{NTO} values are much smaller than the ADC(2) values, d_{exc} values are much larger in this case. It is worth reiterating here that B3LYP and PBE0 excitation energies are red-shifted in comparison to the ADC(2) results as mentioned previously. Results of pure functionals for $\mathbf{(PT)}_1$ are similar to each other and close to the hybrid functional, although the excitation energies are much smaller. But for $\mathbf{(PT)}_5$, clear discrepancies are observed between the results of pure functionals and those of ADC(2) for PR_{NTO} and d_{exc} values. Fig. 3.10 show the variations in the values of d_{exc} and PR_{NTO} as a function of oligomer chain length. In this figure, BLYP serves as an example of a pure functional and similarly, *lc*-BLYP is a representative of a long-range corrected functional. As discussed before, ω_{CT} and d_{exc} behave almost similarly, and hence, variations in ω_{CT} are not shown here. In ADC(2), variations in d_{exc} do not follow any particular trend with respect to n since the system changes from being a planar to a helix as n increases. While d_{exc} values for S_1 and S_3 show gradual increase as a function of n, the values for S_2 and S_4 increase

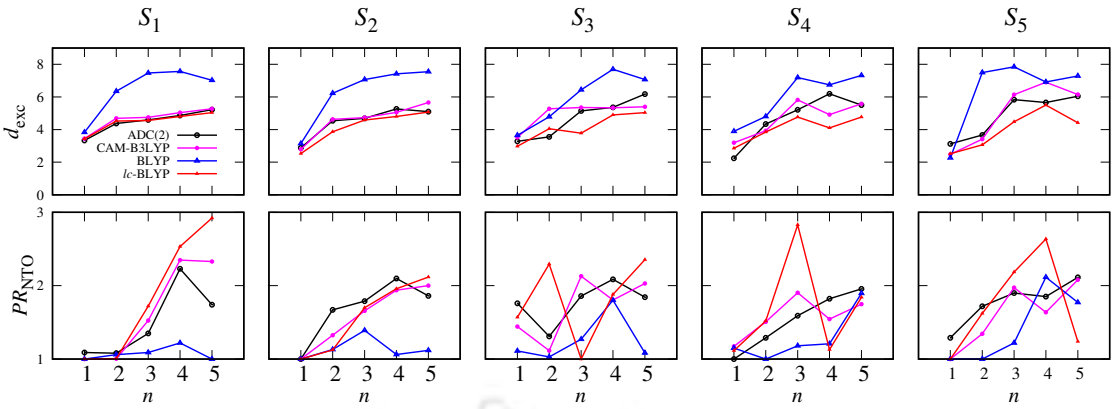

FIGURE 3.10: Exciton size (d_{exc}), charge transfer (ω_{CT}), and participation ratio of NTOs (PR_{NTO}) of lowest five excited states of plotted against oligomer chain length. Results obtained at CAM-B3LYP, BLYP, and *lc*-BLYP functionals are compared against the ADC(2) results.

till n=4 followed by a decrease. CAM-B3LYP is able to reproduce the trend in cases of S_1 and S_2. In case of S_3, while ADC(2) shows an increase vs n, CAM-B3LYP shows convergence at n=3. *lc*-BLYP's behavior is mostly similar to that of CAM-B3LYP, although differences in the values of d_{exc} between *lc*-BLYP and CAM-B3LYP seem to increase as the state number increases. Overall, these results show that d_{exc} values for the pentamer are between 5-6 Å. This is in accordance with the values reported in Ref.[188]. Mewes et al.[188] examined a variety of extended π-conjugated systems and concluded that the exciton size for the lowest singlet excited state converges to about 5-7 Å using ωPBE, CAM-B3LYP, M06-2X functionals and the ADC(2) method. In our case, the values do not clearly show a convergence pattern as a function of n except for S_3 using CAM-B3LYP. A definite conclusion regarding this can only be made when studies for few larger oligomers are carried out and this is beyond the purview of this work. It was also concluded in Ref.[188] that value of d_{exc} is dependent on the amount of nonlocal orbital exchange in TD-DFT. Similar observations are made in our cases too. For example, BLYP shows much larger d_{exc} values in cases of S_1 and S_2. For the other three, the value remains large in many of the oligomers. In case of PR_{NTO} for the S_1 state, ADC(2), CAM-B3LYP and *lc*-BLYP results remain close to each other till n=4. For S_2, results of these three methods produce similar results for all the five oligomers. But for these two states, BLYP produces much smaller numbers and the differences seem to increase with n. For the other three states, it is difficult to find a correlation between the methods. But it is observed that CAM-B3LYP numbers are closer to those

TABLE 3.4: Emission energies (λ_{em} in nm), Corresponding Oscillator Strength(f_{osc}), $|\boldsymbol{\mu}|$, $|\boldsymbol{m}|$, cos θ, R, g_{CPL}, K_f, and $|\boldsymbol{\mu}|/|\boldsymbol{m}|$ of **(PT)**$_3$,**(PT)**$_4$, and **(PT)**$_5$. $|\boldsymbol{\mu}|$, $|\boldsymbol{m}|$ and R are in esu·cm, erg·G^{-1} and esu·cm·erg·G^{-1} units, respectively. K_f is in ns^{-1}. All the considered transitions are $S_1 \rightarrow S_0$.

System	λ_{em}	f_{osc}	$\|\boldsymbol{\mu}\|/10^{-20}$	$\|\boldsymbol{m}\|/10^{-20}$	cos θ	$R/10^{-40}$	g_{CPL}	$\|\boldsymbol{m}\|/\|\boldsymbol{\mu}\|$	K_f
(PT)$_3$	388	0.705	762.72	4.55	0.000	-0.18	0.000	0.006	0.3120
(PT)$_4$	389	0.438	602.18	6.41	-0.138	-533.93	-0.006	0.011	0.1926
(PT)$_5$	393	0.318	516.08	4.61	-0.120	-284.74	-0.004	0.009	0.1372

by ADC(2).

3.4 Emission properties

In this section, luminescence properties for **(PT)**$_3$-**(PT)**$_5$ are discussed, obtained at the TD-CAM-B3LYP/vdz-avdz method. The CAM-B3LYP functional was chosen as the excited state results obtained using this functional matched with the RI-ADC(2) results, as shown in sections 3.3.3 and 3.3.4 . In typical organic molecules, emission follows the Kasha's rule[240] and occurs from the S_1 state. In Table 3.4, λ_{em} values, corresponding f_{osc}s, dipole transition moments (DTM), cos θ, g_{CPL} and fluorescence rate constants (K_f) are shown for the $S_1 \rightarrow S_0$ transitions. In case **(PT)**$_3$, R value is close to zero, and the corresponding g_{CPL} is zero. This is because of the orthogonal orientation of the vectors μ, and m. On the other hand, the K_f value is the largest for **(PT)**$_3$ among all the three systems shown in the table. For **(PT)**$_4$ and **(PT)**$_5$, improved chiroptical properties are observed in comparison to **(PT)**$_3$. In both the cases, R and g_{CPL} are significantly larger. Here, the angles between the two vectors are close to 100°. Between these two, **(PT)**$_4$ is the better emissive oligomer, with K_f=0.1926 and the largest g_{CPL} value of -0.006.

3.5 Conclusions

In this work, UV and CD spectra of pyridine-thiophene oligomers (n=1-5) are investigated using the *ab initio* ADC(2) method and various DFT functionals. While the monomer and dimer are planar, formation of helical system starts from trimer, and **(PT)**$_4$ and **(PT)**$_5$ are helical. Both UV and CD results obtained using the CAM-B3LYP,

M06-2X and ωB97XD functionals match well with the benchmark ADC(2) results. Results of PBE0 and B3LYP are very different than the ADC(2) results, even for the planar oligomers. For the UV spectra, while the pure functionals' results are red-shifted, results of long-range corrected pure functionals are blue-shifted in comparison to the ADC(2) results. Analysis of excited states was also carried out by computing descriptors such as exciton sizes, charge transfer numbers, and number of NTOs participating in a particular transition. Here the results of CAM-B3LYP, M06-2X, and ωB97XD functionals match with each other. But these DFT descriptor results sometimes differ from the ADC(2) results regarding the state ordering and number of NTOs participating. Overall, it is found that functionals like CAM-B3LYP, M06-2X, and ωB97XD work better than the others for oligomers of pyridine-thiophene. Future work will focus on the exciton dynamics in these types of helical systems.

Chapter 4

Chiroptical properties of polyaza[9]helicene and its derivatives

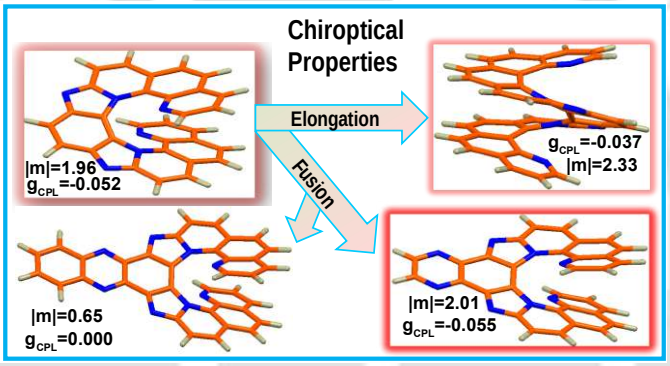

In this chapter, the effect of lateral and helical extensions on the physical and chiroptical properties of azahelicenes is reported. Starting with the experimentally reported azahelicene **9Ha**, three derivatives, two with laterally fused rings and the third with larger helical length, are designed. For the excited state properties such as UV-vis and CD spectra, performance of different DFT functionals is evaluated by comparing the results against the ADC(2) results. CPL properties are calculated at DFT level. Among the three designed systems, pyrazine based **9HaP** shows improved g_{CPL} value compared to the parent **9Ha**. On the other hand, quinoxaline based **9HaQ** is found to be the worst CPL emitter with the lowest dissymmetry factor. The helically extended derivative, **11Ha**, shows good CPL results, but the g_{CPL} remains smaller than for the parent system. The CPL results are analyzed in terms of electric and magnetic dipole transition moment vectors, and angles between these two vectors. A part of the content of this chapter is published in *J. Phys. Chem. A*, **2022**, 126, 8, 1412-1421.

4.1 Introduction

Efficiencies of CD and CPL active systems are evaluated in terms of dissymmetry factors, g_{CD} and g_{CPL}, corresponding to CD and CPL, respectively,[27] as mentioned in Section 2.9. A good light emitter should also show high Φ_{FL}, in addition to showing good CPL properties. Achieving good values for both g_{CPL} and Φ_{FL} simultaneously is difficult, and this has been an active area of research. For carbohelicenes, both the Φ_{FL} and g_{CPL} values have been found to be small.[7,59,108,109] The smaller value of Φ_{FL} is attributed to the favored intersystem crossing pathways.

In many cases, substitutions by different groups[53,54,57] and introduction of aromatic rings to produce ring-fused carbo[n]helicenes[7,58–62] have been shown to be good strategies to improve the Φ_{FL} values and alter the chiroptical properties. Introduction of quinoxaline (Qx) unit has been shown to result in a four-fold increase in Φ_{FL} in carbo[7]he-licene.[58] In addition, it was also shown that introduction of alkyl chains in Qx-fused carbohelicenes produced a much larger Φ_{FL} at 0.25.[7] Similarly, fusion of maleimide unit with the carbo[5]helicene resulted in a larger Φ_{FL} and good g_{CPL} values.[59] Recently, two carbo[6]helicenic fragments fused with the perylene diimide unit showed excellent Φ_{FL} and CPL properties.[60]

In addition to carbo[n]helicenes, hetero[n]helicenes having aromatic rings with heteroatoms in the main skeleton have also been explored in recent times. Presence of atoms such as S, O, and N helps in tuning the electronic structures and properties.[28,29,66–69,111] Yamamoto et al.[69] showed that introduction of modified Qx onto tetrathia[9]helicene skeleton enhanced both the Φ_{FL} and g_{CPL} values. Helicenes consisting of one or more nitrogen atoms are known as azahelicenes. Otani and co-workers[112] have synthesized orange-to-red CPL emitting Qx-fused polyaza[7]helicenes (denoted as **7HQ**). Recently, Otani et al.[11] reported the synthesis of polyaza[5]-[9]helicenes. While g_{CPL} value was the highest for the polyaza[9]helicene (denoted as **9Ha** in this work), Φ_{FL} was found to be the largest for the polyaza[7]helicene. In the present work, we have designed three azahelicenes: two in which pyrazine and quinoxaline units are laterally fused with

the central unit of **9Ha** (the resultant systems are denoted as **9HaP** and **9HaQ**, respectively) and the third one is with a larger helical length containing eleven rings, polyaza[11]helicene (denoted as **11Ha**). As mentioned in the previous paragraph, many *Qx*-based helicenes have been synthesized recently and chiroptical properties have been studied.[7,58,69,112,241–244] Similarly, many pyrazine-fused helicenes are also reported in the literature.[241–244] In addition, extension of helical length has also been shown to improve the results in many cases.[4,11,62,245–247] Keeping the above in mind, our aim is to explore the effects of introduction of these two aromatic acceptor rings and the enlargement of the helical size on the chiroptical properties such as $g_{\mathrm{CD}}/g_{\mathrm{CPL}}$ and K_{f}. For an electronic transition, these dissymmetry factors are calculated by using the Eq. 2.46, mentioned in Chapter 2. Typically, magnitudes of $\boldsymbol{m}$ are very small for π-π^* transitions in most organic molecules.[28,66] Therefore, there is a large number of studies in the literature to maximize the $|\boldsymbol{m}|$.[28,29,57,66,248] Keeping the above in mind, DFT based calculations are carried out to explore the absorption, CD and CPL properties of these three systems, and compare these results against the values for **9Ha**. In the following section, we provide the computational details of the calculations. This is followed by presentation of results in the Results & discussion section. In the last section, we provide a conclusion of our studies.

4.2 Computational methodology

Ground state (S_0) optimizations were performed in the gas phase at DFT level using PBE0-D3[249] functional and def2-SVP[211] basis set. Here, D3 represents Grimme's D3 empirical dispersion correction.[142,143,146] The minima were confirmed by having no imaginary frequencies on frequency analysis.

Excited state studies were performed using TD-DFT method. Test calculations were carried out for **9Ha** using five different functionals: B3LYP[229], PBE0[230], M06-2X,[250] CAM-B3LYP[141] and ωB97XD[144,231]. All these excited state calculations used the def2-TZVP[211] basis set. It is well-known that linear response TD-DFT method using standard DFT functionals has inherent deficiencies; e.g., to describe closely located

excited states,[168,169] states comprising of multiple excitations,[169,172,173,251,252] charge-transfer excited states[174–180] and extended π-conjugated systems. In these scenarios, range-separated functionals such as CAM-B3LYP and ωB97XD have been shown to suit better.[174,253–258] In our case, to verify the applicability of DFT functionals, vertical excitation calculations were also performed at the second order algebraic diagrammatic construction schemes for the polarization propagator ADC(2)[152,153] level using the same basis set. RI approximation was used in the ADC(2) calculations. In TD-DFT and RI-ADC(2) calculations, dichloromethane (DCM) solvent was employed using integral equation formalism-polarizable continuum model (IEF-PCM)[259] and conductor like screening model (COSMO)[260,261] model, respectively. All the DFT and TD-DFT calculations were performed using Gaussian 16 software[262]. Ten singlet excited states were considered in the TD-DFT calculations. For ADC(2) calculations, TURBOMOLE V.7.1 software[214] was utilized. For the studies of directions and densities of transition dipole moments, the Multiwfn v3.8 software[263] was used.

4.3 Results and discussion

4.3.1 Ground state structures

Ground state (S_0) structures of the four azahelicenes are shown in Figure 4.1. As the three new systems are derived from **9Ha**, the central regions of the three new molecules remain the same as that in **9Ha**, i.e., three fused rings in the middle, one benzene ortho-fused with two imidazole rings on either side (denoted as *5-6-5* unit). While **9Ha** and **9HaP** contain nine and ten rings, respectively, both **9HaQ** and **11Ha** contain eleven rings. However, the structures of **9HaQ** and **11Ha** are different from each other. Helical pitch (R_{pitch}), and torsional angles at the terminals and helical turns are key parameters to explain the structural properties of a spiral system. Various torsional angles, ϕ_1, ϕ_2, $\phi_3(\angle a-b-c-d)$, $\phi_4(\angle a-b-c-d')$, and $\phi_5(\angle d-b-c-d')$ are marked in the Figure 4.1. Angles ϕ_3 and ϕ_4 are the angles between the planes of benzene ring in *5-6-5* and the terminal pyridine units. In **9Ha**, the values for ϕ_1 and ϕ_2 are -11 and -4°, respectively. These values are consistent with the reported torsional angles of 10°

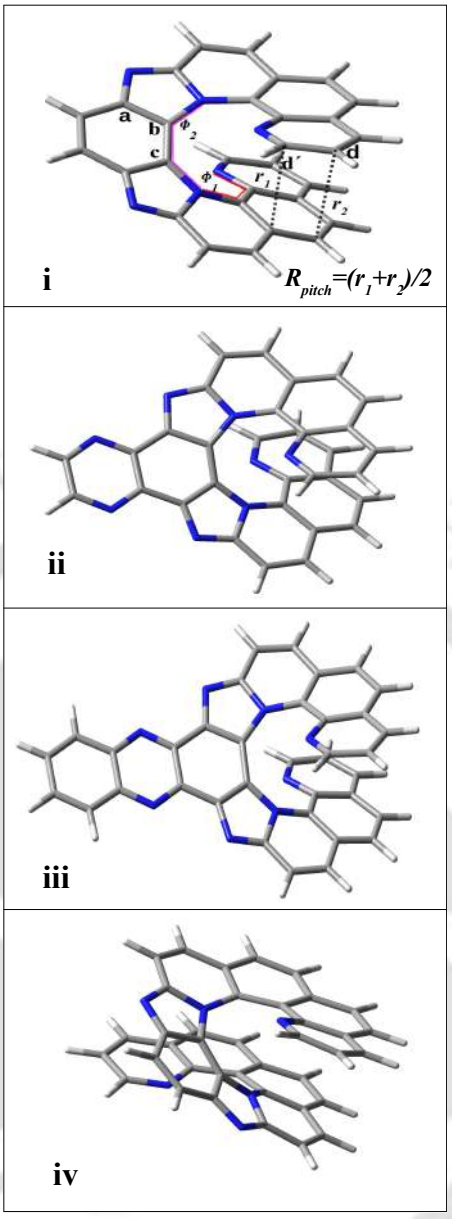

FIGURE 4.1: Optimized geometries of **9Ha**(i), **9HaP**(ii), **9HaQ**(iii), and **11Ha**(iv). Optimizations were carried out at PBE0-D3/def2-SVP level. Torsional angles ϕ_1 and ϕ_2 are marked. In addition, the torsional angles ∠abcd, ∠abcd′, and ∠dbcd′ denoted as ϕ_3, ϕ_4, and ϕ_5, respectively, are also shown for **9Ha**. The same set of angles is also used in cases of **9HaP**, **9HaQ**, and **11Ha**. In this figure, carbon, hydrogen and nitrogen atoms are shown in grey, white and blue colors, respectively.

and 4°, respectively.[11] The values of ϕ_1 and ϕ_2 for the three newly designed systems remain similar to those in **9Ha**. As **9HaP** and **9HaQ** are laterally extended versions of **9Ha**, values of ϕ_3, ϕ_4, and ϕ_5 for **9HaP** and **9HaQ** remain similar to the values in **9Ha**. However, as expected, differences in ϕ_3, ϕ_4, and ϕ_5 are observed for **11Ha**. The terminal units in this case are away by 40-43° compared to **9Ha**. As a result, **11Ha**

TABLE 4.1: Values of Selected Torsional Angles (ϕ in degrees) and R_{pitch} (in Å) of the Ground State (S_0) and the Lowest Singlet Excited State (S_1) Optimized Geometries of **9Ha**, **9HaP**, **9HaQ**, and **11Ha**.

	S_0 geometries						S_1 geometries					
System	Torsional angles					R_{pitch}	Torsional angles					R_{pitch}
	ϕ_1	ϕ_2	ϕ_3	ϕ_4	ϕ_5		ϕ_1	ϕ_2	ϕ_3	ϕ_4	ϕ_5	
9Ha	-11	-4	-151	133	-77	3.70	-6	2	-153	132	-74	3.49
9HaP	-11	-6	-151	131	-78	3.71	-6	1	-154	130	-76	3.49
9HaQ	-11	-7	-151	130	-79	3.72	-9	1	-153	129	-76	3.67
11Ha	-13	-5	-107	90	-163	3.77	-16	4	-106	79	-175	3.65

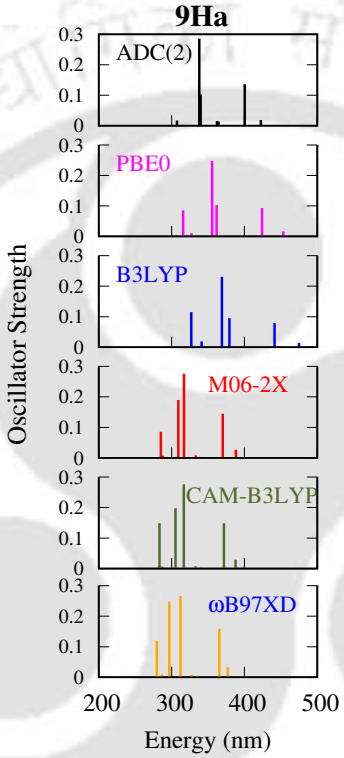

FIGURE 4.2: Absorption spectra of **9Ha**. Results obtained using PBE0, B3LYP, M06-2X CAM-B3LYP and ωB97XD functionals are plotted and compared against the ADC(2) results.

has the largest R_{pitch} value of 3.77Å. While ϕ_5 values for **9Ha**, **9HaP** and **9HaQ** are around -80°, the value is -163° for **11Ha**.

Selection of a DFT functional for studying the excited states

Choosing a DFT functional which provides accurate the excited state energies and properties is important. Therefore, at this point, excited state properties of **9Ha** obtained from calculations with different functionals are compared against the results from

ADC(2). In addition to comparing the excitation energies (λ_{abs}), corresponding oscillator strengths (f_{osc}) and rotatory strengths (R), characters of the excited states are also evaluated using the TheoDORE v2.4 software[264,265]. The characterization is based on the analysis of the transition density matrix (TDM). Three excited state descriptors (charge transfer value (ω_{CT}), participation ratio of natural transition orbitals (PR_{NTO}) and exciton sizes (d_{exc}))[264] are considered in this study. For this purpose, **9Ha** is divided into three fragments, as shown in Figure B1.

Computed stick absorption spectra for **9Ha** using different functionals and ADC(2) are shown in Figure 4.2. In addition, values of λ_{abs}s, R and excited state descriptors are tabulated in Table B1. The range-separated functionals, CAM-B3LYP and ωB97XD, and M06-2X produce similar results: in all the three cases, the λ_{abs}s are similar, and the $S_0 \rightarrow S_5$ excitations show the highest f_{osc} and R. On the other hand, the $S_0 \rightarrow S_6$ excitation carries the highest f_{osc} and R value in PBE0 and B3LYP results, similar to the values obtained in the case of ADC(2). In addition, the character of the S_6 state remains also the same in all the above three cases, i.e., all of those are charge-transfer (CT) states with $\omega_{CT} \approx$ 0.6-0.7, $PR_{NTO} \approx$ 2 and $d_{exc} \approx$ 4.8 Å. These results are further supported by the electron-hole correlation plots (as shown in Figure B2). While the plots for PBE0 and B3LYP are almost the same as that obtained in ADC(2), the results for the other three functionals show differences (particularly at the lower-left and upper-right squares). In B3LYP, the λ_{abs}s corresponding to $S_0 \rightarrow S_1$ and $S_0 \rightarrow S_6$ excitations are red-shifted by 50 and 30 nm, respectively. In case of PBE0, however, the differences are less, and the peaks are red-shifted by 31 and 18 nm, respectively. The peaks at 356 nm (with $f_{osc} = 0.248$) in PBE0 corresponds well with the experimental value of 342 nm.[11] For emission in **9Ha**, optimization was carried out in the S_1 state using PBE0 functional. For **9Ha**, emission energy (λ_{em}) appears at 558 nm, red-shifted by 12 nm from the reported value.[11] At PBE0/def2-TZVP level, the value of g_{CPL} was found to be 0.052, close the experimentally reported value of 0.027. Considering the above results, PBE0 functional is chosen for studies of newly designed molecules.

TABLE 4.2: Excitation Energy (λ_{abs} in nm), Corresponding Oscillator Strength(f_{osc}), Orbitals Involved in the Transitions, $|\boldsymbol{\mu}|$, $|\boldsymbol{m}|$, cos θ, R, g_{CD} and $|\boldsymbol{m}|/|\boldsymbol{\mu}|$of **9Ha**, **9HaP**, **9HaQ**, **11Ha**. $|\boldsymbol{\mu}|$, $|\boldsymbol{m}|$, and R are in esu·cm, erg·G^{-1} and esu·cm·erg·G^{-1} units, respectively.

States	λ_{abs}	f_{osc}	Configurations	$\lvert\boldsymbol{\mu}\rvert/10^{-20}$	$\lvert\boldsymbol{m}\rvert/10^{-20}$	cos θ	$R/10^{-40}$	g_{CD}	$\lvert\boldsymbol{m}\rvert/\lvert\boldsymbol{\mu}\rvert$
9Ha									
S_1	453	0.016	H→L (98%)	125.49	2.08	-0.997	-260.66	-0.066	0.017
S_2	424	0.093	H→L+1(95%)	289.53	0.41	1.0	119.47	0.006	0.001
S_6	356	0.248	H→L+3(49%) H-1→L+1(43%)	432.78	3.04	-0.457	-601.41	-0.013	0.007
S_7	331	0.0	H-3→L(63%) H-1→L+3(24%)	13.6	0.30	1.0	4.06	0.088	0.022
9HaP									
S_1	465	0.015	H→L(98%)	119.99	1.98	-0.923	-219.72	-0.061	0.017
S_2	428	0.139	H→L+1(96%)	355.25	0.45	1.0	158.65	0.005	0.001
S_6	353	0.242	H-1→L(78%)	426.17	0.06	0.999	25.72	0.001	0.0
S_7	342	0.184	H-1→L+1(76%)	365.75	2.22	-0.444	-361.02	-0.011	0.006
9HaQ									
S_1	518	0.017	H →L(99%)	138.75	1.05	-0.295	-42.96	-0.009	0.008
S_2	453	0.034	H→L+2(99%)	181.97	2.08	-0.801	-302.74	-0.037	0.011
S_3	435	0.163	H →L+1(95%)	388.45	0.45	1.0	173.80	0.005	0.001
S_7	369	0.721	H-1→L(52%) H→L+3(26%)	752.68	0.21	0.967	150.46	0.001	0.0
S_{10}	335	0.111	H-1→L+1(87%)	282.35	1.49	-0.507	-213.52	-0.011	0.005
11Ha									
S_1	462	0.06	H→L(98%)	243.84	2.64	-0.975	-627.68	-0.042	0.011
S_2	441	0.072	H→L+1(98%)	261.31	0.39	1.0	100.64	0.006	0.001
S_6	372	0.108	H-1→L+1(75%) H→L+2(12%)	293.23	0.08	0.942	21.28	0.001	0.0
S_8	348	0.069	H-2→L(87%)	227.45	1.13	0.270	69.56	0.005	0.005

4.3.1.1 UV spectra

The absorption spectra of all the four systems are compared in Figure 4.3. λ_{abs}, f_{osc} and major transitions involved in four major excitations are tabulated in Table 4.2. Two prominent bands, appearing in 300-600 nm range, are observed in each spectrum. For **9Ha**, the two peaks appearing at 356 nm (f_{osc}=0.248) and 424 nm (f_{osc}=0.093) are due to S_0→S_6 and S_0→S_2 excitations, respectively. While the major peak at 356 nm arises from a combination of highest occupied molecular orbital (H)→lowest unoccupied molecular orbital (L) and H-1→ L+1 transitions, the one at 424 nm arises mainly from the H→L+1 transition. **9HaP** exhibits a similar absorption spectrum to that of **9Ha**, and even the peak positions are also very close to **9Ha**. However, the ϵs of the two prominent peaks are a little larger than those in **9Ha**. **9HaQ** shows a high intensity peak at 369 nm (f_{osc}=0.721) and a very low intensity peak at 435 nm (f_{osc}=0.163). These two peaks correspond to S_0→S_7 and S_0→S_3 excitations, respectively. The higher

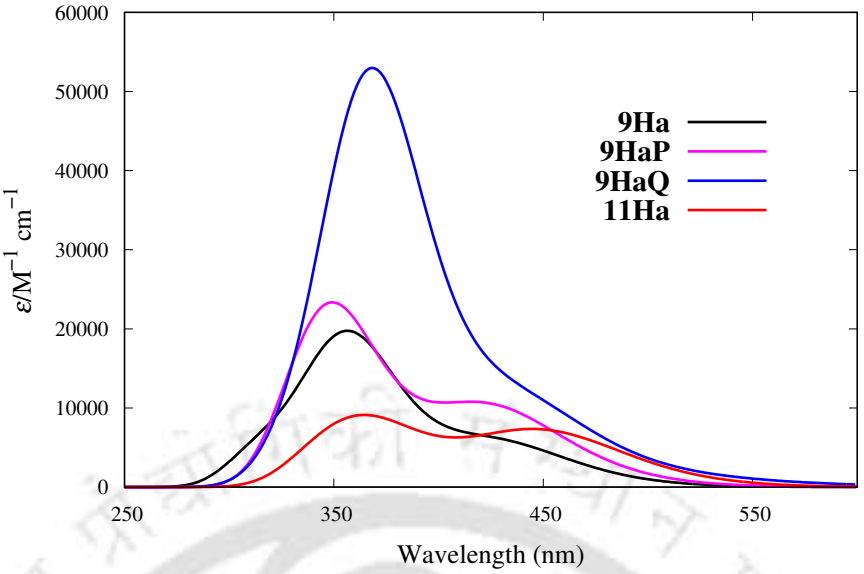

FIGURE 4.3: Absorption spectra of **9Ha**, **9HaP**, **9HaQ**, and **11Ha**. The results are obtained at PBE0-D3/def2-TZVP level. A half-width at half-maximum of 0.25 eV is used.

intensity of the peak at 369 nm is due to a comparatively large value of EDTM (i.e., $|\boldsymbol{\mu}|$= 752.68×10^{-20} esu·cm), as shown in Table 4.2. Hence, from **9Ha** to **9HaQ**, absorption intensities increase with the increase in total number of rings. The presence of quinoxaline ring in **9HaQ** makes it strongly polarizable and gives rise to large value of EDTM. In **11Ha**, the major peaks appear at 372 nm (f_{osc}=0.108) and 441 nm (f_{osc}=0.072) corresponding to $S_0 \rightarrow S_6$ and $S_0 \rightarrow S_2$, respectively. Again, while the S_6 state is due to a pair of transitions (H-1→L+1 and H→L+2), the S_2 state appears solely due to the H→L+1 transition. It is observed that the bands are red-shifted by 16-17 nm from **9Ha** to **11Ha** and this is due to the extension of π-conjugation. Although both **9HaQ** and **11Ha** contain the same number of rings, **11Ha** shows very small intensity peaks.

Analysis of the excited states to determine whether a state is an LE or a CT has been performed by looking at the values of descriptors such as ω_{CT}, PR_{NTO} and d_{exc}. Similar to **9Ha**, three fragments are considered for the three derivatives. Results are tabulated in Table B2. In addition, NTOs corresponding to various transitions are also shown in Figures 4.4 and B3-B5. The table shows that the ω_{CT} values of many of the excited states are quite large (between 0.6-0.8), and so are the d_{exc} values. This shows that these excited states are of CT type. Some exceptions occur in cases of S_3 of **9HaP** and S_1, S_6, and S_7 of **9HaQ**. For these excited states, the ω_{CT} is comparatively smaller,

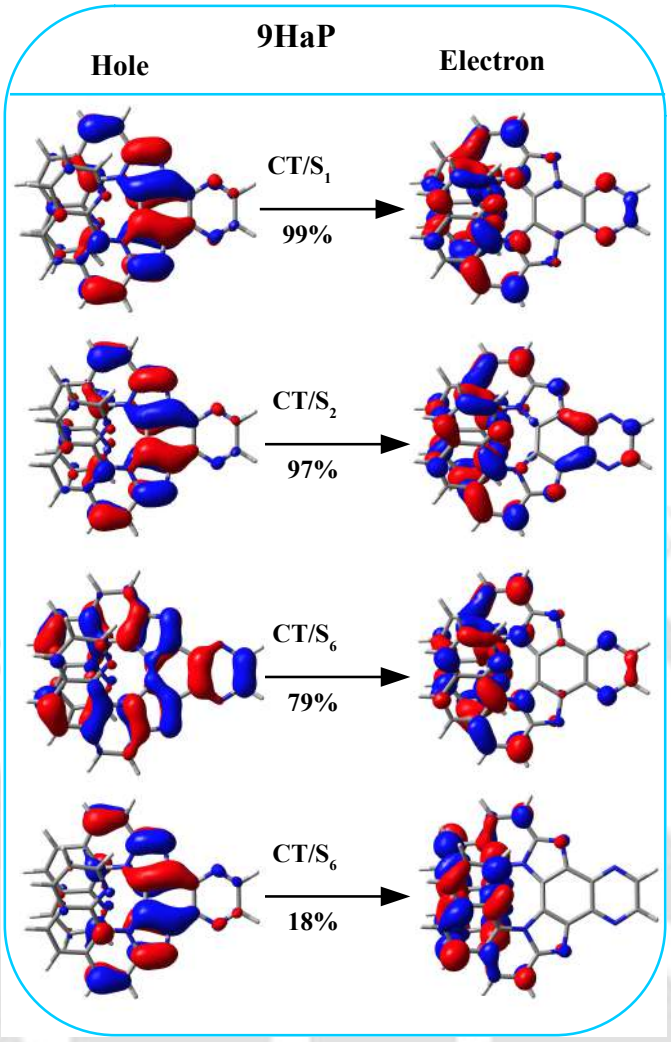

FIGURE 4.4: Natural transition orbitals for some selected excited state transitions of **9HaP**. Results are obtained at TD-PBE0/def2-TZVP level. An isovalue of 0.03 a.u. is used in each case. Charge-transfer and locally excited transitions are denoted as CT and LE, respectively.

i.e, less than 0.53. For **9HaQ**, while S_1 and S_7 are partial CT states with $\omega_{CT} \approx 0.50$, S_6 is LE in nature with $\omega_{CT} \approx 0.14$ and $d_{exc} \approx 3.70$ Å. NTOs, shown in Figure B4 corresponding to the above three states, corroborate the above results. The transitions corresponding to the major peaks (S_6 in **9Ha**, **9HaP** and **11Ha**, and S_7 in **9HaQ**) are of multiconfigurational character, where PR_{NTO} values are greater than one. These findings are also supported by the NTOs shown in the Figures 4.4 and B3-B5. For the S_1 state in **9Ha** and **9HaP**, holes and electrons are localized mainly in *5-6-5* donor unit and terminals rings, respectively. Comparing the S_6 states between **9Ha** and **9HaP**, it is observed that the hole/electron densities are not fully localized in different parts in the case of **9Ha** and this makes the ω_{CT} value comparatively small. On the other hand,

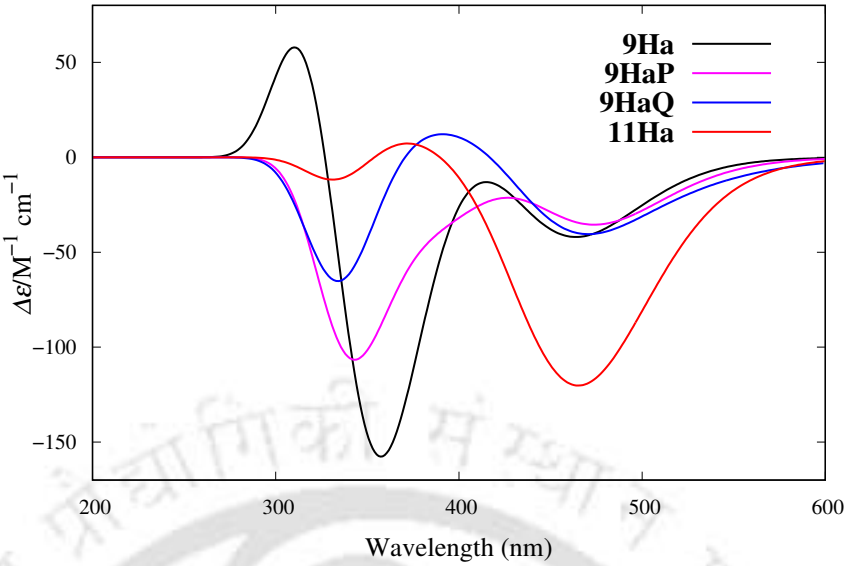

FIGURE 4.5: CD spectra of **9Ha**, **9HaP**, **9HaQ**, and **11Ha**. Results are obtained at TD-PBE0/def2-TZVP level of theory.

in **9HaP**, ω_{CT} is quite large for the same excited state as holes and electrons are better separated as shown in Figure 4.4. In **9HaQ**, for S_1, PR_{NTO} is one and electrons are localized mainly in the Qx unit. For the S_7 state, on the other hand, two pairs of NTOs participate. While the first pair shows the localization in the *5-6-5*+Qx and Qx units, the second pair shows the localization in the *5-6-5* and terminal units. In the case of **11Ha**, the hole/electron distributions in the S_1, S_2 and S_6 states are similar to those in **9Ha**.

4.3.1.2 CD spectra

Figure 4.5 shows the CD spectra of all the four systems. Strongest CD bands are observed for **9Ha**, with one positive and two negative CD bands. The lower-energy negative band, the weakest one, corresponds to the $S_0 \rightarrow S_1$ transition. The R and g_{CD} values corresponding to this peak are -260.66 and -0.066, respectively. This transition is both electronically and magnetically allowed with a significant amount of $|\boldsymbol{\mu}|$ and $|\boldsymbol{m}|$. The second CD band arises from the $S_0 \rightarrow S_6$ transition. $|\boldsymbol{\mu}|$ and $|\boldsymbol{m}|$ for this transition are larger by factors of 3.45 and 1.46, respectively, compared to the values for the $S_0 \rightarrow S_1$ transition. However, the magnitude of cos θ decreases to 0.46. As a result, R increases by more than two-fold, and g_{CD} decreases almost five-fold. The overall

TABLE 4.3: Emission Energy (λ_{em} in nm), Corresponding Oscillator Strength(f_{osc}), $|\boldsymbol{\mu}|$, $|\boldsymbol{m}|$, cos θ, R, g_{CPL}, K_f, and $|\boldsymbol{m}|/|\boldsymbol{\mu}|$ of **9Ha**,**9HaP**, **9HaQ**, and **11Ha**. $|\boldsymbol{\mu}|$, $|\boldsymbol{m}|$ and R are in esu·cm, erg·G^{-1} and esu·cm·erg·G^{-1} units, respectively. K_f is in ns^{-1}. Reported g_{CPL} of **9Ha** is 0.027 at 546 nm. All the Considered Transitions are $S_1 \rightarrow S_0$.

System	λ_{em}	f_{osc}	$\lvert\boldsymbol{\mu}\rvert/10^{-20}$	$\lvert\boldsymbol{m}\rvert/10^{-20}$	cos θ	$R/10^{-40}$	g_{CPL}	K_f	$\lvert\boldsymbol{m}\rvert/\lvert\boldsymbol{\mu}\rvert$
9Ha	558	0.018	149.23	1.96	-0.999	-291.84	-0.052	0.0039	0.013
9HaP	563	0.017	145.72	2.01	-0.986	-289.39	-0.055	0.0036	0.014
9HaQ	612	0.034	212.74	0.65	-0.019	-2.70	-0.000	0.0061	0.003
11Ha	635	0.050	259.60	2.33	-0.990	-598.16	-0.036	0.0083	0.009

spectrum is consistent with the reported CD spectrum of **9Ha**.[11] For **9HaP**, the two negative bands correspond to $S_0 \rightarrow S_1$ and $S_0 \rightarrow S_7$ transitions, respectively. Like **9Ha**, the transition corresponding to the lowest-energy band shows the largest g_{CD} value of -0.061 while the value decreases to -0.011 in the case of $S_0 \rightarrow S_7$ transition. As mentioned before, magnitude of $|\boldsymbol{\mu}|$ is much larger than the magnitude of $|\boldsymbol{m}|$ in organic molecules. In this scenario, the Eq. 2.46 can be rewritten to show that $g_{CD}(g_{CPL}) \propto |\boldsymbol{m}|/|\boldsymbol{\mu}|$ (keeping cos θ the same). The above trend in **9HaP** is due to a much larger value of $|\boldsymbol{m}|/|\boldsymbol{\mu}|$ in the case of first band compared to the value for $S_0 \rightarrow S_7$. In both **9Ha** and **9HaP**, g_{CD} remains $\approx$ -0.06. This implies that the degree of chirality of ground state geometries is maintained in both the systems. Results for **9HaQ** are different than both **9Ha** and **9HaP**. For **9HaQ**, $S_0 \rightarrow S_2$ transition shows the largest g_{CD} value of -0.037 (with $|\boldsymbol{m}|/|\boldsymbol{\mu}|$ of 0.011) while $S_0 \rightarrow S_{10}$ shows a smaller value for g_{CD} of -0.011 (with $|\boldsymbol{m}|/|\boldsymbol{\mu}|$ of 0.005). Hence, in **9HaQ**, chirality of ground state geometry decreases in comparison to **9Ha** and **9HaP**. In the case of **11Ha**, one negative peak with the largest R appears at 462 nm, corresponding to $S_0 \rightarrow S_1$ transition (see Table 4.2). g_{CD} value of this transition is lower than the g_{CD} values of corresponding transitions of both **9Ha** and **9HaP**. This trend is clear from the values of $|\boldsymbol{m}|/|\boldsymbol{\mu}|$ in these three cases.

4.3.2 Excited-state structures and chiroptical properties

In helicenes, fluorescence usually occurs from the S_1 state.[240] Therefore, to study the emission properties and CPL activities, optimizations of the four structures in their S_1 states were performed at the PBE0-D3/def2-SVP level in DCM solvent using the IEF-PCM model. The S_1 optimized geometries are shown in Figure B6. Few structural parameters of the systems in the S_1 states are tabulated in Table 4.1. Comparison of

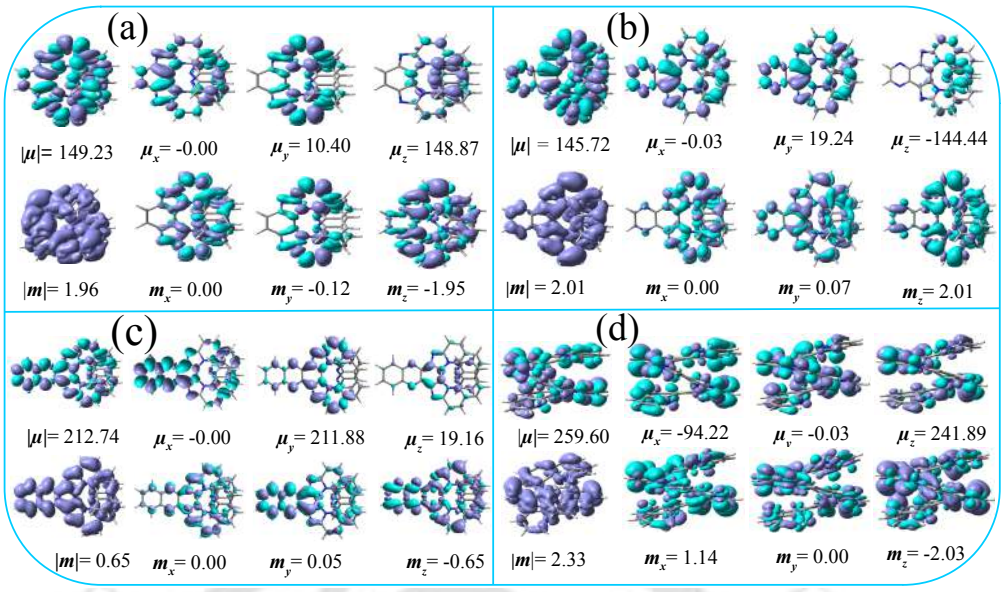

FIGURE 4.6: EDTM (first row) and MDTM (second row) densities of **9Ha** (a), **9HaP** (b), **9HaQ** (c), and **11Ha** (d) for the $S_1 \rightarrow S_0$ transitions. The four columns in each section correspond to total and three components, respectively. Magnitudes of these vectors are in CGS units. The magnitudes in CGS units are obtained from the values in atomic units (a.u.) as follows: $|\boldsymbol{\mu}|$/esu·cm=(254.1746 × 10^{-20} esu·cm) × $|\boldsymbol{\mu}|$/a.u. and $|\boldsymbol{m}|$/erg·G^{-1} =(-1) × (0.927401 × 10^{-20}/erg·G^{-1}) × $|\boldsymbol{m}|$/a.u.. Results are obtained using the Multiwfn3.8 software.[263] Isovalue = 0.002 a.u. is used.

the values of ϕ_1 between S_0 and S_1 for **9Ha**, **9HaP** and **9HaQ** shows that the absolute values in S_1 are smaller by 2-5°. Similarly, ϕ_2 changes only by 6-9°. As shown in Table 4.1, in all the four cases one terminal unit is tilted outwards by 20-27° more than the other terminal unit, similar to the ground state results. **11Ha** shows the largest difference of 27° between $|\phi_3|$ and $|\phi_4|$. Comparing the R_{pitch} values, it is observed that the values in the S_1 state are smaller than the values in S_0. It implies that excited state geometries are more compact, consistent with the results of previous studies.[266,267]

Various properties such as emission energies, corresponding $|\boldsymbol{\mu}|$ and $|\boldsymbol{m}|$ values, angles between the vectors and g_{CPL} values are tabulated in Table 4.3. There are two possible ways to achieve a large value of g_{CPL}: 1. by decreasing the value of $|\boldsymbol{\mu}|$ which can be achieved by forming a fully CT state and 2. by increasing the value of $|\boldsymbol{m}|$. In case of **9Ha**, $|\boldsymbol{m}|$ and cos θ values do not change significantly from the corresponding values in absorption. However, there is an increase in the value of $|\boldsymbol{\mu}|$ in the case of emission and this results in a decrease in dissymmetry factor for $S_1 \rightarrow S_0$ compared to $S_0 \rightarrow S_1$. Both $|\boldsymbol{\mu}|$ and $|\boldsymbol{m}|$ comprise mainly of Z-axis components (as shown in Figure 4.6) and both are directed along the helical axes. Density plots for the Z-components

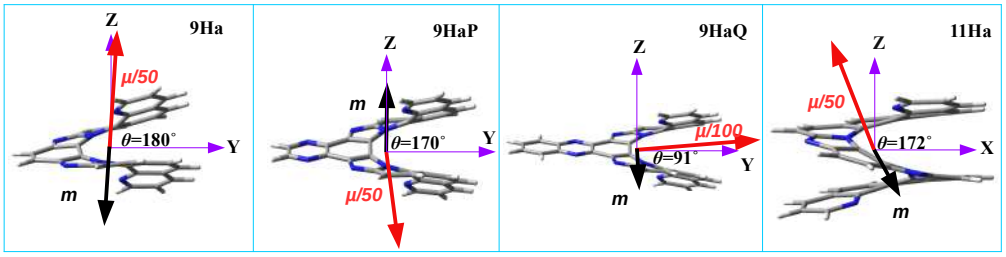

FIGURE 4.7: Directions of EDTM and MDTM vectors of **9Ha**, **9HaP**, **9HaQ**, and **11Ha** for the transitions $S_1 \rightarrow S_0$. While the vectors in **9Ha**, **9HaP**, and **9HaQ** lie in the YZ plane, these are in the XZ plane for **11Ha**.

of both the vectors show relatively larger slate blue (positive) region compared to cyan (negative) region. On the other hand, for X-components as examples, the cyan and slate blue isosurfaces cancel each other out. Maximum contribution to the $|\boldsymbol{\mu_z}|$ comes from the phenanthroline units at the terminals. For **9HaP**, $|\boldsymbol{\mu}|$, $|\boldsymbol{m}|$ and cos θ do not change much from the corresponding values for **9Ha**, and the two vectors make an angle of 170° with each other, as shown in Figure 4.7. The largest value of $|\boldsymbol{m}|/|\boldsymbol{\mu}|$ (or decrease in the value of $|\boldsymbol{\mu}|$ and a small increase in the value of $|\boldsymbol{m}|$) in **9HaP** results in the largest value of g_{CPL}, i.e., -0.055 among all the systems (as shown in Table 4.3). Similar to **9Ha**, both the DTM vectors comprise mainly of their respective Z-axis components. In **9HaQ**, g_{CPL} is the smallest among all. This is due to the smallest value of $|\boldsymbol{m}|$ for the $S_1 \rightarrow S_0$ transition, and almost an orthogonal orientation of the two vectors (as shown in Figure 4.7). While the value of $|\boldsymbol{m}|$ is only 0.65×10^{-20} erg·G^{-1} in **9HaQ**, values are either close to or greater than 2×10^{-20} erg·G^{-1} for the other three cases. Like in **9Ha** and **9HaP**, $\boldsymbol{\mu}$ and $\boldsymbol{m}$ in **9HaQ** comprise mainly of Y- and Z- components, respectively (as shown in Figure 4.6). However, the presence of *Qx* unit changes the scenario affecting the electronic and magnetic properties. Here, the $\boldsymbol{\mu_y}$ densities are distributed over a larger area resulting in comparatively larger values for $\boldsymbol{\mu_y}$ and $|\boldsymbol{\mu}|$ relative to that of **9Ha** and **9HaP**. In **9HaQ**, electrons and holes are located in the *Qx* and *5-6-5* units, respectively (as shown in Figure B7). Therefore, $\boldsymbol{m}$ arises from the delocalized motion of electron over the small *Qx* unit only producing small $|\boldsymbol{m}|$ and R values. This result is in contrast to the results for carbohelicenes where improved CPL performance was obtained by fusion with *Qx* units.[7] Table 4.3 also reports K_{f} calculated as[268,269] $K_{\mathrm{f}} = \dfrac{2\pi e^2}{\epsilon_0 m_{\mathrm{e}} c}\tilde{\nu}^2\ f_{\mathrm{osc}} = 0.667 \times \tilde{\nu}^2\ f_{\mathrm{osc}}$, where ϵ_0 is the vacuum permittivity, m_{e} is the mass of electron and $\tilde{\nu}$ is the corresponding transition energy in cm^{-1}. Φ_{FL}

is calculated as $\Phi_{FL}=\frac{K_f}{(K_f+K_{nr})}$, where K_{nr} stands for non-radiative rate constants. For high spontaneous emission systems, K_f is much larger than K_{nr}. Faster emission infers larger quantum yield. *Qx*-fused polyaza[5]-helicene and **7HQ** show smaller Φ_{FL} values compared to the respective parent systems.[112] However, **9HaQ** shows larger K_f compared to that of parent **9Ha** as well as **9HaP**. This is due to larger value of f_{osc} for the corresponding transition. In **11Ha**, delocalization of electron over a larger area (as shown in Figure B7) leads to the largest values of $|\boldsymbol{\mu}|$ and $|\boldsymbol{m}|$. However, g_{CPL} value is smaller compared to those of **9Ha** and **9HaP**. It is to be noted that experimental g_{CPL} values were shown to increase with increase in the number of nitrogen atoms,[11] i.e., from **7H** to **9Ha**. Similar to **9Ha** and **9HaP**, DTM densities in **11Ha** are distributed along the whole molecule (as shown in Figure 4.6), and the two DTM vectors are directed almost anti-parallel to each other (as shown in Figure 4.7). In this case, however, contributions of X-components are much larger than in **9Ha**. While the terminal rings contribute primarily to the X- and Z-axes components of EDTM (the densities in the *5-6-5* unit cancel each other), *5-6-5* and its adjacent rings participate for MDTM components. **11Ha**, with the largest f_{osc} value of 0.05, shows the largest K_f for the transition $S_1 \rightarrow S_0$. A large value of K_f hints at a small intersystem crossing decay in **11Ha**.

From Figure B7, it is clear that the $S_1 \rightarrow S_0$ transitions in the four cases are CT transitions. Analysis using TheoDORE has also been carried out to check the values of ω_{CT}. The results are tabulated along with $|\boldsymbol{\mu}|$ in Table B3. While the value of ω_{CT} is 0.72 in **9Ha**, it increases to 0.76 in the case of **9HaP** and decreases to 0.41 in **9HaQ**. On the other hand, ω_{CT} value for **11Ha** is very close to that of **9Ha**. It is worth noting that while CT occurs between *5-6-5* units and the terminals in **9Ha**, **9HaP** and **11Ha**, the central *5-6-5* and *Qx* units take part in **9HaQ**(as shown in Figure B7), as mentioned in the previous paragraph. Generally, a state resulting from a smaller overlap of initial and final orbitals, i.e., a state with stronger CT character results in decrease in $|\boldsymbol{\mu}|$ value. This is due to the fact that EDTM operates on the spatial part only. Accordingly, while the $|\boldsymbol{\mu}|$ value decreases from **9Ha** to **9HaP** accompanied by an increase in ω_{CT}, the value increases to 212.74×10^{-20} esu·cm for **9HaQ**. On the other hand, **11Ha** having an ω_{CT} value similar to **9Ha** shows a much larger $|\boldsymbol{\mu}|$, not showing the ω_{CT} *vs* $|\boldsymbol{\mu}|$ trend.

4.4 Conclusions

In this article, effects of lateral and helical extension of an azahelicene on the UV, CD, and CPL properties are reported. Starting from the experimentally reported **9Ha**, three azahelicenes are designed. While **9HaP** and **9HaQ** are laterally extended versions of **9Ha** obtained by fusing pyrazine and quinoxaline units to the **9Ha** unit, respectively, **11Ha** is helically extended one. **9HaP** shows UV and CD results similar to that of **9Ha**. In case of **11Ha**, the spectral positions are slightly red-shifted compared to **9Ha**. In these three cases, g_{CPL} values are smaller than the corresponding g_{CD} values which are related to the decrease in the R_{pitch} values for S_1 compared to the values for S_0. While **9Ha** shows the largest g_{CD} value corresponding to S_1 state, **9HaP** shows the largest g_{CPL} value. The largest value of $|\boldsymbol{m}|/|\boldsymbol{\mu}|$ and anti-parallel arrangement of the two vectors in case of **9HaP** result in the best result among all. **11Ha** shows a smaller g_{CPL} value compared to that of **9Ha** and **9HaP**. On the other hand, fusion of the electron-accepting Qx unit shows results very different to the above three systems. Fusion with Qx unit leads to the largest K_{f} value, however g_{CPL} value is very small compared to parent system. For the $S_1 \rightarrow S_0$ transition in **9HaQ**, EDTM and MDTM vectors are almost orthogonal to each other, and the magnitude of $|\boldsymbol{m}|$ is the smallest. Therefore, we conclude that in cases of azahelicenes like the ones studied in this work it is beneficial to fuse with a pyrazine unit rather than a Qx unit although Qx possesses better electron-withdrawing ability. Fusion with pyrazine unit and extending the helical length lead to increase in the magnitude of $|\boldsymbol{m}|$.

Chapter 5

Effect of fluorination on chiroptical properties of carbo[5-8]helicenes

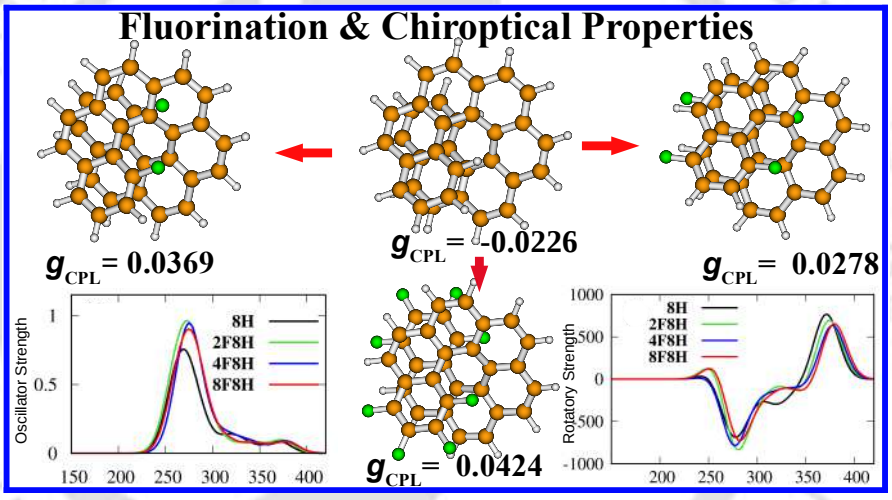

In this chapter, effects of di-, tetra- and octafluorination on structural and chiroptical properties of carbo[5-8]helicenes are reported. From each parent carbohelicene, three fluorinated derivatives are designed by substituting either one or two, or four hydrogens at each terminal ring with fluorine atoms. A part of the content of this chapter is accepted for publication in *J. Phys. Chem. A*.

5.1 Introduction

In typical organic molecules, $|\boldsymbol{\mu}|$ is much larger than $|\boldsymbol{m}|$ which leads to small g-factors, and values are usually in the range of 10^{-4}-10^{-2}.[28,108,109] This value is far away from the maximum value of ± 2. Keeping this in mind, several modifications have been proposed in recent times[28,29,242,270] aiming at improving the g-factor and Φ_{FL}. As mentioned in the previous chapter, typical modifications based on either substitution of hydrogens in helicenes by other atoms/groups[49–57,271,272] or fusion of aromatic rings onto the helical backbone to produce ring-fused carbo[n]helicenes[7,58–63] have been done so far. Recently, Kubo et al.[57] reported dimethoxy and dicyano substituted-carbo[7]helicenes with improved g_{CPL} values compared to the results for parents systems. While 3.5- and 6-fold increments were obtained for Φ_{FL} and K_{f}, respectively, for dicyanocarbo[5]helicene[54], $\geq$ 4-fold increments were obtained for the dicyano-carbo[7]helicene.[57]

Similar to pristine carbohelicenes, Φ_{FL} was also found to decrease for substituted-carbohelicenes with increase in chain length.[54,57] Halogenation of carbohelicene rings is another strategy to tune the chiroptical properties.[51,55] Synthesis of various fluorinated carbohelicenes are reported in the literature.[50,55,56,273–275] In the work of Nakai et al.[51], a systematic improvement in CD intensities of the $^1\mathrm{B_b}$ band was observed along with their corresponding dissymmetry factors, after substitutions by F, Cl and Br atoms. This was attributed to increase in $|\boldsymbol{\mu}|$ and $|\boldsymbol{m}|$, and a small angle between the two vectors. In 2019, Církva et al.[55] reported the synthesis of tetrafluoro- and octafluoro-carbo[6]helicenes. While the specific rotation of a fluoro-substituted compound was found to be smaller than the value for the parent system, Φ_{FL} was found to increase with increase in the number of fluorine atoms. It is apparent that a systematic and critical study of effect of fluorination of carbohelicene is yet to be reported. In this chapter, we report the chiroptical properties of di-, tetra- and octafluorinated carbo[5-8]helicenes, and analyze the effect of degree of fluorination on a particular carbohelicene and on the length of the helical chain. Hydrogen atoms in the terminal rings of each of these carbohelicenes are substituted by either two or four or eight fluorine atoms to produce di-substituted,

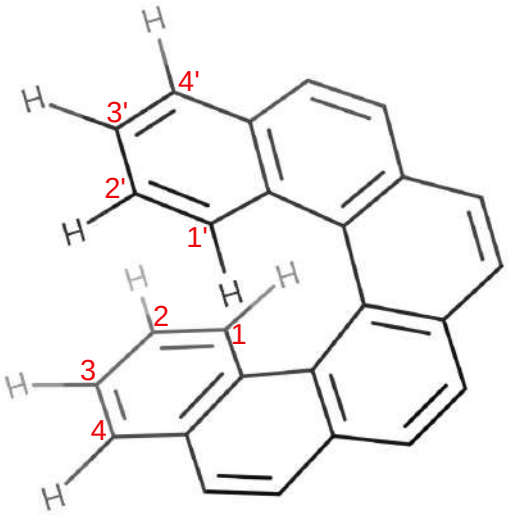

FIGURE 5.1: Structure of **6H**. The hydrogens at the terminal rings are replaced by fluorine atoms to produce di- (substituting the hydrogens by fluorine atoms at 1 and 1′ positions) tetra- (substituting the hydrogens by fluorine atoms at 1, 1′, 4 and 4′ positions) and octafluoro-**6H** (substituting all the four hydrogens by fluorine atoms at each terminal unit). Similar substitutions are carried out for **5H**, **7H** and **8H**.

tetra-substituted and octa-substituted helicenes. A schematic picture of **6H**, and locations of fluorine substitutions are shown in Figure 5.1. The fluorinated molecules studied here are 1,1′-difluoro[5]helicene (**2F5H**), 1,1′,4,4′-tetrafluoro[5]helicene (**4F5H**), 1,1′,2,2′,3,3′,4,4′-octafluoro[5]helicene (**8F5H**), 1,1′-difluoro[6]helicene (**2F6H**), 1,1′,4,4′-tetrafluoro[6]helicene (**4F6H**), 1,1′,2,2′,3,3′,4,4′-octafluoro[6]helicene (**8F6H**), 1,1′-difluoro[7]helicene (**2F7H**), 1,1′,4,4′-tetrafluoro[7]helicene (**4F7H**), 1,1′,2,2′,3,3′,4,4′-octafluoro[7]helicene (**8F7H**), 1,1′-difluoro[8]helicene (**2F8H**), 1,1′,4,4′-tetrafluoro[8]helicene (**4F8H**), and 1,1′,2,2′,3,3′,4,4′-octafluoro[8]helicene (**8F8H**). It is to be noted that synthesis of **8F6H** is already reported[55]. Geometries of all di-, tetra- and octafluoro systems are shown in Figure 5.2. In the next section, we show the computational methodology used in the study. This is followed by the Results and Discussion section. In the last section, we provide the conclusions of our study.

5.2 Computational methodology

All the calculations were performed for (*P*)-type enantiomers. Ground state (S_0) optimizations of parent and fluorinated **5H**, **6H**, **7H** and **8H** were performed in the gas

phase at MP2 level. In particular, the spin-component-scaled (SCS) version was used for these optimizations. The SCS-MP2 method was proposed by Grimme[276] to improve upon the MP2 results. Here, the same-spin and the opposite-spin components of the MP correlation energy were scaled separately. The method has been found to perform better than MP2 for non-covalent interactions such as in cases of π-stacked systems.[277–280] The default scaling parameters, cos=6/5 and css=1/3, were used in our studies. Vertical excitation energy calculations at the ground state optimized geometries were carried out at ADC(2)[152,153] scheme level. RI approximation[216] was used in both MP2 and ADC(2) calculations. Geometry optimizations in lowest singlet excited states (S_1) of all the sixteen systems were performed in gas phase at the same level of theory. It is to be noted here that excitation energies in case of ADC(2) are obtained as eigenvalues of a Hermitian secular matrix.[217] In comparison, excitation energies in coupled-cluster methods such as CC2,[189] are produced as eigenvalues of a non-Hermitian matrix. In addition to the above advantage of ADC(2) which results in improved numerical stability, the combination of ADC(2) with the RI approximation reduces the computational time. The methods used in this study are, therefore, denoted as RI-SCS-MP2 and RI-ADC(2), for the ground and excited states, respectively. In all the calculations, the def2-TZVP[211] basis set was used. For all the calculations, TURBOMOLE V.7.1 software[214] was used. In all the calculations, C_2 symmetry was imposed for saving the computational time. UV and CD spectra were obtained using the Gabedit software.[233] Excited state characterizations were carried out using the TheoDORE v2.4 software.[264,265] Analysis using TheoDORE is based on the 1-TDM. In practice, the molecule is partitioned into various fragments, and contributions from those fragments are calculated. As shown in Figure C1, each ring is considered as a fragment in our study. For analysis purpose, three descriptors named d_{exc}, PR_{NTO} and ω_{CT} are used. A comparatively larger value of d_{exc} and a value of ω_{CT} closer to one for an excited state indicate CT character for the state, while an LE state shows smaller values for d_{exc} and ω_{CT}. PR_{NTO} shows the number of NTOs taking part in producing an excited state.

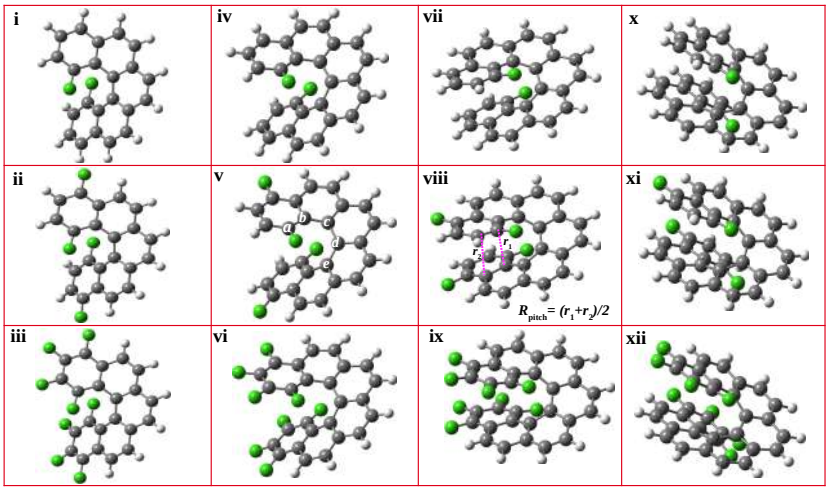

FIGURE 5.2: Ground state optimized geometries of **2F5H**(i), **4F5H**(ii), **8F5H**(iii), **2F6H**(iv), **4F6H**(v), **8F6H**(vi), **2F7H**(vii), **4F7H**(viii), **8F7H**(ix), **2F8H**(x), **4F8H**(xi) and **8F8H**(xii). Optimizations were carried out at RI-SCS-MP2/def2-TZVP level. In the case of **4F6H**, five carbon atoms are marked as *a*, *b*, *c*, *d* and *e*, and two torsional angles, ∠*a*-*b*-*c*-*d* (denoted as ϕ_1) and ∠*b*-*c*-*d*-*e*, (denoted as ϕ_2) are defined. The same set of angles is used in other cases as well. In **4F7H**, two carbon-carbon bond distances are marked as r_1 and r_2. R_{pitch} is calculated as $(r_1+r_2)/2$. Carbon, hydrogen and fluorine atoms are shown as grey, white, and green colors, respectively.

5.3 Results and discussion

5.3.1 Ground-state structures, absorption and CD spectra

Ground state (S_0) structures of di-, tetra- and octafluoro substituted carbo[5-8]helicenes are shown in Figure 5.2. In this figure, two torsional angles, ∠*a*-*b*-*c*-*d* and ∠*b*-*c*-*d*-*e*, denoted as ϕ_1 and ϕ_2, respectively, are marked. Table 5.1 and Figure 5.3 show the

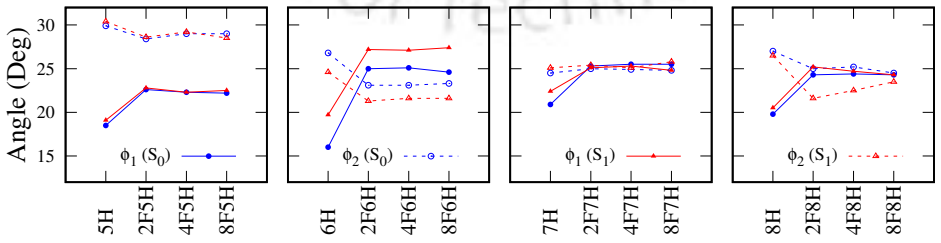

FIGURE 5.3: Dihedral angles ϕ_1 and ϕ_2 plotted for pristine helicenes and their fluorinated derivatives.

values of the two dihedral angles. In case of **5H**, the ϕ_1 values of the fluorinated **5H**s

TABLE 5.1: Values of selected torsional angles (ϕ, degrees) and R_{pitch} (Å) of ground state (S_0) and lowest singlet excited state (S_1) optimized geometries of **5H**-**8H**, and their di-, tetra- and octafluorinated derivatives

	S_0 Geometry			S_1 Geometry		
Systems	Torsional angles		R_{pitch}	Torsional angles		R_{pitch}
	ϕ_1	ϕ_2		ϕ_1	ϕ_2	
5H	18.5	29.9	3.73	19.1	30.4	3.69
2F5H	22.6	28.4	3.88	22.8	28.6	3.81
4F5H	22.3	29.0	3.88	22.3	29.2	3.83
8F5H	22.2	29.0	3.85	22.5	28.5	3.76
6H	16.0	26.8	3.59	19.7	24.6	3.34
2F6H	25.0	23.1	3.51	27.2	21.3	3.27
4F6H	25.1	23.1	3.53	27.1	21.6	3.30
8F6H	24.6	23.3	3.50	27.4	21.6	3.25
7H	20.9	24.5	3.34	22.4	25.1	3.17
2F7H	25.3	25.0	3.36	25.1	25.4	3.20
4F7H	25.5	24.9	3.31	25.3	25.1	3.17
8F7H	25.5	24.8	3.29	24.8	25.8	3.17
8H	19.8	27.0	3.31	20.5	26.5	3.21
2F8H	24.3	25.0	3.40	25.2	21.6	3.16
4F8H	24.4	25.2	3.38	24.7	22.5	3.16
8F8H	24.3	24.5	3.34	24.3	23.5	3.22

* The S_0 and S_1 states optimizations were carried out at RI-SCS-MP2/def2-TZVP and RI-ADC(2)/def2-TZVP levels, respectively. For **8F6H**, the reported R_{pitch} is 3.76 Å, and average ϕ_1 and ϕ_2 values are 22° and 26°, respectively obtained from the crystal structure data.[55]

are larger than the value in **5H**. However, the ϕ_1 values in the fluorinated systems remain almost the same. Similar results are seen for ϕ_2 too; after an initial decrease of 1.5°, the value remains almost the same. Accordingly, the R_{pitch}, after a sudden increase from **5H** to **2F5H**, remains also almost the same. As shown in Figure 5.3, in case **6H**, values of ϕ_1 and ϕ_2 increase and decrease, respectively, while going from **6H** to **2F6H**. However, these values, after the initial changes from 16° to 25°and 26.8° to 23°, do not change much for the fluorinated systems. This is mostly consistent with the results obtained from the crystal structure data of fluorinated **6H** (as shown in Table C1).[55,275] As a result, the R_{pitch} decreases by 0.08 Å from **6H** to **2F6H**, and remains almost the same for the fluorinated systems, which matches with the corresponding results obtained from the reported fluorinated **6H**[55,275] (as shown in Table C1). For **6H** and **8F6H**, the R_{pitch} values are smaller by $\sim$ 0.3 Å compared to R_{pitch} of their respective crystal structures.

In contrast to C_2 symmetric structures considered for **6H** and **8F6H** in this study, the corresponding crystal structures are unsymmetrical and produce larger R_{pitch} values. Similar to the results for fluorinated **5H** and **6H**, ϕ_1 in **7H** increases after fluorination. On the other hand, changes in ϕ_2 are very small for all the four systems in this case. It is observed that **2F7H** shows similar structural features to that of experimentally reported homologous 1,2-difluoro[7]helicene.[56] Values of R_{pitch} increase by 0.02 Å from **7H** to **2F7H**. After this, the value decreases for **4F7H** and **8F7H**. In case of **8H**, variation in ϕ_1 is similar to the previous result in **7H**. However, value of ϕ_2, showing a sudden decrease of 2° from **8H** to **2F8H**, remains almost the same. While the R_{pitch} value increases from **8H** to **2F8H** by 0.09 Å, it decreases for tetra- and octafluorinated **8H**s, similar to the results for **7H** and its derivatives.

5.3.2 UV spectra

Absorption spectra of the parent and fluorinated carbo[5-8]helicenes are compared in Figure 5.4. The values of λ_{abs}, f_{osc}, and major transitions corresponding to few prominent peaks of the spectra are tabulated in the Tables 5.2. Results for all the excited states are shown in Tables C2–C17. In case of **5H** as shown in Table C2, the first two excited states appearing at 352 and 309 nm have negligible f_{osc} values. The first excited state with a prominent f_{osc} value appears at 293 nm corresponding to the S_4 state. It is to be noted that both S_3 and S_4 are very close in energy, and they together produce the lowest energy band. The largest contributor to this excited state is the transition from highest occupied molecular orbital (H) → lowest unoccupied molecular orbital (L)+1. Results are different in fluorinated **5H**s. In the three fluorinated systems, the lower energy peaks with large f_{osc} values are obtained for $S_0 \rightarrow S_5$ excitations where S_5 is the 3 ^{1}B state. In all the three cases, the same two sets of transitions are involved, i.e., H-1→L+1 and H→L excitations. The second transition with a comparatively larger f_{osc} value appear at 213, 213 and 215, respectively, for **2F5H**, **4F5H**, and **8F5H**. All these peaks correspond to large values of $|\boldsymbol{\mu}|$ ($f_{\text{osc}} \propto |\boldsymbol{\mu}|^2$).[57]

In case of **6H**, the first two excited states appear at 368 and 328 nm with f_{osc} values close to zero. The first prominent peak for **6H** appears at 315 nm with f_{osc}=0.425

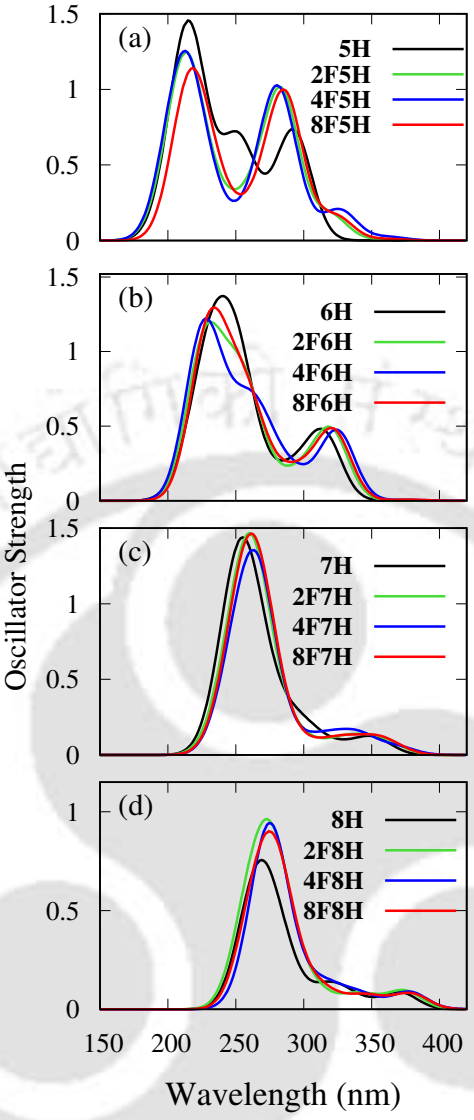

FIGURE 5.4: Absorption spectra of **5H** (a), **6H** (b), **7H**(c) and **8H** (d) along with their respective derivatives. The results are obtained at RI-ADC(2)/def2-TZVP level. A half-width at half-maximum value of 15 nm is used for each curve.

corresponding to the $S_0 \rightarrow 2\ ^1$B transition (as shown in Table C6). This transition arises predominantly from a combination of two excitations; H$\rightarrow$ L+1 (48%) and H-1$\rightarrow$L (40%). The strongest peak, however, appears at 233 nm with f_{osc}=0.728, and this one corresponds to the $S_0 \rightarrow 8\ ^1$A transition. Two sets of excitations, H-2$\rightarrow$L+2 (62%) and H$\rightarrow$L+3 (15%), contribute to this transition. It is worth noting that the 8 ^{1}B state with a smaller f_{osc} value is degenerate with the 8 ^{1}A state. Similarly, as the Table C6 shows, there are other closely-lying excited states with considerable f_{osc} values, e.g., peaks

appearing at 222 nm, 236 nm, 250 nm and 252 nm. The spectrum, as shown in Figure 5.4, is consistent with the previously reported results.[4,55] Similar to the results for **6H**, the first two excited states show negligible f_{osc} values for **2F6H** too. The prominent peaks at 320 and 228 nm are red- and blue-shifted, respectively, compared to those in **6H**. The peak at 320 nm corresponds to the same transition as in **6H**, and shows similar intensity too. However, the peak at 228 nm exhibits smaller intensity (as shown in the Figure 5.4) and so as the other fluorinated derivatives. As in the case of **6H**, two more excited states, 9 ^{1}A and 10 ^{1}A with f_{osc} values of 0.313 and 0.012, are very close in energy to the 8 ^{1}A state. In cases of **4F6H** and **8F6H**, shapes and intensities of the spectra remain almost unchanged compared to that of **2F6H**. However, the positions of the peaks get red-shifted slightly (by $\approx$ 2-5 nm, as shown in the Table 5.2). The results for **8F6H** are well in accordance with the reported spectrum.[55] While the first major peak in **4F6H** at 325 nm correspond to the same set of excitations as in the case of **2F6H**, the peak at 322 nm for **8F6H** correspond to H-1→L+1 and H→L excitations. In **2F6H**, **4F6H** and **8F6H**, $|\boldsymbol{\mu}|$ values for the second major peaks are smaller than the corresponding value in **6H**, and this results in decrease in the f_{osc} values.

With elongation in chain length, i.e., going from **5H** to **7H** and their derivatives, the peaks get red-shifted. For example, for **7H**, the two major peaks appear at 354 and 258 nm with f_{osc} values of 0.087 and 0.438, respectively, (as shown in the Figure 5.4), red-shifted by 39 and 25 nm, respectively, from the peaks of **6H**. The above mentioned peak values are consistent with the previous experimental and computational results[4,57]. The peak at 354 nm arises also from the S_0→1 ^{1}B transition and is a result of H-1→L (82%) and H→L+1 (10%) excitations. On the other hand, the peak at 258 nm corresponds to the S_0→8 ^{1}A transition, with major contributions from H-4→L (36%) and H-1→L+3 (20%) excitations. Similar to fluorinated **6H**, the fluorinated **7H** molecules produce very similar absorption spectra. In the case **2F7H**, both 1 ^{1}B and 2 ^{1}B state have very similar f_{osc} values. The peak at 363 nm, primarily due to H→L (92%) excitation, is red-shifted by 9 nm compared to the corresponding peak in **7H**. However, the position of the lower intensity peak does not change much (as shown in Tables 5.2 and C11). In **4F7H**, the peak at 370 nm is again a purely H→L excitation. For **8F7H**, in the low energy region, the two peaks at 367 and 352 nm have large f_{osc} values. While the peak

TABLE 5.2: Excitation Energy (λ_{abs} in nm), Corresponding Oscillator Strength (f_{osc}), $|\boldsymbol{\mu}|$, $|\boldsymbol{m}|$, cos θ, R, g_{CD}, $|\boldsymbol{m}|/|\boldsymbol{\mu}|$ and Orbitals Involved in the Transitions for **2F5H**, **8F5H**, **2F6H**, **8F6H**, **2F7H**, **8F7H**, **2F8H** and **8F8H**

Excited State	λ_{abs}	f_{osc}	R	$\|\boldsymbol{\mu}\|$	$\|\boldsymbol{m}\|$	cos θ	g_{CD}	$\|\boldsymbol{m}\|/\|\boldsymbol{\mu}\|$	Configurations
2F5H									
$1\ ^1$A (S_1)	358	0.008	-10.86	77.82	0.14	-1	-0.0072	0.002	H →L+1(57.%),H-1→L (37.%)
$1\ ^1$B (S_2)	319	0.172	83.95	342.00	1.50	0.16	0.0029	0.004	H →L (80.%),H-1→L+1(10.%)
$3\ ^1$B (S_5)	284	0.763	345.99	678.71	2.87	0.18	0.003	0.004	H-1→L+1(77.%),H →L (12.%)
$8\ ^1$A (S_{16})	213	0.927	-30.46	647.77	0.05	-1	-0.0003	0	H-1→L+3(61.%),H-3→L+1(16.%)
8F5H									
$1\ ^1$A (S_1)	362	0.011	-7.50	91.01	0.08	-1	-0.0036	0.001	H →L+1(60.%),H-1→L (34.%)
$1\ ^1$B (S_2)	323	0.161	77.99	332.86	1.42	0.16	0.0028	0.004	H →L (77.%),H-1→L+1(10.%)
$3\ ^1$B (S_5)	287	0.726	352.02	664.98	2.87	0.18	0.0032	0.004	H-1→L+1(82.%),H →L (10.%)
$8\ ^1$A (S_{15})	215	0.528	-55.56	491.15	0.11	-1	-0.0009	0	H-1→L+3(60.%),H →L+2(7.%)
2F6H									
$1\ ^1$B (S_1)	375	0.004	-2.39	58.51	0.18	-0.23	-0.0028	0.003	H-1→L (50.%),H →L+1(40.%)
$1\ ^1$A (S_2)	335	0.000	-0.69	8.06	0.09	-1.00	-0.0426	0.011	H →L (71.%),H-1→L+1(20.%)
$2\ ^1$B (S_3)	320	0.410	567.34	528.43	3.91	0.27	0.0081	0.007	H →L+1(50.%),H-1→L (39.%)
$8\ ^1$A (S_{16})	228	0.566	-255.54	523.95	0.49	-1.00	-0.0037	0.001	H-2→L+3(27.%),H-5→L (26.%)
8F6H									
$1\ ^1$B (S_1)	377	0.008	-1.22	79.65	0.3	-0.05	-0.0008	0.004	H →L (52.%),H-1→L+1(39.%)
$1\ ^1$A (S_2)	339	0.002	1.61	40.61	0.04	1.00	0.0039	0.001	H-1→L (55.%),H →L+1(28.%)
$2\ ^1$B (S_3)	322	0.397	512.27	521.89	3.69	0.27	0.0075	0.007	H-1→L+1(47.%),H →L (40.%)
$8\ ^1$A (S_{16})	231	0.693	-295.57	582.81	0.51	-1.00	-0.0035	0.001	H-2→L+3(26.%),H-5→L (23.%)
2F7H									
$1\ ^1$A (S_1)	397	0.000	-0.28	4.43	0.06	-1	-0.0574	0.014	H →L+1(55.%),H-1→L (37.%)
$1\ ^1$B (S_2)	363	0.062	301.72	219.17	2.91	0.47	0.0251	0.013	H →L (92.%),H →L+3(2.%)
$2\ ^1$B (S_3)	346	0.081	324.80	244.66	2.81	0.47	0.0217	0.011	H-1→L+1(75.%),H-3→L (9.%)
$8\ ^1$A (S_{15})	260	0.454	-145.55	500.7	0.29	-1	-0.0023	0.001	H-3→L+1(24.%),H-4→L+1(20.%)
8F7H									
$1\ ^1$A (S_1)	399	0.000	0.17	3.87	0.04	1	0.0457	0.011	H →L+1(54.%),H-1→L (38.%)
$1\ ^1$B (S_2)	367	0.041	258.47	177.77	2.64	0.55	0.0327	0.015	H →L (87.%),H-2→L+1(3.%)
$2\ ^1$B (S_3)	352	0.093	349.49	263.23	3.03	0.44	0.0202	0.012	H-1→L+1(76.%),H-1→L+2(7.%)
$8\ ^1$A (S_{15})	261	0.458	-187.02	504.38	0.37	-1	-0.0029	0.001	H-3→L+1(32.%),H-4→L+1(15.%)
2F8H									
$1\ ^1$B (S_1)	412	0.001	3.26	30.17	0.45	0.24	0.0143	0.015	H →L (55.%),H-1→L+1(34.%)
$1\ ^1$A (S_2)	376	0.009	-39.93	83.21	0.48	-1	-0.0231	0.006	H →L+1(59.%),H-1→L (19.%)
$2\ ^1$B (S_3)	374	0.084	747.28	258.14	4.04	0.72	0.0448	0.016	H-1→L+1(58.%),H →L (34.%)
$10\ ^1$A (S_{19})	259	0.266	120.30	382.72	0.31	1	0.0033	0.001	H-5→L (23.%),H →L+4(20.%)
8F8H									
$1\ ^1$B (S_1)	415	0.000	0.27	15.31	0.2	0.09	0.0047	0.013	H →L (49.%),H-1→L+1(41.%)
$1\ ^1$A (S_2)	383	0.004	-22.30	55.55	0.4	-1	-0.0289	0.007	H →L+1(54.%),H-1→L (23.%)
$2\ ^1$B (S_3)	379	0.074	690.94	244.05	3.98	0.71	0.0464	0.016	H-1→L+1(51.%),H →L (41.%)
$10\ ^1$A (S_{19})	262	0.260	145.22	380.81	0.38	1	0.004	0.001	H →L+4(26.%),H-5→L (21.%)

* $|\boldsymbol{\mu}|$, $|\boldsymbol{m}|$, and R are in 10^{-20} esu·cm, 10^{-20} erg·G^{-1} and 10^{-40} esu·cm·erg·G^{-1} units, respectively. Results are obtained at RI-ADC(2)/def2-TZVP level.

at 367 nm is because of H→L excitation, the one at 352 nm is mostly due to H-1→L+1 excitation. The peak in the high energy region (at 261 nm) arises due to the same set of excitations as in the case of **2F7H**. For **8H**, energies of the excited states mostly match with the previously reported values.[4] Similar to **6H** and **7H**, in **8H**, there are two major peaks which appear at 371 nm and 268 nm, respectively. The low-energy peak is due to S_0→2 ^{1}B transition, and so are the low-energy peaks in the fluorinated **8H**s. Over fluorination, this low-energy peak gets red-shifted as observed in the previous cases.

Properties of the excited states of the parent and the fluorinated systems are explored using ω_{CT}, PR_{NTO} and d_{exc} descriptors. The values are tabulated in Table C18–C21. Results are similar for all the four series of systems. For **5H** and its derivatives, ω_{CT} values for most of the states are in 0.7-0.8 range indicating that these are CT states. Accordingly, the corresponding d_{exc} values are $\geq$ 4 Å. NTOs for 3 ^{1}B and 8 ^{1}A states in fluorinated **5H**s are shown in Figures C2-C4. Two NTOs participate in all the cases except for **8F5H**, in accordance with the PR_{NTO} values in the table. In **2F5H** and **4F5H**, the units participating in the CT process are the same. In the case of the dominant NTO for 3 ^{1}B, CT occurs from the terminal rings and rings adjacent to the terminal rings. However, in the case of 8 ^{1}A, rings adjacent to the terminal rings dominantly participate in the charge transfer. In the case of **8F5H**, while the hole NTO is almost delocalized over the whole system, the particle NTO is spread mostly over the middle rings for the $S_0 \rightarrow 3\ ^1$B transition. All the states shown in the table for **6H** and its two fluorinated derivatives are also CT states in nature with ω_{CT}=0.7-0.8 and d_{exc}=4.0-4.5 Å. For most of states, the table also shows that PR_{NTO} value remains almost the same for the parent and fluorinated systems. NTOs for **2F6H**, **4F6H** and **8F6H** are shown in Figures C5-C7. In case of 2 ^{1}B for **2F6H**, the first set of NTOs show that while the hole is distributed over the whole chain, the terminals are devoid of electron distribution. The second set of NTOs for this state shows the opposite scenario, i.e., the differences appear in the middle of the chain. In the case of 8 ^{1}A of **2F6H**, CT occurs between the central naphthalene unit and the rest of the rings. Similar to **2F6H**, for the $S_0 \rightarrow 2\ ^1$B transitions of **4F6H** and **8F6H**, charge transfer occurs predominantly from the terminal rings to the rest part of the system. PR_{NTO} values for the 2 ^{1}B states shown in Figures C5-C7 are the same. However, in cases of the peaks in the high energy region, PR_{NTO} values for the four **6H** systems differ from each other. For a few other higher excited states, differences in PR_{NTO} values are observed. Similar results are obtained for **7H** and **8H** and their derivatives, i.e., the states have ω_{CT} values $\approx$ 0.8 and $d_{exc}>$ 4. The results are shown in Tables C20 and C21. In the cases fluorinated **7H**s, the dominant NTOs show that CT happens between the terminal rings and other rings for the $S_0 \rightarrow 8\ ^1$A transitions. For the 2 ^{1}B state in **2F8H**, two sets of NTOs contribute. The dominant NTO shows charge transfer from the central region to other parts of the

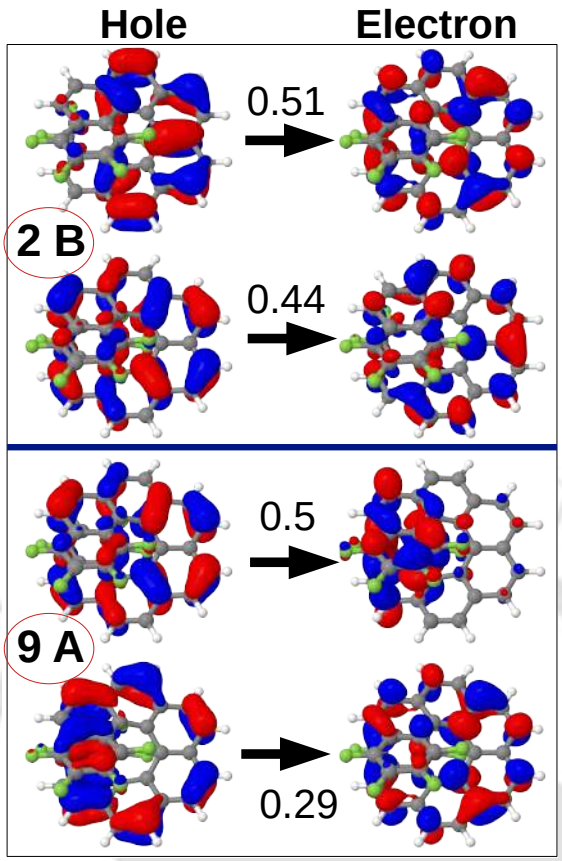

FIGURE 5.5: Natural transition orbitals for some selected excited states of **8F8H**. Results are obtained at RI-ADC(2)/def2-TZVP level.

unit. On the other hand, the second set of NTO depicts that while hole is distributed over the whole unit, the terminals are devoid of electron densities. A similar scenario is observed in case of **4F8H**. NTOs for two excited states in **8F8H** are shown in Figure 5.5. For the 9 ^{1}A in this case, while the dominant hole NTO is delocalized over the whole chain, the corresponding particle NTO is localized in the terminal and its adjacent rings only.

5.3.3 CD spectra

Figure 5.6 shows the CD spectra of **5H**, **6H**, **7H**, and **8H** along with their fluorinated derivatives. As mentioned previously, R is a scalar product of $\boldsymbol{\mu}$ and $\boldsymbol{m}$, and therefore, $|\boldsymbol{\mu}|$, $|\boldsymbol{m}|$ and orientations of these two vectors with respect to each other play important roles in predicting the intensity of the spectrum. In organic molecules, magnitudes of $|\boldsymbol{\mu}|$ are typically much larger than the magnitude of $|\boldsymbol{m}|$. Accordingly, $g_{\mathrm{CD}}(g_{\mathrm{CPL}}) \propto$

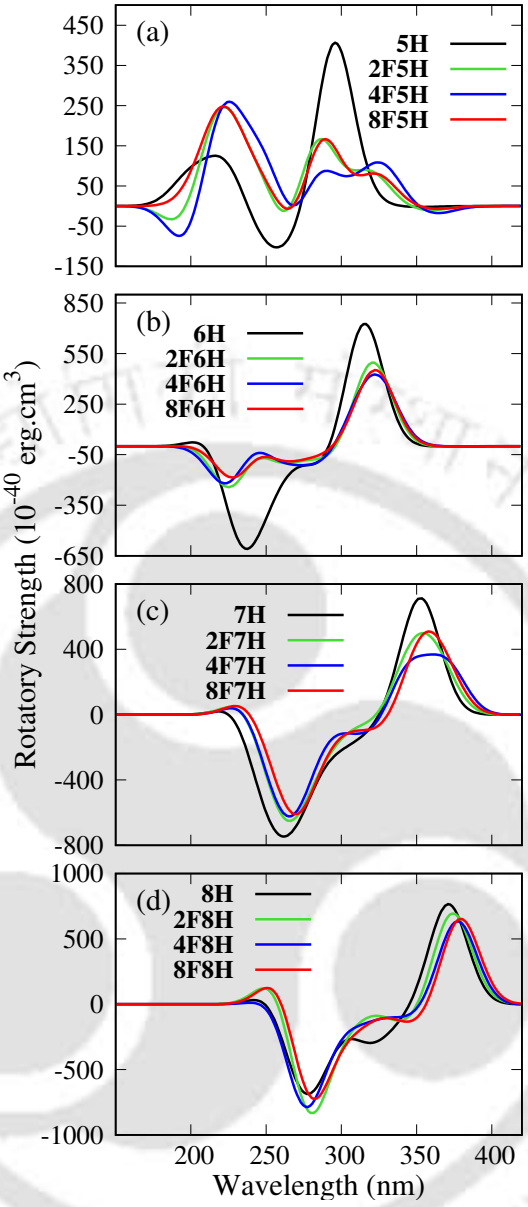

FIGURE 5.6: CD spectra of **5H** (a), **6H** (b), **7H** (c) and **8H** (d) along with their fluorinated derivatives. Results are obtained at RI-ADC(2)/def2-TZVP level of theory. A half-width at half-maximum value of 15 nm is used for each curve.

$|\boldsymbol{m}|/|\boldsymbol{\mu}|$. In **5H**, three bands are observed; two with positive Cotton effect (CE) and one with negative CE. The peak at 293 nm corresponds to the previously reported ^1B_b band (observed at 298 nm[4]). This peak has the largest R value, and corresponds to a large $|\boldsymbol{\mu}|$ value of 580.17 esu·cm and an $|\boldsymbol{m}|$ value of 3.08 erg·G^{-1}, shown in Table C2. The angle between $\boldsymbol{\mu}$ and $\boldsymbol{m}$ is $\approx 80°$. A small value of $|\boldsymbol{m}|/|\boldsymbol{\mu}|$ results in a g_{CD} value of 0.0042 for this transition which matches well with both experimental and computed g_{CD} values.[4] On the other hand, the S_2 state with a much larger value of $|\boldsymbol{m}|/|\boldsymbol{\mu}|$ (i.e., 0.01) and a

cos θ value of 0.82 shows a value of 0.0344 for g_{CD}. The structures of the CD curves of the fluorinated systems are mostly similar to each other. For **2F5H**, the peak at 284 nm with an R value of 346 esu·cm·erg·G^{-1} arises due to a large value of $|\boldsymbol{\mu}|$. However, an angle of $\approx 80°$ between the two vectors and a $|\boldsymbol{m}|/|\boldsymbol{\mu}|$ =0.004 results in g_{CD}=0.003. In the case of **4F5H**, R value of the peak at 283 nm decreases to 241 cgs units with g_{CD}=0.0023. However, both R and g_{CD} values increase for the same peak in the case of **8F5H**. The improvement in the R value is a result of increase both in magnitudes of the two vectors and the cosine of the angle of between the two transition vectors, while it is only the angle which affects the g_{CD} value. In case of **6H**, two major bands appear; one with positive CE at ∼316 nm and other one with negative CE at ∼233 nm. These two correspond to the previously computed ^1B_b (at 317 nm) and ^1B_a (at 233 nm) transitions, respectively.[4] Table C6 shows that the transition corresponding to ^1B_b band at 315 nm has comparatively large electric and magnetic dipole moment values, i.e., 533.7 esu.cm and 4.03 erg.G^{-1} for $|\boldsymbol{\mu}|$ and $|\boldsymbol{m}|$, respectively, and therefore, this results in a large R value. In contrast, transition to the almost degenerate 2 ^{1}A state is accompanied with smaller values of $|\boldsymbol{\mu}|$ and $|\boldsymbol{m}|$ which results in a small R value. Similarly, while the band at 232 nm corresponds to large values of $|\boldsymbol{\mu}|$ and $|\boldsymbol{m}|$, the degenerate 8 ^{1}B state shows a very small value for $|\boldsymbol{m}|$ (or a small value of $|\boldsymbol{m}|/|\boldsymbol{\mu}|$). In the cases of fluorinated **6H**, the positions of the bands get red-shifted. In **2F6H**, the major positive CD band corresponding to $S_0 \rightarrow 2$ ^{1}B transition at 320 nm shows the largest values of $|\boldsymbol{\mu}|$, $|\boldsymbol{m}|$ and R (as shown in Table 5.2). However, a drastic decrease in R value is observed in the case of transition to the nearly degenerate 2 ^{1}A state. In the case of the negative band, g_{CD} and $|\boldsymbol{m}|/|\boldsymbol{\mu}|$ decrease for both the nearby transitions, i.e., $S_0 \rightarrow 8$ ^{1}A and $S_0 \rightarrow 9$ ^{1}A. In the case of **4F6H**, the positive band around 325 nm arises from the same set of two degenerate transitions as observed in the case of **2F6H**. Here also the $S_0 \rightarrow 2$ ^{1}B is the dominant transition for the positive band. The g_{CD} values follow the $|\boldsymbol{m}|/|\boldsymbol{\mu}|$ pattern, although the anti-parallel orientation of the two vectors in the second case improves the g_{CD}. However, the negative band comprises of three nearby transitions, $S_0 \rightarrow 8$ ^{1}A $S_0 \rightarrow 9$ ^{1}A and $S_0 \rightarrow 10$ ^{1}A, with different R values. Similar to **2F6H** and **4F6H**, both the positive and negative bands of **8F6H** comprise of two nearby transitions. Between the two, one transition is accompanied with larger values of $|\boldsymbol{m}|/|\boldsymbol{\mu}|$ and R for the positive

band. However, in the case of negative band, both the states show the same $|\boldsymbol{m}|/|\boldsymbol{\mu}|$ (as shown in Table C9). It is worth noting that there are few other excited states which contribute to the negative band.

The bisignate CD spectrum of **7H** matches well with previously reported spectra.[4,57] The positive and the negative peaks at ≈354 nm and 263 nm correspond to the known ^1B_b (at 351 nm) and ^1B_a (at 262 nm) bands of **7H**, respectively.[4] It is to be noted that the ^1B_b peak is very close to another peak with a smaller rotatory strength at 347 nm. Similarly, there are more than two peaks contributing to the ^1B_a band, at 274 nm, 258 nm, and 246 nm. However, the R value for the peak at 263 nm is 1.92 times larger than the value at 258 nm owing to ≈ three-fold increase in the value of $|\boldsymbol{m}|$. Around this region, the peak at 257 nm shows positive CE due to angle of ∼25° between the two vectors. Table C10 also shows that the value of g_{CD} is larger for the ^1B_b band in **7H** compared to that in **6H**, and this is due to a larger $|\boldsymbol{m}|/|\boldsymbol{\mu}|$ value in **7H**. Results after fluorination are also shown in Figure 5.6 and data are tabulated in Table 5.2. For **2F7H**, the R value of the peak for the $S_0 \rightarrow 1\ ^1B$ transition becomes smaller than the same transition in **7H**. In addition, the value of g_{CD} also decreases (from 0.039 to 0.0251) for this transition. As mentioned before, the above peak is always associated with another peak arising from $S_0 \rightarrow 2\ ^1B$ transition, and the R value for this transition in **2F7H** is a little larger than the value of the $S_0 \rightarrow 1\ ^1B$. The g_{CD} value, on the other hand, becomes smaller due to a smaller $|\boldsymbol{m}|/|\boldsymbol{\mu}|$ value. In this case, the two peaks are well separated from each other. g_{CD} value for the $S_0 \rightarrow 7\ ^1A$ transition is also smaller over double fluorination than the value in **7H**. While the magnitudes of R for $S_0 \rightarrow 7\ ^1A$ transitions are the largest among the transitions shown for both **2F7H** and **8F7H**, the magnitude is the second largest in case of **7H**. It is noted that the g_{CD} value is the largest for the $S_0 \rightarrow S_4$ transition due the largest value of $|\boldsymbol{m}|/|\boldsymbol{\mu}|$ amongst all. Over tetrafluorination of **7H**, the shape of the CD bands remain of almost unchanged. The two peaks corresponding to the positive band, at 370 and 345 nm, get separated further in comparison to **2F7H** and produce a little flat band compared to the others. While the R and g_{CD} values remain almost the same as those for the corresponding peak in **2F7H**, the values decrease for the higher energy $2\ ^1B$ peak. The two dominant peaks for the negative band show similar R values in **4F7H**. In the case **8F7H**, the

positive band mostly comprises of transitions to 1 ^{1}B and 2 ^{1}B states. In comparison to **4F7H**, while the R value of the lower energy peak decreases for **8F7H**, it increases for the other peak. **8H** also shows two major CD bands, shown in Figure 5.6. As Table C14 shows, the major contributor to the highest intensity positive band is the peak at 371 nm, which corresponds to the reported ^1B_b transition at 372 nm. The R value for this peak is 807.44 esu.cm.erg.G^{-1} with a g_{CD} value of 0.0539. On the other hand, the ^1B_a transition at 268 nm is blue-shifted by 12 nm and 20 nm from the RI-CC2 and experimental results, respectively.[4] For the negative peak at 268 nm, values of R and g_{CD} decrease by 1.71 and 5.61 factors, respectively, in comparison to the values for the peak at 371 nm. The larger value of g_{CD} in case of $S_0 \rightarrow S_2$ transition is due to a larger value of $|\boldsymbol{m}|/|\boldsymbol{\mu}|$. For **2F8H**, the positive peak appears at 374 nm with R=747.28 in cgs units and g_{CD}=0.0448, owing to a large value of $|\boldsymbol{m}|/|\boldsymbol{\mu}|$. Similar to **8H**, it shows higher intensity than the major negative peak at 278 nm. In the case of **4F8H**, the R value of the peak at 377 nm is smaller than that of **2F8H**. In addition, the $S_0 \rightarrow 9$ ^{1}A peak at 273 nm appears as the strongest negative peak among all with an R=-622.93 cgs units. It is also observed that the g_{CD} values for the corresponding peaks of negative bands in cases of **2F8H** and **4F8H** are smaller than the g-values of the 2 ^{1}B peaks. Similar trend is observed in the case **8F8H**. In cases of fluorinated **8H**s, the dominant positive peaks appear from $S_0 \rightarrow S_3$ transitions, unlike in the case of **8H** for which the dominant transition is $S_0 \rightarrow S_2$.

5.3.4 Structures in the S_1 states and emission properties

Fluorescence in common organic molecules usually follow the Kasha's rule[240], i.e., the emission occurs from the S_1 state. Therefore, in our case, all the excited state optimizations were carried out in the S_1 states at RI-ADC(2)/def2-TZVP level using the C_2 symmetry in each case. In the S_1 states, geometries of the carbohelicenes are squeezed in comparison to the ground states structures (as shown in Figure 5.3, and Tables 5.1 and C1), showing substantial differences between the ground and excited state geometries. The fluorinated **5H** systems show larger R_{pitch} values compared to **5H**, and **8F5H** shows

TABLE 5.3: Emission energies (λ_{em}, nm), Corresponding Oscillator Strength(f_{osc}), $|\boldsymbol{\mu}|$, $|\boldsymbol{m}|$, cos θ, R, g_{CPL}, $|\boldsymbol{m}|/|\boldsymbol{\mu}|$, and K_f of **5H**, **6H**, **7H** and **8H**, and their fluorinated derivatives.

System	λ_{em}	f_{osc}	$\|\boldsymbol{\mu}\|/10^{-20}$	$\|\boldsymbol{m}\|/10^{-20}$	cos θ	$R/10^{-40}$	g_{CPL}	$\|\boldsymbol{m}\|/\|\boldsymbol{\mu}\|$	$K_f \times 10^{-1}$
5H	390	0.002	36.56	0.10	-1.0	-3.51	-0.0105	0.003	0.007
2F5H	397	0.009	85.23	0.14	-1.0	-12.13	-0.0067	0.002	0.036
4F5H	403	0.025	147.69	0.15	-1.0	-22.89	-0.0042	0.001	0.105
8F5H	402	0.012	101.31	0.03	-1.0	-9.41	-0.0037	0.0009	0.049
6H	411	0.0002	14.13	0.07	-0.77	-0.76	-0.0152	0.005	0.0009
2F6H	421	0.0066	76.77	0.42	-0.02	-0.62	-0.0004	0.005	0.0248
4F6H	422	0.0065	76.1	0.27	-0.1	-1.97	-0.0014	0.004	0.0240
8F6H	424	0.0088	89.01	0.53	0.02	0.94	0.0005	0.006	0.0325
7H	447	0.0002	13.16	0.03	1.0	0.40	0.0092	0.002	0.0006
2F7H	451	0.0003	16.44	0.07	-1.0	-1.12	-0.0166	0.004	0.0009
4F7H	453	0.0008	27.86	0.09	-1.0	-2.61	-0.0134	0.003	0.003
8F7H	453	0.0001	7.61	0.01	1.0	0.07	0.0046	0.001	0.0002
8H	462	0.0	4.52	0.03	-0.77	-0.12	-0.0226	0.007	0.0001
2F8H	496	0.0087	96.03	1.86	0.48	85.14	0.0369	0.019	0.0237
4F8H	493	0.0093	98.63	1.69	0.4	67.7	0.0278	0.017	0.0260
8F8H	472	0.0001	11.83	0.22	0.56	1.48	0.0424	0.019	0.0004

the smallest R_{pitch} among the fluorinated ones, similar to the trend in S_0-optimized geometries. However, only minor changes are observed in the values of torsional angles when compared to the values in S_0. In case of **6H**, R_{pitch} for S_1 is smaller by 0.25 Å compared to the value in the ground state. Similar to the results for S_0 geometries, R_{pitch} values for S_1 geometries of fluorinated **6H** are smaller than the value for the parent molecule (as shown in Table 5.1), and the smallest value of 3.25 Å occurs for **8F6H**. Figure 5.3 shows that while ϕ_1 increases from **6H** to **2F6H**, it remain almost constant after that. On the other hand, value of ϕ_2 decreases over fluorination, i.e., from **6H** to **2F6H**, a decrease of 3° is observed. Beyond **2F6H**, the value remains the same as was the scenario in case of ϕ_1. In **7H**, **8H** and their derivatives, R_{pitch} parameter does not show any systematic change with the increase in the degree of fluorination. For example, it increases by 0.03 Å in the case of **2F7H** and later levels off at 3.17 Å, exactly the same value for the parent **7H** (as shown in Table 5.1). As it is observed in Figure 5.3, ϕ_1 shows an increase from **7H** to **2F7H**, and thereafter, the value remains the same. For **8H** and its derivatives, R_{pitch} decreases from **8H** to **2F8H**. Thereafter, while the value for **4F8H** is exactly the same as **2F8H**, it increases for **8F8H**. In this case, after a sudden decrease in the value for ϕ_2 from **8H** to **2F8H**, the values increase with more fluorination.

Emission energies (λ_{em}), $|\boldsymbol{\mu}|$, $|\boldsymbol{m}|$ and cos θ for $S_1 \rightarrow S_0$ transitions are compiled in Table 5.3. λ_{em} of **5H** is 390 nm (with f_{osc}=0.002) which is close to the reported values of 406 nm (in dichloromethane)[110] and 424 nm (in chloroform)[54]. The orbitals involved, and contributions of various deexcitations are tabulated in Table C22. For **5H**, involved transitions are L→H (56%) and L+1→H-1 (39%). In both the above cases, the initial and final orbitals share the same symmetry.[110] As shown in Figures C13 and C14, while H and L are C_2-symmetric, and H-1 and L+1 are C_2-antisymmetric. Among carbo[5-8]helicenes, **5H** shows the largest R and K_f values, corresponding to the largest values of $|\boldsymbol{\mu}|$ and $|\boldsymbol{m}|$ for the $S_1 \rightarrow S_0$ emission in **5H**. It is worth mentioning that K_f is directly proportional to f_{osc}.[268,269] Over fluorination of **5H**, both R and K_f values increase till **4F5H** due to significant increase in values of $|\boldsymbol{\mu}|$. For **8F5H**, a slightly different result is obtained. The λ_{em} for **8F5H** is slightly smaller (by 1 nm) than the value for **4F5H** at ADC(2) level of theory. Both $|\boldsymbol{\mu}|$ and $|\boldsymbol{m}|$ values for the emission in **8F5H** is smaller than in **4F5H**. This leads to smaller values of R and K_f values in case of **8F5H**. A plot of $|\boldsymbol{\mu}|$ and $|\boldsymbol{m}|$ as a function of compounds is shown in Figure 5.7. For **5H**, both $|\boldsymbol{\mu}|$ and $|\boldsymbol{m}|$ show a similar type of variation, i.e., values of both increase from **5H** to **4F5H**, and this is followed by a decrease for **8F5H**. g_{CPL} values, on the other hand, decrease gradually with increase in the number of fluorine atoms following the order of $|\boldsymbol{m}|/|\boldsymbol{\mu}|$. With regard to the symmetries of the involved orbitals, in all fluorinated systems, the pattern observed in **5H** is followed.

In case of **6H**, λ_{em} corresponding to the $S_1 \rightarrow S_0$ transition is 411 nm, close to the reported fluorescence peak maximum around 420 nm[55,108,281]. The magnitudes of the two vectors decrease to less than half of the values for those in the $S_0 \rightarrow S_1$ transition (as shown in Tables 5.3 and C6). As a result, the overall R value for the emission decreases in comparison to absorption although the *cos* θ value between the two vectors increases. This change in the chiroptical properties is attributed to the decrease in the R_{pitch} value in the S_1 state.[281] K_f for this emission is only 0.00009 ns^{-1}. With fluorination, a systematic increase in λ_{em} and K_f is observed for **6H**, consistent with the experimental results.[55] Improvements in the values f_{osc} and K_f in this case is observed due to the many-fold increase in the values of $|\boldsymbol{\mu}|$ and $|\boldsymbol{m}|$ over fluorination. Figure 5.7 shows that after initial increase in both $|\boldsymbol{\mu}|$ and $|\boldsymbol{m}|$ values from **6H** to **2F6H**, there is a small

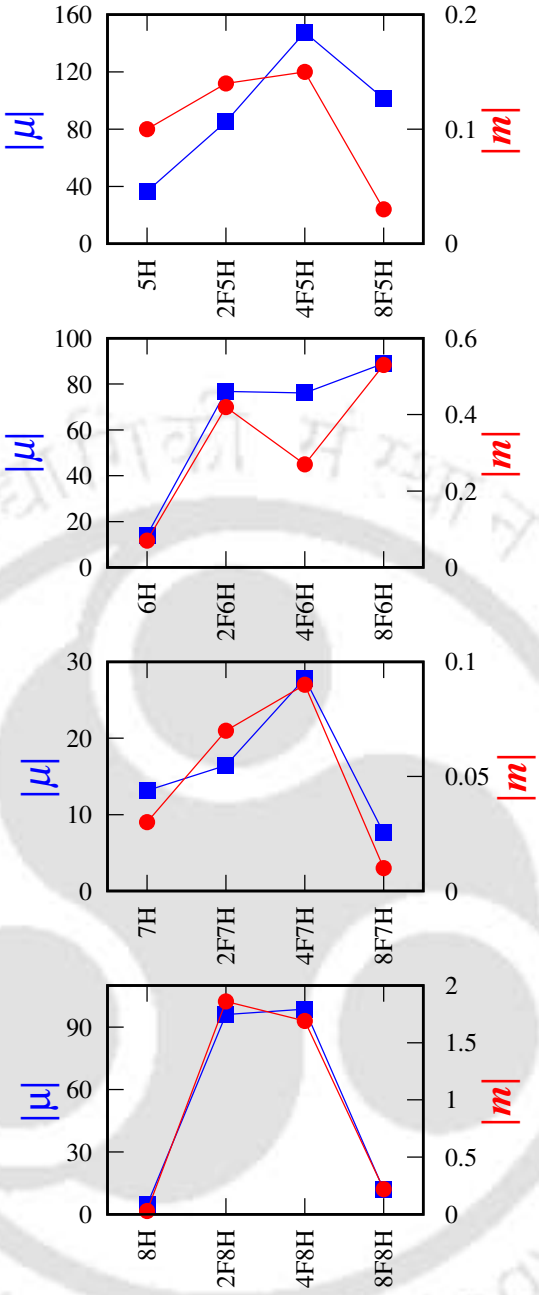

FIGURE 5.7: Variations in magnitudes of electric dipole transition ($|\boldsymbol{\mu}|$) and magnetic dipole transition moments ($|\boldsymbol{m}|$) for carbo[5-8]helicenes and their fluorinated derivatives for $S_1 \rightarrow S_0$ transitions

decrease for **4F6H** before the largest values for **8F6H** are obtained. Largest value of $|\boldsymbol{\mu}|$ for **8F6H** leads to the largest value of K_f (as shown in Table 5.3). The improvement in the K_f value is attributed to the many-fold increase in the value f_osc for the $S_1 \rightarrow S_0$ transition. For **2F6H**, as shown in Table 5.3, magnitudes of both the vectors increase by more than five times compared to the values for **6H**, and this resulted in a ∼30-fold increase in the value of K_f. However, the two vectors are almost perpendicular to each

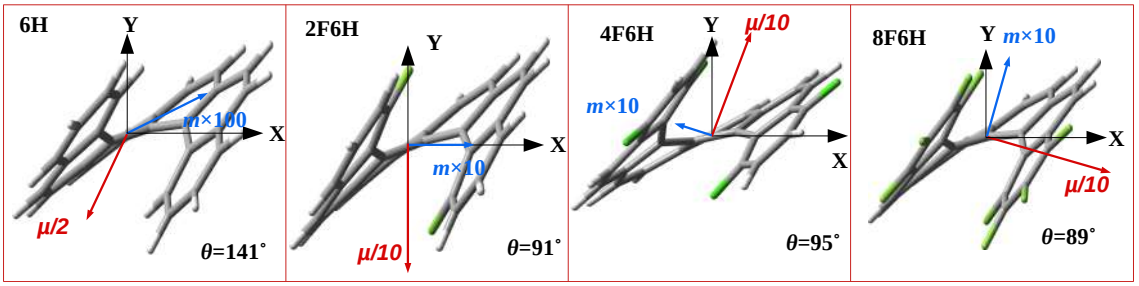

FIGURE 5.8: Directions of EDTM (red) and MDTM (black) vectors of **6H**, **2F6H**, **4F6H**, and **8F6H** for the $S_1 \rightarrow S_0$ transitions. Results are obtained at RI-ADC(2)/def2-TZVP level of theory.

other (as shown in the Figure 5.8), and this makes the g_{CPL} value small. R value for **4F6H** is more than two times larger in comparison to **6H** and **2F6H**. In the case of **4F6H**, the λ_{em} value is close to that of **2F6H**. Combinations of MOs involved in this transition for **4F6H** are the same as observed in cases of **6H** and **2F6H**.

For **7H**, the value λ_{em} gets red-shifted by 36 nm compared to that of **6H**, and the value of 447 nm is close to the experimental value of 443 nm.[57] The two sets of NTOs corresponding to $S_1 \rightarrow S_0$ transition are shown in Figure C17 for **7H**. Unlike **6H** and its derivatives, orbitals involved in **7H** share the same symmetry which is consistent with the previously reported results.[57] As a result, f_{osc} of the corresponding transition becomes small. As shown in Table 5.3, $|\boldsymbol{\mu}|$ values of **7H** and **6H** do not differ much from each other. However, the $|\boldsymbol{m}|$ value decreases by a factor of 2, and as a result, the overall value of $|\boldsymbol{m}|/|\boldsymbol{\mu}|$ decreased for **7H** resulting in smaller value of g_{CPL} compared to that of **6H**. Similar to the case of **6H**, λ_{em} increases over fluorination for **7H** as well (as shown in Table 5.3), before settling at 453 nm for both **4F7H** and **8F7H**. As shown in Figures C17 and C18, orbitals involved in each of the deexcitations for fluorinated **7H**s share the same symmetry, similar to the case of **7H**. As a result, fluorinated **7H**s do not exhibit any discernible change in the f_{osc} values. However, small increase in the f_{osc} values from **7H** to **4F7H** results in a little larger values of K_{f}. Variations in $|\boldsymbol{\mu}|$ and $|\boldsymbol{m}|$ in this case are similar to the results in **5H** and its derivatives. Unlike fluorinated **6H**, both **2F7H** and **4F7H** show improved results for g_{CPL}. The larger value of g_{CPL} can be understood in terms of more than two-fold increase in the $|\boldsymbol{m}|$ value and an anti-parallel orientation of the two vectors (as shown in Figure C22), and follows the order of $|\boldsymbol{m}|/|\boldsymbol{\mu}|$. For **8F7H**, magnitudes of the vectors decrease multiple times compared to the

corresponding values of the previous three. As a consequence, f_{osc}, K_f and g_{CPL} become the smallest. It suggested that **8F7H** would be the worst CPL emitter among the four. Similar to **7H**, both the vectors lie parallel to each other, but along the negative Z-axis in this case (as shown in Figure C22).

For **8H**, the $S_1 \rightarrow S_0$ transition arises from the same two sets of deexcitations as in the case of **6H**, i.e., H-1←L and H←L+1, as shown in Table C22. The NTOs and the corresponding MOs are shown in Figures C19 and C20, respectively. As observed, the orbitals involved in each deexcitation share the different symmetries. While the H and L orbitals are C_2-symmetric, L+1 and H-1 orbitals are C_2-antisymmetric. As a result, the magnitudes of vectors as well as f_{osc} do not improve over chain length, and the value of K_f decreased further to 0.00001 for **8H**. Unlike **8H**, the $S_1 \rightarrow S_0$ transition in **2F8H** consists of mainly the L→H (89%) deexcitation. Both the MOs involved in this transition belong to different symmetries (as shown in Figure C20), and this results in many fold increments in the values of vectors and f_{osc}. Variations in $|\boldsymbol{\mu}|$ and $|\boldsymbol{m}|$ are again shown in Figure 5.7. Similar to **2F7H**, **2F8H** shows significantly larger values of $|\boldsymbol{\mu}|$ and $|\boldsymbol{m}|$ resulting in a 1.6 and 237 times increase in g_{CPL} and K_f, respectively, compared to its parent **8H**. For **4F8H**, λ_{em} is 493 nm with the highest f_{osc}=0.0093 value. However, while $|\boldsymbol{\mu}|$ value increases a little, $|\boldsymbol{m}|$ value decreases, and this results in decrease in the values $|\boldsymbol{m}|/|\boldsymbol{\mu}|$ as well as g_{CPL}. The NTOs and the corresponding MOs involved in $S_1 \rightarrow S_0$ transition for **8F8H** are also shown in Figures C19 and C20, respectively. For **8F8H**, the $S_1 \rightarrow S_0$ transition arises from two deexcitations, similar to **8H**. Orbitals involved in each of these transitions are of different symmetries. As a result, $|\boldsymbol{\mu}|$ and $|\boldsymbol{m}|$ increase in comparison to **8H**, but not as much as in the case of **2F8H** or in **4F8H**. However, the value of g_{CPL} increases due to decrease in the angle between the two vectors as shown in Figure C23, and the maximum value of 0.0424 is obtained. The value of K_f, however, does not improve as much as in cases of **2F8H** and **4F8H** because of a smaller value of f_{osc}. An overall picture of results for g_{CPL} and K_f is shown in Figure 5.9. It is clear that the magnitude of g_{CPL} increases from **5H** to **6H**, and then decreases a little for **7H**, before showing the highest value for **8H**. Fluorination in **5H** and **6H** does not improve the g_{CPL} results. However, in **7H** and in **8H**, in particular, the results improve over fluorination, except in **8F7H**. While K_f

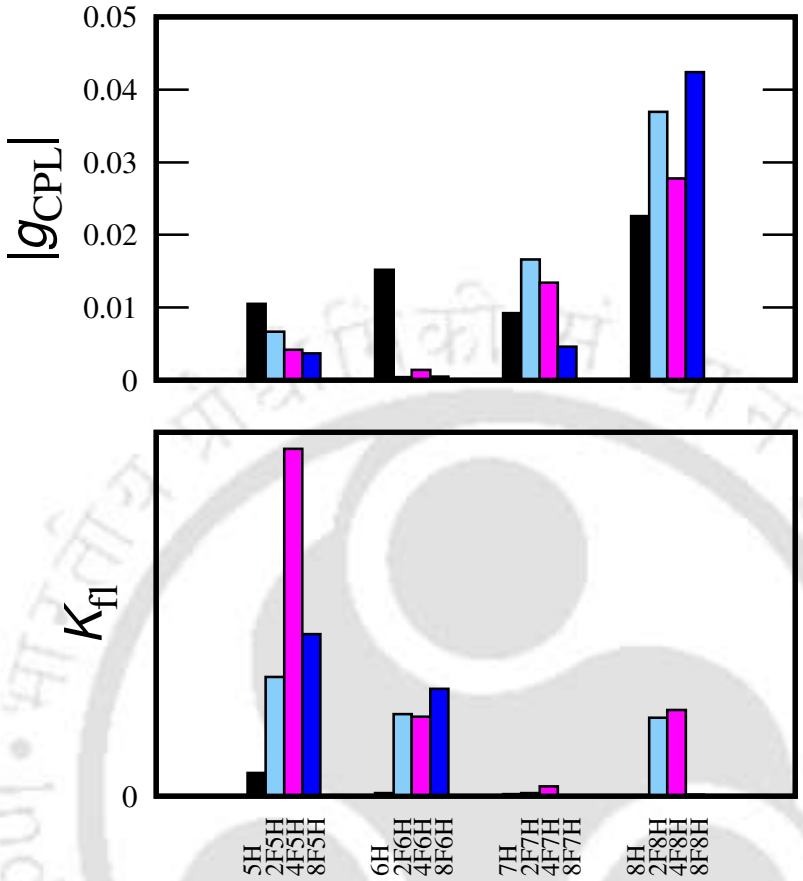

FIGURE 5.9: Dissymmetry factors for emission (g_{CPL} in top panel) and fluorescence rate constants (K_f in ns^{-1} in the bottom panel) for carbo[5-8]helicenes and their fluorinated derivatives

value in **5H** increases until tetrafluorination, the value shows a continuous increase over fluorination for **6H** (although the value for **4F6H** is slightly smaller than in **2F6H**). While the corresponding values for **7H** and its derivatives remain very small, values for **2F8H** and **4F8H** are much larger than the K_f for **8H**.

5.4 Conclusions

In this chapter, the effects of di-, tetra- and octafluorination of carbo[5-8]helicenes on the UV, CD, and CPL properties are presented. Fluorination in carbo[6-8]helicenes

show a decrease in the R_{pitch}, except in the case of **2F8H**. Due to this change in electronic structures, fluorinated carbohelicenes show a little bathochromic shift in spectral properties in comparison to their respective parents. In case of emission, fluorination in **6H** increased the values of $|\boldsymbol{\mu}|$ and $|\boldsymbol{m}|$ multiple times, and this resulted in an increase in the K_{f} values. However, the dissymmetry factor, i.e., g_{CPL} decreased several times due to the almost orthogonal orientations of the vectors. Unlike **6H**, fluorination of **7H** shows small K_{f} values and values do not differ much from each other. In addition, an increase in the g_{CPL} value for **2F7H** is also observed. Amongst all, **2F8H**, **4F8H** and **8F8H** show far better results, for which both g_{CPL} and K_{f} are improved simultaneously. Further studies using molecular dynamics simulations are under progress, and those will shed more light on the structure-property relationships in these types of substituted helicenes.

Chapter 6

Summary and conclusions

Helical-shaped systems based on extended π-conjugation are considered as promising candidates in materials sciences for various applications, in particular for designing OLED-based displays used in different devices. Much progress has been made in recent times in designing circularly polarized luminescent systems with improved values of fluorescence rates and disymmetry factors. Single- and multi-stranded helicenes have been the center of attention in this regard, and many of these helicenes have already been synthesized. However, only in a few cases, both Φ_{FL} and g_{CPL} have shown improvements, simultaneously. There are various ways to tune the chiroptical properties: by substitution of hydrogen atoms in the helix by other atoms/groups, by lateral or helical ring extensions, by fusion of multiple helicenic units or helicenic and non-helicenic units. At this juncture, computational studies play very important role in understanding the structure-property relationships which leads to better designing of CPL emitters by taking chemistry knowledge into account In this thesis, structural, charge-transfer and chiroptical properties of pyridine-thiophene-based oligomers, azahelicenes, and carbohelicenes are explored at TD-DFT and/or RI-ADC(2) levels.

In chapter 3, structural and excited-state properties of pyridine-thiophene (**PT**) oligomers (n=1-5) are studied by using three different sets of DFT functionals. The DFT results are compared against the RI-ADC(2) result. Among the DFT functionals, CAM-B3LYP, M06-2X, and ωB97XD show results comparable to those obtained using RI-ADC(2). $\mathbf{(PT)}_4$ shows the best results for both K_{f} and g_{CPL}.

In chapter 4, effects of heterocyclic ring fusion and chain elongation on structural and chiroptical properties of **9Ha** are presented. Two laterally-extended (denoted as

9HaP and **9HaQ**) and one helically-extended (denoted as **11Ha**) derivatives are designed starting from the reported **9Ha** molecule. Structural, CT, and chiroptical properties of these four systems are studied at TD-DFT level. All the four compounds are found to be CD and CPL active. For **9HaQ** and **11Ha**, K_{f} values for the $S_1 \rightarrow S_0$ transitions get improved compared to that of the parent **9Ha**, due to significant increase in the values of electric dipole transition moment. However, g_{CPL} follows the order of $|\boldsymbol{m}|/|\boldsymbol{\mu}|$, i.e., **9HaP**>**9Ha**>**11Ha**>**9HaQ**.

In chapter 5, chiroptical properties of di-, tetra- and octafluorinated carbo[5-8]helicenes are explored at RI-ADC(2)/def2-TZVP level. Degree of fluorination is found to have different effect on different carbohelicenes. While K_{f} is found to increase with fluorination in **6H**, g_{CPL} values in fluorinated **6H**s are foudn to be smaller than in **6H**. However, in the cases of fluorinated **8H**, both the g_{CPL} and K_{f} values improve simultaneously.

My work presented in this thesis has provided valuable insights into the understanding of chiroptical properties of helical systems. Computationally, while it is a little difficult to choose a DFT functional for this type of studies, DFT has been the go-to method. We show that DFT functionals have to carefully chosen. Otherwise, methods such as ADC(2) can be used to study these extended π-conjugated systems. We would like to conclude saying that the approach presented in this thesis can be extended to design various other helical systems, in particular multihelicences, to explore their CPL activity. We would also like to take the studies further to computationally explore excited-state properties and dynamics of self-assemblies of small molecules.

References

[1] D. Beljonne, Z. Shuai, J.-L. Brédas, M. Kauranen, T. Verbiest and A. Persoons, *J. Chem. Phys.*, 1998, **108**, 1301–1304.

[2] F. Lebon, G. Longhi, F. Gangemi, S. Abbate, J. Priess, M. Juza, C. Bazzini, T. Caronna and A. Mele, *J. Phys. Chem. A*, 2004, **108**, 11752–11761.

[3] Y. Shen and C.-F. Chen, *Chem. Rev.*, 2012, **112**, 1463–1535.

[4] Y. Nakai, T. Mori and Y. Inoue, *J. Phys. Chem. A*, 2012, **116**, 7372–7385.

[5] T. Caronna, R. Sinisi, M. Catellani, S. Luzzati and S. Abbate, *Synth. Met.*, 2001, **119**, 79–80.

[6] S. Abbate, C. Bazzini, T. Caronna, F. Fontana, F. Gangemi, F. Lebon, G. Longhi, A. Mele and I. N. Sora, *Inorganica Chimica Acta*, 2007, **360**, 908–912.

[7] H. Sakai, S. Shinto, J. Kumar, Y. Araki, T. Sakanoue, T. Takenobu, T. Wada, T. Kawai and T. Hasobe, *J. Phys. Chem. C*, 2015, **119**, 13937–13947.

[8] W. Hua, Z. Liu, L. Duan, G. Dong, Y. Qiu, B. Zhang, D. Cui, X. Tao, N. Cheng and Y. Liu, *RSC Adv.*, 2015, **5**, 75–84.

[9] S. Jhulki, A. K. Mishra, T. J. Chow and J. N. Moorthy, *New J. Chem.*, 2017, **41**, 14730–14737.

[10] T. Otani, A. Tsuyuki, T. Iwachi, S. Someya, K. Tateno, H. Kawai, T. Saito, K. S. Kanyiva and T. Shibata, *Angew. Chem. Int. Ed.*, 2017, **129**, 3964–3968.

[11] T. Otani, T. Sasayama, C. Iwashimizu, K. S. Kanyiva, H. Kawai and T. Shibata, *Chem. Commun.*, 2020, **56**, 4484–4487.

[12] J. Wang, Y. Wang, X. Xie, Y. Ren, B. Zhang, L. He, J. Zhang, L.-D. Wang and P. Wang, *ACS Energy Lett.*, 2021, **6**, 1764–1772.

[13] L. Fang, Y. Zhang, M. Ren, X. Xie, T. Li, Y. Yuan, J. Zhang and P. Wang, *Energy Environ. Sci.*, 2022, **15**, 1630–1637.

[14] N. Xu, Y. Li, D. Ricciarelli, J. Wang, E. Mosconi, Y. Yuan, F. De Angelis, S. M. Zakeeruddin, M. Grätzel and P. Wang, *Iscience*, 2019, **15**, 234–242.

[15] Q. Zhu, C. Kan, Y. Cao, Z. Tang, K. Xu, P. Hang, B. Li, Y. Yao, M. Lei and X. Yu, *Org. Lett.*, 2022, **24**, 7053–7057.

[16] Y.-S. Lin, S. Y. Abate, K.-W. Lai, C.-W. Chu, Y.-D. Lin, Y.-T. Tao and S.-S. Sun, *ACS Appl. Mater. Interfaces*, 2018, **10**, 41439–41449.

[17] J. Wang, H. Shi, N. Xu, J. Zhang, Y. Yuan, M. Lei, L. Wang and P. Wang, *Adv. Funct. Mater.*, 2020, **30**, 2002114.

[18] Y. Wei, A. Zheng, X. Xie, J. Zhang, L. He and P. Wang, *ACS Materials Lett.*, 2021, **3**, 947–955.

[19] Y.-S. Lin, S. Y. Abate, C.-I. Wang, Y.-S. Wen, C.-I. Chen, C.-P. Hsu, C.-C. Chueh, Y.-T. Tao and S.-S. Sun, *ACS Appl. Mater. Interfaces*, 2021, **13**, 20051–20059.

[20] Z.-Z. Sun, J. Yang, W.-L. Ding, J.-L. Liu and X.-L. Xu, *J. Phys. Chem. C*, 2022, **126**, 11529–11536.

[21] P. Aillard, A. Voituriez and A. Marinetti, *Dalton Trans.*, 2014, **43**, 15263–15278.

[22] M. J. Narcis and N. Takenaka, *Eur. J. Org. Chem.*, 2014, **2014**, 21–34.

[23] N. Takenaka, R. S. Sarangthem and B. Captain, *Angew. Chem. Int. Ed.*, 2008, **47**, 9708–9710.

[24] M. T. Reetz and S. Sostmann, *Tetrahedron*, 2001, **57**, 2515–2520.

[25] M. C. Heffern, L. M. Matosziuk and T. J. Meade, *Chem. Rev.*, 2014, **114**, 4496–4539.

[26] D.-Y. Kim, *J. Korean Phys. Soc.*, 2006, **49**, s505–s508.

[27] J. P. Riehl and F. S. Richardson, *Chem. Rev.*, 1986, **86**, 1–16.

[28] T. Mori, *Chem. Rev.*, 2021, **121**, 2373–2412.

[29] K. Dhbaibi, L. Favereau and J. Crassous, *Chem. Rev.*, 2019, **119**, 8846–8953.

[30] B. Langeveld-Voss, R. Janssen and E. Meijer, *J. Mol. Struct.*, 2000, **521**, 285–301.

[31] C. X. Cui and M. Kertesz, *Phys. Rev. B*, 1989, **40**, 9661–9670.

[32] M. Melucci, G. Barbarella, M. Gazzano, M. Cavallini, F. Biscarini, A. Bongini, F. Piccinelli, M. Monari, M. Bandini, A. Umani-Ronchi *et al.*, *Chem. Eur. J.*, 2006, **12**, 7304–7312.

[33] A. Mishra, C.-Q. Ma and P. Bauerle, *Chem. Rev.*, 2009, **109**, 1141–1276.

[34] R. Yang, K. M. Dalsin, D. F. Evans, L. Christensen and W. A. Hendrickson, *J. Phys. Chem.*, 1989, **93**, 511–512.

[35] R. Yang, D. F. Evans, L. Christensen and W. A. Hendrickson, *J. Phys. Chem.*, 1990, **94**, 6117–6122.

[36] G. Caple, B. L. Wheeler, R. Swift, T. L. Porter and S. Jeffers, *J. Phys. Chem.*, 1990, **94**, 5639–5641.

[37] J. D. Ripoll, A. Serna, D. Guerra and A. Restrepo, *J. Phys. Chem. A*, 2010, **114**, 10917–10921.

[38] J. C. Dobrowolski and M. E. Jamróz, *RSC Adv.*, 2018, **8**, 2116–2122.

[39] A. J. Varni, A. Fortney, M. A. Baker, J. C. Worch, Y. Qiu, D. Yaron, S. Bernhard, K. J. T. Noonan and T. Kowalewski, *J. Am. Chem. Soc.*, 2019, **141**, 8858–8867.

[40] O. Gidron and M. Bendikov, *Angew. Chem. Int. Ed.*, 2014, **53**, 2546–2555.

[41] O. Gidron, Y. Diskin-Posner and M. Bendikov, *J. Am. Chem. Soc.*, 2010, **132**, 2148–2150.

[42] S. Glenis, M. Benz, E. LeGoff, J. L. Schindler, C. R. Kannewurf and M. G. Kanatzidis, *J. Am. Chem. Soc.*, 1993, **115**, 12519–12525.

[43] C. S. Hartley, *Acc. Chem. Res.*, 2016, **49**, 646–654.

[44] S. M. Mathew, J. T. Engle, C. J. Ziegler and C. S. Hartley, *J. Am. Chem. Soc.*, 2013, **135**, 6714–6722.

[45] S. Mathew, L. A. Crandall, C. J. Ziegler and C. S. Hartley, *J. Am. Chem. Soc.*, 2014, **136**, 16666–16675.

[46] C. S. Hartley, *J. Org. Chem.*, 2011, **76**, 9188–9191.

[47] M. S. Newman and D. Lednicer, *J. Am. Chem. Soc.*, 1956, **78**, 4765–4770.

[48] K. Mori, T. Murase and M. Fujita, *Angew. Chem. Int. Ed.*, 2015, **54**, 6847–6851.

[49] F. Furche, R. Ahlrichs, C. Wachsmann, E. Weber, A. Sobanski, F. Vögtle and S. Grimme, *J. Am. Chem. Soc.*, 2000, **122**, 1717–1724.

[50] R. Suzuki, Y. Uziie, W. Fujiwara, H. Katagiri and T. Murase, *Chem. - Asian J.*, 2020, **15**, 1330–1338.

[51] Y. Nakai, T. Mori and Y. Inoue, *J. Phys. Chem. A*, 2013, **117**, 83–93.

[52] M. Jakubec, T. Beránek, P. Jakubík, J. Sýkora, J. Žádný, V. Církva and J. Storch, *J. Org. Chem.*, 2018, **83**, 3607–3616.

[53] Y. Yamamoto, H. Sakai, J. Yuasa, Y. Araki, T. Wada, T. Sakanoue, T. Takenobu, T. Kawai and T. Hasobe, *J. Phys. Chem. C*, 2016, **120**, 7421–7427.

[54] H. Kubo, T. Hirose and K. Matsuda, *Org. Lett.*, 2017, **19**, 1776–1779.

[55] V. Církva, P. Jakubík, T. Strašák, J. Hrbáč, J. Sýkora, I. Císařová, J. Vacek, J. Žádný and J. Storch, *J. Org. Chem.*, 2019, **84**, 1980–1993.

[56] C. Matsuda, Y. Suzuki, H. Katagiri and T. Murase, *Chem. - Asian J.*, 2021, **16**, 538–547.

[57] H. Kubo, T. Hirose, T. Nakashima, T. Kawai, J.-y. Hasegawa and K. Matsuda, *J. Phys. Chem. Lett.*, 2021, **12**, 686–695.

[58] H. Sakai, S. Shinto, Y. Araki, T. Wada, T. Sakanoue, T. Takenobu and T. Hasobe, *Chem. Eur. J.*, 2014, **20**, 10099–10109.

[59] H. Sakai, T. Kubota, J. Yuasa, Y. Araki, T. Sakanoue, T. Takenobu, T. Wada, T. Kawai and T. Hasobe, *J. Phys. Chem. C*, 2016, **120**, 7860–7869.

[60] B. Liu, M. Böckmann, W. Jiang, N. L. Doltsinis and Z. Wang, *J. Am. Chem. Soc.*, 2020, **142**, 7092–7099.

[61] A. K. Swain, K. Kolanji, C. Stapper and P. Ravat, *Org. Lett.*, 2021, **23**, 1339–1343.

[62] Z. Qiu, C.-W. Ju, L. Frédéric, Y. Hu, D. Schollmeyer, G. Pieters, K. Müllen and A. Narita, *J. Am. Chem. Soc.*, 2021, **143**, 4661–4667.

[63] Y. Nakakuki, T. Hirose and K. Matsuda, *Org. Lett.*, 2022, **24**, 648652.

[64] H. Oyama, M. Akiyama, K. Nakano, M. Naito, K. Nobusawa and K. Nozaki, *Org. Lett.*, 2016, **18**, 3654–3657.

[65] M. Jakubec, S. Hansen-Troøyen, I. Cisarova, J. Sykora and J. Storch, *Org. Lett.*, 2020, **23**, 3905–3910.

[66] F. Zhou, Z. Huang, Z. Huang, R. Cheng, Y. Yang and J. You, *Org. Lett.*, 2021, **23**, 4559–4563.

[67] H. Chang, H. Liu, E. Dmitrieva, Q. Chen, J. Ma, P. He, P. Liu, A. A. Popov, X.-Y. Cao, X.-Y. Wang, Y. Zou, A. Narita, K. Müllen, H. Peng and Y. Hu, *Chem. Commun.*, 2020, **56**, 15181–15184.

[68] J. Hong, X. Xiao, H. Liu, L. Fu, X.-C. Wang, L. Zhou, X.-Y. Wang, Z. Qiu, X.-Y. Cao, A. Narita, K. Müllen and Y. Hu, *Chem. Commun.*, 2021, **57**, 5566–5569.

[69] Y. Yamamoto, H. Sakai, J. Yuasa, Y. Araki, T. Wada, T. Sakanoue, T. Takenobu, T. Kawai and T. Hasobe, *Chem. Eur. J.*, 2016, **22**, 4263–4273.

[70] E. Clar, C. Ironside and M. Zander, *J. Chem. Soc.*, 1959, 142–147.

[71] J. Luo, X. Xu, R. Mao and Q. Miao, *J. Am. Chem. Soc.*, 2012, **134**, 13796–13803.

[72] H. Kashihara, T. Asada and K. Kamikawa, *Chem. Eur. J.*, 2015, **21**, 6523–6527.

[73] H. Bock, S. Huet, P. Dechambenoit, E. A. Hillard and F. Durola, *Eur. J. Org. Chem.*, 2015, **2015**, 1033–1039.

[74] A. Robert, P. Dechambenoit, E. A. Hillard, H. Bock and F. Durola, *Chem. Commun.*, 2017, **53**, 11540–11543.

[75] G. M. Upadhyay and A. V. Bedekar, *Tetrahedron*, 2015, **71**, 5644–5649.

[76] W. Laarhoven and T. J. Cuppen, *Tetrahedron Lett.*, 1971, **12**, 163–164.

[77] W. Laarhoven and T. H. Cuppen, *Recl. Trav. Chim. Pays-Bas.*, 1973, **92**, 553–562.

[78] R. Martin, C. Eyndels and N. Defay, *Tetrahedron*, 1974, **30**, 3339–3342.

[79] W. Marsh and J. D. Dunitz, *Bull. Soc. Chim. Belg.*, 1979, **88**, 847–852.

[80] W. Laarhoven and M. De Jong, *Recl. Trav. Chim. Pays-Bas.*, 1973, **92**, 651–657.

[81] H. Tanaka, M. Ikenosako, Y. Kato, M. Fujiki, Y. Inoue and T. Mori, *Commun. Chem.*, 2018, **1**, 38.

[82] K. Nakamura, S. Furumi, M. Takeuchi, T. Shibuya and K. Tanaka, *J. Am. Chem. Soc.*, 2014, **136**, 5555–5558.

[83] D. Peña, A. Cobas, D. Pérez, E. Guitián and L. Castedo, *Org. Lett.*, 2003, **5**, 1863–1866.

[84] M. Yanney, F. R. Fronczek, W. P. Henry, D. J. Beard and A. Sygula, *Cyclotrimerization of corannulyne: steric hindrance tunes the inversion barriers of corannulene bowls*, 2011.

[85] T. Fujikawa, Y. Segawa and K. Itami, *J. Am. Chem. Soc.*, 2015, **137**, 7763–7768.

[86] Y. Zhu, Z. Xia, Z. Cai, Z. Yuan, N. Jiang, T. Li, Y. Wang, X. Guo, Z. Li, S. Ma *et al.*, *J. Am. Chem. Soc.*, 2018, **140**, 4222–4226.

[87] Y. Wang, Z. Yin, Y. Zhu, J. Gu, Y. Li and J. Wang, *Angew. Chem. Int. Ed.*, 2019, **58**, 587–591.

[88] Y. Hu, G. M. Paternò, X.-Y. Wang, X.-C. Wang, M. Guizzardi, Q. Chen, D. Schollmeyer, X.-Y. Cao, G. Cerullo, F. Scotognella *et al.*, *J. Am. Chem. Soc.*, 2019, **141**, 12797–12803.

[89] Y.-F. Wu, S.-W. Ying, L.-Y. Su, J.-J. Du, L. Zhang, B.-W. Chen, H.-R. Tian, H. Xu, M.-L. Zhang, X. Yan, Q. Zhang, S.-Y. Xie and L.-S. Zheng, *J. Am. Chem. Soc.*, 2022, **144**, 10736–10742.

[90] N. P. Hacker, J. F. McOmie, J. Meunier-Piret and M. Van Meerssche, *J. Chem. Soc., Perkin Trans. 1*, 1982, 19–23.

[91] L. Barnett, D. M. Ho, K. K. Baldridge and R. A. Pascal, *J. Am. Chem. Soc.*, 1999, **121**, 727–733.

[92] D. Pena, D. Pérez, E. Guitián and L. Castedo, *Org. Lett.*, 1999, **1**, 1555–1557.

[93] M. A. Bennett, M. R. Kopp, E. Wenger and A. C. Willis, *J. Organomet. chem.*, 2003, **667**, 8–15.

[94] H. Saito, A. Uchida and S. Watanabe, *J. Org. Chem.*, 2017, **82**, 5663–5668.

[95] D. Meng, H. Fu, C. Xiao, X. Meng, T. Winands, W. Ma, W. Wei, B. Fan, L. Huo, N. L. Doltsinis *et al.*, *J. Am. Chem. Soc.*, 2016, **138**, 10184–10190.

[96] Z. Ma, T. Winands, N. Liang, D. Meng, W. Jiang, N. L. Doltsinis and Z. Wang, *Sci. China Chem.*, 2020, **63**, 208–214.

[97] H. Arslan, F. J. Uribe-Romo, B. J. Smith and W. R. Dichtel, *Chem. Sci.*, 2013, **4**, 3973–3978.

[98] T. Fujikawa, Y. Segawa and K. Itami, *J. Am. Chem. Soc.*, 2016, **138**, 3587–3595.

[99] L. Wang, Y. Han, J. Zhang, X. Li, X. Liu and J. Xiao, *Org. Lett.*, 2019, **22**, 261–264.

[100] K. Kato, Y. Segawa, L. T. Scott and K. Itami, *Angew. Chem. Int. Ed.*, 2018, **130**, 1337–1341.

[101] H.-A. Lin, K. Kato, Y. Segawa, L. T. Scott and K. Itami, *Chem. Sci.*, 2019, **10**, 2326–2330.

[102] K. Kise, S. Ooi, H. Saito, H. Yorimitsu, A. Osuka and T. Tanaka, *Angew. Chem. Int. Ed.*, 2021, **61**, e202112589(1–9).

[103] T. Hosokawa, Y. Takahashi, T. Matsushima, S. Watanabe, S. Kikkawa, I. Azumaya, A. Tsurusaki and K. Kamikawa, *J. Am. Chem. Soc.*, 2017, **139**, 18512–18521.

[104] V. Berezhnaia, M. Roy, N. Vanthuyne, M. Villa, J.-V. Naubron, J. Rodriguez, Y. Coquerel and M. Gingras, *J. Am. Chem. Soc.*, 2017, **139**, 18508–18511.

[105] G. Naulet, L. Sturm, A. Robert, P. Dechambenoit, F. Röhricht, R. Herges, H. Bock and F. Durola, *Chem. Sci.*, 2018, **9**, 8930–8936.

[106] A. U. Malik, F. Gan, C. Shen, N. Yu, R. Wang, J. Crassous, M. Shu and H. Qiu, *J. Am. Chem. Soc.*, 2018, **140**, 2769–2772.

[107] X. Jiang, J. D. Laffoon, D. Chen, S. Pérez-Estrada, A. S. Danis, J. Rodréguez-López, M. A. Garcia-Garibay, J. Zhu and J. S. Moore, *J. Am. Chem. Soc.*, 2020, **142**, 6493–6498.

[108] J. Birks, D. Birch, E. Cordemans and E. V. Donckt, *Chem. Phys. Lett.*, 1976, **43**, 33–36.

[109] M. Sapir and E. Donckt, *Chem. Phys. Lett.*, 1975, **36**, 108–110.

[110] H. Tanaka, Y. Kato, M. Fujiki, Y. Inoue and T. Mori, *J. Phys. Chem. A*, 2018, **122**, 7378–7384.

[111] T. Yanagi, T. Tanaka and H. Yorimitsu, *Chem. Sci.*, 2021, **12**, 2784–2793.

[112] T. Otani, T. Sasayama, M. Horiuchi, S. Okauchi, H. Kawai, M. Kitahara, Y. Imai and T. Shibata, *Helv. Chim. Acta*, 2021, **104**, e2100016.

[113] A. Szabo and N. S. Ostlund, *Modern quantum chemistry: introduction to advanced electronic structure theory*, Courier Corporation, 2012.

[114] D. R. Hartree, Mathematical Proceedings of the Cambridge Philosophical Society, 1928, pp. 89–110.

[115] W. E. F. Pauli, *Z. Phys.*, 1925, **31**, 765.

[116] V. Fock, *Z. Phys.*, 1930, **61**, 126–148.

[117] C. Møller and M. S. Plesset, *Physical review*, 1934, **46**, 618–622.

[118] J. Čížek, *J. Chem. Phys.*, 1966, **45**, 4256–4266.

[119] T. D. Crawford and H. F. Schaefer III, *Rev. Comput. Chem.*, 2000, **14**, 33.

[120] B. O. Roos, P. R. Taylor and P. E. Sigbahn, *Chem. Phys.*, 1980, **48**, 157–173.

[121] K. Andersson, P. A. Malmqvist, B. O. Roos, A. J. Sadlej and K. Wolinski, *J. Phys. Chem.*, 1990, **94**, 5483–5488.

[122] P. E. Siegbahn, J. Almlöf, A. Heiberg and B. O. Roos, *J. Phys. Chem.*, 1981, **74**, 2384–2396.

[123] L. Brillouin, *J. Phys. Radium*, 1932, **3**, 373–389.

[124] L. Piela, in *Ideas of Quantum Chemistry (Second Edition)*, Elsevier, Oxford, Second Edition edn., 2014, pp. e109–e120.

[125] S. Grimme, *J. Chem. Phys.*, 2003, **118**, 9095–9102.

[126] T. Schwabe and S. Grimme, *Acc. Chem. Res.*, 2008, **41**, 569–579.

[127] S. Grimme, L. Goerigk and R. F. Fink, *WIREs Comput. Mol. Sci.*, 2012, **2**, 886–906.

[128] W. Kohn and L. J. Sham, *Phys. Rev.*, 1965, **140**, A1133–A1138.

[129] J. P. Perdew and K. Schmidt, AIP Conf. Proc., 2001, pp. 1–20.

[130] J. P. Perdew, A. Ruzsinszky, J. Tao, V. N. Staroverov, G. E. Scuseria and G. I. Csonka, *J. Chem. Phys.*, 2005, **123**, 062201.

[131] J. Tao, J. P. Perdew, V. N. Staroverov and G. E. Scuseria, *Phys. Rev. Lett.*, 2003, **91**, 146401.

[132] A. D. Becke, *Phys. Rev. A*, 1988, **38**, 3098.

[133] C. Lee, W. Yang and R. G. Parr, *Phys. Rev. B*, 1988, **37**, 785–789.

[134] J. P. Perdew and Y. Wang, *Phys. Rev. B*, 1992, **45**, 13244–13249.

[135] J. P. Perdew, K. Burke and M. Ernzerhof, *Phys. Rev. Lett.*, 1996, **77**, 3865–3868.

[136] C. Adamo and V. Barone, *J. Chem. Phys.*, 1999, **110**, 6158–6170.

[137] A. V. Krukau, O. A. Vydrov, A. F. Izmaylov and G. E. Scuseria, *J. Chem. Phys.*, 2006, **125**, 224106.

[138] A. J. Cohen and N. C. Handy, *Mol. Phys.*, 2001, **99**, 607–615.

[139] T. Leininger, H. Stoll, H.-J. Werner and A. Savin, *Chem. Phys. Lett.*, 1997, **275**, 151–160.

[140] R. D. Adamson, J. P. Dombroski and P. M. Gill, *J. Comput. Chem.*, 1999, **20**, 921–927.

[141] T. Yanai, D. P. Tew and N. C. Handy, *Chem. Phys. Lett.*, 2004, **393**, 51–57.

[142] S. Grimme, *J. Comput. Chem.*, 2004, **25**, 1463–1473.

[143] S. Grimme, *J. Comput. Chem.*, 2006, **27**, 1787–1799.

[144] J.-D. Chai and M. Head-Gordon, *Phys. Chem. Chem. Phys.*, 2008, **10**, 6615–6620.

[145] Q. Wu and W. Yang, *J. Chem. Phys.*, 2002, **116**, 515–524.

[146] S. Grimme, J. Antony, S. Ehrlich and H. Krieg, *J. Chem. Phys.*, 2010, **132**, 154104.

[147] S. Grimme, J. Antony, S. Ehrlich and H. Krieg, *J. Chem. Phys.*, 2010, **132**, 154104.

[148] S. Grimme, *WIREs Comput. Mol. Sci.*, 2011, **1**, 211–228.

[149] E. Runge and E. K. U. Gross, *Phys. Rev. Lett.*, 1984, **52**, 997–1000.

[150] M. A. Marques and E. K. Gross, *Annu. Rev. Phys. Chem.*, 2004, **55**, 427–455.

[151] M. A. Marques and E. K. Gross, *Time-dependent density functional theory*, Springer, 2003, pp. 144–184.

[152] J. Schirmer, *Phys. Rev. A*, 1982, **26**, 2395–2416.

[153] A. B. Trofimov and J. Schirmer, *J. Phys. B: At., Mol. Opt. Phys.*, 1995, **28**, 2299–2324.

[154] A. B. Trofimov, G. Stelter and J. Schirmer, *J. Chem. Phys.*, 1999, **111**, 9982–9999.

[155] J. Schirmer and A. B. Trofimov, *J. Chem. Phys.*, 2004, **120**, 11449–11464.

[156] A. Trofimov, I. Krivdina, J. Weller and J. Schirmer, *Chem. Phys.*, 2006, **329**, 1–10.

[157] A. Dreuw and M. Wormit, *WIREs Comput. Mol. Sci.*, 2015, **5**, 82–95.

[158] S. Bureekaew, J. ya Hasegawa and H. Nakatsuji, *Chem. Phys. Lett.*, 2006, **425**, 367–371.

[159] T. Miyahara and H. Nakatsuji, *J. Phys. Chem. A*, 2013, **117**, 14065–14074.

[160] I. Warnke and F. Furche, *WIREs Computational Molecular Science*, 2011, **2**, 150–166.

[161] F. S. Richardson and J. P. Riehl, *Chem. Rev.*, 1977, **77**, 773–792.

[162] F. Plasser and H. Lischka, *J. Chem. Theory Comput.*, 2012, **8**, 2777–2789.

[163] F. Plasser, M. Wormit and A. Dreuw, *J. Chem. Phys.*, 2014, **141**, 024106.

[164] A. Luzanov and O. Zhikol, *Int. J. Quantum Chem.*, 2010, **110**, 902–924.

[165] S. A. Mewes, J.-M. Mewes, A. Dreuw and F. Plasser, *Phys. Chem. Chem. Phys.*, 2016, **18**, 2548–2563.

[166] F. Plasser, *J. Chem. Phys.*, 2016, **144**, 194107.

[167] M. E. CASIDA, in *Recent Advances in Density Functional Methods*, WORLD SCIENTIFIC, 1995, pp. 155–192.

[168] E. Tapavicza, I. Tavernelli, U. Rothlisberger, C. Filippi and M. E. Casida, *J. Chem. Phys.*, 2008, **129**, 124108.

[169] B. G. Levine, C. Ko, J. Quenneville and T. J. MartÍnez, *Mol. Phys.*, 2006, **104**, 1039–1051.

[170] P. Elliott, S. Goldson, C. Canahui and N. T. Maitra, *Chem. Phys.*, 2011, **391**, 110 – 119.

[171] D. J. Tozer, *J. Chem. Phys.*, 2003, **119**, 12697–12699.

[172] N. T. Maitra, F. Zhang, R. J. Cave and K. Burke, *J. Chem. Phys.*, 2004, **120**, 5932–5937.

[173] R. J. Cave, F. Zhang, N. T. Maitra and K. Burke, *Chem. Phys. Lett.*, 2004, **389**, 39–42.

[174] A. Dreuw, J. L. Weisman and M. Head-Gordon, *J. Chem. Phys.*, 2003, **119**, 2943–2946.

[175] A. Dreuw and M. Head-Gordon, *J. Am. Chem. Soc.*, 2004, **126**, 4007–4016.

[176] R. J. Magyar and S. Tretiak, *J. Chem. Theory Comput.*, 2007, **3**, 976–987.

[177] T. A. Niehaus, T. Hofbeck and H. Yersin, *RSC Adv.*, 2015, **5**, 63318–63329.

[178] C. M. Isborn, B. D. Mar, B. F. E. Curchod, I. Tavernelli and T. J. Martínez, *J. Phys. Chem. B*, 2013, **117**, 12189–12201.

[179] J. J. Eriksen, S. P. Sauer, K. V. Mikkelsen, O. Christiansen, H. J. A. Jensen and J. Kongsted, *Mol. Phys.*, 2013, **111**, 1235–1248.

[180] S. Kümmel, *Adv. Ener. Mat.*, 2017, **7**, 1700440.

[181] Z.-L. Cai, K. Sendt and J. R. Reimers, *J. Chem. Phys.*, 2002, **117**, 5543–5549.

[182] S. Grimme and M. Parac, *Chem. Phys. Chem.*, 2003, **4**, 292–295.

[183] Y.-L. Wang and G.-S. Wu, *Int. J. Quantum Chem.*, 2007, **108**, 430–439.

[184] K. I. Igumenshchev, S. Tretiak and V. Y. Chernyak, *J. Chem. Phys.*, 2007, **127**, 114902.

[185] B. M. Wong and T. H. Hsieh, *J. Chem. Theory Comput.*, 2010, **6**, 3704–3712.

[186] R. M. Richard and J. M. Herbert, *J. Chem. Theory Comput.*, 2011, **7**, 1296–1306.

[187] N. Kuritz, T. Stein, R. Baer and L. Kronik, *J. Chem. Theory Comput.*, 2011, **7**, 2408–2415.

[188] S. A. Mewes, F. Plasser and A. Dreuw, *J. Chem. Phys.*, 2017, **8**, 1205–1210.

[189] O. Christiansen, H. Koch and P. Jørgensen, *Chem. Phys. Lett.*, 1995, **243**, 409–418.

[190] P. H. P. Harbach, M. Wormit and A. Dreuw, *J. Chem. Phys.*, 2014, **141**, 064113.

[191] H. Nakatsuji and K. Hirao, *J. Chem. Phys.*, 1978, **68**, 2053–2065.

[192] M. Ehara, J. Hasegawa and H. Nakatsuji, in *Theory and Applications of Computational Chemistry*, Elsevier, 2005, pp. 1099–1141.

[193] H. Nakatsuji, in *Computational Chemistry: Reviews of Current Trends*, WORLD SCIENTIFIC, 1997, pp. 62–124.

[194] H. Sahu, S. Gupta, P. Gaur and A. N. Panda, *Phys. Chem. Chem. Phys.*, 2015, **17**, 20647–20657.

[195] H. Sahu, R. Shukla, J. Goswami, P. Gaur and A. N. Panda, *Chem. Phys. Lett.*, 2018, **692**, 152 – 159.

[196] K. Watanabe and K. Akagi, *Sci. Technol. Adv. Mater.*, 2014, **15**, 044203.

[197] K. Watanabe, K. Suda and K. Akagi, *J. Mater. Chem. C*, 2013, **1**, 2797–2805.

[198] E. Yashima, N. Ousaka, D. Taura, K. Shimomura, T. Ikai and K. Maeda, *Chem. Rev.*, 2016, **116**, 13752–13990.

[199] E. Schwartz, M. Koepf, H. J. Kitto, R. J. M. Nolte and A. E. Rowan, *Polym. Chem.*, 2011, **2**, 33–47.

[200] T. Ikai, K. Takayama, Y. Wada, S. Minami, C. Apiboon and K. ichi Shinohara, *Chem. Sci.*, 2019, **10**, 4890–4895.

[201] B. Li, S. Zhang, L. Li, Z. Ma, C. Li, L. Xu and H. Wang, *ACS Omega*, 2018, **3**, 16014–16020.

[202] H. Wynberg, T. J. V. Bergen and R. M. Kellogg, *J. Org. Chem.*, 1969, **34**, 3175–3178.

[203] K. Tamao, S. Kodama, I. Nakajima, M. Kumada, A. Minato and K. Suzuki, *Tetrahedron*, 1982, **38**, 3347–3354.

[204] Z.-H. Zhou, T. Maruyama, T. Kanbara, T. Ikeda, K. Ichimura, T. Yamamoto and K. Tokuda, *J. Chem. Soc., Chem. Commun.*, 1991, 1210–1212.

[205] T. Yamamoto, M. Shimura, K. Osakada and K. Kubota, *Chem. Lett.*, 1992, **21**, 1003–1004.

[206] T. Yamamoto, Z.-H. Zhou, T. Maruyama and T. Kanbara, *Syn. Metals*, 1993, **55**, 1209–1213.

[207] T. Yamamoto, Z. hua Zhou, T. Kanbara, M. Shimura, K. Kizu, T. Maruyama, Y. Nakamura, T. Fukuda, B.-L. Lee, N. Ooba, S. Tomaru, T. Kurihara, T. Kaino, K. Kubota and S. Sasaki, *J. Am. Chem. Soc.*, 1996, **118**, 10389–10399.

[208] I. H. Jenkins, U. Salzner and P. G. Pickup, *Chem. Mater.*, 1996, **8**, 2444–2450.

[209] S. V. Rocha and N. S. Finney, *Org. Lett.*, 2010, **12**, 2598–2601.

[210] S. V. Rocha and N. S. Finney, *J. Org. Chem.*, 2013, **78**, 11255–11261.

[211] F. Weigend and R. Ahlrichs, *Phys. Chem. Chem. Phys.*, 2005, **7**, 3297–3305.

[212] R. A. Kendall, T. H. Dunning Jr and R. J. Harrison, *J. Chem. Phys.*, 1992, **96**, 6796–6806.

[213] T. H. Dunning Jr, *J. Chem. Phys.*, 1989, **90**, 1007–1023.

[214] *TURBOMOLE V7.1 2016, a development of University of Karlsruhe and Forschungszentrum Karlsruhe GmbH, 1989-2007, TURBOMOLE GmbH, since 2007; available from* `http://www.turbomole.com`.

[215] C. Hä and F. Weigend, *J. Chem. Phys.*, 2000, **113**, 5154.

[216] C. Hättig, *J. Chem. Phys.*, 2003, **118**, 7751–7761.

[217] C. Hättig, in *Response Theory and Molecular Properties (A Tribute to Jan Linderberg and Poul Jørgensen)*, Elsevier, 2005, pp. 37–60.

[218] M. J. Frisch, G. W. Trucks, H. B. Schlegel, G. E. Scuseria, M. A. Robb, J. R. Cheeseman, G. Scalmani, V. Barone, B. Mennucci, G. A. Petersson, H. Nakatsuji, M. Caricato, X. Li, H. P. Hratchian, A. F. Izmaylov, J. Bloino, G. Zheng, J. L.

Sonnenberg, M. Hada, M. Ehara, K. Toyota, R. Fukuda, J. Hasegawa, M. Ishida, T. Nakajima, Y. Honda, O. Kitao, H. Nakai, T. Vreven, J. A. Montgomery, Jr., J. E. Peralta, F. Ogliaro, M. Bearpark, J. J. Heyd, E. Brothers, K. N. Kudin, V. N. Staroverov, R. Kobayashi, J. Normand, K. Raghavachari, A. Rendell, J. C. Burant, S. S. Iyengar, J. Tomasi, M. Cossi, N. Rega, J. M. Millam, M. Klene, J. E. Knox, J. B. Cross, V. Bakken, C. Adamo, J. Jaramillo, R. Gomperts, R. E. Stratmann, O. Yazyev, A. J. Austin, R. Cammi, C. Pomelli, J. W. Ochterski, R. L. Martin, K. Morokuma, V. G. Zakrzewski, G. A. Voth, P. Salvador, J. J. Dannenberg, S. Dapprich, A. D. Daniels, O. Farkas, J. B. Foresman, J. V. Ortiz, J. Cioslowski and D. J. Fox, *Gaussian 09 Revision D.01*, Gaussian Inc. Wallingford CT 2009.

[219] A. D. Becke, *Phys. Rev. A*, 1988, **38**, 3098–3100.

[220] C. Lee, W. Yang and R. G. Parr, *Physical review B*, 1988, **37**, 785.

[221] B. Miehlich, A. Savin, H. Stoll and H. Preuss, *Chem. Phys. Lett.*, 1989, **157**, 200–206.

[222] J. C. Slater, *Phys. Rev.*, 1951, **81**, 385.

[223] S. H. Vosko, L. Wilk and M. Nusair, *Can. J. Phys.*, 1980, **58**, 1200–1211.

[224] J. P. Perdew, K. Burke and M. Ernzerhof, *Phys. Rev. Lett.*, 1996, **77**, 3865.

[225] J. P. Perdew, K. Burke and M. Ernzerhof, *Phys. Rev. Lett.*, 1997, **78**, 1396–1396.

[226] N. C. Handy and A. J. Cohen, *Molecular Physics*, 2001, **99**, 403–412.

[227] J. Tao, J. P. Perdew, V. N. Staroverov and G. E. Scuseria, *Phys. Rev. Lett.*, 2003, **91**, 146401.

[228] H. Iikura, T. Tsuneda, T. Yanai and K. Hirao, *J. Chem. Phys.*, 2001, **115**, 3540–3544.

[229] A. D. Becke, *J. Chem. Phys.*, 1993, **98**, 5648–5652.

[230] C. Adamo and V. Barone, *J. Chem. Phys.*, 1999, **110**, 6158–6170.

[231] J.-D. Chai and M. Head-Gordon, *J. Chem. Phys.*, 2008, **128**, 084106.

[232] Y. Zhao and D. G. Truhlar, *Theor. Chem. Acc.*, 2008, **120**, 215–241.

[233] A. R. Allouche, *J. Comput. Chem.*, 2011, **32**, 174–182.

[234] F. Plasser, *A Package for Theoretical Density, Orbital Relaxation, and Exciton Analysis, http://theodore-qc.sourceforge.net/contact.html.*

[235] S. A. Mewes, F. Plasser, A. Krylov and A. Dreuw, *J. Chem. Theory Comput.*, 2018, **14**, 710–725.

[236] A. N. Panda, F. Plasser, A. J. A. Aquino, I. Burghardt and H. Lischka, *J. Phys. Chem. A*, 2013, **117**, 2181–2189.

[237] F. Plasser, S. A. Bäppler, M. Wormit and A. Dreuw, *J. Chem. Phys.*, 2014, **141**, 024107.

[238] S. A. Bäppler, F. Plasser, M. Wormit and A. Dreuw, *Phys. Rev. A*, 2014, **90**, 052521.

[239] S. A. Mewes and A. Dreuw, *Phys. Chem. Chem. Phys.*, 2019, **21**, 2843–2856.

[240] M. Kasha, *Discuss. Faraday Soc.*, 1950, **9**, 14–19.

[241] A. V. Gulevskaya, E. A. Shvydkova and D. I. Tonkoglazova, *Chem. Eur. J.*, 2018, **2018**, 5030–5043.

[242] M. Jakubec and J. Storch, *J. Org. Chem.*, 2020, **85**, 13415–13428.

[243] D. I. Tonkoglazova, A. V. Gulevskaya, K. A. Chistyakov and O. I. Askalepova, *Beilstein J. Org. Chem.*, 2021, **17**, 11–21.

[244] A. V. Gulevskaya, D. I. Tonkoglazova, A. S. Guchunov and A. D. Misharev, *Eur. J. Org. Chem.*, 2019, **2019**, 4879–4890.

[245] Y. Nakakuki, T. Hirose and K. Matsuda, *J. Am. Chem. Soc.*, 2018, **140**, 15461–15469.

[246] T. Otani, A. Tsuyuki, T. Iwachi, S. Someya, K. Tateno, H. Kawai, T. Saito, K. S. Kanyiva and T. Shibata, *Angew. Chem. Int. Ed.*, 2017, **56**, 3906–3910.

[247] F. Saal, F. Zhang, M. Holzapfel, M. Stolte, E. Michail, M. Moos, A. Schmiedel, A.-M. Krause, C. Lambert, F. Würthner and P. Ravat, *J. Am. Chem. Soc.*, 2020, **142**, 21298–21303.

[248] J. L. Greenfield, J. Wade, J. R. Brandt, X. Shi, T. J. Penfold and M. J. Fuchter, *Chemical Science*, 2021, **12**, 8589–8602.

[249] C. Adamo and V. Barone, *J. Chem. Phys.*, 1999, **110**, 6158–6170.

[250] Y. Zhao and D. G. Truhlar, *Theor. Chem. Acc.*, 2008, **120**, 215–241.

[251] P. Elliott, S. Goldson, C. Canahui and N. T. Maitra, *Chem. Phys.*, 2011, **391**, 110 – 119.

[252] D. J. Tozer, *J. Chem. Phys.*, 2003, **119**, 12697–12699.

[253] J.-W. Song, S. Tokura, T. Sato, M. A. Watson and K. Hirao, *J. Chem. Phys.*, 2007, **127**, 154109.

[254] T. Stein, L. Kronik and R. Baer, *J. Am. Chem. Soc.*, 2009, **131**, 2818–2820.

[255] T. Körzdörfer, J. S. Sears, C. Sutton and J.-L. Brédas, *J. Chem. Phys.*, 2011, **135**, 204107.

[256] H. Li, R. Nieman, A. J. A. Aquino, H. Lischka and S. Tretiak, *J. Chem. Theory Comput.*, 2014, **10**, 3280–3289.

[257] I. Borges Jr, E. Uhl, L. Modesto-Costa, A. J. Aquino and H. Lischka, *J. Phys. Chem. C*, 2016, **120**, 21818–21826.

[258] B. Mahato and A. N. Panda, *J. Phys. Chem. A*, 2020, **125**, 115–125.

[259] J. Tomasi, B. Mennucci and R. Cammi, *Chem. Res.*, 2005, **105**, 2999–3094.

[260] A. Klamt and G. Schüürmann, *J. Chem. Soc., Perkin Trans. 2*, 1993, 799–805.

[261] A. Schäfer, A. Klamt, D. Sattel, J. C. Lohrenz and F. Eckert, *Phys. Chem. Chem. Phys.*, 2000, **2**, 2187–2193.

[262] M. J. Frisch, G. W. Trucks, H. B. Schlegel, G. E. Scuseria, M. A. Robb, J. R. Cheeseman, G. Scalmani, V. Barone, G. A. Petersson, H. Nakatsuji, X. Li, M. Caricato, A. V. Marenich, J. Bloino, B. G. Janesko, R. Gomperts, B. Mennucci, H. P. Hratchian, J. V. Ortiz, A. F. Izmaylov, J. L. Sonnenberg, D. Williams-Young, F. Ding, F. Lipparini, F. Egidi, J. Goings, B. Peng, A. Petrone, T. Henderson, D. Ranasinghe, V. G. Zakrzewski, J. Gao, N. Rega, G. Zheng, W. Liang, M. Hada, M. Ehara, K. Toyota, R. Fukuda, J. Hasegawa, M. Ishida, T. Nakajima, Y. Honda, O. Kitao, H. Nakai, T. Vreven, K. Throssell, J. A. Montgomery, Jr., J. E. Peralta, F. Ogliaro, M. J. Bearpark, J. J. Heyd, E. N. Brothers, K. N. Kudin, V. N. Staroverov, T. A. Keith, R. Kobayashi, J. Normand, K. Raghavachari, A. P. Rendell, J. C. Burant, S. S. Iyengar, J. Tomasi, M. Cossi, J. M. Millam, M. Klene, C. Adamo, R. Cammi, J. W. Ochterski, R. L. Martin, K. Morokuma, O. Farkas, J. B. Foresman and D. J. Fox, *Gaussian˜16 Revision C.01*, 2016, Gaussian Inc. Wallingford CT.

[263] T. Lu and F. Chen, *J. Comput. Chem.*, 2011, **33**, 580–592.

[264] F. Plasser, *J. Chem. Phys.*, 2020, **152**, 084108.

[265] F. Plasser, *TheoDORE: a package for theoretical density, orbital relaxation, and exciton analysis*, 2017.

[266] G. Longhi, E. Castiglioni, C. Villani, R. Sabia, S. Menichetti, C. Viglianisi, F. Devlin and S. Abbate, *J. Photochem. Photobiol., A*, 2016, **331**, 138–145.

[267] T. Benincori, G. Appoloni, P. R. Mussini, S. Arnaboldi, R. Cirilli, E. Quartapelle Procopio, M. Panigati, S. Abbate, G. Mazzeo and G. Longhi, *Chem. Eur. J.*, 2018, **24**, 11082–11093.

[268] O. Lehtonen, D. Sundholm and T. Vänskä, *Phys. Chem. Chem. Phys.*, 2008, **10**, 4535–4550.

[269] T. Hirose, Y. Tsunoi, Y. Fujimori and K. Matsuda, *Chem. Eur. J.*, 2015, **21**, 1637–1644.

[270] M. Gingras, *Chem. Soc. Rev.*, 2013, **42**, 1051–1095.

[271] S. Abbate, F. Lebon, G. Longhi, F. Fontana, T. Caronna and D. A. Lightner, *Phys. Chem. Chem. Phys.*, 2009, **11**, 9039–9043.

[272] T. Freese, P. G. Jones and D. B. Werz, *Org. Lett.*, 2022, **24**, 1367–1371.

[273] P. Ravat, R. Hinkelmann, D. Steinebrunner, A. Prescimone, I. Bodoky and M. Juríček, *Org. Lett.*, 2017, **19**, 3707–3710.

[274] Z. Li and R. J. Twieg, *Chem. Eur. J.*, 2015, **21**, 15534–15539.

[275] M. Dračínskỳ, J. Storch, V. Církva, I. Císařová and J. Sỳkora, *Phys. Chem. Chem. Phys.*, 2017, **19**, 2900–2907.

[276] S. Grimme, *J. Chem. Phys.*, 2003, **118**, 9095–9102.

[277] R. A. Bachorz, F. A. Bischoff, S. Höfener, W. Klopper, P. Ottiger, R. Leist, J. A. Frey and S. Leutwyler, *Phys. Chem. Chem. Phys.*, 2008, **10**, 2758–2766.

[278] J. Grant Hill, J. A. Platts and H.-J. Werner, *Phys. Chem. Chem. Phys.*, 2006, **8**, 4072–4078.

[279] M. Piacenza and S. Grimme, *Chem. Phys. Chem.*, 2005, **6**, 1554–1558.

[280] M. Gerenkamp and S. Grimme, *Chem. Phys. Lett.*, 2004, **392**, 229–235.

[281] H. Tanaka, M. Ikenosako, Y. Kato, M. Fujiki, Y. Inoue and T. Mori, *Commun. Chem.*, 2018, **1**, 1–8.

[282] S. Fujino, M. Yamaji, H. Okamoto, T. Mutai, I. Yoshikawa, H. Houjou and F. Tani, *Photochem. Photobiol. Sci.*, 2017, **16**, 925–934.

[283] M. J. Fuchter, M. Weimar, X. Yang, D. K. Judge and A. J. White, *Tetrahedron Letters*, 2012, **53**, 1108–1111.

[284] C. Shen, G. Zhang, Y. Ding, N. Yang, F. Gan, J. Crassous and H. Qiu, *Nat. Commun.*, 2021, **12**, 1–8.

[285] M. Van Meerssche, J.-P. Declercq and B. Soubrier-Payen, *Bulletin des Societes Chimiques Belges,*, 1986, **95**, 609–618.

[286] T. Murase, C. Matsuda, K. Adachi, T. Sawada and M. Fujita, *Commun. Chem.*, 2018, **1**, 1–6.

Appendices

Appendix A

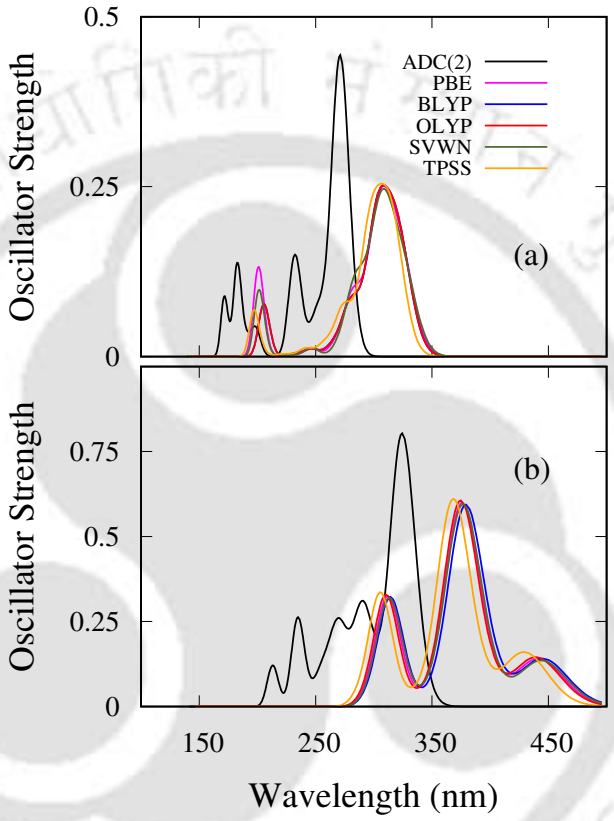

FIGURE A1: Absorption spectra of $(\mathbf{PT})_1$(a) and $(\mathbf{PT})_2$(b). Results obtained using RI-ADC(2) and various pure functionals are shown.

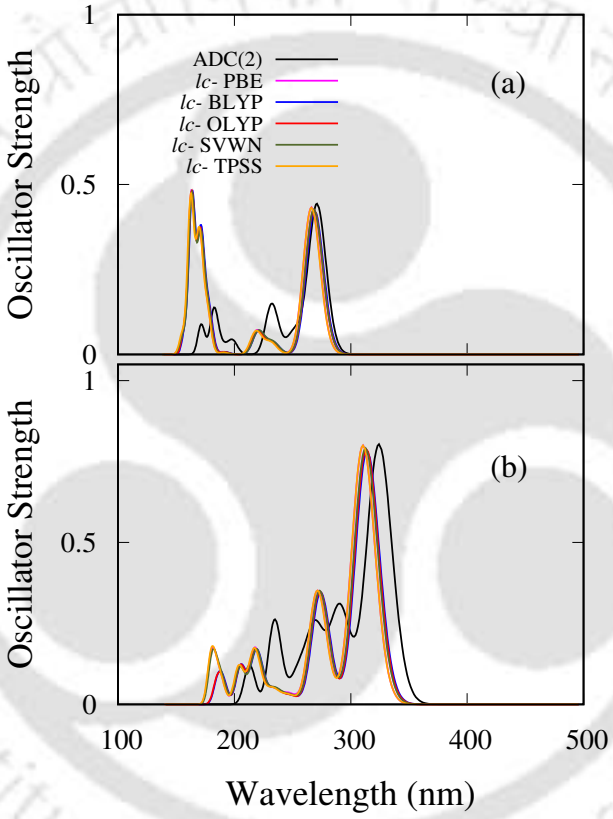

FIGURE A2: Absorption spectra of $\mathbf{(PT)}_1$(a) and $\mathbf{(PT)}_2$(b). Results obtained using RI-ADC(2) and various long-range corrected pure functionals are shown.

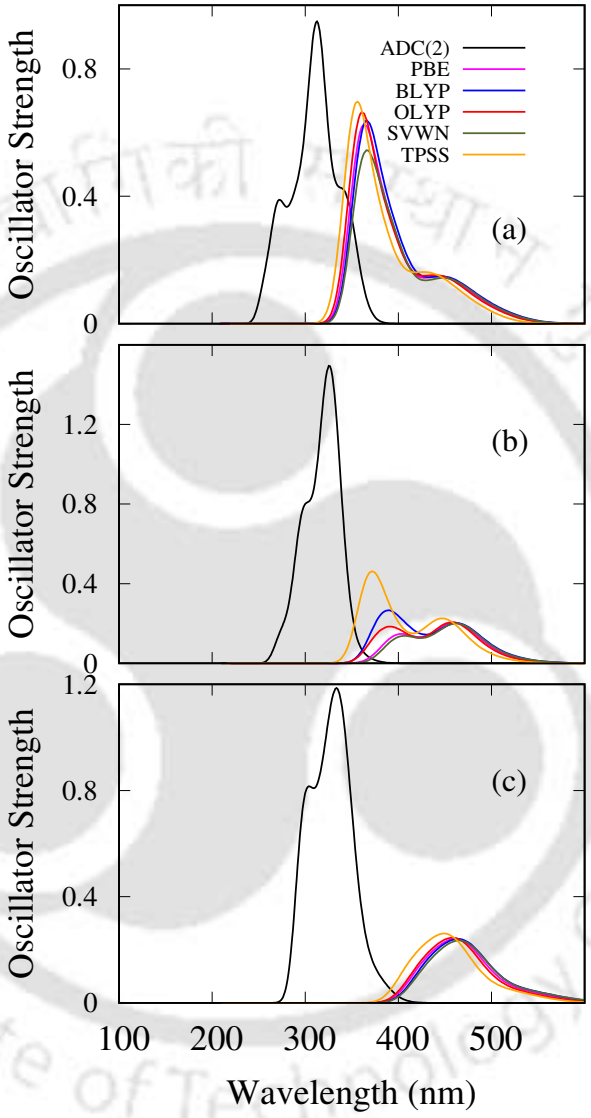

FIGURE A3: Absorption spectra of PT oligomers, n=3 (a), 4 (b) and 5 (c). Results obtained using RI-ADC(2) and various pure functionals are shown.

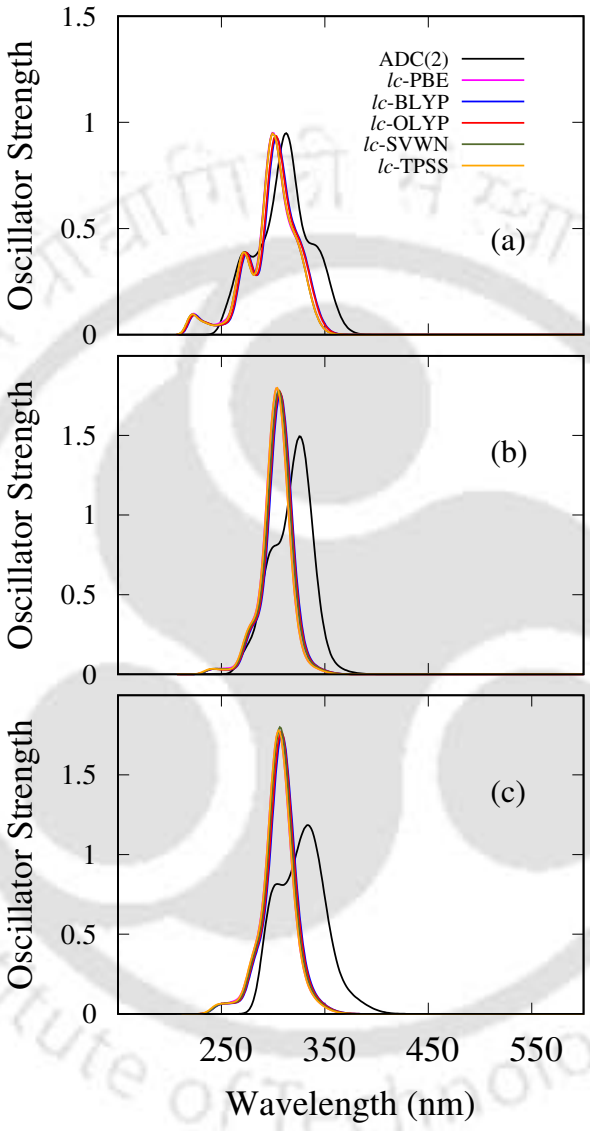

FIGURE A4: Absorption spectra of PT oligomers, n=3 (a), 4 (b) and 5 (c). Results obtained using RI-ADC(2) and various long-range corrected pure functionals are shown.

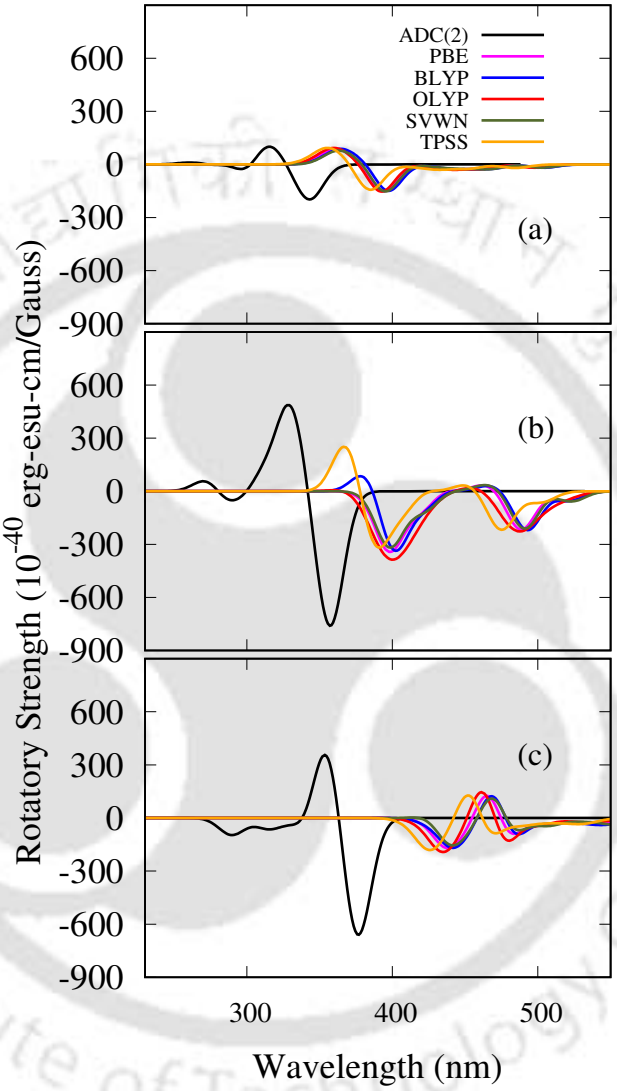

FIGURE A5: CD spectra of PT oligomers, n=3 (a), 4 (b) and 5 (c). Results obtained using RI-ADC(2) and various pure functionals are shown.

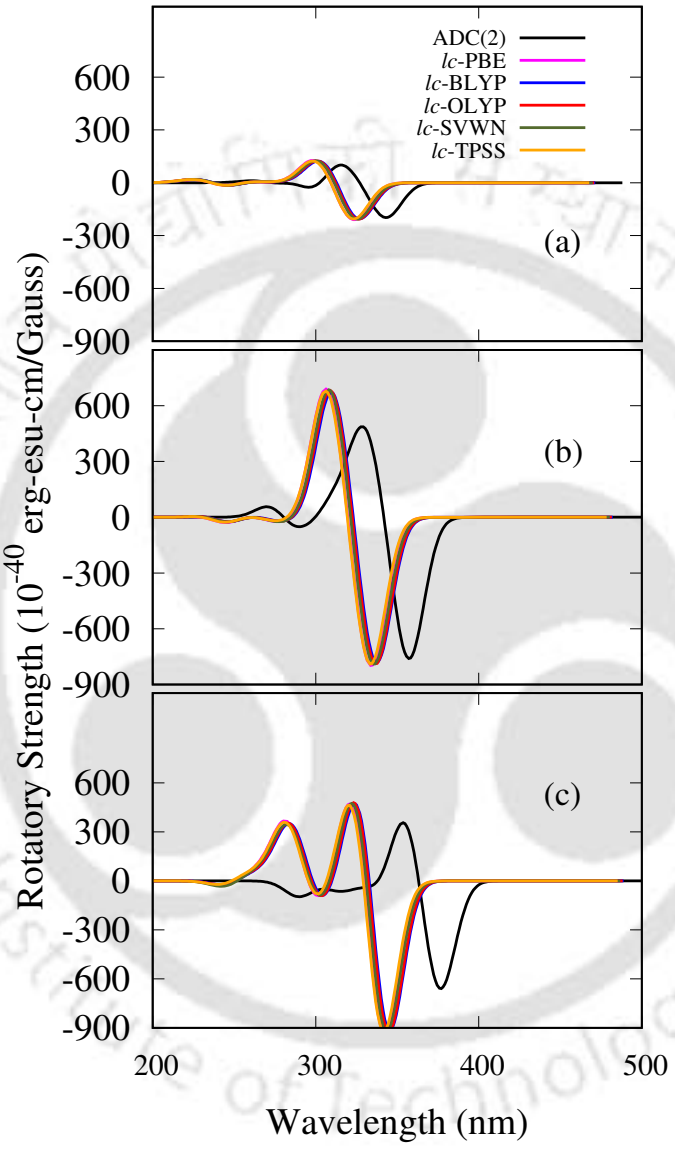

FIGURE A6: CD spectra of PT oligomers, n=3 (a), 4 (b) and 5 (c). Results obtained using RI-ADC(2) and various long-range corrected pure functionals are shown.

TABLE A1: Excitation energies (λ_{abs}s), oscillator strengths (f_{osc}s), major configurations involved in the transitions, rotatory strengths (R), PR_{NTO}s, ω_{CT}s, and d_{exc}s of first five excited states of $\mathbf{(PT)}_1$ at ADC(2) and TD-DFT levels using hybrid fuctionals.

State	λ_{abs}(nm)	f_{osc}	Transitions	R	ω_{CT}	PR_{NTO}	d_{exc}
	ADC(2)						
S_1	271	0.44	H→L (80%)	0.00	0.46	1.09	3.33
S_2	256	0.00	H-4→L(88%)	0.00	0.35	1.00	2.88
S_3	252	0.07	H-1→L+2(53%)	0.00	0.43	1.76	3.28
S_4	235	0.00	H-4→L+2(92%)	0.00	0.05	1.00	2.24
S_5	232	0.15	H-2→L(62%)	0.01	0.41	1.29	3.12
	CAM-B3LYP						
S_1	282	0.42	H→L(92%)	0.01	0.51	1	3.45
S_2	250	0	H-2→L(87%)	0	0.3	1	2.79
S_3	248	0.03	H→L+1(74%)	0	0.51	1.44	3.51
S_4	234	0.05	H-1→L(82%)	0	0.42	1.17	3.19
S_5	228	0	H-2→L+1(90%)	0	0.14	1	2.47
	M06-2X						
S_1	278	0.43	H→L(92%)	0.01	0.51	1	3.46
S_2	258	0	H-2→L(72%)	-0.01	0.23	1	2.59
S_3	246	0.03	H→L+1(74%)	0	0.53	1.44	3.56
S_4	233	0.06	H-1→L(82%)	0.01	0.43	1.14	3.14
S_5	230	0	H-2→L+1(74%)	0	0.17	1	2.54
	ωB97XD						
S_1	281	0.43	H→L(92%)	0.01	0.51	1	3.44
S_2	252	0	H-2→L(87%)	0	0.31	1	2.8
S_3	246	0.03	H→L+1(74%)	0	0.5	1.47	3.46
S_4	233	0.05	H-1→L(82%)	0.01	0.41	1.17	3.16
S_5	230	0	H-2→L+1(90%)	0	0.13	1	2.45
	B3LYP						
S_1	299	0.38	H→L(90%)	0	0.53	1	3.55
S_2	275	0.06	H-1→L+1(95%)	0.01	0.62	1.16	3.79
S_3	273	0	H-2→L(98%)	-0.01	0.48	1	3.13
S_4	255	0.05	H-1→L(90%)	0	0.53	1.14	3.45
S_5	244	0	H-2→L+1(98%)	0	0.08	1	2.32
	PBE0						
S_1	292	0.60	H→L(92%)	0	0.52	1	3.52
S_2	267	0.22	H-2→L(95%)	0.02	0.48	1	3.14
S_3	266	0.11	H→L+1(87%)	-0.02	0.61	1.19	3.79
S_5	240	0.25	H-2→L+1(95%)	0	0.08	1	2.33

TABLE A2: Excitation energies (λ_{abs}s), oscillator strengths (f_{osc}s), major configurations involved in the transitions, rotatory strengths (R), PR_{NTO}s, ω_{CT}s, and d_{exc}s of first five excited states of $\mathbf{(PT)}_1$ at TD-DFT level using pure fuctionals.

State	λ_{abs}(nm)	f_{osc}	Transitions	R	ω_{CT}	PR_{NTO}	d_{exc}
			BLYP				
S_1	325	0.14	H→L(52%)	0	0.62	1	3.83
S_2	316	0	H-1→L(95%)	0	0.48	1	3.14
S_3	308	0.21	H→L+1(48%)	0	0.57	1.11	3.65
S_4	284	0.09	H-2→L(74%)	0.01	0.72	1.15	3.89
S_5	272	0	H-1→L+1(98%)	-0.01	0.06	1	2.26
			OLYP				
S_1	321	0.17	H→L(56%)	0	0.61	1	3.81
S_2	314	0	H-1→L(98%)	0	0.49	1	3.15
S_3	303	0.2	H→L+1(52%)	0	0.57	1.11	3.66
S_4	281	0.08	H-2→L(77%)	0.01	0.71	1.14	3.87
S_5	268	0	H-1→L+1(98%)	-0.01	0.05	1	2.25
			PBE				
S_1	323	0.14	H→L(52%)	0	0.62	1	3.83
S_2	319	0	H-1→L(98%)	0	0.48	1	3.14
S_3	305	0.21	H→L+1(46%)	0	0.57	1.12	3.65
S_4	283	0.09	H-2→L(74%)	0.01	0.72	1.16	3.89
S_5	274	0	H-1→L+1(95%)	-0.01	0.06	1	2.27
			SVWN				
S_1	325	0	H-1→L(95%)	0.02	0.47	1	3.13
S_2	325	0.12	H-1→L+1(40%)	-0.02	0.63	1	3.86
S_3	306	0.22	H→L+1(41%)	0	0.58	1.31	3.65
S_4	286	0.11	H-2→L(67%)	0	0.73	1.21	3.92
S_5	279	0	H-1→L+1(86%)	0	0.06	1	2.28
			TPSS				
S_1	315	0.2	H→L(61%)	-0.01	0.6	1	3.77
S_2	303	0	H-1→L(98%)	0	0.47	1	3.12
S_3	297	0.19	H-1→L+1(58%)	0	0.58	1.11	3.68
S_4	275	0.07	H-2→L(79%)	0.01	0.7	1.13	3.84
S_5	261	0	H-1→L+1(98%)	-0.01	0.07	1	2.3

TABLE A3: Excitation energies (λ_{abs}s), oscillator strengths (f_{osc}s), major configurations involved in the transitions, rotatory strengths (R), PR_{NTO}s, ω_{CT}s, and d_{exc}s of first five excited states of $\mathbf{(PT)}_1$ at TD-DFT level using long-range corrected versions of pure fuctionals.

State	λ_{abs}(nm)	f_{osc}	Transitions	R	ω_{CT}	PR_{NTO}	d_{exc}
			lc-BLYP				
S_1	269	0.42	H→L(90%)	0.01	0.51	1	3.43
S_2	234	0	H-1→L(70%)	-0.02	0.22	1	2.53
S_3	233	0.03	H→L+1(58%)	0.02	0.32	1.57	2.97
S_4	221	0.07	H-1→L(74%)	0.01	0.32	1.11	2.85
S_5	213	0	H-2→L+1(98%)	0	0.17	1	2.52
			lc-OLYP				
S_1	268	0.43	H→L (90%)	0.01	0.51	1	3.43
S_2	233	0	H-2→L(70%)	-0.21	0.22	1	2.54
S_3	233	0.03	H→L+1(58%)	0.21	0.32	1.57	2.97
S_4	220	0.07	H-1→L(77%)	0.01	0.32	1.11	2.85
S_5	212	0	H-2→L+1(72%)	0	0.17	1	2.52
			lc-PBE				
S_1	267	0.43	H→L (90%)	0.01	0.51	1	3.43
S_2	236	0	H-2→L(72%)	-0.01	0.21	1	2.52
S_3	232	0.04	H→L+1(58%)	0	0.29	1.62	2.89
S_4	219	0.07	H-1→L(74%)	0.01	0.31	1.17	2.87
S_5	215	0	H-2→L+1(74%)	0	0.16	1	2.5
			lc-SVWN				
S_1	268	0.43	H→L (90%)	0.01	0.51	1	3.43
S_2	235	0	H-2→L(72%)	-0.01	0.21	1	2.5
S_3	233	0.04	H→L+1(58%)	0.01	0.28	1.63	2.88
S_4	221	0.07	H-1→L(76%)	0.01	0.3	1.17	2.86
S_5	214	0	H-2→L+1(72%)	0	0.16	1	2.49
			lc-TPSS				
S_1	266	0.43	H→L (90%)	0.01	0.51	1	3.43
S_2	233	0	H-2→L(72%)	-0.01	0.21	1	2.52
S_3	231	0.04	H→L+1(58%)	0.01	0.28	1.62	2.88
S_4	219	0.07	H-1→L(76%)	0.01	0.3	1.17	2.86
S_5	212	0	H-2→L+1(74%)	0	0.16	1	2.51

TABLE A4: Excitation energies (λ_{abs}s), oscillator strengths (f_{osc}s), major configurations involved in the transitions, rotatory strengths (R), PR_{NTO}s, ω_{CT}s, and d_{exc}s of first five excited states of $\mathbf{(PT)}_2$ at ADC(2) and TD-DFT levels using hybrid fuctionals.

State	λ_{abs}(nm)	f_{osc}	Transitions	R	ω_{CT}	PR_{NTO}	d_{exc}
	ADC(2)						
S_1	324	0.8	H→L (80%)	-0.04	0.62	1.08	4.37
S_2	291	0.3	H→L+1(51%)	-0.02	0.66	1.67	4.54
S_3	271	0	H-8→L(87%)	-2.07	0.52	1.31	3.55
S_4	271	0.2	H-1→L+1(29%)	2.25	0.61	1.29	4.33
S_5	267	0.04	H-3→L+1(55%)	-0.01	0.52	1.72	3.66
	CAM-B3LYP						
S_1	337	0.77	H→L (87%)	-0.04	0.66	1	4.69
S_2	292	0.28	H→L+1(51%)	0.02	0.65	1.32	4.63
S_3	272	0.11	H-1→L(49%)	0.02	0.78	1.12	5.27
S_4	262	0	H-2→L(70%)	-0.02	0.59	1.51	3.93
S_5	261	0	H-4→L(77%)	0.02	0.46	1.34	3.41
	M06-2X						
S_1	333	0.77	H→L (87%)	-0.05	0.67	1.00	4.75
S_2	290	0.25	H→L+1(51%)	0.01	0.68	1.39	4.91
S_3	273	0.13	H-1→L+1(25%)	0.02	0.75	1.03	5.09
S_4	267	0.00	H-2→L(70%)	0.02	0.42	1.50	3.30
S_5	262	0.00	H-3→L(44%)	-0.02	0.61	1.64	4.09
	ωB97XD						
S_1	333	0.78	H→L (82%)	-0.04	0.66	1.01	4.64
S_2	289	0.31	H→L+1(61%)	0.03	0.62	1.27	4.36
S_3	267	0.09	H-1→L(41%)	0.02	0.74	1.31	4.78
S_4	262	0	H-4→L(77%)	0	0.45	1.37	3.37
S_5	259	0	H-2→L(74%)	-0.01	0.59	1.42	3.79
	B3LYP						
S_1	376	0.51	H→L (87%)	-0.02	0.75	1.01	5.51
S_2	338	0.23	H→L+1(61%)	-0.03	0.81	1.15	5.78
S_3	330	0.13	H-1→L(77%)	0.01	0.84	1.54	6.03
S_4	294	0	H-4→L(95%)	-0.16	0.62	1.06	4.25
S_5	293	0.19	H-1→L+1(48%)	0.17	0.76	2.13	5.84
	PBE0						
S_1	364	0.6	H→L (90%)	-0.03	0.71	1	5.16
S_2	325	0.22	H→L+1(61%)	-0.02	0.81	1.32	5.76
S_3	316	0.11	H-1→L(41%)	0.01	0.83	1.66	5.98
S_4	285	0	H-4→L(92%)	-0.1	0.6	1.08	4.18
S_5	285	0.25	H-1→L+1(87%)	0.16	0.67	1.1	4.84

TABLE A5: Excitation energies (λ_{abs}s), oscillator strengths (f_{osc}s), major configurations involved in the transitions, rotatory strengths (R), PR_{NTO}s, ω_{CT}s, and d_{exc}s of first five excited states of **(PT)$_2$** at TD-DFT level using pure fuctionals.

State	λ_{abs}(nm)	f_{osc}	Transitions	R	ω_{CT}	PR_{NTO}	d_{exc}
	BLYP						
S_1	446	0.14	H→L (56%)	-0.06	0.86	1.06	6.35
S_2	405	0.02	H→L+1(72%)	-0.02	0.89	1.13	6.23
S_3	379	0.58	H-1→L(54%)	-0.19	0.68	1.03	4.78
S_4	360	0	H-2→L(98%)	0	0.71	1	4.8
S_5	355	0.04	H→L+2(90%)	0	0.9	1	7.49
	OLYP						
S_1	440	0.14	H→L (56%)	0.02	0.86	1.06	6.36
S_2	400	0.02	H→L+1(72%)	0	0.89	1.2	6.28
S_3	375	0.6	H-1→L(56%)	0.07	0.68	1.03	4.78
S_4	357	0	H-2→L(98%)	0	0.71	1	4.81
S_5	349	0.04	H→L+2(90%)	0	0.89	1	7.47
	PBE						
S_1	441	0.14	H→L (56%)	-0.04	0.86	1.06	6.35
S_2	401	0.02	H→L+1(72%)	0	0.89	1.2	6.27
S_3	376	0.59	H-1→L(56%)	-0.16	0.68	1.03	4.79
S_4	365	0	H-2→L(98%)	0	0.7	1	4.82
S_5	352	0.04	H→L+2(90%)	0	0.9	1	7.51
	SVWN						
S_1	444	0.14	H→L (58%)	0.04	0.86	1.05	6.36
S_2	403	0.02	H→L+1(72%)	0.01	0.88	1.13	6.2
S_3	377	0.58	H-1→L(54%)	0.23	0.69	1.07	4.82
S_4	375	0	H-2→L(98%)	-0.07	0.7	1	4.83
S_5	356	0.05	H→L+2(90%)	0	0.9	1	7.58
	TPSS						
S_1	429	0.16	H→L (58%)	-0.04	0.86	1.06	6.32
S_2	391	0.02	H→L+1(74%)	-0.02	0.89	1.2	6.28
S_3	368	0.6	H-1→L(56%)	-0.05	0.68	1.03	4.81
S_4	344	0	H-2→L(98%)	0	0.71	1	4.8
S_5	340	0.03	H→L+2(90%)	0	0.89	1	7.39

TABLE A6: Excitation energies (λ_{abs}s), oscillator strengths (f_{osc}s), major configurations involved in the transitions, rotatory strengths (R), PR_{NTO}s, ω_{CT}s, and d_{exc}s of first five excited states of **(PT)**$_2$ at TD-DFT level using long-range corrected versions of pure fuctionals.

State	λ_{abs}(nm)	f_{osc}	Transitions	R	ω_{CT}	PR_{NTO}	d_{exc}
	lc-BLYP						
S_1	314	0.78	H→L (79%)	-0.05	0.64	1.01	4.52
S_2	274	0.35	H→L+1(70%)	0.05	0.56	1.12	3.87
S_3	249	0.03	H-1→L(25%)	0.02	0.61	2.29	4.05
S_4	244	0	H-2→L(52%)	-0.03	0.53	1.52	3.85
S_5	240	0	H-5→L+2(56%)	0.02	0.38	1.62	3.06
	lc-OLYP						
S_1	313	0.79	H→L (79%)	-0.05	0.64	1.01	4.53
S_2	274	0.35	H→L+1(50%)	0.05	0.56	1.13	3.87
S_3	248	0.03	H-1→L(25%)	0.02	0.61	2.29	4.06
S_4	243	0	H-2→L(54%)	-0.03	0.53	1.52	3.85
S_5	238	0	H-5→L+2(56%)	0.02	0.38	1.61	3.06
	lc-PBE						
S_1	311	0.8	H→L (79%)	-0.03	0.65	1.01	4.53
S_2	272	0.35	H→L+1(74%)	0.04	0.56	1.14	3.9
S_3	248	0.03	H-1→L(25%)	0.03	0.62	2.27	4.08
S_4	243	0	H-2→L(58%)	-0.09	0.62	1.52	4.06
S_5	242	0	H-4→L+2(58%)	0.06	0.38	1.56	3.06
	lc-SVWN						
S_1	313	0.79	H→L (79%)	-0.04	0.64	1.01	4.52
S_2	273	0.35	H→L+1(50%)	0.04	0.56	1.13	3.87
S_3	248	0.03	H-1→L(23%)	0.02	0.62	2.31	4.11
S_4	244	0	H-2→L(56%)	-0.04	0.62	1.52	4.08
S_5	241	0	H-5→L+2(56%)	0.02	0.37	1.61	3.04
	lc-TPSS						
S_1	311	0.8	H→L (79%)	-0.03	0.64	1.01	4.53
S_2	271	0.35	H→L+1(50%)	0.03	0.56	1.12	3.88
S_3	247	0.03	H-1→L(26%)	0.02	0.62	2.28	4.12
S_4	242	0	H-2→L(61%)	-0.03	0.62	1.52	4.09
S_5	238	0	H-5→L(56%)	0.02	0.38	1.58	3.06

TABLE A7: Excitation energies (λ_{abs}s), oscillator strengths (f_{osc}s), major configurations involved in the transitions, rotatory strengths (R), PR_{NTO}s, ω_{CT}, and d_{exc}s of first five excited states of $\mathbf{(PT)_3}$ at ADC(2) and TD-DFT levels using hybrid fuctionals.

State	λ_{abs}(nm)	f_{osc}	Transitions	R	ω_{CT}	PR_{NTO}	d_{exc}
	ADC(2)						
S_1	343	0.39	H→L (69%)	-198.54	0.64	1.35	4.59
S_2	314	0.85	H→L+1(50%)	120.72	0.67	1.79	4.69
S_3	300	0.19	H-1→L+1(44%)	-65.37	0.74	1.86	5.14
S_4	289	0.26	H-2→L+1(26%)	22.7	0.75	1.59	5.21
S_5	278	0.05	H-1→L+1(44%)	-10.14	0.81	1.9	5.84
	CAM-B3LYP						
S_1	354	0.37	H→L (56%)	-210.22	0.66	1.53	4.75
S_2	322	0.9	H→L+1(54%)	142	0.66	1.66	4.74
S_3	295	0.11	H→L+2(25%)	-51.41	0.74	2.13	5.35
S_4	286	0.22	H-1→L+1(26%)	48.02	0.79	1.9	5.82
S_5	276	0.04	H-1→L (34%)	-17.71	0.85	1.97	6.14
	M06-2X						
S_1	350	0.37	H→L (63%)	-225.62	0.67	1.46	4.84
S_2	318	0.89	H→L+1(56%)	153.85	0.69	1.55	5
S_3	296	0.04	H-1→L+1(39%)	-66.07	0.83	2.15	5.98
S_4	287	0.25	H-1→L+1(27%)	53.84	0.81	1.37	6.02
S_5	279	0.04	H-1→L(44%)	-13.75	0.86	1.71	6.49
	ωB97XD						
S_1	350	0.38	H→L (51%)	-215.97	0.66	1.61	4.66
S_2	318	0.92	H→L+1(50%)	144.78	0.66	1.69	4.66
S_3	290	0.22	H→L+2(29%)	-32.12	0.67	1.61	4.76
S_4	279	0.14	H-1→L+1(35%)	35.54	0.77	2.39	5.49
S_5	268	0.07	H-2→L+1(26%)	-23.8	0.78	1.77	5.33
	B3LYP						
S_1	407	0.22	H→L (90%)	-124.1	0.8	1	6.18
S_2	377	0.19	H→L+1(67%)	-8.4	0.88	1.08	6.96
S_3	364	0.01	H-1→L+1(62%)	-19.88	0.92	1.15	6.92
S_4	352	0.4	H-1→L(50%)	14.17	0.79	1.71	5.99
S_5	340	0.11	H→L+2(77%)	-9.03	0.87	1.25	6.56
	PBE0						
S_1	390	0.27	H→L (85%)	-153.55	0.8	1	6.1
S_2	358	0.26	H→L+1(65%)	21.32	0.84	1.05	6.59
S_3	345	0.01	H-1→L+1(63%)	-27.02	0.92	1.14	6.96
S_4	339	0.43	H-1→L+1(65%)	34.02	0.75	1.4	5.67
S_5	324	0.17	H→L+2(74%)	-5.6	0.87	1.33	6.54

TABLE A8: Excitation energies (λ_{abs}s), oscillator strengths (f_{osc}s), major configurations involved in the transitions, rotatory strengths (R), PR_{NTO}s, ω_{CT}s, and d_{exc}s of first five excited states of **(PT)**$_3$ at TD-DFT level using pure fuctionals.

State	λ_{abs}(nm)	f_{osc}	Transitions	R	ω_{CT}	PR_{NTO}	d_{exc}
	BLYP						
S_1	504	0.03	H→L (80%)	-18.37	0.94	1.09	7.47
S_2	468	0.07	H→L+1(48%)	-23.1	0.92	1.39	7.07
S_3	448	0.06	H-1→L+1(50%)	-22.47	0.88	1.27	6.44
S_4	432	0.05	H-2→L (57%)	-14.3	0.94	1.18	7.19
S_5	426	0.02	H→L+2 (67%)	2.4	0.96	1.22	7.85
	OLYP						
S_1	498	0.03	H→L (81%)	-18.28	0.94	1.09	7.48
S_2	463	0.07	H→L+1(49%)	-22.98	0.92	1.38	7.07
S_3	443	0.06	H-1→L+1(52%)	-24.99	0.88	1.26	6.45
S_4	428	0.05	H-2→L(59%)	-12.7	0.95	1.17	7.19
S_5	422	0.02	H→L+2(68%)	2.34	0.96	1.21	7.85
	PBE						
S_1	500	0.03	H→L (79%)	-18.32	0.94	1.1	7.48
S_2	464	0.07	H→L+1(48%)	-22.62	0.92	1.4	7.08
S_3	444	0.06	H-1→L+1(49%)	-21.86	0.88	1.26	6.45
S_4	429	0.05	H-2→L(56%)	-13.9	0.94	1.18	7.18
S_5	423	0.02	H→L+2(67%)	2.18	0.96	1.21	7.86
	SVWN						
S_1	503	0.03	H→L (79%)	-18.11	0.94	1.09	7.49
S_2	467	0.07	H→L+1(47%)	-24.93	0.92	1.40	7.07
S_3	448	0.05	H-1→L+1(48%)	-18.59	0.88	1.23	6.45
S_4	432	0.04	H-2→L(55%)	-14.29	0.94	1.19	7.17
S_5	425	0.02	H→L+2(67%)	2.42	0.97	1.13	7.89
	TPSS						
S_1	484	0.04	H→L (80%)	-19.93	0.94	1.11	7.44
S_2	453	0.07	H→L+1(50%)	-22.46	0.92	1.42	7.08
S_3	432	0.06	H-1→L+1(51%)	-24.66	0.88	1.25	6.44
S_4	416	0.06	H-2→L+1(55%)	-14.34	0.94	1.17	7.17
S_5	412	0.02	H→L+2(67%)	1.92	0.96	1.23	7.85

TABLE A9: Excitation energies (λ_{abs}s), oscillator strengths (f_{osc}s), major configurations involved in the transitions, rotatory strengths (R), PR_{NTO}s, ω_{CT}s, and d_{exc}s of first five excited states of **(PT)**$_3$ at TD-DFT level using long-range corrected versions of pure fuctionals.

State	λ_{abs}(nm)	f_{osc}	Transitions	R	ω_{CT}	PR_{NTO}	d_{exc}
	lc-BLYP						
S_1	326	0.38	H→L (42%)	-209.62	0.65	1.72	4.55
S_2	302	0.9	H→L+1(44%)	129.36	0.65	1.7	4.58
S_3	274	0.38	H-1→L+2(32%)	2.27	0.55	1	3.78
S_4	257	0.03	H-1→L+1(27%)	10.95	0.68	2.83	4.77
S_5	249	0.01	H-3→L+1(32%)	-10.93	0.66	2.19	4.48
	lc-OLYP						
S_1	325	0.39	H→L (44%)	-211.36	0.65	1.72	4.55
S_2	302	0.91	H→L+1(46%)	130.84	0.65	1.71	4.58
S_3	274	0.38	H-1→L+2(34%)	1.84	0.55	1	3.78
S_4	256	0.03	H-1→L+1(27%)	11.17	0.68	2.82	4.79
S_5	248	0.01	H-3→L+1(29%)	-11.69	0.66	2.26	4.51
	lc-PBE						
S_1	323	0.39	H→L+1 (30%)	-214.59	0.65	1.67	4.59
S_2	300	0.93	H→L+1(34%)	134	0.64	1.8	4.47
S_3	272	0.38	H-1→L+2(34%)	0.11	0.56	1.13	3.89
S_4	255	0.04	H-1→L+1(25%)	13.31	0.7	2.88	4.82
S_5	248	0.01	H-3→L+1(37%)	-11.54	0.67	1.98	4.61
	lc-SVWN						
S_1	325	0.39	H→L+1 (34%)	-211.5	0.65	1.67	4.59
S_2	301	0.92	H→L+1(32%)	131.56	0.64	1.81	4.45
S_3	273	0.38	H-1→L+2(32%)	2.45	0.56	1.13	3.87
S_4	256	0.04	H-1→L+1(23%)	11.5	0.68	2.84	4.65
S_5	248	0.01	H-3→L+1(37%)	-10.91	0.65	1.98	4.48
	lc-TPSS						
S_1	323	0.39	H→L+1 (30%)	-211.63	0.65	1.68	4.58
S_2	300	0.92	H→L+1(35%)	130.68	0.64	1.81	4.46
S_3	271	0.38	H-1→L+2(34%)	1.8	0.56	1.12	3.88
S_4	255	0.04	H-1→L+1(26%)	11.71	0.73	2.71	5.01
S_5	247	0.01	H-3→L+1(32%)	-12.44	0.67	2.3	4.67

TABLE A10: Excitation energies (λ_{abs}s), oscillator strengths (f_{osc}s), major configurations involved in the transitions, rotatory strengths (R), PR_{NTO}s, ω_{CT}s, and d_{exc}s of first five excited states of $\mathbf{(PT)}_4$ at ADC(2) and TD-DFT levels using hybrid fuctionals.

State	λ_{abs}(nm)	f_{osc}	Transitions	R	ω_{CT}	PR_{NTO}	d_{exc}
	ADC(2)						
S_1	357	0.04	H→L (20%)	-766.44	0.66	2.23	4.86
S_2	329	0.87	H-1→L (40%)	508.64	0.69	2.1	5.27
S_3	324	0.6	H→L (39%)	-36.56	0.73	2.09	5.36
S_4	311	0.17	H→L+1 (32%)	131.27	0.8	1.82	6.19
S_5	300	0.3	H-1→L+1(26%)	-87.3	0.75	1.85	5.66
	CAM-B3LYP						
S_1	369	0.04	H→L (22%)	-749.58	0.67	2.35	5.03
S_2	333	1	H→L +2(29%)	673.92	0.65	1.94	5.05
S_3	325	0.75	H-1→L+1 (37%)	-20.8	0.71	1.81	5.33
S_4	302	0.09	H→L+3 (35%)	-10.73	0.68	1.54	4.92
S_5	297	0.08	H→L+1(29%)	-27.71	0.87	1.64	6.9
	M06-2X						
S_1	366	0.03	H→L (26%)	-805.81	0.68	2.29	5.14
S_2	331	0.97	H-1→L (34%)	699.83	0.68	1.91	5.37
S_3	323	0.7	H-1→L+1 (39%)	-18.42	0.74	1.86	5.68
S_4	302	0.02	H→L+1 (34%)	88.49	0.87	1.54	6.93
S_5	299	0.12	H→L+3 (26%)	-134.15	0.74	1.69	5.65
	ωB97XD						
S_1	365	0.04	H→L (20%)	-774.24	0.67	2.4	5.01
S_2	329	1.03	H→L+2 (30%)	710.94	0.64	1.95	4.98
S_3	320	0.79	H-1→L+1 (35%)	-18.9	0.69	1.9	5.11
S_4	297	0.16	H→L+3 (37%)	-34.98	0.64	1.27	4.47
S_5	286	0.04	H→L+1(25%)	-7.14	0.83	2.11	6.15
	B3LYP						
S_1	426	0.01	H→L (50%)	-487.51	0.76	1.84	5.93
S_2	401	0.07	H→L +1(67%)	50.36	0.89	1.68	7.32
S_3	397	0.08	H→L (42%)	-39.64	0.91	1.15	7.39
S_4	392	0.04	H-1→L (37%)	-18.42	0.9	1.18	7.61
S_5	378	0.42	H→L+2(74%)	211.86	0.78	1.36	6.21
	PBE0						
S_1	411	0.02	H→L (44%)	-559.29	0.75	1.93	5.78
S_2	379	0.13	H-1→L (30%)	96.56	0.89	1.79	7.35
S_3	377	0.15	H→L(50%)	-44.53	0.89	1.41	7.16
S_4	369	0.05	H-1→L (41%)	9	0.91	1.27	7.6
S_5	362	0.49	H-1→L+1(80%)	266.49	0.79	1.21	6.43

TABLE A11: Excitation energies (λ_{abs}s), oscillator strengths (f_{osc}s), major configurations involved in the transitions, rotatory strengths (R), PR_{NTO}s, ω_{CT}s, and d_{exc}s of first five excited states of **(PT)**$_4$ at TD-DFT level using pure fuctionals.

State	λ_{abs}(nm)	f_{osc}	Transitions	R	ω_{CT}	PR_{NTO}	d_{exc}
	BLYP						
S_1	521	0.01	H→L+1 (44%)	-24.38	0.92	1.22	7.57
S_2	521	0.01	H→L+1 (46%)	-32.48	0.9	1.06	7.41
S_3	515	0.01	H-1→L (65%)	3.97	0.92	1.8	7.69
S_4	492	0.03	H-1→L+1 (67%)	-220.16	0.84	1.21	6.75
S_5	466	0.12	H→L+2(41%)	34.85	0.89	2.12	6.92
	OLYP						
S_1	515	0	H→L+1 (82%)	1.92	0.94	1	7.69
S_2	512	0.01	H→L (77%)	-47.01	0.9	1.17	7.36
S_3	506	0	H-1→L (63%)	-5.7	0.91	1.72	7.67
S_4	486	0.03	H-1→L+1 (67%)	-224.59	0.85	1.15	6.82
S_5	461	0.13	H→L+2(41%)	40.92	0.89	1.99	6.81
	PBE						
S_1	519	0.01	H→L+1 (79%)	-1.19	0.94	1.06	7.7
S_2	519	0.01	H→L (72%)	-52.41	0.89	1.13	7.31
S_3	510	0	H-1→L (65%)	-2.86	0.92	1.71	7.72
S_4	488	0.03	H-1→L+1 (67%)	-216.84	0.84	1.18	6.79
S_5	463	0.12	H→L+2(41%)	38.77	0.89	1.97	6.86
	SVWN						
S_1	523	0.01	H→L+1 (77%)	-2.98	0.94	1.06	7.7
S_2	523	0.01	H→L (70%)	-53.95	0.89	1.12	7.27
S_3	515	0.01	H-1→L (65%)	0.55	0.92	1.73	7.74
S_4	490	0.03	H-1→L+1 (67%)	-212.2	0.82	1.1	6.61
S_5	466	0.12	H→L+2(41%)	38.1	0.89	2.2	6.9
	TPSS						
S_1	504	0.01	H→L+1 (72%)	-4.32	0.95	1.08	7.74
S_2	502	0.01	H→L (65%)	-51.17	0.9	1.09	7.35
S_3	494	0.01	H-1→L (65%)	-8.71	0.91	1.67	7.69
S_4	475	0.03	H-1→L+1 (67%)	-217.46	0.85	1.05	6.85
S_5	451	0.14	H→L+2(41%)	41.33	0.89	1.96	6.87

TABLE A12: Excitation energies (λ_{abs}s), oscillator strengths (f_{osc}s), major configurations involved in the transitions, rotatory strengths (R), PR_{NTO}s, ω_{CT}s, and d_{exc}s of first five excited states of **(PT)**$_4$ at TD-DFT level using long-range corrected versions of pure fuctionals.

State	λ_{abs}(nm)	f_{osc}	Transitions	R	ω_{CT}	PR_{NTO}	d_{exc}
	lc-BLYP						
S_1	337	0.04	H-1→L (15%)	-790.39	0.64	2.53	4.81
S_2	310	1.07	H→L+2 (26%)	715.1	0.62	1.96	4.8
S_3	303	0.79	H-1→L+1 (29%)	-40.01	0.67	1.88	4.9
S_4	281	0.27	H-1→L+3 (25%)	-22.83	0.6	1.13	4.1
S_5	260	0.01	H→L+2(12%)	-5.52	0.77	2.64	5.5
	lc-OLYP						
S_1	337	0.04	H-1→L (16%)	-797.77	0.64	2.52	4.83
S_2	309	1.08	H→L+2 (26%)	726.08	0.62	1.96	4.83
S_3	302	0.79	H-1→L+1 (29%)	-43.35	0.67	1.88	4.92
S_4	280	0.28	H-1→L+3 (25%)	-24.72	0.6	1.13	4.1
S_5	259	0.01	H→L+1(13%)	-5.7	0.77	2.66	5.47
	lc-PBE						
S_1	333	0.04	H→L (17%)	-807.73	0.65	2.51	4.85
S_2	306	1.09	H→L+2 (29%)	734.77	0.61	1.89	4.77
S_3	300	0.81	H-1→L+1 (34%)	-41.9	0.67	1.86	4.93
S_4	278	0.28	H→L+3 (29%)	-26.67	0.6	1.13	4.14
S_5	258	0.01	H→L+1(15%)	-6.91	0.77	2.73	5.4
	lc-SVWN						
S_1	335	0.05	H-1→L (17%)	-800.75	0.64	2.52	4.82
S_2	308	1.09	H→L+2 (26%)	737.39	0.63	1.97	4.85
S_3	302	0.79	H-1→L+1 (29%)	-50.15	0.67	1.88	4.91
S_4	279	0.28	H-1→L+3 (26%)	-27.22	0.6	1.13	4.09
S_5	259	0.01	H→L+1(12%)	-5.8	0.77	2.65	5.38
	lc-TPSS						
S_1	333	0.04	H→L (17%)	-800.48	0.65	2.51	4.84
S_2	306	1.09	H→L+2 (20%)	721.81	0.61	1.89	4.76
S_3	300	0.8	H-1→L+1 (34%)	-38.66	0.67	1.86	4.93
S_4	278	0.28	H→L+3 (27%)	-22.16	0.6	1.13	4.12
S_5	258	0.01	H→L+1(15%)	-6.12	0.77	2.65	5.41

TABLE A13: Excitation energies (λ_{abs}s), oscillator strengths (f_{osc}s), major configurations involved in the transitions, rotatory strengths (R), PR_{NTO}s, ω_{CT}s, and d_{exc}s of first five excited states of $\mathbf{(PT)_5}$ at ADC(2) and TD-DFT levels using hybrid fuctionals.

State	λ_{abs}(nm)	f_{osc}	Transitions	R	ω_{CT}	PR_{NTO}	d_{exc}
	ADC(2)						
S_1	376	0.08	H→L(63.9%)	-684.71	0.75	1.74	5.22
S_2	353	0.1	H-2→L(51%)	478.56	0.73	1.86	5.1
S_3	344	0.17	H→L+1(32%)	-101.95	0.86	1.84	6.18
S_4	341	0.36	H-1→L+1(43.3%)	-66.95	0.83	1.96	5.5
S_5	335	0.19	H→L+3(26.3%)	40.79	0.9	2.11	6.04
	CAM-B3LYP						
S_1	382	0.04	H→L(49.7%)	-820.47	0.75	2.33	5.28
S_2	356	0.11	H-2→L(37.8%)	562.56	0.77	2	5.66
S_3	340	0.74	H-1→L+1(30%)	-65.57	0.8	2.03	5.4
S_4	329	0.57	H→L+1(28.8%)	-265.05	0.75	1.75	5.58
S_5	320	0.15	H→L+3(34.4%)	140.23	0.95	2.08	6.15
	M06-2X						
S_1	378	0.04	H→L(53.1%)	-848.62	0.76	2.2	5.36
S_2	354	0.1	H-2→L(36.2%)	584.61	0.78	2	5.61
S_3	339	0.62	H-1→L+1(31.5%)	-75.51	0.8	2.06	5.44
S_4	329	0.43	H→L+1(40.4%)	-287.57	0.8	1.81	5.99
S_5	323	0.17	H→L+3(33.2%)	105.58	0.95	2.18	6.14
	ωB97XD						
S_1	375	0.04	H→L(45.13%)	-879.2	0.75	2.47	5.25
S_2	352	0.12	H→L+3(35.62%)	585.64	0.75	2	5.51
S_3	334	0.82	H-1→L+1(24.5%)	-50.42	0.78	2.05	5.29
S_4	324	0.65	H→L+1(28.7%)	-261.26	0.72	1.76	5.19
S_5	311	0.21	H→L+3(34.44%)	247.31	0.9	2.09	5.73
	B3LYP						
S_1	451	0.04	H→L(80.6%)	-289.03	0.85	1.32	6.05
S_2	425	0	H-1→L(47.2%)	17.33	0.92	1.21	6.28
S_3	419	0.01	H→L+1(74.1%)	-61.64	0.94	1.45	7.32
S_4	415	0.01	H-1→L+1(43.8%)	-66.61	0.93	1.82	7.14
S_5	408	0.09	H→L+3(43.7%)	-23.37	0.9	1.73	6.54
	PBE0						
S_1	432	0.04	H→L(74.42%)	-375.7	0.85	1.36	6.05
S_2	405	0.01	H-1→L(46.08%)	29.13	0.91	1.17	6.2
S_3	397	0.01	H→L+1(72%)	-76.51	0.94	1.41	7.26
S_4	394	0.02	H-1→L+1(32.48%)	-61.42	0.94	1.77	7.01
S_5	390	0.16	H→L+3(35.45%)	137.21	0.88	1.58	6.01

TABLE A14: Excitation energies (λ_{abs}s), oscillator strengths (f_{osc}s), major configurations involved in the transitions, rotatory strengths (R), PR_{NTO}s, ω_{CT}s, and d_{exc}s of first five excited states of $\mathbf{(PT)_5}$ at TD-DFT level using pure fuctionals.

State	λ_{abs}(nm)	f_{osc}	Transitions	R	ω_{CT}	PR_{NTO}	d_{exc}
	BLYP						
S_1	554	0.02	H→L(77%)	-11.53	0.91	1	7.02
S_2	546	0.01	H→L+1(90%)	-17.88	0.96	1.12	7.55
S_3	539	0	H-1→L(85%)	-17.1	0.95	1.08	7.07
S_4	525	0.01	H-1→L+1(41%)	2.85	0.93	1.9	7.32
S_5	523	0.01	H-1→L+1(41%)	-23.12	0.97	1.77	7.29
	PBE						
S_1	554	0.01	H→L(76%)	-10.9	0.92	1	7.16
S_2	546	0.01	H→L+1(87%)	-15.92	0.96	1.11	7.55
S_3	537	0	H-1→L(85%)	-11.96	0.95	1.08	7.1
S_4	523	0	H-1→L+1(77%)	3.19	0.93	1.13	7.18
S_5	521	0.01	H→L+2(50%)	-14.82	0.95	1.79	7.11
	OLYP						
S_1	546	0.01	H→L(74%)	-5.63	0.93	1	7.31
S_2	539	0.01	H→L+1(85%)	-13.64	0.95	1.07	7.36
S_3	530	0	H-1→L(82%)	-10.72	0.95	1.06	7.09
S_4	519	0	H-1→L+1(74%)	-13.29	0.96	1.07	7.22
S_5	519	0.01	H→L+2(54%)	3.24	0.92	1.73	7.08
	SVWN						
S_1	559	0.02	H→L(77%)	-15.45	0.92	1	7.13
S_2	551	0.01	H→L+1(87%)	-17.12	0.96	1.13	7.54
S_3	544	0	H-1→L(86%)	-9.96	0.96	1.1	7.09
S_4	530	0	H-1→L+1(82%)	-9.96	0.93	1	7.12
S_5	525	0.02	H→L+2(56%)	-8.77	0.94	1.61	7.05
	TPSS						
S_1	534	0.02	H→L(77%)	-14.31	0.92	1	7.14
S_2	528	0.01	H→L+1(87%)	-16	0.96	1.06	7.54
S_3	519	0	H-1→L(87%)	-11.48	0.95	1.06	7.08
S_4	506	0.01	H-1→L+1(48%)	1.76	0.91	1.77	7.02
S_5	506	0.01	H→L+2(34%)	-23.59	0.97	1.9	7.31

TABLE A15: Excitation energies (λ_{abs}s), oscillator strengths (f_{osc}s), major configurations involved in the transitions, rotatory strengths (R), PR_{NTO}s, ω_{CT}s, and d_{exc}s of first five excited states of $\mathbf{(PT)_5}$ at TD-DFT level using long-range corrected versions of pure fuctionals.

State	λ_{abs}(nm)	f_{osc}	Transitions	R	ω_{CT}	PR_{NTO}	d_{exc}
	lc-BLYP						
S_1	343	0.04	H→L(37%)	-1021.58	0.72	2.92	5.04
S_2	327	0.13	H→L+3(35%)	618.08	0.71	2.12	5.07
S_3	311	1.07	H→L(20%)	50.22	0.73	2.36	5.04
S_4	305	0.73	H-1→L+2(25%)	-200.71	0.68	1.84	4.77
S_5	285	0.33	H-2→L+4(45%)	361.56	0.65	1.24	4.42
	lc-OLYP						
S_1	343	0.04	H→L(35%)	-1030.35	0.72	2.93	5.05
S_2	326	0.13	H→L+3(35%)	626.44	0.71	2.12	5.08
S_3	310	1.08	H→L+2(20%)	49.22	0.73	2.35	5.05
S_4	304	0.73	H-1→L+2(25%)	-203.89	0.67	1.78	4.75
S_5	284	0.33	H-2→L+4(46%)	365.62	0.65	1.24	4.41
	lc-PBE						
S_1	341	0.05	H→L(36%)	-1038.48	0.73	3.02	5.11
S_2	324	0.13	H→L+3(35%)	625.36	0.71	2.13	5.09
S_3	308	1.09	H→L+2(20%)	43.18	0.73	2.32	5.05
S_4	302	0.74	H-1→L+2(18%)	-208.46	0.68	1.61	4.82
S_5	282	0.34	H-2→L+4(37%)	380.11	0.66	1.28	4.44
	lc-SVWN						
S_1	342	0.04	H→L(35%)	-1040.13	0.72	2.93	5.07
S_2	325	0.14	H→L+3(35%)	635.57	0.72	2.11	5.25
S_3	308	1.1	H→L+2(20%)	49.92	0.72	2.3	5.04
S_4	303	0.73	H-1→L+2(20%)	-202.41	0.68	1.7	4.75
S_5	283	0.33	H-2→L+4(48%)	355.02	0.64	1.22	4.34
	lc-TPSS						
S_1	340	0.05	H→L(35%)	-1032.03	0.73	3.02	5.11
S_2	324	0.13	H→L+3(35%)	618.3	0.71	2.13	5.08
S_3	308	1.09	H→L+2(20%)	47.9	0.72	2.33	5.04
S_4	302	0.74	H-1→L+2(19%)	-199.08	0.68	1.6	4.81
S_5	282	0.34	H-2→L+4(39%)	372.51	0.65	1.25	4.41

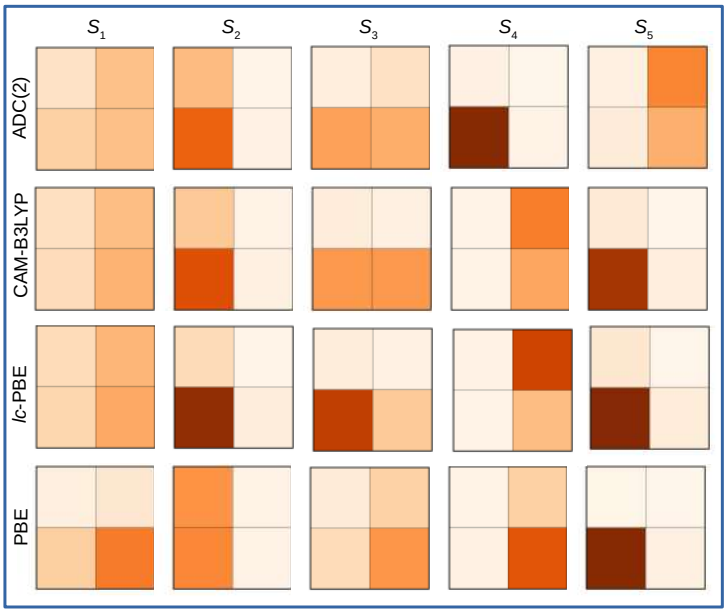

FIGURE A7: Electron hole correlation plots of $\mathbf{(PT)}_1$ at ADC(2), CAM-B3LYP, *lc*-PBE, and PBE levels. Results for first five excited states are shown. The main diagonal going from lower left to upper right indicates local excitations and the off-diagonal elements indicate excitations between different sites.

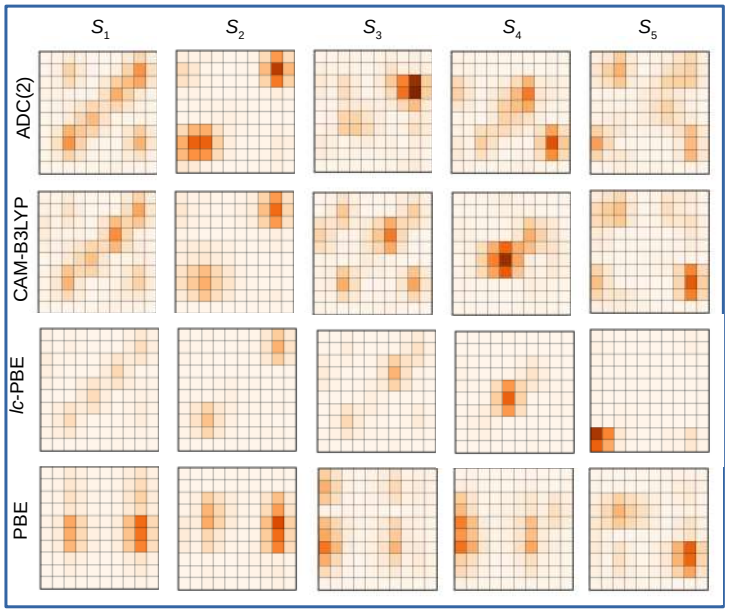

FIGURE A8: Electron hole correlation plots of $\mathbf{(PT)}_5$ at ADC(2), CAM-B3LYP, *lc*-PBE, and PBE levels. Results for first five excited states are shown. The main diagonal going from lower left to upper right indicates local excitations and the off-diagonal elements indicate excitations between different sites.

Appendix B

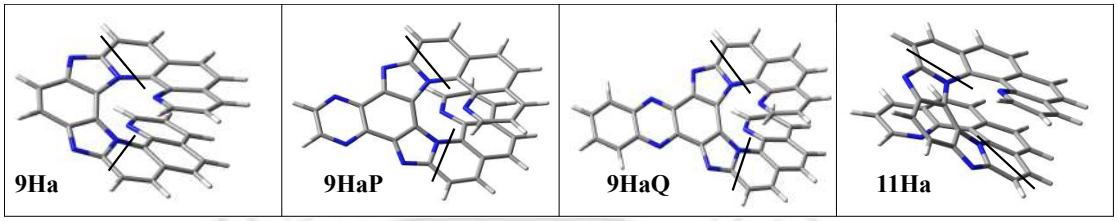

FIGURE B1: Fragmentation scheme of **9Ha**, **9HaP**, **9HaQ**, and **11Ha** for CT analysis.

TABLE B1: Excitation energies (λ_{abs} in nm), corresponding Oscillator Strength (f_{osc}), R, ω_{CT}, PR_{NTO}, and d_{exc} of **9Ha**. Results obtained at different TD-DFT and RI-ADC(2) levels.

9Ha	CAM-B3LYP						M06-2X					
States	λ_{abs}	f_{osc}	R	ω_{CT}	PR_{NTO}	d_{exc}	λ_{abs}	f_{osc}	R	ω_{CT}	PR_{NTO}	d_{exc}
S_1	388	0.029	-424.40	0.61	1.11	4.38	388	0.027	-398.77	0.63	1.07	4.47
S_2	372	0.149	185.22	0.54	1.24	4.38	370	0.145	187.47	0.56	1.19	4.45
S_3	341	0.003	-2.48	0.48	2.49	4.23	339	0.003	-13.89	0.49	2.42	4.28
S_4	333	0.008	-3.61	0.54	1.99	4.16	333	0.008	-2.89	0.57	1.95	4.26
S_5	317	0.276	-574.19	0.49	2.45	4.23	317	0.276	-632.62	0.50	2.42	4.29
S_6	305	0.198	57.73	0.61	1.92	4.72	309	0.190	82.74	0.65	1.83	4.81
S_7	291	0.000	6.85	0.66	2.32	4.32	293	0.000	1.82	0.63	1.93	4.10
S_8	288	0.006	-18.09	0.51	2.74	4.28	288	0.007	-35.42	0.54	2.40	4.29
States	ωB97XD						B3LYP					
S_1	377	0.033	-462.50	0.59	1.16	4.25	475	0.014	-234.72	0.72	1.01	4.83
S_2	365	0.159	195.99	0.52	1.29	4.26	441	0.079	105.25	0.69	1.07	4.89
S_3	336	0.005	3.27	0.47	2.62	4.13	398	0.001	-1.43	0.74	1.79	4.88
S_4	327	0.008	-3.74	0.50	2.18	4.00	394	0.001	-11.05	0.63	2.02	4.80
S_5	312	0.266	-566.89	0.46	2.47	4.11	379	0.095	22.62	0.77	1.89	5.20
S_6	297	0.248	86.02	0.55	2.11	4.51	369	0.231	-579.49	0.68	2.05	4.92
S_7	287	0.009	49.62	0.63	1.96	3.96	344	0.001	5.44	0.69	2.01	4.51
S_8	283	0.003	-25.74	0.51	2.96	4.08	341	0.019	22.42	0.76	2.07	4.86
States	PBE0						ADC(2)					
S_1	453	0.016	-260.66	0.70	1.01	4.78	423	0.019	-312.29	0.72	1.00	5.02
S_2	424	0.093	119.47	0.67	1.07	4.83	400	0.136	150.12	0.62	1.08	4.86
S_3	381	0.002	-1.68	0.72	1.74	4.79	364	0.014	-7.98	0.66	1.29	4.62
S_4	380	0.001	-11.68	0.61	2.04	4.72	362	0.016	6.64	0.58	1.97	4.66
S_5	362	0.103	28.10	0.76	1.81	5.16	340	0.102	30.94	0.68	1.54	5.11
S_6	356	0.248	-601.41	0.65	2.06	4.82	338	0.286	-542.15	0.61	1.92	4.81
S_7	331	0.000	4.06	0.68	2.02	4.47	312	0.001	-6.22	0.66	2.09	4.47
S_8	327	0.011	14.78	0.75	2.33	4.77	307	0.017	-33.40	0.58	1.93	4.73

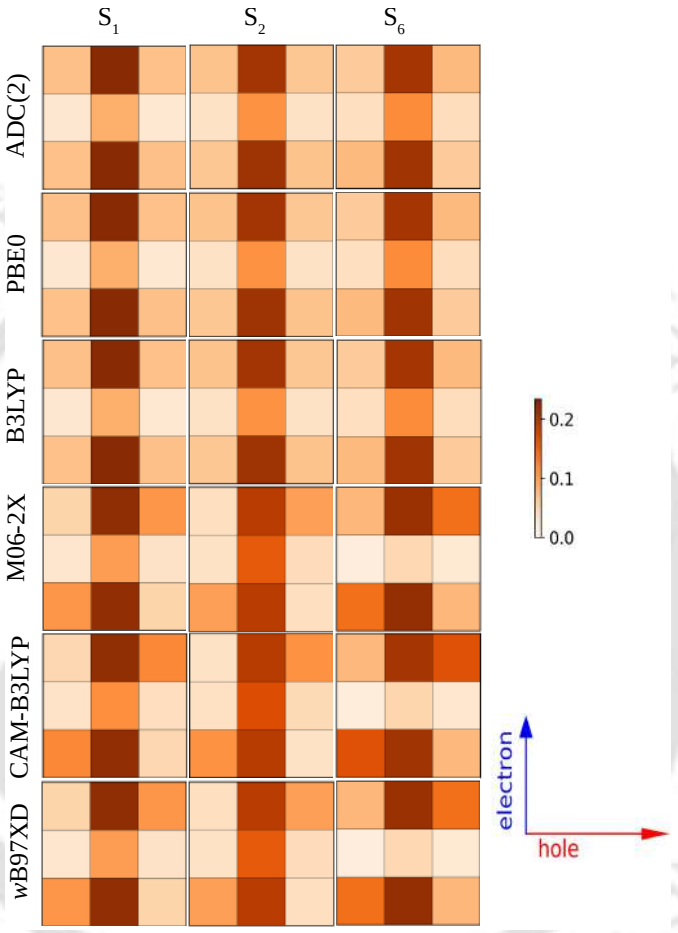

FIGURE B2: Electron-hole correlation plots of S_1, S_2, and S_6 states of **9Ha** at ADC(2), PBE0, B3LYP, M06-2X, CAM-B3LYP and ωB97XD levels. **9Ha** is divided into three fragments, hence each plot shows a $3 \times 3\ \Omega$ matrix. Diagonal field going from lower left to upper right indicates local excitations and the off-diagonal elements show charge-transfer excitations. The squares in the middle and terminals of the plot represent the *5-6-5* and terminals units, respectively, as shown in the Figure B1. The vertical axis shows the location of an electron, while the horizontal axis indicates the location of a hole.

TABLE B2: Excitation energies(λ_{abs} in nm), corresponding Oscillator Strength (f_{osc}), R, ω_{CT}, PR_{NTO}, and d_{exc} of **9HaP**, **9HaQ**, and **11Ha**. Results obtained at TD-PBE0/def2-TZVP/DCM level.

9HaP						
States	λ_{abs}	f_{osc}	R	ω_{CT}	PR_{NTO}	d_{exc}
S_1	465	0.015	-219.72	0.73	1.02	4.94
S_2	428	0.139	158.65	0.70	1.06	4.95
S_3	404	0.055	-174.35	0.40	1.09	4.72
S_4	373	0.013	3.64	0.73	1.46	5.12
S_5	361	0.009	-39.16	0.57	1.38	5.03
S_6	353	0.242	25.72	0.76	1.53	5.20
S_7	342	0.184	-361.02	0.63	1.47	4.99
S_8	331	0.002	12.37	0.61	1.82	4.65
9HaQ						
S_1	518	0.017	-42.96	0.46	1.02	5.47
S_2	453	0.034	-302.74	0.61	1.02	4.95
S_3	435	0.163	173.8	0.70	1.08	5.20
S_4	382	0.026	10.2	0.69	1.84	5.50
S_5	372	0.052	-107.84	0.64	1.21	5.22
S_6	369	0.123	23.54	0.14	1.15	3.70
S_7	369	0.721	150.46	0.52	1.89	5.37
S_8	347	0.028	-46.37	0.56	1.16	5.94
11Ha						
S_1	462	0.06	-627.68	0.71	1.02	4.89
S_2	441	0.073	100.64	0.72	1.07	5.03
S_3	405	0.014	-20.12	0.67	1.43	4.78
S_4	394	0.002	-13.35	0.65	1.85	4.74
S_5	378	0.002	24.52	0.75	1.92	4.86
S_6	372	0.109	21.28	0.78	1.52	5.07
S_7	352	0	3.48	0.66	2.59	4.77
S_8	348	0.07	69.56	0.60	1.31	4.74

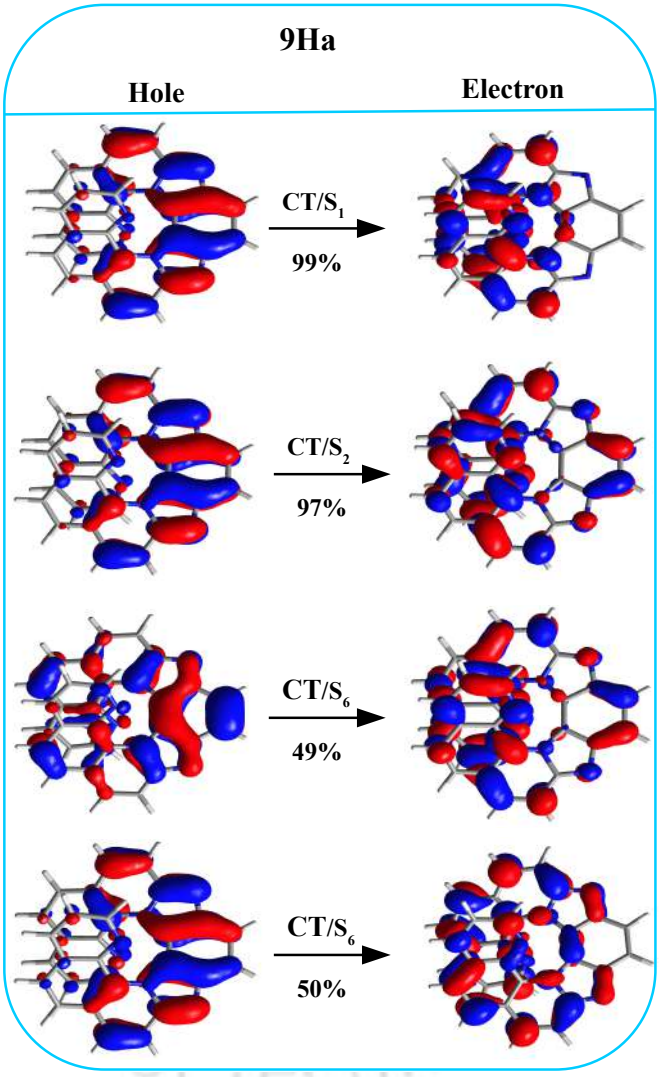

FIGURE B3: Natural transition orbitals for some selected excited states of **9Ha**. Results are obtained at TD-PBE0/def2-TZVP level. Isovalue = 0.03 a.u. is used. Charge transfer and locally excited transitions are written as CT and LE, respectively.

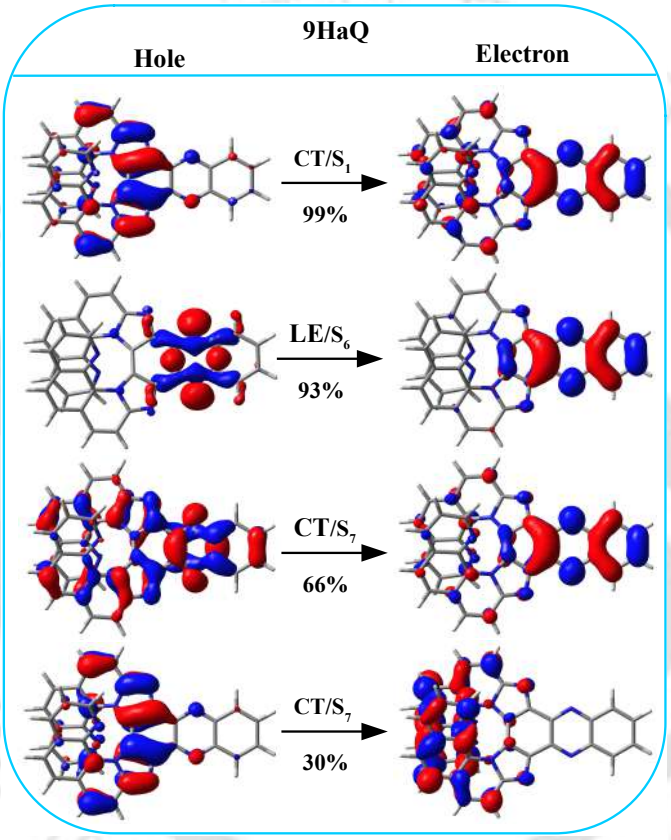

FIGURE B4: Natural transition orbitals for some selected excited states of **9HaQ**. Results are obtained at TD-PBE0/def2-TZVP level. Isovalue = 0.03 a.u. is used. Charge transfer and locally excited transitions are written as CT and LE, respectively.

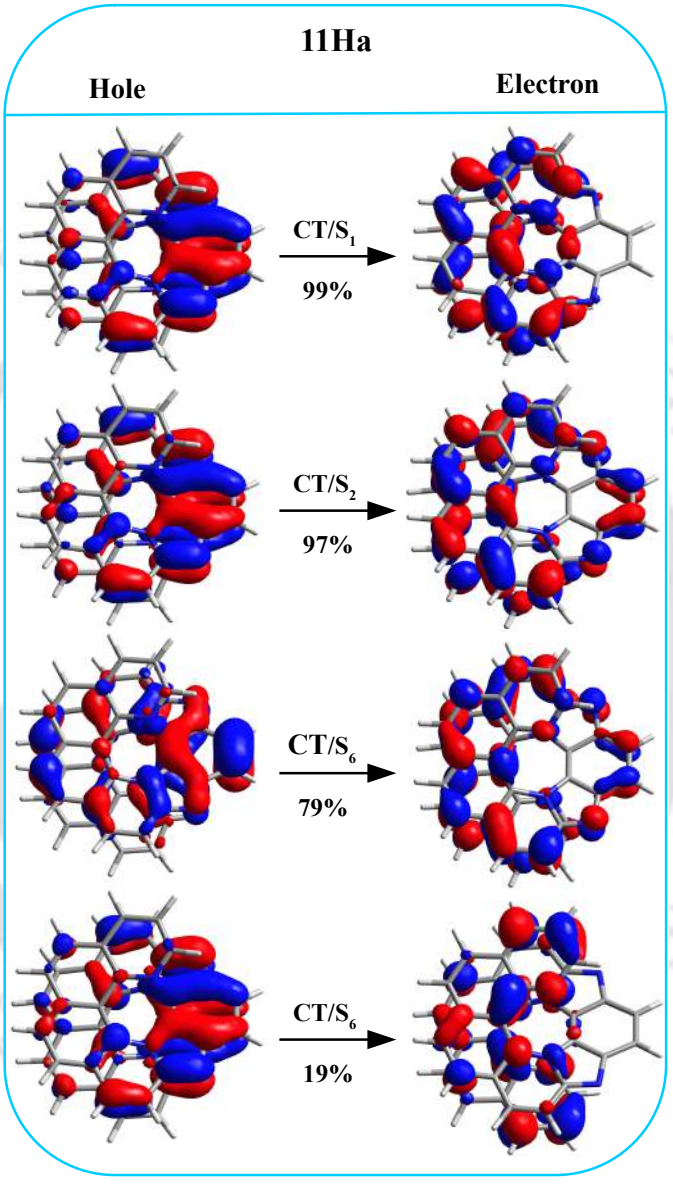

FIGURE B5: Natural transition orbitals for some selected excited states of **11Ha**. Results are obtained at TD-PBE0/def2-TZVP level. Isovalue = 0.03 a.u. is used. Charge transfer and locally excited transitions are written as CT and LE, respectively.

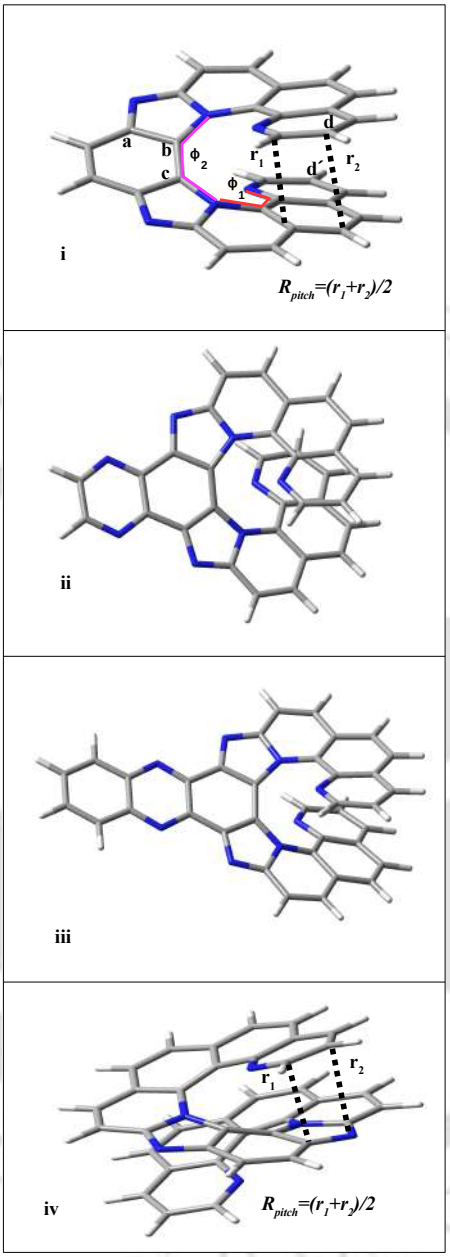

FIGURE B6: Lowest excited state optimized geometries of **9Ha**(i), **9HaP**(ii), **9HaQ**(iii), and **11Ha**(iv). Optimizations were carried out at PBE0-D3/def2-SVP level. Torsional angles ϕ_1 and ϕ_2 are shown. In addition, the torsional angles $\angle$abcd and $\angle$abcd$'$ are also shown, these two are denoted as ϕ_2 and ϕ_4, respectively, for **9Ha**. Same pattern is followed for **9HaP**, **9HaQ**, and **11Ha** to show the torsional angles. In this figure, carbon, hydrogen and nitrogen atoms are shown as grey, white, and blue colors, respectively.

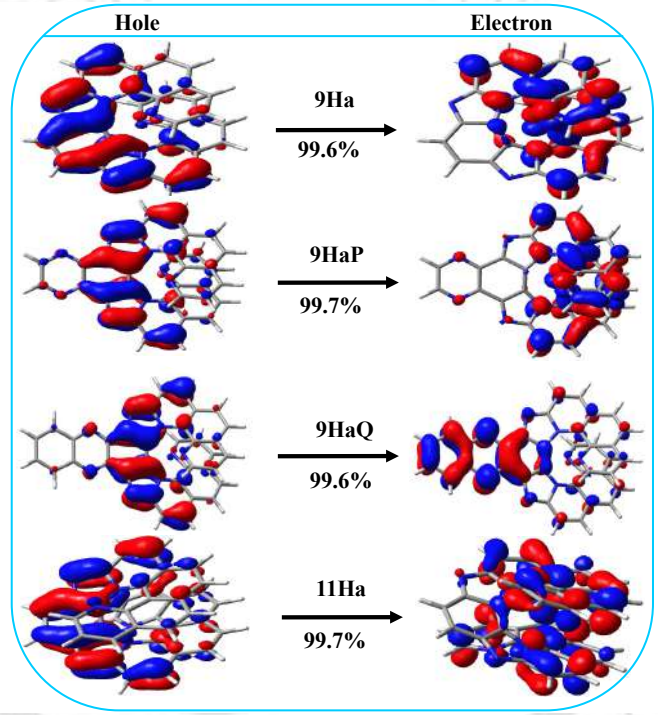

FIGURE B7: Natural transition orbitals for $S_1 \rightarrow S_0$ transitions of **9Ha**, **9HaP**, **9HaQ**, and **11Ha**. Calculated from S_1 optimized geometry at PBE0-D3/def2-SVP level. Isovalue= 0.03 a.u. is used.

TABLE B3: Charge-transfer (ω_{CT}) and $|\boldsymbol{\mu}|$ of **9Ha**,**9HaP**, **9HaQ**, and **11Ha** for $S_1 \rightarrow S_0$ transitions.

	Transitions	ω_{CT}	$\lvert\boldsymbol{\mu}\rvert$
9Ha	$S_1 \rightarrow S_0$	0.72	149.23
9HaP	$S_1 \rightarrow S_0$	0.76	145.72
9HaQ	$S_1 \rightarrow S_0$	0.41	212.74
11Ha	$S_1 \rightarrow S_0$	0.73	259.60

Appendix C

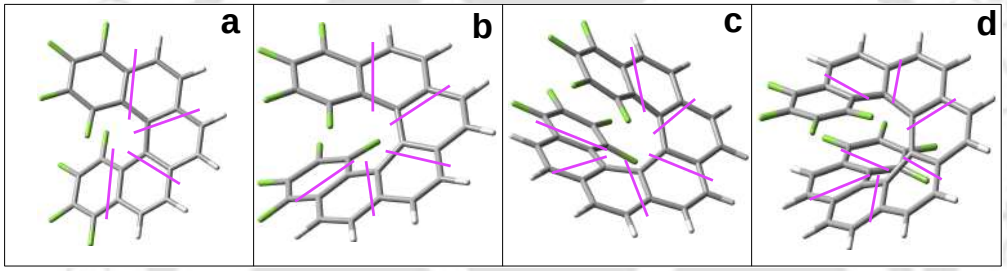

FIGURE C1: Fragmentation Scheme Used for Excited State Analysis using TheoDORE in cases of octafluorinated **5H**(a), **6H** (b), **7H** (c), and **8H** (d). Similar fragment definitions are used for other cases.

TABLE C1: Values of Selected Torsional Angles (ϕ, degrees) and R_{pitch} (Å) of Crystal Structures of **6H**, **4F6H**, **8F6H**, **7H**, **1F7H**, **2F′7H**, **4F7H**, **8H**, and **1F8H**. [a]See Ref[275]. [b]See Ref[55]. [c]See Ref[282]. [j]See Ref[283]. [d]See Ref[284]. [e]See Ref[285]. [f]See Ref[56]. [g]See Ref[286].

System	Torsional angles		R_{pitch}
	ϕ_1	ϕ_2	
6H[a]	12, 16	30, 31	3.94
4F6H[a]	17, 20	26, 25	3.63
4F6H[b]	19,14	30, 25	3.75
8F6H[b]	23, 22	27,24	3.76
7H[j]	17, 19	25,24	3.46
7H[c]	-18, -19	-24	3.49
7H[d]	-18, -21	-24, -26	3.59
1F7H[e]	-26, -19	-23, -27	3.51
	-25, -16	-23, -27	3.61
2F′7H[f]	-26, -16	-24, -31	3.51
	-26, -15	-24, -28	3.63
4F7H[g]	25-27, 15-16	18-21, 28	3.42
	-25 to -27, -17 to -21	-21 to -22, -27 to -28	3.36-3.44
1F8H[d]	-18, -16	-25, -28	3.46
	-20, -18	-27	3.48

TABLE C2: Excitation energies (λ_{abs}, nm), Corresponding Oscillator Strength(f_{osc}), Orbitals involved in the transitions, $|\boldsymbol{\mu}|$, $|\boldsymbol{m}|$, cos θ, R, g_{CD} and $|\boldsymbol{m}|/|\boldsymbol{\mu}|$ of **5H**. $|\boldsymbol{\mu}|$, $|\boldsymbol{m}|$, and R are in esu·cm, erg·G^{-1} and esu·cm·erg·G^{-1} units, respectively.

5H									
Excited States	λ_{abs}	f_{osc}	$R/10^{-40}$	$\|\boldsymbol{\mu}\|/10^{-20}$	$\|\boldsymbol{m}\|/10^{-20}$	cos θ	g_{CD}	$\|\boldsymbol{m}\|/\|\boldsymbol{\mu}\|$	Configurations
1 ^{1} A (S_1)	352	0.001	-2.25	26.97	0.08	-1	-0.0124	0.003	H →L (53.%),H-1→L+1(40.%)
1 ^{1} B (S_2)	309	0.004	21.85	50.42	0.53	0.82	0.0344	0.01	H-1→L (58.%),H →L+1(31.%)
2 ^{1} B (S_3)	294	0.096	131.00	245.22	1.71	0.31	0.0087	0.007	H-2→L (47.%),H-1→L (18.%)
3 ^{1} B (S_4)	293	0.539	352.70	580.17	3.08	0.2	0.0042	0.005	H →L+1(61.%),H-1→L (17.%)
2 ^{1} A (S_5)	285	0.112	-118.00	260.93	0.45	-1	-0.0069	0.002	H-1→L+1(46.%),H →L (38.%)
3 ^{1} A (S_6)	264	0.005	-8.29	53.62	0.15	-1	-0.0115	0.003	H-2→L+1(58.%),H →L+2(31.%)
4 ^{1} A (S_7)	261	0.124	-57.49	262.11	0.22	-1	-0.0033	0.001	H-3→L (31.%),H-2→L+1(24.%)
4 ^{1} B (S_8)	251	0.430	0.34	478.62	0.03	0.02	0	0	H-2→L (40.%),H-1→L+2(36.%)
5 ^{1} A (S_9)	248	0.145	-50.00	276.39	0.18	-1	-0.0026	0.001	H →L+2(27.%),H-1→L+3(25.%)
5 ^{1} B (S_{10})	243	0.019	-2.35	98.41	0.49	-0.05	-0.001	0.005	H-3→L+1(38.%),H →L+3(27.%)
6 ^{1} A (S_{11})	225	0.024	-6.52	106.47	0.06	-1	-0.0023	0.001	H-3→L (24.%),H-4→L (16.%)
6 ^{1} B (S_{12})	222	0.061	99.57	169.72	1.18	0.5	0.0138	0.007	H →L+3(45.%),H-3→L+1(30.%)
7 ^{1} B (S_{13})	216	0.082	215.80	193.70	1.34	0.83	0.023	0.007	H-2→L+2(55.%),H-4→L+1(8.%)
7 ^{1} A (S_{14})	216	1.136	-229.15	721.70	0.32	-1	-0.0018	0	H-1→L+3(54.%),H-3→L (22.%)
8 ^{1} B (S_{15})	215	0.018	23.36	90.18	0.37	0.7	0.0115	0.004	H →L+4(39.%),H-4→L+1(33.%)
8 ^{1} A (S_{16})	209	0.019	-15.24	92.50	0.16	-1	-0.0071	0.002	H-4→L (26.%),H-5→L+1(24.%)
9 ^{1} B (S_{17})	206	0.011	12.62	68.00	0.33	0.56	0.0109	0.005	H-5→L (32.%),H-1→L+8(21.%)
9 ^{1} A (S_{18})	203	0.030	7.27	113.29	0.06	1	0.0023	0.001	H-4→L (27.%),H-5→L+1(24.%)
10 ^{1} B (S_{19})	201	0.140	40.75	245.10	0.70	0.24	0.0027	0.003	H →L+4(37.%),H-4→L+1(32.%)
10 ^{1} A (S_{20})	199	0.030	31.20	113.57	0.27	1	0.0097	0.002	H-1→L+4(45.%),H-3→L+2(22.%)

TABLE C3: Excitation energies (λ_{abs}, nm), Corresponding Oscillator Strength(f_{osc}), Orbitals involved in the transitions, $|\boldsymbol{\mu}|$, $|\boldsymbol{m}|$, cos θ, R, g_{CD} and $|\boldsymbol{m}|/|\boldsymbol{\mu}|$ of **2F5H**. $|\boldsymbol{\mu}|$, $|\boldsymbol{m}|$, and R are in esu·cm, erg·G^{-1} and esu·cm·erg·G^{-1} units, respectively.

2F5H									
Excited States	λ_{abs}	f_{osc}	$R/10^{-40}$	$\|\boldsymbol{\mu}\|/10^{-20}$	$\|\boldsymbol{m}\|/10^{-20}$	cos θ	g_{CD}	$\|\boldsymbol{m}\|/\|\boldsymbol{\mu}\|$	Configurations
1 ^{1} A (S_1)	358	0.008	-10.86	77.82	0.14	-1	-0.0072	0.002	H →L+1(57.%),H-1→L (37.%)
1 ^{1} B (S_2)	319	0.172	83.95	342.00	1.50	0.16	0.0029	0.004	H →L (80.%),H-1→L+1(10.%)
2 ^{1} B (S_3)	292	0.005	26.36	56.07	0.47	0.99	0.0335	0.008	H-2→L+1(45.%),H →L+3(14.%)
2 ^{1} A (S_4)	286	0.168	-173.14	319.11	0.54	-1	-0.0068	0.002	H-1→L (47.%),H →L+1(32.%)
3 ^{1} B (S_5)	284	0.763	345.99	678.71	2.87	0.18	0.003	0.004	H-1→L+1(77.%),H →L (12.%)
3 ^{1} A (S_6)	266	0.165	-94.76	305.76	0.31	-1	-0.0041	0.001	H-2→L (79.%),H-1→L (6.%)
4 ^{1} A (S_7)	261	0.066	-18.61	191.02	0.10	-1	-0.002	0.001	H →L+2(62.%),H-3→L+1(16.%)
4 ^{1} B (S_8)	250	0.059	59.92	176.41	0.81	0.42	0.0077	0.005	H-2→L+1(38.%),H-3→L (25.%)
5 ^{1} A (S_9)	246	0.022	-0.93	106.44	0.01	-1	-0.0003	0	H-4→L+1(39.%),H →L+2(11.%)
5 ^{1} B (S_{10})	238	0.009	82.20	66.98	1.23	1	0.0733	0.018	H →L+3(30.%),H-4→L (30.%)
6 ^{1} A (S_{11})	235	0.105	-51.69	229.32	0.23	-1	-0.0039	0.001	H-3→L+1(47.%),H-4→L+1(17.%)
6 ^{1} B (S_{12})	234	0.050	-4.68	158.23	0.27	-0.11	-0.0007	0.002	H-1→L+2(38.%),H-4→L (22.%)
7 ^{1} B (S_{13})	223	0.146	174.76	262.83	1.42	0.47	0.0101	0.005	H →L+3(31.%),H-3→L (21.%)
7 ^{1} A (S_{14})	214	0.002	1.53	30.29	0.05	1	0.0067	0.002	H-4→L+1(23.%),H-5→L (17.%)
8 ^{1} B (S_{15})	214	0.031	91.72	118.16	0.79	0.98	0.0263	0.007	H-2→L+2(54.%),H →L+4(22.%)
8 ^{1} A (S_{16})	213	0.927	-30.46	647.77	0.05	-1	-0.0003	0	H-1→L+3(61.%),H-3→L+1(16.%)
9 ^{1} B (S_{17})	207	0.034	23.58	122.82	0.26	0.74	0.0063	0.002	H-5→L+1(38.%),H-6→L+1(15.%)
10 ^{1} B (S_{18})	206	0.031	12.83	115.71	1.27	0.09	0.0038	0.011	H →L+4(53.%),H-2→L+2(26.%)
9 ^{1} A (S_{19})	204	0.035	16.44	123.17	0.13	1	0.0043	0.001	H-5→L (43.%),H-2→L+3(17.%)
10 ^{1} A (S_{20})	197	0.123	-82.96	227.41	0.36	-1	-0.0064	0.002	H-6→L (38.%),H-4→L+2(17.%)

TABLE C4: Excitation energies (λ_{abs}, nm), Corresponding Oscillator Strength(f_{osc}), Orbitals involved in the transitions, $|\boldsymbol{\mu}|$, $|\boldsymbol{m}|$, cos θ, R, g_{CD} and $|\boldsymbol{m}|/|\boldsymbol{\mu}|$ of **4F5H**. $|\boldsymbol{\mu}|$, $|\boldsymbol{m}|$, and R are in esu·cm, erg·G^{-1} and esu·cm·erg·G^{-1} units, respectively.

4F5H									
Excited States	λ_{abs}	f_{osc}	$R/10^{-40}$	$\|\boldsymbol{\mu}\|/10^{-20}$	$\|\boldsymbol{m}\|/10^{-20}$	cos θ	g_{CD}	$\|\boldsymbol{m}\|/\|\boldsymbol{\mu}\|$	Configurations
1 ^{1} A (S_1)	362	0.024	-19.02	137.22	0.14	-1	-0.004	0.001	H →L+1(63.%),H-1→L (31.%)
1 ^{1} B (S_2)	326	0.203	101.88	375.00	1.50	0.18	0.0029	0.004	H →L (80.%),H-2→L+1(5.%)
2 ^{1} B (S_3)	300	0.018	64.40	106.36	0.70	0.87	0.0228	0.007	H-2→L+1(49.%),H-1→L+1(19.%)
2 ^{1} A (S_4)	291	0.076	-101.25	216.46	0.47	-1	-0.0086	0.002	H-1→L (41.%),H-2→L (28.%)
3 ^{1} B (S_5)	283	0.707	240.55	651.92	2.55	0.14	0.0023	0.004	H-1→L+1(70.%),H →L (10.%)
3 ^{1} A (S_6)	273	0.302	-162.44	418.71	0.39	-1	-0.0037	0.001	H-2→L (60.%),H-1→L (18.%)
4 ^{1} A (S_7)	263	0.038	3.47	145.52	0.02	1	0.0007	0	H →L+2(63.%),H-3→L+1(9.%)
4 ^{1} B (S_8)	255	0.023	48.77	111.65	0.87	0.5	0.0156	0.008	H-2→L+1(28.%),H-3→L (22.%)
5 ^{1} A (S_9)	250	0.014	-5.39	84.85	0.06	-1	-0.003	0.001	H-4→L+1(48.%),H-1→L+3(10.%)
5 ^{1} B (S_{10})	243	0.042	110.48	147.67	1.52	0.49	0.0203	0.01	H-4→L (47.%),H →L+3(38.%)
6 ^{1} A (S_{11})	236	0.044	-23.15	148.22	0.16	-1	-0.0042	0.001	H-3→L+1(45.%),H-1→L+3(24.%)
6 ^{1} B (S_{12})	232	0.052	-4.50	160.06	0.21	-0.13	-0.0007	0.001	H-1→L+2(56.%),H-3→L (25.%)
7 ^{1} B (S_{13})	224	0.188	182.38	299.07	1.16	0.52	0.0082	0.004	H-3→L (29.%),H →L+3(23.%)
7 ^{1} A (S_{14})	217	0.176	8.02	284.67	0.03	1	0.0004	0	H-4→L+1(25.%),H-3→L+1(22.%)
8 ^{1} B (S_{15})	216	0.020	52.54	96.61	0.84	0.65	0.0225	0.009	H-2→L+2(71.%),H-1→L+2(8.%)
8 ^{1} A (S_{16})	213	0.532	22.43	490.93	0.05	1	0.0004	0	H-1→L+3(52.%),H-2→L+3(18.%)
9 ^{1} B (S_{17})	208	0.050	59.37	148.26	0.75	0.53	0.0108	0.005	H-5→L+1(52.%),H-6→L+1(10.%)
9 ^{1} A (S_{18})	206	0.287	-52.93	354.78	0.15	-1	-0.0017	0	H-5→L (59.%),H-2→L+3(14.%)
10 ^{1} B (S_{19})	202	0.015	-3.92	79.92	0.99	-0.05	-0.0025	0.012	H →L+5(66.%),H →L+6(8.%)
10 ^{1} A (S_{20})	199	0.141	-105.93	243.94	0.43	-1	-0.0071	0.002	H-4→L+2(51.%),H-6→L (18.%)

TABLE C5: Excitation energies (λ_{abs}, nm), Corresponding Oscillator Strength(f_{osc}), Orbitals involved in the transitions, $|\boldsymbol{\mu}|$, $|\boldsymbol{m}|$, cos θ, R, g_{CD} and $|\boldsymbol{m}|/|\boldsymbol{\mu}|$ of **8F5H**. $|\boldsymbol{\mu}|$, $|\boldsymbol{m}|$, and R are in esu·cm, erg·G^{-1} and esu·cm·erg·G^{-1} units, respectively.

8F5H									
Excited States	λ_{abs}	f_{osc}	$R/10^{-40}$	$\|\boldsymbol{\mu}\|/10^{-20}$	$\|\boldsymbol{m}\|/10^{-20}$	cos θ	g_{CD}	$\|\boldsymbol{m}\|/\|\boldsymbol{\mu}\|$	Configurations
1 ^{1} A (S_1)	362	0.011	-7.50	91.01	0.08	-1	-0.0036	0.001	H →L+1(60.%),H-1→L (34.%)
1 ^{1} B (S_2)	323	0.161	77.99	332.86	1.42	0.16	0.0028	0.004	H →L (77.%),H-1→L+1(10.%)
2 ^{1} B (S_3)	296	0.021	1.69	115.92	0.06	0.23	0.0005	0.001	H-2→L+1(50.%),H →L+3(13.%)
2 ^{1} A (S_4)	288	0.145	-143.62	298.32	0.48	-1	-0.0065	0.002	H-1→L (45.%),H →L+1(28.%)
3 ^{1} B (S_5)	287	0.726	352.02	664.98	2.87	0.18	0.0032	0.004	H-1→L+1(82.%),H →L (10.%)
3 ^{1} A (S_6)	271	0.208	-106.66	346.46	0.31	-1	-0.0036	0.001	H-2→L (69.%),H-1→L (12.%)
4 ^{1} A (S_7)	261	0.014	2.66	87.35	0.03	1	0.0014	0	H →L+2(53.%),H-3→L+1(18.%)
4 ^{1} B (S_8)	253	0.061	44.26	180.47	0.65	0.37	0.0054	0.004	H-2→L+1(35.%),H-3→L (25.%)
5 ^{1} A (S_9)	246	0.037	-25.35	139.00	0.18	-1	-0.0052	0.001	H-4→L+1(36.%),H →L+2(18.%)
5 ^{1} B (S_{10})	239	0.013	101.77	80.86	1.42	0.88	0.0622	0.018	H-4→L (38.%),H →L+3(29.%)
6 ^{1} A (S_{11})	235	0.152	-64.39	275.65	0.23	-1	-0.0034	0.001	H-3→L+1(49.%),H-4→L+1(18.%)
6 ^{1} B (S_{12})	232	0.023	14.67	106.47	0.49	0.28	0.0052	0.005	H-3→L (34.%),H-1→L+2(34.%)
7 ^{1} B (S_{13})	225	0.246	140.63	342.93	1.08	0.38	0.0048	0.003	H →L+3(23.%),H-4→L (22.%)
7 ^{1} A (S_{14})	217	0.250	62.33	339.58	0.18	1	0.0022	0.001	H-4→L+1(25.%),H-3→L+1(18.%)
8 ^{1} A (S_{15})	215	0.528	-55.56	491.15	0.11	-1	-0.0009	0	H-1→L+3(60.%),H →L+2(7.%)
8 ^{1} B (S_{16})	214	0.021	89.82	98.66	0.96	0.95	0.0369	0.01	H-2→L+2(61.%),H →L+5(11.%)
9 ^{1} A (S_{17})	211	0.002	10.10	30.01	0.34	1	0.0449	0.011	H →L+4(39.%),H →L+6(11.%)
9 ^{1} B (S_{18})	208	0.024	11.37	103.59	0.27	0.41	0.0042	0.003	H-5→L+1(43.%),H-6→L+1(12.%)
10 ^{1} A (S_{19})	206	0.065	-16.30	168.42	0.10	-1	-0.0023	0.001	H-5→L (50.%),H-2→L+3(22.%)
10 ^{1} B (S_{20})	204	0.004	18.59	41.26	0.56	0.81	0.0437	0.013	H →L+9(25.%),H-2→L+4(22.%)

TABLE C6: Excitation energies (λ_{abs}, nm), Corresponding Oscillator Strength(f_{osc}), Orbitals involved in the transitions, $|\boldsymbol{\mu}|$, $|\boldsymbol{m}|$, cos θ, R, g_{CD} and $|\boldsymbol{m}|/|\boldsymbol{\mu}|$ of **6H**. $|\boldsymbol{\mu}|$, $|\boldsymbol{m}|$, and R are in esu·cm, erg·G^{-1} and esu·cm·erg·G^{-1} units, respectively.

6H									
Excited States	λ_{abs}	f_{osc}	$R/10^{-40}$	$\|\boldsymbol{\mu}\|/10^{-20}$	$\|\boldsymbol{m}\|/10^{-20}$	cos θ	g_{CD}	$\|\boldsymbol{m}\|/\|\boldsymbol{\mu}\|$	Configurations
$1\ ^1$B (S_1)	368	0.001	-0.98	29.06	0.13	-0.26	-0.0046	0.004	H-1→L (46.%),H →L+1(43.%)
$1\ ^1$A (S_2)	328	0.002	-1.62	41.28	0.04	-1.00	-0.0038	0.001	H →L (69.%),H-1→L+1(23.%)
$2\ ^1$B (S_3)	315	0.425	774.64	533.7	4.03	0.36	0.0109	0.008	H →L+1(48.%),H-1→L (40.%)
$2\ ^1$A (S_4)	313	0.013	-21.44	94.33	0.23	-1.00	-0.0096	0.002	H-3→L (28.%),H-2→L+1(18.%)
$3\ ^1$A (S_5)	293	0.151	-148.49	306.45	0.48	-1.00	-0.0063	0.002	H-1→L+1(63.%),H →L (12.%)
$3\ ^1$B (S_6)	292	0.019	25.04	107.59	0.48	0.48	0.0087	0.004	H-2→L (78.%),H-3→L+1(8.%)
$4\ ^1$A (S_7)	275	0.048	-51.85	168.18	0.31	-1.00	-0.0073	0.002	H-2→L+1(39.%),H-3→L (32.%)
$4\ ^1$B (S_8)	274	0.038	10.45	147.69	0.13	0.54	0.0019	0.001	H-3→L+1(38.%),H-2→L+3(13.%)
$5\ ^1$B (S_9)	270	0.009	4.89	71.11	0.47	0.15	0.0039	0.007	H →L+2(75.%),H-1→L+3(8.%)
$6\ ^1$B (S_{10})	261	0.019	-4.24	103.14	0.41	-0.10	-0.0016	0.004	H-3→L+1(31.%),H-1→L+3(30.%)
$5\ ^1$A (S_{11})	259	0.035	18.72	139.81	0.13	1.00	0.0038	0.001	H →L+3(32.%),H-3→L (23.%)
$6\ ^1$A (S_{12})	252	0.472	-185.84	503.06	0.37	-1.00	-0.0029	0.001	H-1→L+2(42.%),H →L+3(14.%)
$7\ ^1$B (S_{13})	250	0.357	-26.65	435.62	0.79	-0.08	-0.0006	0.002	H-1→L+3(44.%),H-2→L+3(16.%)
$7\ ^1$A (S_{14})	236	0.049	27.13	157.22	0.17	1.00	0.0044	0.001	H-4→L+1(42.%),H-1→L+4(10.%)
$8\ ^1$B (S_{15})	233	0.066	-5.89	180.62	0.14	-0.23	-0.0007	0.001	H-4→L (43.%),H-3→L+2(15.%)
$8\ ^1$A (S_{16})	233	0.728	-633.46	600.13	1.06	-1.00	-0.007	0.002	H-2→L+2(62.%),H →L+3(15.%)
$9\ ^1$B (S_{17})	222	0.123	201.29	241.1	1.26	0.66	0.0139	0.005	H-3→L+2(50.%),H-2→L+3(34.%)
$9\ ^1$A (S_{18})	220	0.035	-62.76	127.82	0.49	-1.00	-0.0154	0.004	H-1→L+4(21.%),H-5→L (12.%)
$10\ ^1$A (S_{19})	216	0.011	-50.66	72.27	0.7	-1.00	-0.0388	0.01	H-3→L+3(60.%),H →L+5(18.%)
$10\ ^1$B (S_{20})	214	0.097	73.46	210.07	0.56	0.62	0.0067	0.003	H-6→L (55.%),H →L+4(9.%)

TABLE C7: Excitation energies (λ_{abs}, nm), Corresponding Oscillator Strength(f_{osc}), Orbitals involved in the transitions, $|\boldsymbol{\mu}|$, $|\boldsymbol{m}|$, cos θ, R, g_{CD} and $|\boldsymbol{m}|/|\boldsymbol{\mu}|$ of **2F6H**. $|\boldsymbol{\mu}|$, $|\boldsymbol{m}|$, and R are in esu·cm, erg·G^{-1} and esu·cm·erg·G^{-1} units, respectively.

2F6H									
Excited States	λ_{abs}	f_{osc}	$R/10^{-40}$	$\|\boldsymbol{\mu}\|/10^{-20}$	$\|\boldsymbol{m}\|/10^{-20}$	cos θ	g_{CD}	$\|\boldsymbol{m}\|/\|\boldsymbol{\mu}\|$	Configurations
$1\ ^1$B (S_1)	375	0.004	-2.39	58.51	0.18	-0.23	-0.0028	0.003	H-1→L (50.%),H →L+1(40.%)
$1\ ^1$A (S_2)	335	0.000	-0.69	8.06	0.09	-1.00	-0.0426	0.011	H →L (71.%),H-1→L+1(20.%)
$2\ ^1$B (S_3)	320	0.410	567.34	528.43	3.91	0.27	0.0081	0.007	H →L+1(50.%),H-1→L (39.%)
$2\ ^1$A (S_4)	317	0.056	-69.17	194.88	0.35	-1.00	-0.0073	0.002	H-3→L (24.%),H-2→L+1(20.%)
$3\ ^1$B (S_5)	299	0.009	71.22	76.3	1.12	0.84	0.0489	0.015	H-2→L (87.%),H-1→L (3.%)
$3\ ^1$A (S_6)	296	0.149	-135.62	306.19	0.44	-1.00	-0.0058	0.001	H-1→L+1(63.%),H →L+2(13.%)
$4\ ^1$A (S_7)	278	0.015	-10.22	94.54	0.11	-1.00	-0.0046	0.001	H-2→L+1(48.%),H-3→L (23.%)
$4\ ^1$B (S_8)	276	0.052	-10.82	174.1	0.31	-0.20	-0.0014	0.002	H-4→L (28.%),H-2→L+2(18.%)
$5\ ^1$B (S_9)	267	0.013	-6.68	84.74	0.08	-0.98	-0.0037	0.001	H-1→L+2(61.%),H →L+3(22.%)
$6\ ^1$B (S_{10})	263	0.011	18.91	78.63	0.51	0.47	0.0122	0.006	H →L+3(44.%),H-3→L+1(40.%)
$5\ ^1$A (S_{11})	260	0.337	-83.25	431.57	0.19	-1.00	-0.0018	0	H-3→L (39.%),H →L+2(37.%)
$6\ ^1$A (S_{12})	253	0.215	-35.24	339.96	0.1	-1.00	-0.0012	0	H-1→L+3(64.%),H-4→L+1(10.%)
$7\ ^1$B (S_{13})	249	0.280	-9.17	384.72	0.86	-0.03	-0.0002	0.002	H-3→L+1(30.%),H-2→L+2(24.%)
$7\ ^1$A (S_{14})	237	0.011	24.75	74.43	0.33	1.00	0.0179	0.004	H-4→L+1(34.%),H-2→L+3(13.%)
$8\ ^1$B (S_{15})	237	0.111	159.19	235.8	0.95	0.71	0.0115	0.004	H-4→L (41.%),H-2→L+2(20.%)
$8\ ^1$A (S_{16})	228	0.566	-255.54	523.95	0.49	-1.00	-0.0037	0.001	H-2→L+3(27.%),H-5→L (26.%)
$9\ ^1$A (S_{17})	225	0.313	-159.31	387.3	0.41	-1.00	-0.0042	0.001	H-2→L+3(27.%),H-4→L+1(24.%)
$10\ ^1$A (S_{18})	222	0.012	-24.91	73.66	0.34	-1.00	-0.0184	0.005	H-5→L (26.%),H-3→L+2(26.%)
$9\ ^1$B (S_{19})	221	0.081	30.69	194.53	0.88	0.18	0.0032	0.005	H-3→L+3(29.%),H-2→L+2(20.%)
$10\ ^1$B (S_{20})	217	0.014	56.07	80.67	0.7	0.99	0.0345	0.009	H-6→L (47.%),H-3→L+3(31.%)

TABLE C8: Excitation energies (λ_{abs}, nm), Corresponding Oscillator Strength(f_{osc}), Orbitals involved in the transitions, $|\boldsymbol{\mu}|$, $|\boldsymbol{m}|$, cos θ, R, g_{CD} and $|\boldsymbol{m}|/|\boldsymbol{\mu}|$ of **4F6H**. $|\boldsymbol{\mu}|$, $|\boldsymbol{m}|$, and R are in esu·cm, erg·G^{-1} and esu·cm·erg·G^{-1} units, respectively.

4F6H									
Excited States	λ_{abs}	f_{osc}	$R/10^{-40}$	$\|\boldsymbol{\mu}\|/10^{-20}$	$\|\boldsymbol{m}\|/10^{-20}$	cos θ	g_{CD}	$\|\boldsymbol{m}\|/\|\boldsymbol{\mu}\|$	Configurations
$1\ ^1$B (S_1)	377	0.006	-0.54	71.21	0.08	-0.10	-0.0004	0.001	H-1→L (47.%),H →L+1(43.%)
$1\ ^1$A (S_2)	339	0.002	2.38	33.16	0.07	1.00	0.0087	0.002	H →L (64.%),H-1→L+1(25.%)
$2\ ^1$B (S_3)	325	0.376	461.63	509.48	3.5	0.26	0.0071	0.007	H-1→L (43.%),H →L+1(42.%)
$2\ ^1$A (S_4)	325	0.086	-92.80	243.59	0.38	-1.00	-0.0063	0.002	H →L (22.%),H-3→L (22.%)
$3\ ^1$B (S_5)	306	0.017	178.33	103.69	1.81	0.95	0.0663	0.017	H-2→L (89.%),H-4→L (3.%)
$3\ ^1$A (S_6)	296	0.110	-111.19	263.47	0.42	-1.00	-0.0064	0.002	H-1→L+1(54.%),H →L+2(22.%)
$4\ ^1$A (S_7)	282	0.024	-8.06	118.87	0.07	-1.00	-0.0023	0.001	H-2→L+1(54.%),H-3→L (24.%)
$4\ ^1$B (S_8)	281	0.107	-39.48	253.39	0.34	-0.46	-0.0025	0.001	H-2→L+2(19.%),H-4→L (18.%)
$5\ ^1$B (S_9)	270	0.001	9.84	17.24	0.57	1.00	0.1323	0.033	H-1→L+2(62.%),H-3→L+1(14.%)
$5\ ^1$A (S_{10})	266	0.412	-79.29	482.75	0.16	-1.00	-0.0014	0	H →L+2(39.%),H-3→L (34.%)
$6\ ^1$B (S_{11})	265	0.016	14.82	95.73	0.44	0.35	0.0065	0.005	H →L+3(53.%),H-3→L+1(32.%)
$6\ ^1$A (S_{12})	256	0.087	-7.81	217.86	0.04	-1.00	-0.0007	0	H-1→L+3(69.%),H-4→L+1(11.%)
$7\ ^1$B (S_{13})	251	0.226	-61.46	347.19	0.65	-0.27	-0.002	0.002	H-2→L+2(38.%),H-3→L+1(24.%)
$7\ ^1$A (S_{14})	241	0.008	-30.13	65.72	0.46	-1.00	-0.0279	0.007	H-2→L+3(29.%),H-4→L+1(22.%)
$8\ ^1$B (S_{15})	238	0.156	190.16	281.33	1	0.68	0.0096	0.004	H-4→L (43.%),H →L+4(14.%)
$8\ ^1$A (S_{16})	230	0.237	-48.31	340.09	0.14	-1.00	-0.0017	0	H-3→L+2(41.%),H-5→L (12.%)
$9\ ^1$A (S_{17})	226	0.264	-62.84	356.26	0.18	-1.00	-0.002	0	H-2→L+3(32.%),H-4→L+1(21.%)
$10\ ^1$A (S_{18})	224	0.470	-281.92	472.98	0.6	-1.00	-0.005	0.001	H-5→L (39.%),H-4→L+1(17.%)
$9\ ^1$B (S_{19})	222	0.093	47.89	209.09	1.05	0.22	0.0044	0.005	H-3→L+3(36.%),H-4→L (12.%)
$10\ ^1$B (S_{20})	220	0.022	43.81	102.08	0.47	0.92	0.0168	0.005	H-3→L+3(38.%),H-6→L (36.%)

TABLE C9: Excitation energies (λ_{abs}, nm), Corresponding Oscillator Strength(f_{osc}), Orbitals involved in the transitions, $|\boldsymbol{\mu}|$, $|\boldsymbol{m}|$, cos θ, R, g_{CD} and $|\boldsymbol{m}|/|\boldsymbol{\mu}|$ of **8F6H**. $|\boldsymbol{\mu}|$, $|\boldsymbol{m}|$, and R are in esu·cm, erg·G^{-1} and esu·cm·erg·G^{-1} units, respectively.

8F6H									
Excited States	λ_{abs}	f_{osc}	$R/10^{-40}$	$\|\boldsymbol{\mu}\|/10^{-20}$	$\|\boldsymbol{m}\|/10^{-20}$	cos θ	g_{CD}	$\|\boldsymbol{m}\|/\|\boldsymbol{\mu}\|$	Configurations
$1\ ^1$B (S_1)	377	0.008	-1.22	79.65	0.3	-0.05	-0.0008	0.004	H →L (52.%),H-1→L+1(39.%)
$1\ ^1$A (S_2)	339	0.002	1.61	40.61	0.04	1.00	0.0039	0.001	H-1→L (55.%),H →L+1(28.%)
$2\ ^1$B (S_3)	322	0.397	512.27	521.89	3.69	0.27	0.0075	0.007	H-1→L+1(47.%),H →L (40.%)
$2\ ^1$A (S_4)	319	0.064	-69.56	208.28	0.33	-1.00	-0.0064	0.002	H-1→L (31.%),H-3→L (22.%)
$3\ ^1$B (S_5)	299	0.013	138.18	91.55	1.57	0.96	0.0659	0.017	H-2→L (87.%),H-1→L+1(3.%)
$3\ ^1$A (S_6)	297	0.148	-144.53	305.87	0.47	-1.00	-0.0062	0.002	H →L+1(56.%),H-1→L+2(17.%)
$4\ ^1$B (S_7)	280	0.070	-14.37	203.66	0.09	-0.82	-0.0014	0	H-4→L (27.%),H-2→L+2(14.%)
$4\ ^1$A (S_8)	278	0.029	-16.64	131.45	0.13	-1.00	-0.0039	0.001	H-2→L+1(48.%),H-3→L (29.%)
$5\ ^1$B (S_9)	269	0.002	-3.20	33.91	0.19	-0.49	-0.0111	0.006	H →L+2(52.%),H-1→L+3(31.%)
$6\ ^1$B (S_{10})	265	0.006	11.53	58.4	0.46	0.42	0.0135	0.008	H-3→L+1(41.%),H-1→L+3(36.%)
$5\ ^1$A (S_{11})	262	0.304	-57.29	411.04	0.14	-1.00	-0.0014	0	H-1→L+2(42.%),H-3→L (31.%)
$6\ ^1$A (S_{12})	257	0.166	-34.30	300.84	0.11	-1.00	-0.0015	0	H →L+3(64.%),H-4→L+1(12.%)
$7\ ^1$B (S_{13})	249	0.293	-14.28	393.9	0.82	-0.04	-0.0004	0.002	H-3→L+1(27.%),H-2→L+2(26.%)
$7\ ^1$A (S_{14})	240	0.017	22.38	93.43	0.24	1.00	0.0103	0.003	H-4→L+1(32.%),H-2→L+3(21.%)
$8\ ^1$B (S_{15})	238	0.153	153.91	278.39	0.77	0.72	0.0079	0.003	H-4→L (45.%),H-2→L+2(17.%)
$8\ ^1$A (S_{16})	231	0.693	-295.57	582.81	0.51	-1.00	-0.0035	0.001	H-2→L+3(26.%),H-5→L (23.%)
$9\ ^1$A (S_{17})	228	0.214	-53.65	321.97	0.17	-1.00	-0.0021	0.001	H-4→L+1(26.%),H-2→L+3(17.%)
$10\ ^1$A (S_{18})	222	0.043	-62.55	143.23	0.44	-1.00	-0.0122	0.003	H-5→L (33.%),H-3→L+2(30.%)
$9\ ^1$B (S_{19})	222	0.066	100.76	176.7	1.2	0.47	0.0129	0.007	H-3→L+3(53.%),H-2→L+2(17.%)
$10\ ^1$B (S_{20})	218	0.010	8.21	69.34	0.13	0.92	0.0068	0.002	H-6→L (31.%),H-5→L+1(30.%)

TABLE C10: Excitation energies (λ_{abs}, nm), Corresponding Oscillator Strength(f_{osc}), Orbitals involved in the transitions, $|\boldsymbol{\mu}|$, $|\boldsymbol{m}|$, cos θ, R, g_{CD} and $|\boldsymbol{m}|/|\boldsymbol{\mu}|$ of **7H**. $|\boldsymbol{\mu}|$, $|\boldsymbol{m}|$, and R are in esu·cm, erg·G^{-1} and esu·cm·erg·G^{-1} units, respectively.

7H									
Excited States	λ_{abs}	f_{osc}	$R/10^{-40}$	$\|\boldsymbol{\mu}\|/10^{-20}$	$\|\boldsymbol{m}\|/10^{-20}$	cos θ	g_{CD}	$\|\boldsymbol{m}\|/\|\boldsymbol{\mu}\|$	Configurations
1 ^{1} A (S_1)	392	0.000	0.00	9.61	0	-1	-0.0002	0	H →L (52.%),H-1→L+1(40.%)
1 ^{1} B (S_2)	354	0.087	638.49	255.72	3.8	0.66	0.039	0.015	H-1→L (82.%),H →L+1(10.%)
2 ^{1} B (S_3)	347	0.014	68.44	102.99	1.43	0.47	0.0258	0.014	H →L+1(65.%),H-1→L (13.%)
3 ^{1} B (S_4)	338	0.035	38.71	159.43	1.18	0.2	0.0061	0.007	H-2→L (44.%),H →L+1(19.%)
2 ^{1} A (S_5)	325	0.031	-46.63	145.28	0.32	-1	-0.0088	0.002	H-1→L+1(47.%),H →L (38.%)
3 ^{1} A (S_6)	313	0.042	-39.26	167.85	0.23	-1	-0.0056	0.001	H-2→L+1(60.%),H-3→L (21.%)
4 ^{1} A (S_7)	302	0.059	-78.43	194.85	0.4	-1	-0.0083	0.002	H-3→L (45.%),H-2→L+1(16.%)
4 ^{1} B (S_8)	295	0.106	-44.03	257.67	0.65	-0.26	-0.0027	0.003	H-3→L+1(32.%),H-2→L (29.%)
5 ^{1} A (S_9)	287	0.059	-51.88	189.98	0.27	-1	-0.0057	0.001	H →L+2(49.%),H-1→L+3(17.%)
5 ^{1} B (S_{10})	285	0.020	1.50	108.99	0.54	0.03	0.0005	0.005	H-1→L+2(55.%),H-3→L+1(30.%)
6 ^{1} A (S_{11})	274	0.170	-275.94	314.73	0.88	-1	-0.0111	0.003	H-4→L (29.%),H-3→L (18.%)
6 ^{1} B (S_{12})	270	0.083	-13.50	218.38	0.59	-0.1	-0.0011	0.003	H-5→L (44.%),H →L+3(23.%)
7 ^{1} B (S_{13})	267	0.011	10.77	77.34	0.36	0.39	0.0072	0.005	H-4→L+1(44.%),H →L+3(22.%)
7 ^{1} A (S_{14})	263	0.180	-302.89	317.33	0.95	-1	-0.012	0.003	H-1→L+3(41.%),H-4→L (19.%)
8 ^{1} A (S_{15})	258	0.438	-158.19	490.67	0.32	-1	-0.0026	0.001	H-4→L (36.%),H-1→L+3(20.%)
8 ^{1} B (S_{16})	257	0.049	121.73	163.72	0.81	0.91	0.0182	0.005	H-2→L+2(65.%),H-4→L+1(14.%)
9 ^{1} B (S_{17})	252	0.358	-125.22	438.13	0.29	-0.99	-0.0026	0.001	H-4→L+1(28.%),H →L+3(15.%)
9 ^{1} A (S_{18})	246	0.420	-289.23	468.96	0.62	-1	-0.0053	0.001	H-5→L+1(53.%),H-3→L+2(14.%)
10 ^{1} A (S_{19})	240	0.002	-40.88	34.61	1.18	-1	-0.1363	0.034	H-2→L+3(53.%),H-3→L+2(21.%)
10 ^{1} B (S_{20})	236	0.081	156.71	201.78	1.02	0.76	0.0154	0.005	H →L+4(60.%),H-3→L+3(10.%)

TABLE C11: Excitation energies (λ_{abs}, nm), Corresponding Oscillator Strength(f_{osc}), Orbitals involved in the transitions, $|\boldsymbol{\mu}|$, $|\boldsymbol{m}|$, cos θ, R, g_{CD} and $|\boldsymbol{m}|/|\boldsymbol{\mu}|$ of **2F7H**. $|\boldsymbol{\mu}|$, $|\boldsymbol{m}|$, and R are in esu·cm, erg·G^{-1} and esu·cm·erg·G^{-1} units, respectively.

2F7H									
Excited States	λ_{abs}	f_{osc}	$R/10^{-40}$	$\|\boldsymbol{\mu}\|/10^{-20}$	$\|\boldsymbol{m}\|/10^{-20}$	cos θ	g_{CD}	$\|\boldsymbol{m}\|/\|\boldsymbol{\mu}\|$	Configurations
1 ^{1} A (S_1)	397	0.000	-0.28	4.43	0.06	-1	-0.0574	0.014	H →L+1(55.%),H-1→L (37.%)
1 ^{1} B (S_2)	363	0.062	301.72	219.17	2.91	0.47	0.0251	0.013	H →L (92.%),H →L+3(2.%)
2 ^{1} B (S_3)	346	0.081	324.80	244.66	2.81	0.47	0.0217	0.011	H-1→L+1(75.%),H-3→L (9.%)
3 ^{1} B (S_4)	330	0.008	84.60	75.31	1.12	1	0.0597	0.015	H-2→L+1(35.%),H-1→L+1(18.%)
2 ^{1} A (S_5)	328	0.079	-133.47	234.95	0.57	-1	-0.0097	0.002	H-1→L (50.%),H →L+1(39.%)
3 ^{1} A (S_6)	307	0.035	-10.64	150.35	0.07	-1	-0.0019	0	H-2→L (59.%),H-3→L+1(21.%)
4 ^{1} A (S_7)	299	0.016	-14.32	100.02	0.14	-1	-0.0057	0.001	H →L+2(59.%),H-3→L+1(17.%)
4 ^{1} B (S_8)	296	0.018	-25.32	105.45	0.34	-0.7	-0.0091	0.003	H-2→L+1(42.%),H →L+3(19.%)
5 ^{1} A (S_9)	290	0.048	-24.28	171.87	0.14	-1	-0.0033	0.001	H-1→L+3(25.%),H-4→L+1(22.%)
6 ^{1} A (S_{10})	284	0.067	-163.82	201.37	0.81	-1	-0.0162	0.004	H-4→L+1(38.%),H-3→L+1(30.%)
5 ^{1} B (S_{11})	283	0.018	55.22	102.74	0.76	0.71	0.0209	0.007	H →L+3(34.%),H-4→L (31.%)
6 ^{1} B (S_{12})	280	0.034	-44.37	143.02	0.34	-0.91	-0.0087	0.002	H-1→L+2(52.%),H-4→L (18.%)
7 ^{1} B (S_{13})	268	0.203	-46.55	340.54	0.53	-0.26	-0.0016	0.002	H-5→L+1(29.%),H-3→L (16.%)
7 ^{1} A (S_{14})	266	0.337	-357.04	436.55	0.82	-1	-0.0075	0.002	H-1→L+3(40.%),H-5→L (13.%)
8 ^{1} A (S_{15})	260	0.454	-145.55	500.7	0.29	-1	-0.0023	0.001	H-3→L+1(24.%),H-4→L+1(20.%)
8 ^{1} B (S_{16})	258	0.282	-43.17	393.08	0.11	-0.99	-0.0011	0	H-4→L (15.%),H-5→L+1(15.%)
9 ^{1} B (S_{17})	254	0.022	65.32	108.95	0.68	0.88	0.022	0.006	H-2→L+2(71.%),H-3→L+3(7.%)
9 ^{1} A (S_{18})	248	0.261	-157.57	371.41	0.42	-1	-0.0046	0.001	H-5→L (45.%),H-3→L+2(12.%)
10 ^{1} A (S_{19})	242	0.084	-193.12	207.48	0.93	-1	-0.0179	0.004	H-2→L+3(55.%),H-4→L+2(18.%)
10 ^{1} B (S_{20})	239	0.092	297.26	216.5	1.37	1	0.0254	0.006	H →L+4(26.%),H-3→L+3(20.%)

TABLE C12: Excitation energies (λ_{abs}, nm), Corresponding Oscillator Strength(f_{osc}), Orbitals involved in the transitions, $|\boldsymbol{\mu}|$, $|\boldsymbol{m}|$, cos θ, R, g_{CD} and $|\boldsymbol{m}|/|\boldsymbol{\mu}|$ of **4F7H**. $|\boldsymbol{\mu}|$, $|\boldsymbol{m}|$, and R are in esu·cm, erg·G^{-1} and esu·cm·erg·G^{-1} units, respectively.

4F7H									
Excited States	λ_{abs}	f_{osc}	$R/10^{-40}$	$\|\boldsymbol{\mu}\|/10^{-20}$	$\|\boldsymbol{m}\|/10^{-20}$	cos θ	g_{CD}	$\|\boldsymbol{m}\|/\|\boldsymbol{\mu}\|$	Configurations
1 ^{1} A (S_1)	399	0.000	-1.76	18.63	0.09	-1	-0.0203	0.005	H →L+1(56.%),H-1→L (36.%)
1 ^{1} B (S_2)	370	0.051	304.25	200.36	2.84	0.53	0.0303	0.014	H →L (89.%),H →L+3(4.%)
2 ^{1} B (S_3)	345	0.091	282.61	258.34	2.86	0.38	0.0169	0.011	H-1→L+1(73.%),H-3→L (9.%)
3 ^{1} B (S_4)	335	0.014	80.95	100.14	0.92	0.88	0.0323	0.009	H-2→L+1(42.%),H-1→L+1(17.%)
2 ^{1} A (S_5)	330	0.067	-124.72	216.2	0.58	-1	-0.0107	0.003	H-1→L (48.%),H →L+1(36.%)
3 ^{1} A (S_6)	315	0.083	-60.43	235.91	0.26	-1	-0.0043	0.001	H-2→L (72.%),H-3→L+1(7.%)
4 ^{1} B (S_7)	302	0.009	-25.27	75.81	0.44	-0.75	-0.0176	0.006	H-2→L+1(36.%),H →L+3(21.%)
4 ^{1} A (S_8)	301	0.027	-34.45	131	0.26	-1	-0.008	0.002	H →L+2(59.%),H-3→L+1(14.%)
5 ^{1} A (S_9)	295	0.025	12.17	124.86	0.1	1	0.0031	0.001	H-4→L+1(39.%),H-1→L+3(16.%)
5 ^{1} B (S_{10})	291	0.008	41.15	69.61	0.78	0.76	0.034	0.011	H-4→L (54.%),H →L+3(34.%)
6 ^{1} A (S_{11})	286	0.016	-60.97	99.66	0.61	-1	-0.0246	0.006	H-3→L+1(32.%),H-1→L+3(29.%)
6 ^{1} B (S_{12})	281	0.013	-24.39	89.2	0.4	-0.68	-0.0123	0.005	H-1→L+2(60.%),H-3→L (25.%)
7 ^{1} B (S_{13})	272	0.269	-39.53	394.77	0.42	-0.24	-0.001	0.001	H-3→L (28.%),H-5→L+1(23.%)
7 ^{1} A (S_{14})	271	0.234	-233.52	366.63	0.64	-1	-0.0069	0.002	H-1→L+3(36.%),H-5→L (16.%)
8 ^{1} A (S_{15})	264	0.463	-251.87	509.36	0.49	-1	-0.0039	0.001	H-3→L+1(37.%),H-4→L+2(13.%)
8 ^{1} B (S_{16})	261	0.158	-35.68	296.46	0.41	-0.29	-0.0016	0.001	H-2→L+2(42.%),H-4→L (14.%)
9 ^{1} B (S_{17})	258	0.085	42.75	215.82	0.75	0.26	0.0037	0.003	H-2→L+2(33.%),H-4→L+3(17.%)
9 ^{1} A (S_{18})	250	0.310	-170.03	405.76	0.42	-1	-0.0041	0.001	H-5→L (34.%),H-4→L+2(18.%)
10 ^{1} A (S_{19})	248	0.081	-171.41	205.98	0.83	-1	-0.0162	0.004	H-2→L+3(40.%),H-4→L+2(30.%)
10 ^{1} B (S_{20})	242	0.098	238.06	224.26	1.09	0.98	0.0189	0.005	H-4→L+3(33.%),H-5→L+1(31.%)

TABLE C13: Excitation energies (λ_{abs}, nm), Corresponding Oscillator Strength(f_{osc}), Orbitals involved in the transitions, $|\boldsymbol{\mu}|$, $|\boldsymbol{m}|$, cos θ, R, g_{CD} and $|\boldsymbol{m}|/|\boldsymbol{\mu}|$ of **8F7H**. $|\boldsymbol{\mu}|$, $|\boldsymbol{m}|$, and R are in esu·cm, erg·G^{-1} and esu·cm·erg·G^{-1} units, respectively.

8F7H									
Excited States	λ_{abs}	f_{osc}	$R/10^{-40}$	$\|\boldsymbol{\mu}\|/10^{-20}$	$\|\boldsymbol{m}\|/10^{-20}$	cos θ	g_{CD}	$\|\boldsymbol{m}\|/\|\boldsymbol{\mu}\|$	Configurations
1 ^{1} A (S_1)	399	0.000	0.17	3.87	0.04	1	0.0457	0.011	H →L+1(54.%),H-1→L (38.%)
1 ^{1} B (S_2)	367	0.041	258.47	177.77	2.64	0.55	0.0327	0.015	H →L (87.%),H-2→L+1(3.%)
2 ^{1} B (S_3)	352	0.093	349.49	263.23	3.03	0.44	0.0202	0.012	H-1→L+1(76.%),H-1→L+2(7.%)
3 ^{1} B (S_4)	332	0.007	61.42	71.97	0.9	0.95	0.0474	0.012	H-2→L+1(44.%),H-1→L+1(14.%)
2 ^{1} A (S_5)	330	0.081	-140.38	238.39	0.59	-1	-0.0099	0.002	H-1→L (49.%),H →L+1(40.%)
3 ^{1} A (S_6)	314	0.047	-31.44	177.95	0.18	-1	-0.004	0.001	H-2→L (67.%),H-3→L+1(12.%)
4 ^{1} A (S_7)	300	0.012	-9.26	88.45	0.1	-1	-0.0047	0.001	H →L+2(56.%),H-3→L+1(17.%)
4 ^{1} B (S_8)	299	0.015	-25.99	96.27	0.39	-0.69	-0.0112	0.004	H-2→L+1(39.%),H →L+3(27.%)
5 ^{1} A (S_9)	293	0.034	-16.07	145.22	0.11	-1	-0.003	0.001	H-1→L+3(25.%),H-4→L+1(20.%)
5 ^{1} B (S_{10})	284	0.022	2.40	114.13	0.56	0.04	0.0007	0.005	H-4→L (57.%),H →L+3(29.%)
6 ^{1} A (S_{11})	284	0.013	-57.20	89.93	0.64	-1	-0.0283	0.007	H-4→L+1(43.%),H-3→L+1(26.%)
6 ^{1} B (S_{12})	282	0.014	-20.44	92.79	0.38	-0.58	-0.0095	0.004	H-1→L+2(59.%),H-3→L (24.%)
7 ^{1} B (S_{13})	273	0.179	-30.85	322.06	0.45	-0.21	-0.0012	0.001	H-5→L+1(33.%),H-3→L (30.%)
7 ^{1} A (S_{14})	271	0.364	-386.00	457.91	0.84	-1	-0.0074	0.002	H-1→L+3(35.%),H-5→L (19.%)
8 ^{1} A (S_{15})	261	0.458	-187.02	504.38	0.37	-1	-0.0029	0.001	H-3→L+1(32.%),H-4→L+1(15.%)
8 ^{1} B (S_{16})	259	0.166	-28.94	302.09	0.46	-0.21	-0.0013	0.002	H-2→L+2(46.%),H-4→L (16.%)
9 ^{1} B (S_{17})	258	0.184	62.80	317.8	0.79	0.25	0.0025	0.002	H-2→L+2(28.%),H-5→L+1(12.%)
9 ^{1} A (S_{18})	251	0.262	-14.38	373.87	0.04	-1	-0.0004	0	H-5→L (52.%),H →L+5(7.%)
10 ^{1} A (S_{19})	245	0.110	-228.95	239.15	0.96	-1	-0.016	0.004	H-2→L+3(39.%),H-4→L+2(38.%)
10 ^{1} B (S_{20})	241	0.092	259.84	217.08	1.21	0.99	0.0221	0.006	H-4→L+3(33.%),H →L+4(21.%)

TABLE C14: Excitation energies (λ_{abs}, nm), Corresponding Oscillator Strength(f_{osc}), Orbitals involved in the transitions, $|\boldsymbol{\mu}|$, $|\boldsymbol{m}|$, cos θ, R, g_{CD} and $|\boldsymbol{m}|/|\boldsymbol{\mu}|$ of **8H**. $|\boldsymbol{\mu}|$, $|\boldsymbol{m}|$, and R are in esu·cm, erg·G^{-1} and esu·cm·erg·G^{-1} units, respectively.

8H									
Excited States	λ_{abs}	f_{osc}	$R/10^{-40}$	$\|\boldsymbol{\mu}\|/10^{-20}$	$\|\boldsymbol{m}\|/10^{-20}$	cos θ	g_{CD}	$\|\boldsymbol{m}\|/\|\boldsymbol{\mu}\|$	Configurations
$1\ ^1$B (S_1)	406	0.000	-0.30	7.08	0.05	-0.93	-0.0242	0.006	H-1→L+1(45.%),H →L (40.%)
$2\ ^1$B (S_2)	371	0.076	807.44	244.74	4.23	0.78	0.0539	0.017	H-1→L+1(48.%),H →L (38.%)
$1\ ^1$A (S_3)	369	0.009	-34.44	83.46	0.41	-1	-0.0198	0.005	H →L+1(63.%),H-1→L (14.%)
$2\ ^1$A (S_4)	354	0.004	-13.47	57.11	0.24	-1	-0.0165	0.004	H-1→L (45.%),H-2→L+1(35.%)
$3\ ^1$B (S_5)	340	0.009	2.27	79.54	0.58	0.05	0.0014	0.007	H-2→L (77.%),H →L (15.%)
$3\ ^1$A (S_6)	337	0.038	-74.16	166.05	0.45	-1	-0.0108	0.003	H-1→L (37.%),H →L+1(29.%)
$4\ ^1$A (S_7)	319	0.093	-228.78	250.72	0.91	-1	-0.0146	0.004	H-3→L (49.%),H-2→L+1(25.%)
$4\ ^1$B (S_8)	318	0.020	-25.54	117.52	0.23	-0.93	-0.0074	0.002	H-3→L+1(59.%),H-4→L (12.%)
$5\ ^1$B (S_9)	302	0.002	9.11	31.39	0.32	0.92	0.037	0.01	H-1→L+2(54.%),H-4→L (14.%)
$5\ ^1$A (S_{10})	300	0.011	-31.38	83.68	0.38	-1	-0.0179	0.004	H →L+2(56.%),H-3→L (18.%)
$6\ ^1$B (S_{11})	293	0.022	-16.79	116.28	0.38	-0.38	-0.005	0.003	H →L+3(32.%),H-1→L+2(24.%)
$6\ ^1$A (S_{12})	290	0.007	3.31	63.07	0.05	1	0.0033	0.001	H-4→L+1(57.%),H-5→L (16.%)
$7\ ^1$A (S_{13})	284	0.081	-106.85	221.11	0.48	-1	-0.0087	0.002	H-1→L+3(30.%),H-2→L+2(22.%)
$7\ ^1$B (S_{14})	284	0.027	-48.64	128.05	0.66	-0.57	-0.0119	0.005	H-2→L+3(29.%),H →L+3(23.%)
$8\ ^1$A (S_{15})	282	0.049	-229.64	170.56	1.35	-1	-0.0316	0.008	H-2→L+2(52.%),H-1→L+3(19.%)
$8\ ^1$B (S_{16})	277	0.128	-46.46	274.68	0.25	-0.68	-0.0025	0.001	H-4→L (31.%),H-5→L+1(16.%)
$9\ ^1$A (S_{17})	268	0.347	-473.30	444.54	1.06	-1	-0.0096	0.002	H →L+4(35.%),H-5→L (18.%)
$9\ ^1$B (S_{18})	265	0.074	-46.97	203.86	0.6	-0.38	-0.0045	0.003	H-5→L+1(30.%),H-1→L+4(22.%)
$10\ ^1$B (S_{19})	259	0.170	303.77	306.18	1.07	0.93	0.013	0.003	H-3→L+2(40.%),H-2→L+3(18.%)
$10\ ^1$A (S_{20})	256	0.031	-23.70	130.37	0.18	-1	-0.0056	0.001	H-2→L+4(38.%),H-4→L+2(15.%)

TABLE C15: Excitation energies (λ_{abs}, nm), Corresponding Oscillator Strength(f_{osc}), Orbitals involved in the transitions, $|\boldsymbol{\mu}|$, $|\boldsymbol{m}|$, cos θ, R, g_{CD} and $|\boldsymbol{m}|/|\boldsymbol{\mu}|$ of **2F8H**. $|\boldsymbol{\mu}|$, $|\boldsymbol{m}|$, and R are in esu·cm, erg·G^{-1} and esu·cm·erg·G^{-1} units, respectively.

2F8H									
Excited States	λ_{abs}	f_{osc}	$R/10^{-40}$	$\|\boldsymbol{\mu}\|/10^{-20}$	$\|\boldsymbol{m}\|/10^{-20}$	cos θ	g_{CD}	$\|\boldsymbol{m}\|/\|\boldsymbol{\mu}\|$	Configurations
$1\ ^1$B (S_1)	412	0.001	3.26	30.17	0.45	0.24	0.0143	0.015	H →L (55.%),H-1→L+1(34.%)
$1\ ^1$A (S_2)	376	0.009	-39.93	83.21	0.48	-1	-0.0231	0.006	H →L+1(59.%),H-1→L (19.%)
$2\ ^1$B (S_3)	374	0.084	747.28	258.14	4.04	0.72	0.0448	0.016	H-1→L+1(58.%),H →L (34.%)
$2\ ^1$A (S_4)	351	0.017	-49.01	111.15	0.44	-1	-0.0159	0.004	H-1→L (61.%),H-2→L+1(17.%)
$3\ ^1$A (S_5)	340	0.066	-128.19	218.28	0.59	-1	-0.0108	0.003	H →L+1(34.%),H-2→L+1(23.%)
$3\ ^1$B (S_6)	332	0.003	25.62	45.22	1.06	0.53	0.0501	0.023	H-2→L (82.%),H →L (5.%)
$4\ ^1$B (S_7)	312	0.028	2.22	135.8	0.71	0.02	0.0005	0.005	H-3→L+1(30.%),H-4→L (20.%)
$4\ ^1$A (S_8)	311	0.018	-43.32	107.68	0.4	-1	-0.0149	0.004	H-3→L (36.%),H-2→L+1(31.%)
$5\ ^1$B (S_9)	307	0.005	5.27	58.84	0.21	0.42	0.0061	0.004	H-1→L+2(74.%),H →L+3(11.%)
$5\ ^1$A (S_{10})	304	0.041	-64.28	163.61	0.39	-1	-0.0096	0.002	H →L+2(59.%),H-2→L+1(16.%)
$6\ ^1$B (S_{11})	299	0.017	0.57	104.16	0.31	0.02	0.0002	0.003	H →L+3(52.%),H-3→L+1(27.%)
$6\ ^1$A (S_{12})	288	0.093	-183.63	239.16	0.77	-1	-0.0128	0.003	H-1→L+3(34.%),H-4→L+1(30.%)
$7\ ^1$A (S_{13})	284	0.043	19.33	160.02	0.12	1	0.003	0.001	H-2→L+2(44.%),H-4→L+2(11.%)
$7\ ^1$B (S_{14})	282	0.118	-102.36	266.24	0.67	-0.57	-0.0058	0.003	H-2→L+3(28.%),H-3→L+1(26.%)
$8\ ^1$A (S_{15})	278	0.181	-422.85	327.38	1.29	-1	-0.0158	0.004	H-5→L (31.%),H-2→L+2(21.%)
$8\ ^1$B (S_{16})	275	0.204	46.15	345.26	0.66	0.2	0.0015	0.002	H-4→L (40.%),H-2→L+3(15.%)
$9\ ^1$A (S_{17})	273	0.167	-339.65	311.67	1.09	-1	-0.014	0.003	H →L+4(46.%),H-4→L+1(24.%)
$9\ ^1$B (S_{18})	264	0.060	33.93	183.18	0.35	0.53	0.004	0.002	H-5→L+1(26.%),H-3→L+2(25.%)
$10\ ^1$A (S_{19})	259	0.266	120.30	382.72	0.31	1	0.0033	0.001	H-5→L (23.%),H →L+4(20.%)
$10\ ^1$B (S_{20})	258	0.118	135.21	253.88	1	0.53	0.0084	0.004	H-1→L+4(27.%),H-3→L+2(26.%)

TABLE C16: Excitation energies (λ_{abs}, nm), Corresponding Oscillator Strength(f_{osc}), Orbitals involved in the transitions, $|\boldsymbol{\mu}|$, $|\boldsymbol{m}|$, cos θ, R, g_{CD} and $|\boldsymbol{m}|/|\boldsymbol{\mu}|$ of **4F8H**. $|\boldsymbol{\mu}|$, $|\boldsymbol{m}|$, and R are in esu·cm, erg·G^{-1} and esu·cm·erg·G^{-1} units, respectively.

4F8H									
Excited States	λ_{abs}	f_{osc}	$R/10^{-40}$	$\|\boldsymbol{\mu}\|/10^{-20}$	$\|\boldsymbol{m}\|/10^{-20}$	cos θ	g_{CD}	$\|\boldsymbol{m}\|/\|\boldsymbol{\mu}\|$	Configurations
$1\ ^1$B (S_1)	413	0.001	-2.95	32.28	0.2	-0.47	-0.0113	0.006	H →L (50.%),H-1→L+1(40.%)
$1\ ^1$A (S_2)	382	0.013	-61.84	101.21	0.61	-1	-0.0241	0.006	H →L+1(65.%),H-1→L (11.%)
$2\ ^1$B (S_3)	377	0.075	701.30	245.54	3.95	0.72	0.0465	0.016	H-1→L+1(52.%),H →L (40.%)
$2\ ^1$A (S_4)	354	0.012	-40.88	94.28	0.43	-1	-0.0184	0.005	H-1→L (67.%),H-2→L+1(18.%)
$3\ ^1$A (S_5)	340	0.068	-115.05	221.76	0.52	-1	-0.0094	0.002	H →L+1(30.%),H-2→L+1(22.%)
$3\ ^1$B (S_6)	336	0.003	53.02	43.75	1.36	0.89	0.1107	0.031	H-2→L (84.%),H →L (4.%)
$4\ ^1$B (S_7)	319	0.056	-19.80	195.05	0.39	-0.26	-0.0021	0.002	H-3→L+1(33.%),H-4→L (17.%)
$4\ ^1$A (S_8)	316	0.031	-69.00	145.3	0.47	-1	-0.0131	0.003	H-2→L+1(38.%),H-3→L (26.%)
$5\ ^1$B (S_9)	310	0.012	-5.23	87.03	0.07	-0.87	-0.0028	0.001	H-1→L+2(78.%),H →L+3(6.%)
$5\ ^1$A (S_{10})	308	0.024	-33.28	125.68	0.26	-1	-0.0084	0.002	H →L+2(58.%),H-3→L (28.%)
$6\ ^1$B (S_{11})	302	0.018	6.02	107.45	0.29	0.2	0.0021	0.003	H →L+3(57.%),H-3→L+1(30.%)
$6\ ^1$A (S_{12})	292	0.089	-104.55	234.53	0.45	-1	-0.0076	0.002	H-1→L+3(39.%),H-2→L+2(13.%)
$7\ ^1$A (S_{13})	291	0.000	-10.30	14.16	0.73	-1	-0.205	0.051	H-2→L+2(48.%),H-4→L+1(14.%)
$7\ ^1$B (S_{14})	283	0.052	-74.42	176.93	0.59	-0.71	-0.0095	0.003	H-2→L+3(39.%),H-3→L+1(20.%)
$8\ ^1$B (S_{15})	278	0.271	24.89	399.72	0.82	0.08	0.0006	0.002	H-4→L (36.%),H-1→L+4(17.%)
$8\ ^1$A (S_{16})	276	0.105	-180.87	248.87	0.73	-1	-0.0117	0.003	H →L+4(25.%),H-5→L (24.%)
$9\ ^1$A (S_{17})	273	0.413	-622.93	489.65	1.27	-1	-0.0104	0.003	H-4→L+1(34.%),H →L+4(25.%)
$9\ ^1$B (S_{18})	268	0.016	23.35	94.72	0.26	0.97	0.0104	0.003	H-3→L+2(52.%),H-6→L+1(18.%)
$10\ ^1$A (S_{19})	263	0.035	71.58	140.46	0.51	1	0.0145	0.004	H-6→L (36.%),H-5→L (23.%)
$10\ ^1$B (S_{20})	261	0.089	72.68	222.45	0.36	0.9	0.0059	0.002	H-6→L+1(39.%),H-1→L+4(16.%)

TABLE C17: Excitation energies (λ_{abs}, nm), Corresponding Oscillator Strength(f_{osc}), Orbitals involved in the transitions, $|\boldsymbol{\mu}|$, $|\boldsymbol{m}|$, cos θ, R, g_{CD} and $|\boldsymbol{m}|/|\boldsymbol{\mu}|$ of **8F8H**. $|\boldsymbol{\mu}|$, $|\boldsymbol{m}|$, and R are in esu·cm, erg·G^{-1} and esu·cm·erg·G^{-1} units, respectively.

8F8H									
Excited States	λ_{abs}	f_{osc}	$R/10^{-40}$	$\|\boldsymbol{\mu}\|/10^{-20}$	$\|\boldsymbol{m}\|/10^{-20}$	cos θ	g_{CD}	$\|\boldsymbol{m}\|/\|\boldsymbol{\mu}\|$	Configurations
$1\ ^1$B (S_1)	415	0.000	0.27	15.31	0.2	0.09	0.0047	0.013	H →L (49.%),H-1→L+1(41.%)
$1\ ^1$A (S_2)	383	0.004	-22.30	55.55	0.4	-1	-0.0289	0.007	H →L+1(54.%),H-1→L (23.%)
$2\ ^1$B (S_3)	379	0.074	690.94	244.05	3.98	0.71	0.0464	0.016	H-1→L+1(51.%),H →L (41.%)
$2\ ^1$A (S_4)	355	0.029	-94.25	148.28	0.64	-1	-0.0171	0.004	H-1→L (66.%),H-2→L+1(14.%)
$3\ ^1$A (S_5)	342	0.051	-93.95	192.76	0.49	-1	-0.0101	0.003	H →L+1(35.%),H-2→L+1(28.%)
$3\ ^1$B (S_6)	334	0.002	21.27	36.75	0.96	0.6	0.063	0.026	H-2→L (80.%),H →L (4.%)
$4\ ^1$B (S_7)	319	0.018	4.63	111.15	0.55	0.08	0.0015	0.005	H-3→L+1(31.%),H-1→L+2(18.%)
$4\ ^1$A (S_8)	314	0.029	-79.40	138.36	0.57	-1	-0.0166	0.004	H-3→L (36.%),H-2→L+1(30.%)
$5\ ^1$B (S_9)	311	0.024	-4.81	124.68	0.15	-0.26	-0.0012	0.001	H-1→L+2(65.%),H-4→L (9.%)
$5\ ^1$A (S_{10})	308	0.039	-69.35	158.87	0.44	-1	-0.011	0.003	H →L+2(63.%),H-3→L (19.%)
$6\ ^1$B (S_{11})	299	0.007	-7.19	67.87	0.16	-0.66	-0.0062	0.002	H →L+3(53.%),H-3→L+1(28.%)
$6\ ^1$A (S_{12})	291	0.050	-95.90	176.57	0.54	-1	-0.0123	0.003	H-1→L+3(33.%),H-4→L+1(28.%)
$7\ ^1$A (S_{13})	287	0.046	15.48	166.65	0.09	1	0.0022	0.001	H-2→L+2(51.%),H-4→L+2(12.%)
$7\ ^1$B (S_{14})	284	0.143	-95.66	294.21	0.97	-0.34	-0.0044	0.003	H-3→L+1(23.%),H →L+3(20.%)
$8\ ^1$A (S_{15})	280	0.163	-387.17	311.99	1.24	-1	-0.0159	0.004	H-5→L (36.%),H-1→L+3(20.%)
$8\ ^1$B (S_{16})	276	0.145	56.67	291.92	0.63	0.31	0.0027	0.002	H-4→L (38.%),H-2→L+3(22.%)
$9\ ^1$A (S_{17})	274	0.215	-360.81	354.21	1.02	-1	-0.0115	0.003	H →L+4(45.%),H-4→L+1(27.%)
$9\ ^1$B (S_{18})	269	0.032	1.78	134.22	0.12	0.11	0.0004	0.001	H-5→L+1(36.%),H-3→L+2(21.%)
$10\ ^1$A (S_{19})	262	0.260	145.22	380.81	0.38	1	0.004	0.001	H →L+4(26.%),H-5→L (21.%)
$10\ ^1$B (S_{20})	261	0.079	153.01	209.45	1.07	0.68	0.014	0.005	H-3→L+2(41.%),H-1→L+4(16.%)

TABLE C18: Charge Transfer (ω_{CT}), Participation Ratio of Natural Transition Orbitals (PR_{NTO}) and Exciton Size (d_{exc} in Å) for **5H** and its three fluorinated derivatives. Results are obtained at RI-ADC(2)/def2-TZVP level.

5H					**2F5H**				**4F5H**				**8F5H**			
State Number	State	ω_{CT}	PR_{NTO}	d_{exc}	State	ω_{CT}	PR_{NTO}	d_{exc}	State	ω_{CT}	PR_{NTO}	d_{exc}	State	ω_{CT}	PR_{NTO}	d_{exc}
(S_1)	1 ^{1}A	0.78	2.08	4.06	1 ^{1} A	0.78	1.98	4.15	1 ^{1} A	0.77	1.86	4.13	1 ^{1} A	0.78	1.92	4.15
(S_2)	1 ^{1}B	0.77	1.81	4.23	1 ^{1} B	0.76	1.33	4.19	1 ^{1} B	0.75	1.30	4.22	1 ^{1} B	0.76	1.36	4.26
(S_3)	2 ^{1}B	0.74	1.77	4.05	2 ^{1} B	0.68	2.52	3.78	2 ^{1} B	0.69	1.77	3.90	2 ^{1} B	0.69	2.63	3.84
(S_4)	3 ^{1}B	0.78	1.78	4.24	2 ^{1} A	0.78	1.92	4.19	2 ^{1} A	0.78	1.69	4.18	2 ^{1} A	0.78	1.86	4.22
(S_5)	2 ^{1}A	0.78	1.99	4.10	3 ^{1} B	0.77	1.36	4.18	3 ^{1} B	0.77	1.41	4.15	3 ^{1} B	0.77	1.27	4.20
(S_6)	3 ^{1}A	0.90	1.93	4.94	3 ^{1} A	0.80	1.21	4.47	3 ^{1} A	0.79	1.35	4.40	3 ^{1} A	0.79	1.33	4.48
(S_7)	4 ^{1}A	0.74	3.13	4.04	4 ^{1} A	0.75	1.87	4.14	4 ^{1} A	0.76	1.83	4.28	4 ^{1} A	0.77	2.23	4.33
(S_8)	4 ^{1}B	0.78	2.47	4.26	4 ^{1} B	0.82	2.70	4.41	4 ^{1} B	0.81	3.26	4.38	4 ^{1} B	0.82	3.05	4.52
(S_9)	5 ^{1}A	0.73	3.20	4.08	5 ^{1} A	0.65	3.06	3.68	5 ^{1} A	0.69	2.36	3.83	5 ^{1} A	0.68	3.00	3.85
(S_{10})	5 ^{1}B	0.90	2.99	4.87	5 ^{1} B	0.85	3.01	4.64	5 ^{1} B	0.85	2.35	4.63	5 ^{1} B	0.82	2.89	4.46
(S_{11})	6 ^{1}A	0.82	2.29	4.50	6 ^{1} A	0.88	1.87	4.59	6 ^{1} A	0.89	2.30	4.65	6 ^{1} A	0.88	1.84	4.72
(S_{12})	6 ^{1}B	0.82	2.47	4.65	6 ^{1} B	0.92	2.62	4.91	6 ^{1} B	0.91	1.88	4.84	6 ^{1} B	0.92	2.53	5.05
(S_{13})	7 ^{1}B	0.68	1.97	4.01	7 ^{1} B	0.76	2.61	4.22	7 ^{1} B	0.73	2.74	4.06	7 ^{1} B	0.75	3.05	4.15
(S_{14})	7 ^{1}A	0.71	2.37	3.87	7 ^{1} A	0.86	4.23	4.48	7 ^{1} A	0.82	3.13	4.42	7 ^{1} A	0.79	3.36	4.21
(S_{15})	8 ^{1}B	0.79	2.62	4.16	8 ^{1} B	0.64	2.08	3.82	8 ^{1} B	0.76	1.40	4.53	8 ^{1} A	0.78	1.81	4.42
(S_{16})	8 ^{1}A	0.88	4.37	4.40	8 ^{1} A	0.71	1.98	3.92	8 ^{1} A	0.77	1.71	4.34	8 ^{1} B	0.68	1.71	4.21
(S_{17})	9 ^{1}B	0.81	2.60	4.05	9 ^{1} B	0.71	2.53	3.70	9 ^{1} B	0.72	2.00	3.70	9 ^{1} A	0.57	1.83	3.72
(S_{18})	9 ^{1}A	0.87	3.71	4.81	10 ^{1} B	0.89	2.36	4.98	9 ^{1} A	0.84	2.10	4.47	9 ^{1} B	0.73	2.35	3.82
(S_{19})	10 ^{1}B	0.84	3.01	4.65	9 ^{1} A	0.87	3.16	4.67	10 ^{1} B	0.77	1.56	4.38	10 ^{1} A	0.86	2.64	4.72
(S_{20})	10 ^{1}A	0.87	3.07	4.83	10 ^{1} A	0.81	3.66	4.43	10 ^{1} A	0.76	2.35	4.18	10 ^{1} B	0.51	2.25	3.57

TABLE C19: Charge Transfer (ω_{CT}), Participation Ratio of Natural Transition Orbitals (PR_{NTO}) and Exciton Size (d_{exc} in Å) for **6H** and its three fluorinated derivatives. Results are obtained at RI-ADC(2)/def2-TZVP level.

6H					**2F6H**				**4F6H**				**8F6H**			
State Number	State	ω_{CT}	PR_{NTO}	d_{exc}	State	ω_{CT}	PR_{NTO}	d_{exc}	State	ω_{CT}	PR_{NTO}	d_{exc}	State	ω_{CT}	PR_{NTO}	d_{exc}
(S_1)	1 ^{1} B	0.81	2.11	4.19	1 ^{1} B	0.81	2.07	4.22	1 ^{1} B	0.81	2.12	4.20	1 ^{1} B	0.81	2.07	4.21
(S_2)	1 ^{1} A	0.81	1.62	4.38	1 ^{1} A	0.81	1.56	4.35	1 ^{1} A	0.81	1.73	4.35	1 ^{1} A	0.81	1.89	4.35
(S_3)	2 ^{1} B	0.81	2.00	4.31	2 ^{1} B	0.79	1.98	4.25	2 ^{1} B	0.78	2.03	4.20	2 ^{1} B	0.79	1.99	4.25
(S_4)	2 ^{1} A	0.76	2.84	4.10	2 ^{1} A	0.75	2.69	4.10	2 ^{1} A	0.76	2.40	4.16	2 ^{1} A	0.77	2.20	4.17
(S_5)	3 ^{1} A	0.83	1.53	4.37	3 ^{1} B	0.84	1.10	4.46	3 ^{1} B	0.83	1.07	4.41	3 ^{1} B	0.83	1.14	4.42
(S_6)	3 ^{1} B	0.82	1.26	4.43	3 ^{1} A	0.83	1.61	4.43	3 ^{1} A	0.84	1.90	4.49	3 ^{1} A	0.83	1.82	4.43
(S_7)	4 ^{1} A	0.92	3.08	5.00	4 ^{1} A	0.92	2.66	4.88	4 ^{1} A	0.89	2.20	4.78	4 ^{1} B	0.71	3.39	3.92
(S_8)	4 ^{1} B	0.79	2.42	4.35	4 ^{1} B	0.70	3.61	3.87	4 ^{1} B	0.70	3.37	3.93	4 ^{1} A	0.90	2.51	4.85
(S_9)	5 ^{1} B	0.82	1.38	4.43	5 ^{1} B	0.87	1.82	4.77	5 ^{1} B	0.89	1.81	4.89	5 ^{1} B	0.87	2.20	4.75
(S_{10})	6 ^{1} B	0.87	2.86	4.82	6 ^{1} B	0.88	2.46	4.82	5 ^{1} A	0.83	2.53	4.48	6 ^{1} B	0.90	2.80	4.93
(S_{11})	5 ^{1} A	0.91	3.42	4.93	5 ^{1} A	0.87	2.53	4.71	6 ^{1} B	0.87	2.15	4.74	5 ^{1} A	0.86	2.64	4.67
(S_{12})	6 ^{1} A	0.78	2.48	4.28	6 ^{1} A	0.84	1.76	4.59	6 ^{1} A	0.88	1.66	4.79	6 ^{1} A	0.85	1.81	4.65
(S_{13})	7 ^{1} B	0.80	2.06	4.30	7 ^{1} B	0.81	3.00	4.28	7 ^{1} B	0.81	2.93	4.28	7 ^{1} B	0.80	2.93	4.27
(S_{14})	7 ^{1} A	0.75	2.73	4.07	7 ^{1} A	0.72	3.00	3.99	7 ^{1} A	0.70	2.99	3.95	7 ^{1} A	0.73	2.88	4.02
(S_{15})	8 ^{1} B	0.90	3.10	4.83	8 ^{1} B	0.85	2.93	4.55	8 ^{1} B	0.82	2.76	4.34	8 ^{1} B	0.84	2.75	4.50
(S_{16})	8 ^{1} A	0.77	2.00	4.23	8 ^{1} A	0.77	3.66	4.19	8 ^{1} A	0.81	2.56	4.54	8 ^{1} A	0.75	3.56	4.18
(S_{17})	9 ^{1} B	0.82	2.17	4.59	9 ^{1} A	0.84	3.58	4.51	9 ^{1} A	0.88	3.71	4.65	9 ^{1} A	0.86	3.85	4.56
(S_{18})	9 ^{1} A	0.84	4.00	4.52	10 ^{1} A	0.86	3.95	4.61	10 ^{1} A	0.84	3.17	4.44	10 ^{1} A	0.86	3.37	4.70
(S_{19})	10 ^{1} A	0.78	2.27	4.37	9 ^{1} B	0.88	4.90	4.69	9 ^{1} B	0.90	4.03	4.77	9 ^{1} B	0.85	2.48	4.71
(S_{20})	10 ^{1} B	0.85	1.92	4.25	10 ^{1} B	0.84	2.55	4.43	10 ^{1} B	0.83	2.75	4.48	10 ^{1} B	0.88	3.70	4.58

TABLE C20: Charge Transfer (ω_{CT}), Participation Ratio of Natural Transition Orbitals (PR_{NTO}) and Exciton Size (d_{exc} in Å) for **7H** and its three fluorinated derivatives. Results are obtained at RI-ADC(2)/def2-TZVP level.

7H					**2F7H**				**4F7H**				**8F7H**			
State Number	State	ω_{CT}	PR_{NTO}	d_{exc}	State	ω_{CT}	PR_{NTO}	d_{exc}	State	ω_{CT}	PR_{NTO}	d_{exc}	State	ω_{CT}	PR_{NTO}	d_{exc}
(S_1)	$1\,^1$ A	0.84	2.08	4.23	$1\,^1$ A	0.83	2.04	4.26	$1\,^1$ A	0.83	2.03	4.26	$1\,^1$ A	0.83	2.07	4.24
(S_2)	$1\,^1$ B	0.84	1.23	4.36	$1\,^1$ B	0.85	1.05	4.50	$1\,^1$ B	0.84	1.07	4.49	$1\,^1$ B	0.84	1.10	4.49
(S_3)	$2\,^1$ B	0.84	1.71	4.48	$2\,^1$ B	0.82	1.28	4.31	$2\,^1$ B	0.82	1.30	4.28	$2\,^1$ B	0.82	1.27	4.30
(S_4)	$3\,^1$ B	0.82	2.63	4.36	$3\,^1$ B	0.79	2.24	4.18	$3\,^1$ B	0.79	2.11	4.18	$3\,^1$ B	0.78	2.18	4.15
(S_5)	$2\,^1$ A	0.85	1.93	4.36	$2\,^1$ A	0.85	2.00	4.40	$2\,^1$ A	0.85	2.00	4.41	$2\,^1$ A	0.86	2.00	4.45
(S_6)	$3\,^1$ A	0.87	1.79	4.67	$3\,^1$ A	0.82	1.88	4.41	$3\,^1$ A	0.83	1.41	4.47	$3\,^1$ A	0.82	1.55	4.41
(S_7)	$4\,^1$ A	0.88	2.36	4.70	$4\,^1$ A	0.92	2.14	4.86	$4\,^1$ B	0.89	2.79	4.62	$4\,^1$ A	0.90	2.27	4.80
(S_8)	$4\,^1$ B	0.88	3.24	4.63	$4\,^1$ B	0.89	2.65	4.65	$4\,^1$ A	0.88	2.05	4.68	$4\,^1$ B	0.90	2.78	4.67
(S_9)	$5\,^1$ A	0.80	2.35	4.27	$5\,^1$ A	0.79	3.60	4.24	$5\,^1$ A	0.79	3.15	4.24	$5\,^1$ A	0.80	3.45	4.28
(S_{10})	$5\,^1$ B	0.91	1.88	4.80	$6\,^1$ A	0.90	1.81	4.59	$5\,^1$ B	0.91	2.17	4.83	$5\,^1$ B	0.92	1.69	4.72
(S_{11})	$6\,^1$ A	0.87	2.67	4.64	$5\,^1$ B	0.94	2.36	4.84	$6\,^1$ A	0.93	2.05	4.72	$6\,^1$ A	0.88	2.12	4.72
(S_{12})	$6\,^1$ B	0.83	3.02	4.47	$6\,^1$ B	0.88	2.09	4.78	$6\,^1$ B	0.94	1.77	4.90	$6\,^1$ B	0.95	1.94	4.94
(S_{13})	$7\,^1$ B	0.88	2.66	4.65	$7\,^1$ B	0.79	3.20	4.26	$7\,^1$ B	0.80	3.29	4.31	$7\,^1$ B	0.81	3.01	4.36
(S_{14})	$7\,^1$ A	0.89	3.07	4.80	$7\,^1$ A	0.89	2.98	4.79	$7\,^1$ A	0.90	2.81	4.86	$7\,^1$ A	0.88	3.47	4.76
(S_{15})	$8\,^1$ A	0.84	3.08	4.41	$8\,^1$ A	0.81	2.90	4.34	$8\,^1$ A	0.81	2.74	4.37	$8\,^1$ A	0.82	2.81	4.40
(S_{16})	$8\,^1$ B	0.86	1.72	4.65	$8\,^1$ B	0.82	3.61	4.28	$8\,^1$ B	0.87	2.88	4.54	$8\,^1$ B	0.90	2.83	4.63
(S_{17})	$9\,^1$ B	0.85	3.57	4.38	$9\,^1$ B	0.85	1.50	4.51	$9\,^1$ B	0.81	2.91	4.28	$9\,^1$ B	0.80	3.32	4.27
(S_{18})	$9\,^1$ A	0.87	2.46	4.53	$9\,^1$ A	0.88	2.73	4.56	$9\,^1$ A	0.86	3.04	4.48	$9\,^1$ A	0.87	2.34	4.51
(S_{19})	$10\,^1$ A	0.81	2.30	4.32	$10\,^1$ A	0.87	2.38	4.42	$10\,^1$ A	0.88	2.93	4.36	$10\,^1$ A	0.86	2.31	4.38
(S_{20})	$10\,^1$ B	0.86	2.04	4.47	$10\,^1$ B	0.86	3.32	4.40	$10\,^1$ B	0.85	2.87	4.41	$10\,^1$ B	0.82	3.02	4.34

TABLE C21: Charge Transfer (ω_{CT}), Participation Ratio of Natural Transition Orbitals (PR_{NTO}) and Exciton Size (d_{exc} in Å) for **8H** and its three fluorinated derivatives. Results are obtained at RI-ADC(2)/def2-TZVP level.

8H					**2F8H**				**4F8H**				**8F8H**			
State Number	State	ω_{CT}	PR_{NTO}	d_{exc}	State	ω_{CT}	PR_{NTO}	d_{exc}	State	ω_{CT}	PR_{NTO}	d_{exc}	State	ω_{CT}	PR_{NTO}	d_{exc}
(S_1)	$1\,^1$ B	0.86	2.09	4.31	$1\,^1$ B	0.86	1.95	4.39	$1\,^1$ B	0.86	2.05	4.38	$1\,^1$ B	0.86	2.06	4.37
(S_2)	$2\,^1$ B	0.85	2.00	4.42	$1\,^1$ A	0.86	1.65	4.54	$1\,^1$ A	0.86	1.42	4.53	$1\,^1$ A	0.86	1.75	4.52
(S_3)	$1\,^1$ A	0.87	1.55	4.54	$2\,^1$ B	0.85	1.92	4.44	$2\,^1$ B	0.85	1.98	4.44	$2\,^1$ B	0.85	1.99	4.46
(S_4)	$2\,^1$ A	0.84	2.11	4.34	$2\,^1$ A	0.84	1.81	4.34	$2\,^1$ A	0.84	1.69	4.35	$2\,^1$ A	0.85	1.73	4.40
(S_5)	$3\,^1$ B	0.90	1.06	4.65	$3\,^1$ A	0.85	1.97	4.43	$3\,^1$ A	0.86	2.06	4.43	$3\,^1$ A	0.84	1.81	4.39
(S_6)	$3\,^1$ A	0.87	1.97	4.40	$3\,^1$ B	0.88	1.10	4.48	$3\,^1$ B	0.89	1.08	4.51	$3\,^1$ B	0.87	1.16	4.43
(S_7)	$4\,^1$ A	0.91	2.53	4.73	$4\,^1$ A	0.79	3.13	4.26	$4\,^1$ B	0.78	2.97	4.25	$4\,^1$ B	0.83	3.11	4.43
(S_8)	$4\,^1$ B	0.85	1.84	4.48	$4\,^1$ B	0.91	2.78	4.70	$4\,^1$ A	0.89	2.64	4.57	$4\,^1$ A	0.90	2.68	4.64
(S_9)	$5\,^1$ B	0.87	2.03	4.60	$5\,^1$ B	0.89	1.49	4.67	$5\,^1$ B	0.91	1.38	4.74	$5\,^1$ B	0.87	1.69	4.59
(S_{10})	$5\,^1$ A	0.95	1.83	4.85	$5\,^1$ A	0.95	2.11	4.86	$5\,^1$ A	0.96	2.13	4.94	$5\,^1$ A	0.95	1.96	4.89
(S_{11})	$6\,^1$ B	0.88	3.12	4.70	$6\,^1$ B	0.95	2.42	5.04	$6\,^1$ B	0.95	2.09	5.01	$6\,^1$ B	0.95	2.36	5.05
(S_{12})	$6\,^1$ A	0.83	2.08	4.44	$6\,^1$ A	0.83	3.15	4.45	$6\,^1$ A	0.83	3.20	4.40	$6\,^1$ A	0.84	3.11	4.51
(S_{13})	$7\,^1$ A	0.84	3.00	4.45	$7\,^1$ A	0.80	2.20	4.28	$7\,^1$ A	0.81	2.19	4.36	$7\,^1$ A	0.79	1.82	4.26
(S_{14})	$7\,^1$ B	0.89	2.58	4.76	$7\,^1$ B	0.84	2.77	4.40	$7\,^1$ B	0.84	2.63	4.44	$7\,^1$ B	0.84	2.82	4.42
(S_{15})	$8\,^1$ A	0.86	2.29	4.49	$8\,^1$ A	0.83	3.24	4.41	$8\,^1$ B	0.87	3.30	4.65	$8\,^1$ A	0.84	3.10	4.49
(S_{16})	$8\,^1$ B	0.89	3.68	4.63	$8\,^1$ B	0.90	3.06	4.74	$8\,^1$ A	0.84	3.50	4.45	$8\,^1$ B	0.88	2.97	4.67
(S_{17})	$9\,^1$ A	0.85	3.35	4.56	$9\,^1$ A	0.91	2.72	4.90	$9\,^1$ A	0.88	3.16	4.70	$9\,^1$ A	0.91	2.64	4.93
(S_{18})	$9\,^1$ B	0.89	3.56	4.61	$9\,^1$ B	0.89	3.50	4.70	$9\,^1$ B	0.90	2.47	4.73	$9\,^1$ B	0.90	3.02	4.73
(S_{19})	$10\,^1$ B	0.89	3.02	4.68	$10\,^1$ A	0.89	3.47	4.56	$10\,^1$ A	0.91	2.19	4.62	$10\,^1$ A	0.88	3.69	4.54
(S_{20})	$10\,^1$ A	0.87	3.25	4.57	$10\,^1$ B	0.91	4.32	4.73	$10\,^1$ B	0.91	2.35	4.61	$10\,^1$ B	0.90	3.56	4.69

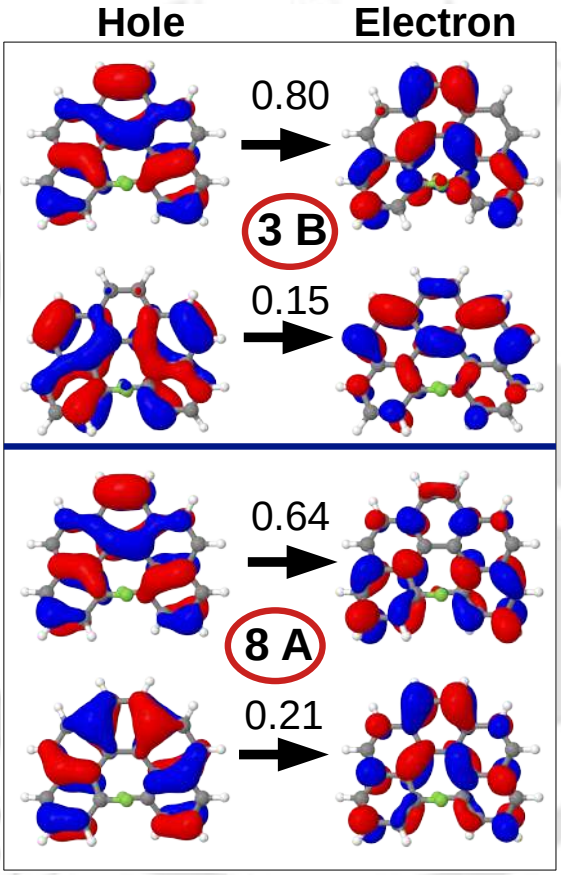

FIGURE C2: Natural transition orbitals for some selected excited states of **2F5H**. Results are obtained from vertical excitation calculation at RI-ADC(2)/def2-TZVP level.

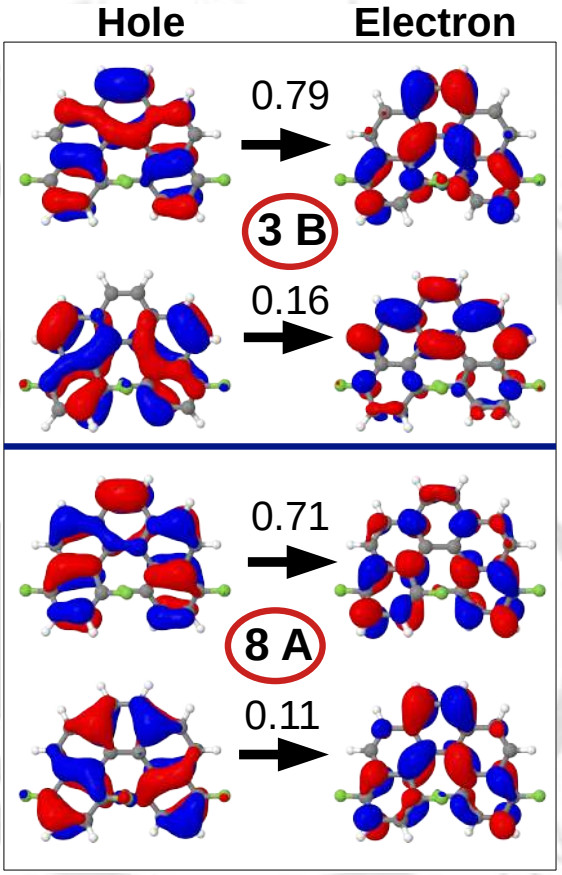

FIGURE C3: Natural transition orbitals for some selected excited states of **4F5H**. Results are obtained from vertical excitation calculation at RI-ADC(2)/def2-TZVP level.

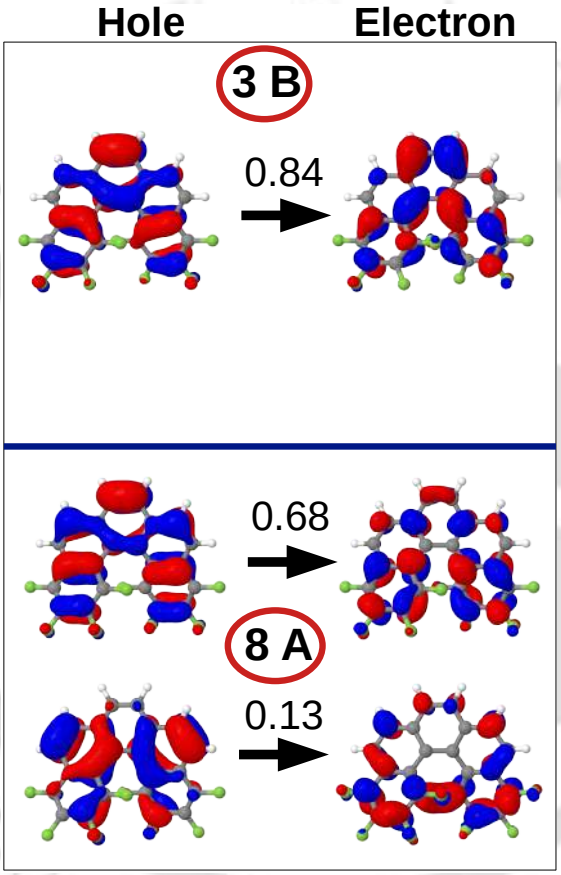

FIGURE C4: Natural transition orbitals for some selected excited states of **8F5H**. Results are obtained from vertical excitation calculation at RI-ADC(2)/def2-TZVP level.

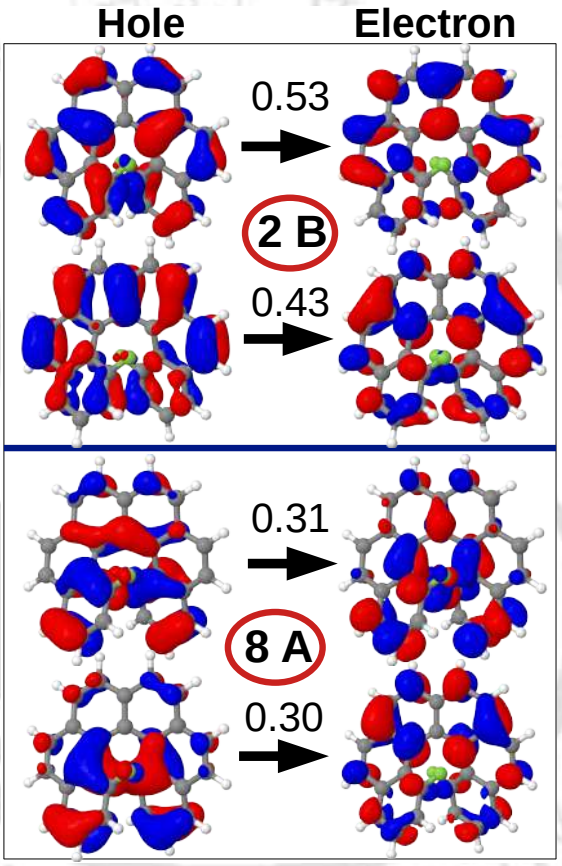

FIGURE C5: Natural transition orbitals for some selected excited states of **2F6H**. Results are obtained from vertical excitation calculation at RI-ADC(2)/def2-TZVP.

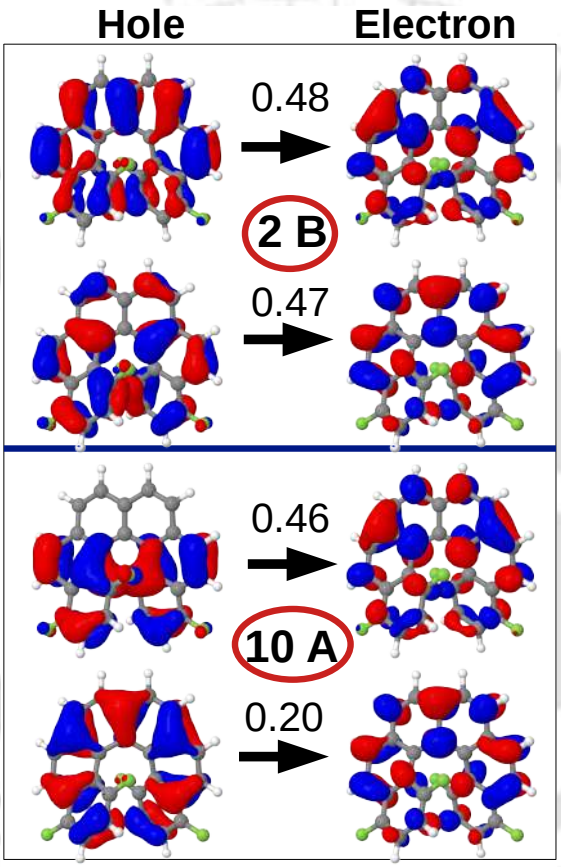

FIGURE C6: Natural transition orbitals for some selected excited states of **4F6H**. Results are obtained from vertical excitation calculation at RI-ADC(2)/def2-TZVP.

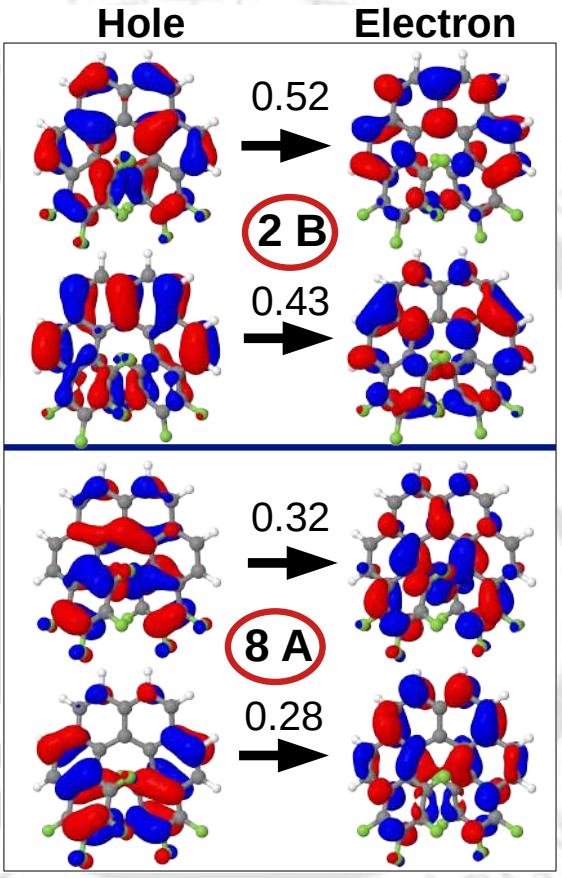

FIGURE C7: Natural transition orbitals for some selected excited states of **8F6H**. Results are obtained from vertical excitation calculation at RI-ADC(2)/def2-TZVP.

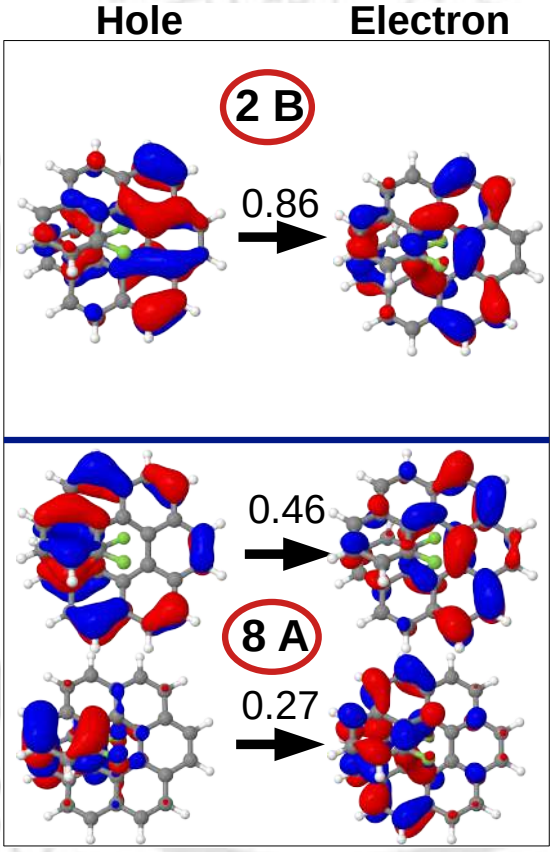

FIGURE C8: Natural transition orbitals for some selected excited states of **2F7H**. Results are obtained from vertical excitation calculation at RI-ADC(2)/def2-TZVP.

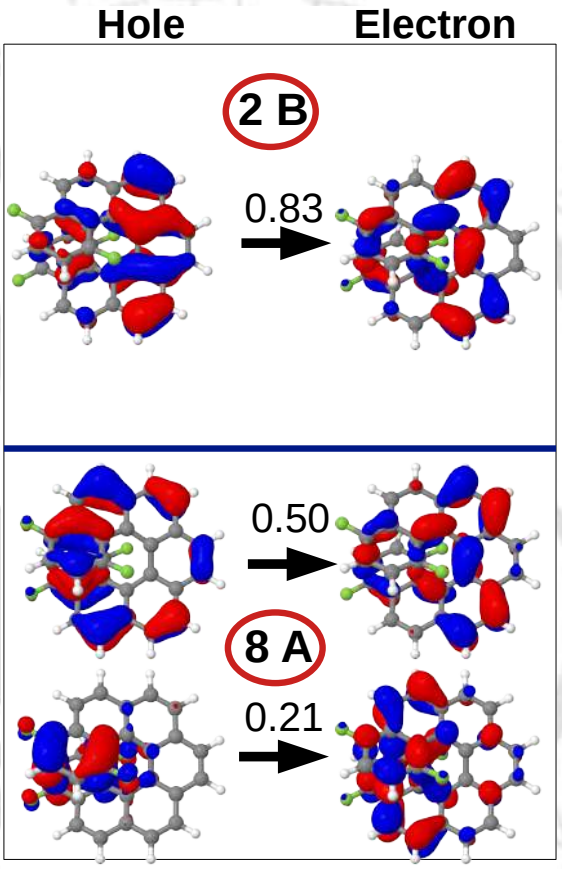

FIGURE C9: Natural transition orbitals for some selected excited states of **4F7H**. Results are obtained from vertical excitation calculation at RI-ADC(2)/def2-TZVP.

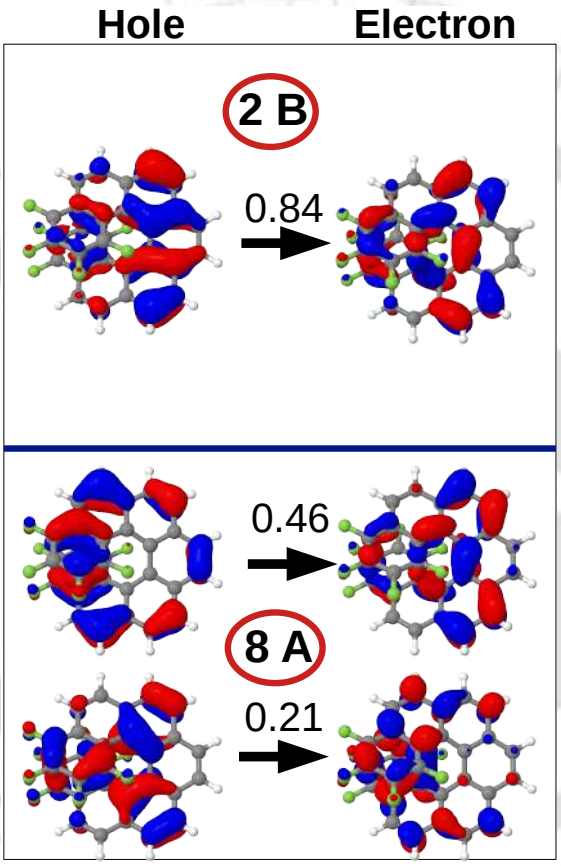

FIGURE C10: Natural transition orbitals for some selected excited states of **8F7H**. Results are obtained from vertical excitation calculation at RI-ADC(2)/def2-TZVP.

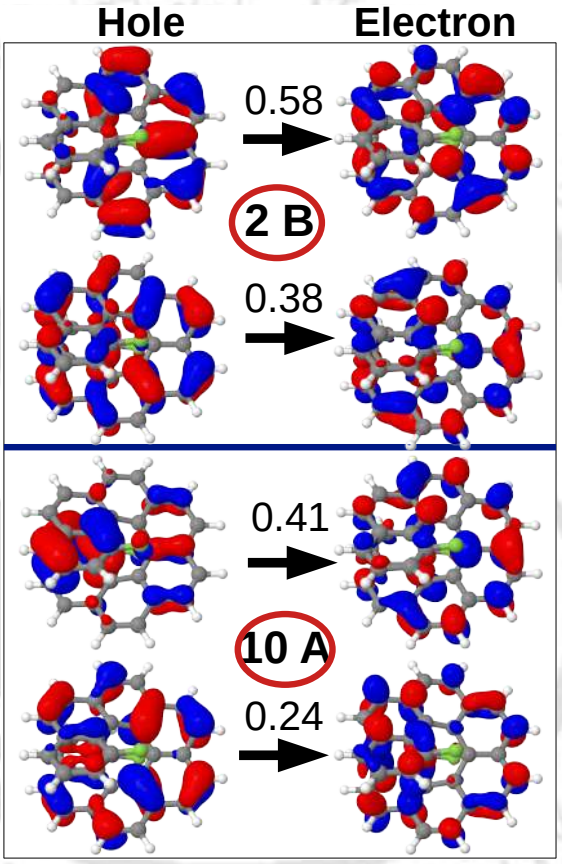

FIGURE C11: Natural transition orbitals for some selected excited states of **2F8H**. Results are obtained from vertical excitation calculation at RI-ADC(2)/def2-TZVP.

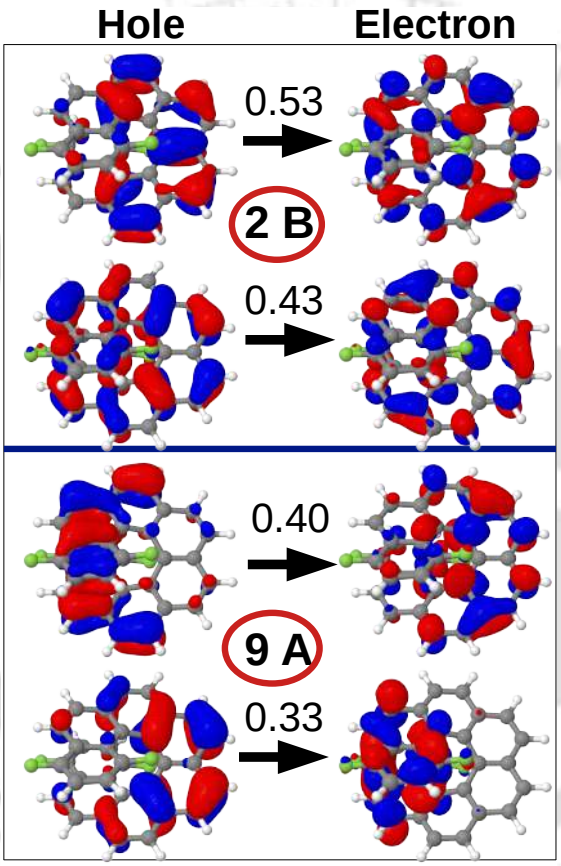

FIGURE C12: Natural transition orbitals for some selected excited states of **4F8H**. Results are obtained from vertical excitation calculation at RI-ADC(2)/def2-TZVP.

TABLE C22: Emission Energies(λ_{em}, nm), Contributions from Various Transitions, Participation Ratio of Natural Transition Orbitals (PR_{NTO}), Exciton Size (d_{exc}, Å), and Charge Transfer (ω_{CT}) of **5H**, **2F5H**, **4F5H**, **8F5H**, **6H**, **2F6H**, **4F6H**, **8F6H**, **7H**, **2F7H**, **4F5H**, **8F7H**, **8H**, **2F8H**, **4F8H**, and **8F8H** for the $S_1 \rightarrow S_0$ transitions. Results are obtained at RI-ADC(2)/def2-TZVP level.

System	λ_{em}	Contributions	PR_{NTO}	d_{exc}	ω_{CT}
5H	390	H ←L (56.%),H-1←L+1(39.%)	1.98	4.15	0.80
2F5H	397	H ←L+1(58.%),H-1←L (36.%)	1.94	4.15	0.78
4F5H	403	H ←L (66.%),H-1←L+1(29.%)	1.79	4.15	0.78
8F5H	402	H ←L+1(63.%),H-1←L (32.%)	1.86	4.15	0.80
6H	411	H-1←L (47.%),H ←L+1(46.%)	2.04	4.26	0.84
2F6H	421	H-1←L (56.%),H ←L+1(36.%)	1.93	4.28	0.84
4F6H	422	H-1←L (51.%),H ←L+1(42.%)	2.02	4.27	0.83
8F6H	424	H ←L (56.%),H-1←L+1(36.%)	1.94	4.24	0.83
7H	447	H ←L (57.%),H-1←L+1(38.%)	1.95	4.29	0.86
2F7H	451	H ←L+1(60.%),H-1←L (34.%)	1.90	4.32	0.86
4F7H	453	H ←L+1(61.%),H-1←L (34.%)	1.89	4.32	0.85
8F7H	453	H ←L+1(54.%),H-1←L (41.%)	2.00	4.29	0.81
8H	462	H-1←L(46.%),H ←L+1 (45.%)	2.03	4.34	0.81
2F8H	496	H ←L (89.%),H-1←L+1(6.%)	1.12	4.55	0.89
4F8H	493	H ←L (89.%) H-1←L+1(7.%)	1.15	4.59	0.92
8F8H	472	H ←L(52.%),H-1←L+1 (42.%)	1.97	4.42	0.84

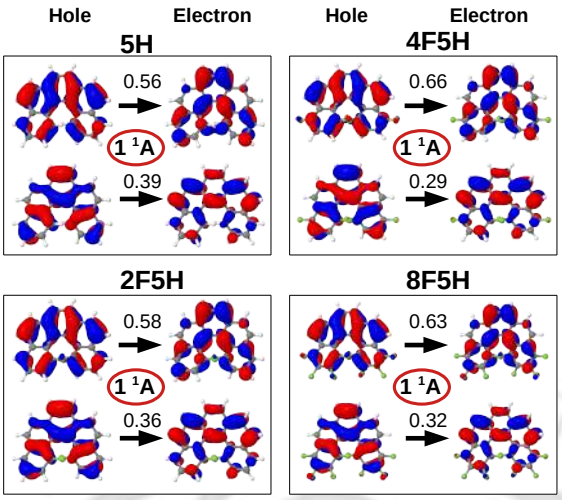

FIGURE C13: Natural transition orbitals corresponding to $S_1 \rightarrow S_0$ transitions in **5H** and its fluorinated derivatives. Results are obtained at RI-ADC(2)/def2-TZVP level.

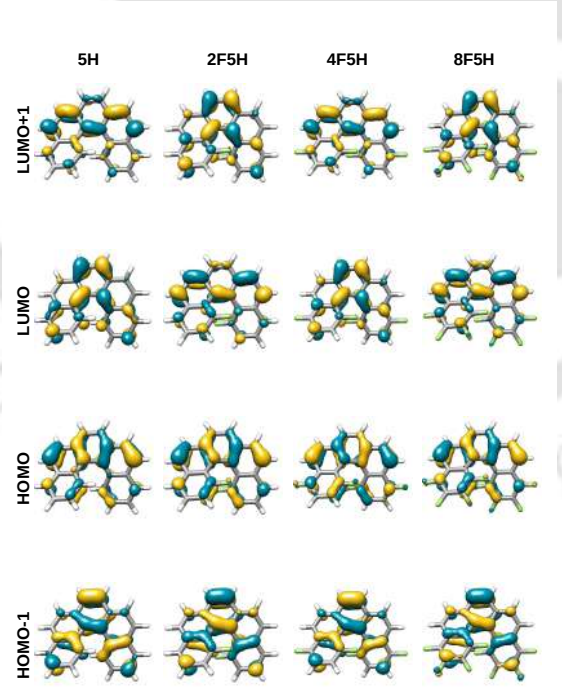

FIGURE C14: Frontier molecular orbitals (HOMO-1 (H-1), HOMO (H), LUMO (L) and LUMO+1 (L+1)) for **5H**, **2F5H**, **4F5H** and **8F6H**.

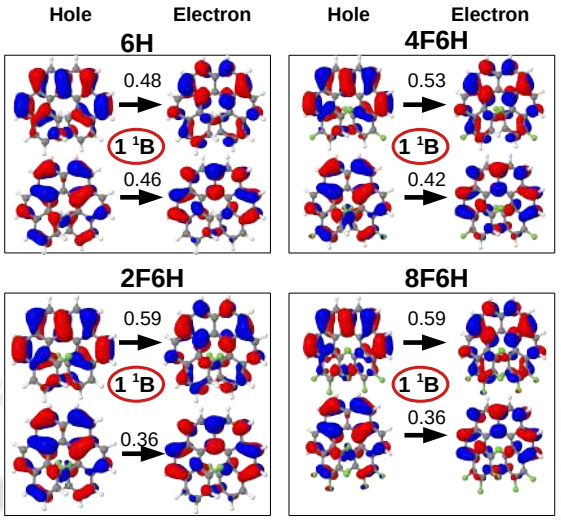

FIGURE C15: Natural transition orbitals corresponding to $S_1 \rightarrow S_0$ transitions in **6H** and its fluorinated derivatives. Results are obtained at RI-ADC(2)/def2-TZVP level.

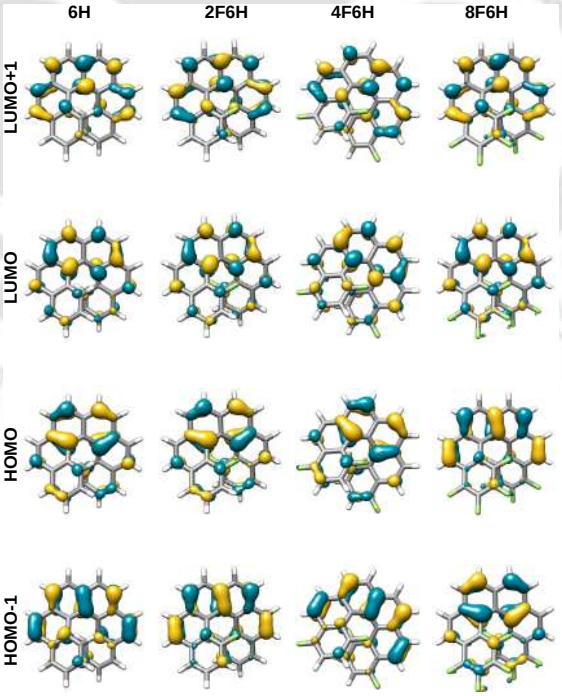

FIGURE C16: Frontier molecular orbitals (HOMO-1 (H-1), HOMO (H), LUMO (L) and LUMO+1 (L+1)) for **6H**, **2F6H**, **4F6H** and **8F6H**.

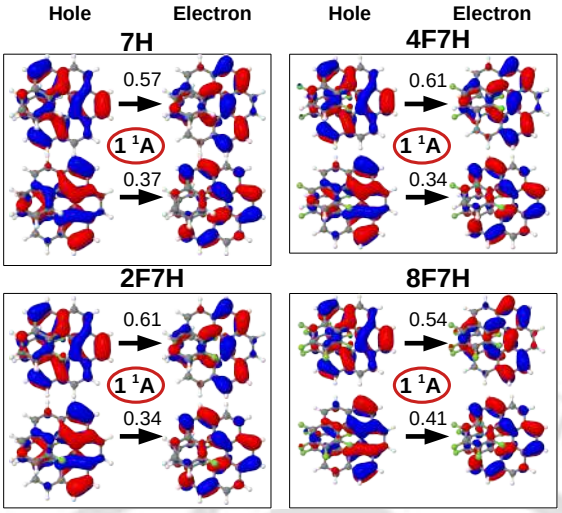

FIGURE C17: Natural transition orbitals corresponding to $S_1 \rightarrow S_0$ transitions in **7H** and fluorinated derivatives. Results are obtained at RI-ADC(2)/def2-TZVP level.

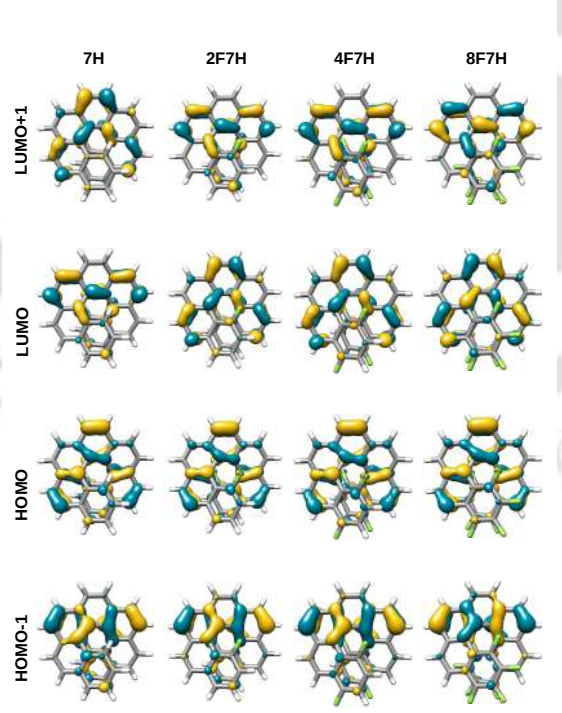

FIGURE C18: Frontier molecular orbitals (HOMO-1 (H-1), HOMO (H), LUMO (L) and LUMO+1 (L+1)) for **7H**, **2F7H**, **4F7H** and **8F7H**.

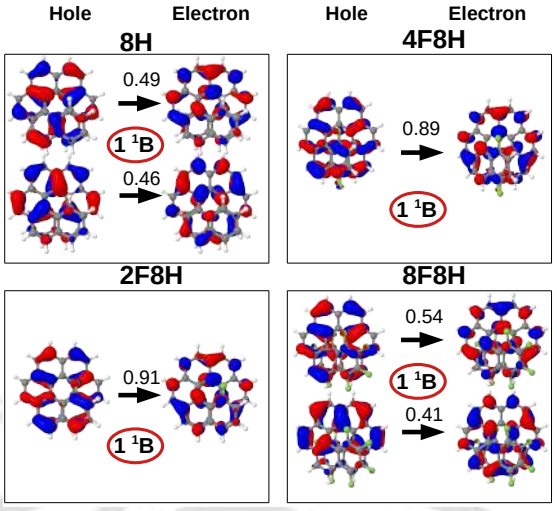

FIGURE C19: Natural transition orbitals corresponding to $S_1 \rightarrow S_0$ transitions in **8H** and fluorinated derivatives. Results are obtained at RI-ADC(2)/def2-TZVP level.

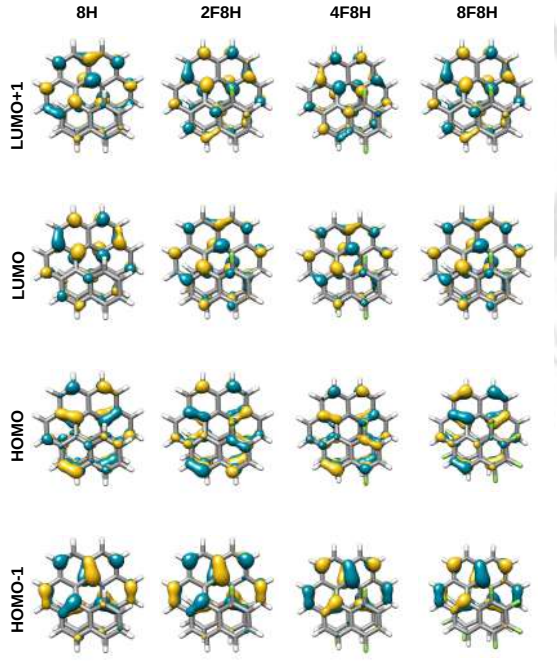

FIGURE C20: Frontier molecular orbitals (HOMO-1 (H-1), HOMO (H), LUMO (L) and LUMO+1 (L+1)) for **8H**, **2F8H**, **4F8H** and **8F8H**.

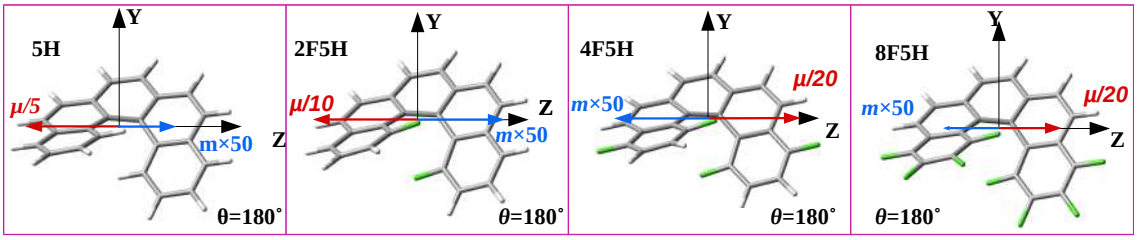

FIGURE C21: Directions of EDTM (in red) and MDTM (in blue) vectors of **5H** along with its three fluorinated derivatives for the $S_1 \rightarrow S_0$ transitions. Results are obtained at RI-ADC(2)/def2-TZVP level of theory.

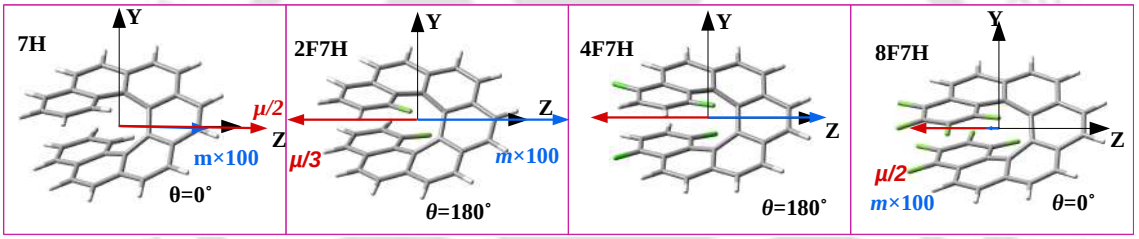

FIGURE C22: Directions of EDTM (in red) and MDTM (in blue) vectors of **7H** along with its three fluorinated derivatives for the $S_1 \rightarrow S_0$ transitions. Results are obtained at RI-ADC(2)/def2-TZVP level of theory.

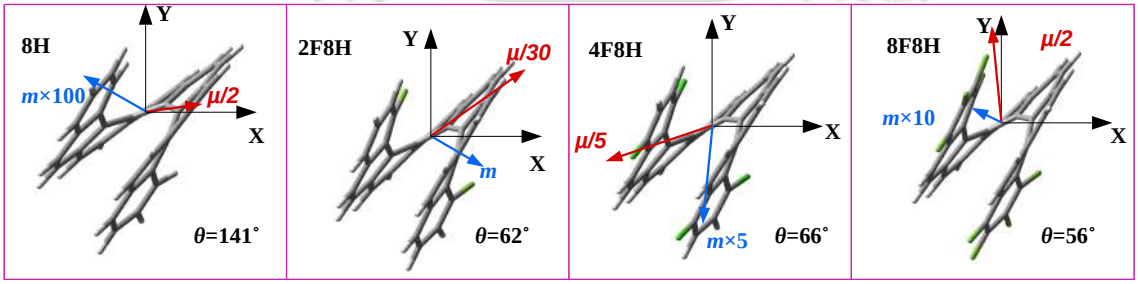

FIGURE C23: Directions of EDTM (in red) and MDTM (in blue) vectors of **8H** along with its three fluorinated derivatives for the $S_1 \rightarrow S_0$ transitions. Results are obtained at RI-ADC(2)/def2-TZVP level of theory.